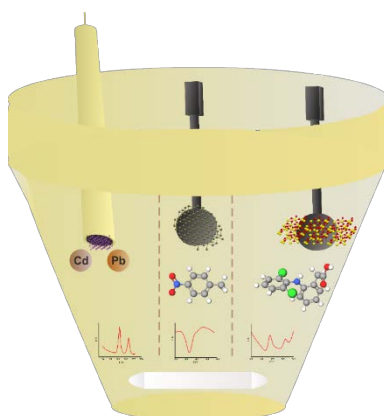




ΠΑΝΕΠΙΣΤΗΜΙΟ ΙΩΑΝΝΙΝΩΝ
ΣΧΟΛΗ ΘΕΤΙΚΩΝ ΕΠΙΣΤΗΜΩΝ
ΤΜΗΜΑ ΧΗΜΕΙΑΣ
ΕΡΓΑΣΤΗΡΙΟ ΑΝΑΛΥΤΙΚΗΣ ΧΗΜΕΙΑΣ

Αλέξανδρος Λαζανάς
Μηχανικός Επιστήμης Υλικών

ΣΥΝΘΕΣΗ ΧΑΡΑΚΤΗΡΙΣΜΟΣ ΚΑΙ ΧΡΗΣΗ ΑΝΟΡΓΑΝΩΝ ΧΑΜΗΛΟΔΙΑΣΤΑΤΩΝ ΥΛΙΚΩΝ ΣΤΗΝ ΑΝΑΠΤΥΞΗ ΗΛΕΚΤΡΟΧΗΜΙΚΩΝ ΑΙΣΘΗΤΗΡΩΝ



Διδακτορική Διατριβή

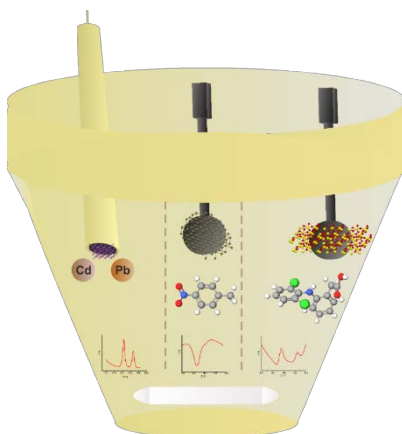
ΙΩΑΝΝΙΝΑ 2022



ΠΑΝΕΠΙΣΤΗΜΙΟ ΙΩΑΝΝΙΝΩΝ
ΣΧΟΛΗ ΘΕΤΙΚΩΝ ΕΠΙΣΤΗΜΩΝ
ΤΜΗΜΑ ΧΗΜΕΙΑΣ
ΕΡΓΑΣΤΗΡΙΟ ΑΝΑΛΥΤΙΚΗΣ ΧΗΜΕΙΑΣ

Αλέξανδρος Λαζανάς
Μηχανικός Επιστήμης Υλικών

ΣΥΝΘΕΣΗ ΧΑΡΑΚΤΗΡΙΣΜΟΣ ΚΑΙ ΧΡΗΣΗ ΑΝΟΡΓΑΝΩΝ ΧΑΜΗΛΟΔΙΑΣΤΑΤΩΝ ΥΛΙΚΩΝ ΣΤΗΝ ΑΝΑΠΤΥΞΗ ΗΛΕΚΤΡΟΧΗΜΙΚΩΝ ΑΙΣΘΗΤΗΡΩΝ



Διδακτορική Διατριβή

ΙΩΑΝΝΙΝΑ 2022

Ημερομηνία ορισμού τριμελούς συμβουλευτικής επιτροπής: 30/03/2018

Ημερομηνία ορισμού θέματος: 23/10/2020

Ημερομηνία άδειας συγγραφής: 20/05/2022

Ημερομηνία ορισμού επταμελούς εξεταστικής επιτροπής: 21/07/2022

Μέλη τριμελούς συμβουλευτικής επιτροπής

Προδρομίδης Μάμας, Καθηγητής (Επιβλέπων)

Αυγερόπουλος Απόστολος, Καθηγητής

Σταλίκας Κωνσταντίνος, Καθηγητής

Μέλη επταμελούς εξεταστικής επιτροπής

Προδρομίδης Μάμας, Καθηγητής (Επιβλέπων)

Αυγερόπουλος Απόστολος, Καθηγητής

Σταλίκας Κωνσταντίνος, Καθηγητής

Οικονόμου Αναστάσιος, Καθηγητής

Σακκάς Βασίλειος, Αναπληρωτής Καθηγητής

Κόκκινος Χρήστος, Αναπληρωτής Καθηγητής

Γκιώκας Δημοσθένης, Αναπληρωτής Καθηγητής

ΤΑ ΜΕΛΗ ΤΗΣ ΕΠΙΤΑΜΕΛΟΥΣ ΕΞΕΤΑΣΤΙΚΗΣ ΕΠΙΤΡΟΠΗΣ

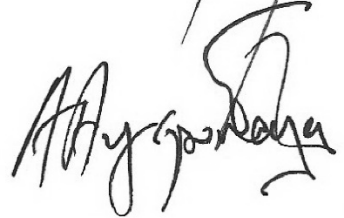
1) Μάμαντος Προδρομίδης,

Καθηγητής Παν/μίου Ιωαννίνων (Π.Ι) (επιβλέπον μέλος Δ.Ε.Π)



2) Απόστολος Αυγερόπουλος,

Καθηγητής Τμήματος Μηχανικών Επιστήμης Υλικών του Π.Ι,
μέλος της συμβουλευτικής επιτροπής



3) Κωνσταντίνος Σταλίκας,

Καθηγητής Π.Ι, μέλος της συμβουλευτικής επιτροπής



4) Αναστάσιος Οικονόμου,

Καθηγητής Τμήματος Χημείας ΕΚΠΑ.



5) Βασίλειος Σακκάς,

Αναπληρωτής καθηγητής Π.Ι.



6) Δημοσθένης Γκιώκας,

Αναπληρωτής καθηγητής Π.Ι



7) Χρήστος Κόκκινος,

Επίκουρος καθηγητής Τμήματος Χημείας ΕΚΠΑ



ΣΤΗ ΜΝΗΜΗ ΤΟΥ ΠΑΠΠΟΥ ΜΟΥ, ΓΕΩΡΓΙΟΥ Π. ΝΙΚΟΛΑΪΔΗ

ΠΡΟΛΟΓΟΣ

Η παρούσα διδακτορική διατριβή εκπονήθηκε στο εργαστήριο Αναλυτικής Χημείας του Πανεπιστημίου Ιωαννίνων. Η εργασία αυτή αποτελείται από δύο μέρη, το θεωρητικό και το πειραματικό. Το θεωρητικό μέρος περιλαμβάνει δύο κεφάλαια, στα οποία δίνεται μία εκτενής περιγραφή της χρήσης ανόργανων χαμηλοδιάστατων φυλλόμορφων υλικών σε ηλεκτροχημικούς αισθητήρες καθώς και σε χημικούς αισθητήρες αερίων. Επίσης, περιγράφονται εκτενώς οι ηλεκτροχημικές τεχνικές που χρησιμοποιήθηκαν στο πλαίσιο της παρούσας διατριβής, όπως επίσης και η διαδικασία εκτύπωσης μέσω πλέγματος για την παρασκευή εκτυπωμένων ηλεκτροδίων γραφίτη που χρησιμοποιήθηκαν κατά τη διάρκεια εκπόνησης της διατριβής αυτής. Το πειραματικό μέρος περιλαμβάνει τέσσερα επιμέρους κεφάλαια. Στο πρώτο κεφάλαιο περιγράφεται η σύνθεση και ο χαρακτηρισμός των υλικών που αναπτύχθηκαν και στα επόμενα τρία κεφάλαια περιγράφονται οι αναλυτικές εφαρμογές αυτών. Συγκεκριμένα, η χρήση διδιάστατου συνθέτου βισμούθινού/γραφενίου για τον προσδιορισμό κατιόντων μολύβδου και καδμίου, η ηλεκτροχημική συμπεριφορά παθητικοποιημένων νανοφύλλων αντιμονενίου και τροποποιημένων ηλεκτροδίων γραφίτη με άμεσα παραγόμενο οξειδίο του αντιμονενίου/πολυ(αιθυλενοδιοξυθειοφαίνιο):πολυστυρενο σουλφονικό οξύ για τον προσδιορισμό του 4-νιτροτολουολίου και η χρήση τροποποιημένων ηλεκτροδίων γραφίτη με νανοφύλλα πεντοξειδίου του βαναδίου ευμεγέθους επιφάνειας για τον προσδιορισμό δικλοφαινάκης.

Στο σημείο αυτό θα ήθελα να εκφράσω τις ευχαριστίες μου στον επιβλέποντα μου Καθηγητή κ. Μάμαντο Προδρομίδη για την αμέριστη συμπαράσταση, την καθοδήγηση, τη βοήθεια και τις εύστοχες υποδείξεις του, καθ'ολη τη διάρκεια εκπόνησης και συγγραφής της παρούσας διδακτορικής διατριβής.

Επίσης ευχαριστώ θερμά και τα υπόλοιπα δύο μέλη της τριμελούς επιτροπής, τον Καθηγητή του τμήματος μηχανικών επιστήμης υλικών του πανεπιστημίου Ιωαννίνων, κ. Απόστολο Αυγερόπουλο, καθηγητή μου και επιβλέπων μέλος ΔΕΠ της μεταπτυχιακής μου εργασίας στο Τμήμα Μηχανικών Επιστήμης Υλικών, για τη βοήθεια και τη συμβολή του σε όλη τη διάρκεια των μεταπτυχιακών μου σπουδών, καθώς και τον Καθηγητή κ. Σταλικά Κωνσταντίνο, για την πολύτιμη βοήθεια του καθ'ολη τη διάρκεια εκπόνησης της διδακτορικής διατριβής στο εργαστήριο Αναλυτικής Χημείας.

Θα ήθελα επίσης να ευχαριστήσω τα υπόλοιπα μέλη της επταμελούς εξεταστικής επιτροπής, τον Καθηγητή του Τμήματος Χημείας του Πανεπιστημίου Αθηνών, κ. Οικονόμου Αναστάσιο, τον Αναπληρωτή καθηγητή του Τμήματος Χημείας του Πανεπιστημίου Αθηνών, κ. Κόκκινο Χρήστο, τον Αναπληρωτή καθηγητή κ. Γκιώκα Δημοσθένη και τον Αναπληρωτή καθηγητή κ. Σακκά Βασίλειο, για τη συμμετοχή τους και τις εύστοχες υποδείξεις τους.

Επίσης θα ήθελα να ευχαριστήσω όλα τα μέλη του εργαστηρίου Αναλυτικής Χημείας και ιδιαίτερα τις Μαρία Τραχιώτη και Ελένη Τζιάννη για την υποστήριξη και βοήθεια καθ' όλη τη διάρκεια εκπόνησης της διδακτορικής μου διατριβής.

Τέλος, ευχαριστώ τους γονείς μου Χρήστο και Γεωργία, τον αδελφό μου Μιχάλη και τη γιαγιά μου Αλεξάνδρα, για την αμέριστη υποστήριξη σε όλη τη διάρκεια της εκπόνησης της διατριβής αυτής.

Αλέξανδρος Χ. Λαζανάς
Ιωάννινα, Σεπτέμβριος 2022

THEORETICAL PART

CHAPTER 1 **1**

1.1	INTRODUCTION	1
1.2	FAMILIES OF INORGANIC LAYERED MATERIALS	5
1.2.1	TRANSITION METAL DICHALCOGENIDES (TMDs)	5
1.2.2	TRANSITION METAL OXIDES (TMOs)	6
1.2.3	MXENES	6
1.2.4	MONOELEMENTAL INORGANIC MATERIALS	7
1.2.5	MISCELLANEOUS	8
1.3	PRODUCTION OF 2D INORGANIC NANOSHEETS	8
1.3.1	HYDROTHERMAL AND SOLVOTHERMAL METHODS	8
1.3.2	BOTTOM-UP METHODS	10
1.3.3	TOP-DOWN METHODS	11
1.4	ANALYTICAL UTILITY OF 2D INORGANIC NANOSHEETS	19
1.4.1	TMDs: ELECTROCHEMICAL SENSING APPLICATIONS	19
1.4.2	TMDs: GAS-PHASE SENSORS	24
1.4.3	TMOs: ELECTROCHEMICAL SENSING APPLICATIONS	26
1.4.4	TMOs: GAS-PHASE SENSORS	28
1.4.5	MXENES: ELECTROCHEMICAL SENSING APPLICATIONS	28
1.4.6	MXENE: GAS-PHASE SENSORS	34
1.4.7	PNICTOGENS: ELECTROCHEMICAL SENSING APPLICATIONS	35
1.4.8	PNICTOGENS: GAS-PHASE SENSORS	38
1.4.9	MISCELLANEOUS ELECTROCHEMICAL SENSING APPLICATIONS	38
1.4.10	MISCELLANEOUS GAS PHASE SENSORS	41

CHAPTER 2 **47**

2.1	CYCLIC VOLTAMMETRY	47
2.1.1	REVERSIBLE SYSTEMS	48
2.1.2	IRREVERSIBLE AND QUASI-REVERSIBLE SYSTEMS	49
2.2	POLAROGRAPHY	50
2.3	PULSE VOLTAMMETRY	51
2.3.1	NORMAL PULSE VOLTAMMETRY	51
2.3.2	DIFFERENTIAL PULSE VOLTAMMETRY	52
2.3.3	SQUARE-PULSE VOLTAMMETRY	53
2.4	STRIPPING ANALYSIS	54
2.4.1	ANODIC STRIPPING VOLTAMMETRY	54
2.4.2	REPLACEMENT OF MERCURY	56
2.5	ELECTROCHEMICAL IMPEDANCE SPECTROSCOPY (EIS)	57
2.5.1	EQUIVALENT ELECTRIC CIRCUITS	57
2.5.2	REPRESENTATION OF IMPEDANCE PLOTS	58
2.5.3	INFLUENCE OF DOUBLE-LAYER CAPACITANCE (C_{dl})	60
2.6	FABRICATION OF SCREEN-PRINTED ELECTRODES (SPEs)	62
2.6.1	THICK-FILM SENSORS	62
2.6.2	SCREEN-PRINTED TECHNOLOGY	62

EXPERIMENTAL PART

3.1	MATERIALS	67
3.2	APPARATUS	68
3.3	SYNTHESIS OF THE MATERIALS	69
3.3.1	SHEAR FORCE EXFOLIATION OF BISMUTHENE/GRAPHENE	69
3.3.2	EXFOLIATION OF ANTIMONENE & ANTIMONENE/PEDOT:PSS	70
3.3.3	EXFOLIATION OF BULK VANADIUM(V) OXIDE	70
3.4	PROCEDURES	71
3.4.1	MODIFICATION OF GLASSY CARBON ELECTRODES WITH BISMUTHENE/GRAPHENE	71
3.4.2	FABRICATION OF SCREEN-PRINTING OF ELECTRODES AND MODIFICATION OF THEIR SURFACE WITH ANTIMONENE AND RELATED COMPOSITES OR VANADIUM(V) OXIDE NANOSHEETS	71
3.4.3	ANALYTICAL MEASUREMENTS	73
3.5	MORPHOLOGICAL AND STRUCTURAL CHARACTERIZATION OF THE MATERIALS	74
3.5.1	CHARACTERIZATION OF BISMUTHENE/GRAPHENE	74
3.5.2	CHARACTERIZATION OF ANTIMONENE & ANTIMONENE/PEDOT:PSS	76
3.5.3	CHARACTERIZATION OF V ₂ O ₅ NANOSHEETS	78
<u>CHAPTER 4</u>		<u>81</u>

4.1	ABSTRACT	81
4.2	INTRODUCTION	82
4.3	RESULTS & DISCUSSION	83
4.3.1	ELECTROCHEMICAL STUDIES	83
4.3.2	OPTIMIZATION STUDIES	86
4.3.3	ANALYTICAL PERFORMANCE	87

CHAPTER 5

5.1	ABSTRACT	93
5.2	INTRODUCTION	94
5.3	RESULTS & DISCUSSION	95
5.3.1	ELECTROCHEMICAL PASSIVATION OF SBENE NANOSHEETS	95
5.3.2	IMPLEMENTATION OF SBENE/SPE IN CATHODIC VOLTAMMETRY	99
5.3.3	ELECTROCHEMICAL CHARACTERIZATION OF SBENE OXIDE/PEDOT:PSS	102
5.3.4	ANALYTICAL PERFORMANCE AND UTILITY TO REAL SAMPLES ANALYSIS	104

CHAPTER 6

6.1	ABSTRACT	109
6.2	INTRODUCTION	110
6.3	RESULTS & DISCUSSION	111
6.3.1	ELECTROCATALYTIC STUDIES	111
6.3.2	EFFECT OF SCAN RATE AND PH	117
6.3.3	ANALYTICAL PERFORMANCE	119

6.3.4	INTERFERENCE STUDIES	122
6.3.5	CALIBRATION FEATURES	123
<u>CONCLUSIONS</u>		<u>127</u>
<u>REFERENCES</u>		<u>129</u>
<u>SYNOPSIS</u>		<u>161</u>
<u>SYNOPSIS</u>		<u>163</u>
<u>PUBLICATIONS</u>		<u>165</u>
<u>CONFERENCE PRESENTATIONS</u>		<u>167</u>

Two-dimensional inorganic layered materials

1.1 Introduction

Inorganic layered materials (ILMs) have been a part of the everyday life for over a thousand years, especially in the form of clays. In their bulk form, these materials have been known to exhibit interesting properties, which however can be dramatically different compared with the properties of their two-dimensional (2D) counterparts [1, 2]. While 2D inorganic materials have been produced for more than 40 years [3], they did not receive their most relatable name until 1996, when Sasaki et al. [4] defined 2D layered materials, as “nanosheets”, in a study regarding the exfoliation of titanium dioxide. It should be noted that even though ILMs had received their fair share of scientific attention, it was not until the emergence of graphene in 2004 [5] that the exploration of the wondrous 2D inorganic nanosheets truly began.

The need to obtain inorganic nanosheets of high quality and at a high quantity generated two inverse synthetic approaches, that is, the “bottom-up” and the “top-down” which have been employed extensively, along with the easy-to-perform hydro(solvo)thermal methods, in the past two decades. “Bottom-up” approach-based methods (thereafter, bottom-up methods) include the epitaxial growth of (ideally) a single layer of ILMs on a suitable substrate by reacting their precursors under certain conditions that favor the growth over the x,y -plane instead of the z -plane [6, 7]. Generally, these methods usually produce high quality monolayers of the respective inorganic materials that promote the full extent of their exotic properties. On the other hand, “top-down” approach-based methods (thereafter, top-down methods) have been implemented in the large-scale production of few-layer nanosheets dispersed in various liquid media [8, 9]. While both approaches have their own advantages and disadvantages, they have produced collectively a plethora of promising new low

dimensional materials, which have in turn been utilized in a wide range of applications. The unique properties of 2D inorganic nanosheets that have made a large impact in the post-graphene era stem from quantum confinement effects that consequently lead to increased anisotropy of the individual layers along with an obviously augmented surface-to-volume ratio [10]. These characteristics greatly affect the electronic, optical, structural, thermal, and mechanical properties of the 2D inorganic materials and render them promising candidates for numerous of applications of the technological pantheon. Today, there are a few major categories of ILMs that have been distinguished for the majestic properties of their 2D counterparts. Among them, transition metal chalcogenides (TMDs) [2] and transition metal oxides (TMOs) [11] have laid the foundations of this genre, while more recent families, such as MXenes [12] and various monoelemental layered materials of Group 14 (silicene, germanene and stanene, also known as “tetrel”) [13, 14] and Group 15 (phosphorene, bismuthene, antimonene, arsenene, also known as “pnictogens”) have gained considerable attention in the past decade [14, 15]. For a detailed description of the diversity of ILMs that can be processed to form 2D nanosheets the reader is referred to Refs. [9, 16]

Considering that depending on the production method diverse properties can be observed even in the same material, a variety of different materials presenting an extensive range of intriguing properties have been produced. For instance, MoS₂, the flagship of the TMDs is subject to polymorphism and can either display metallic or semiconducting behavior depending on the exfoliation process [17]. Ultimately, ILMs offer as many freedom degrees as possible and can be considered as valuable commodities in many applications, including nanomedicine [18], energy storage [19], energy conversion [20], catalysis [21], and (bio)sensing [22]. Prime examples of such applications lie in the fields of nanomedicine (theranostics, multimodal imaging, drug delivery, photothermal therapy etc.) with the use of TMDs (MoS₂, WS₂) and MXenes (Ti₃C₂, Ta₄C₃, and Nb₂C) [23], thermoelectrics with Bi₂Te₃ representing the most efficient 3D topological insulator to date [24], and energy storage with the incorporation of MoS₂, MnS, VS₄ etc. nanosheets in sodium-ion batteries [25]. Other uses include polarizing electrodes in electrical double layer capacitors (1T-MoS₂, VS₂, Ti₃C₂T_x etc.) as well as materials (MnO₂/Ni(OH)₂ hybrids, VOPO₄ etc.) that provide useful combinations of electrosorption, ion intercalation and redox chemistry in the development of pseudocapacitors [26]. TMDs (MoS₂, WS₂) and Group 15 antimonene have also been proposed in photo electrocatalytic water splitting applications [27] and

various electrocatalytic applications such as hydrogen evolution reaction (HER) [28], oxygen evolution reaction (OER), oxygen reduction reaction (ORR) and CO₂ reduction [26]. Inorganic 2D nanosheets have also been involved in the field of electrochemical (bio)sensing by offering attractive detection capabilities for the determination of heavy metal ions [29], pharmaceuticals [30, 31], explosive compounds [32], various biomarkers [33–36] etc., as well as, in various bioelectrochemistry applications by offering a drastic improvement of direct electron transfer (DET) between the electrode surface and the redox centers in biomolecules [37]. In gas-phase applications, inorganic 2D nanosheets have been successfully utilized as transducing surfaces for the determination of volatile organic compounds (VOCs) such as acetone, ammonia, ethanol etc. by exploiting their advanced adsorption properties and semiconducting nature [38].

Fig. 1 presents statistical figures of the past two decades (2000-2022) comparing the number of papers published about “*2D material-based electrochemical sensors*” with the total number of publications about “*electrochemical sensors*”. In this time span publications regarding 2D material based-electrochemical sensors have been increased from approximately 1% of the whole literature regarding electrochemical sensors in 2000 to approximately 24% in 2022. In rough numbers that translates into 1/4 of the publications about electrochemical sensors of contemporary literature. To discriminate among these results, a second statistical analysis over the same time period was conducted comparing the number of papers published about “*2D inorganic material-based electrochemical sensors*” with the total number of publications about “*electrochemical sensors*”. In this case, a smaller growth from ca. 0.5% in 2000 to ca. 11% in 2022 is noted. The difference between these percentages (1 to 0.5% in 2000 and 24 to 11% in 2022) demonstrates that more than half publications regarding 2D material-based electrochemical sensors is related to graphene and its allotropes or other polymer-based low dimensional nanostructures. A third investigation was conducted to illustrate the rapid increase of publications about “*2D inorganic material-based electrochemical sensors*” as a divisible of the general key “*2D inorganic materials*” (in this group, works on the production, characterization and use of 2D inorganic materials in all the aforementioned technological sectors are included), showing an impressive increase from 4 to 19%. Data in **Fig. 1** evidence that 2D inorganic materials play an increasingly important role in the field of electrochemical sensing, while

electrochemical sensing itself occupies an important percentage of the total inorganic 2D materials literature.

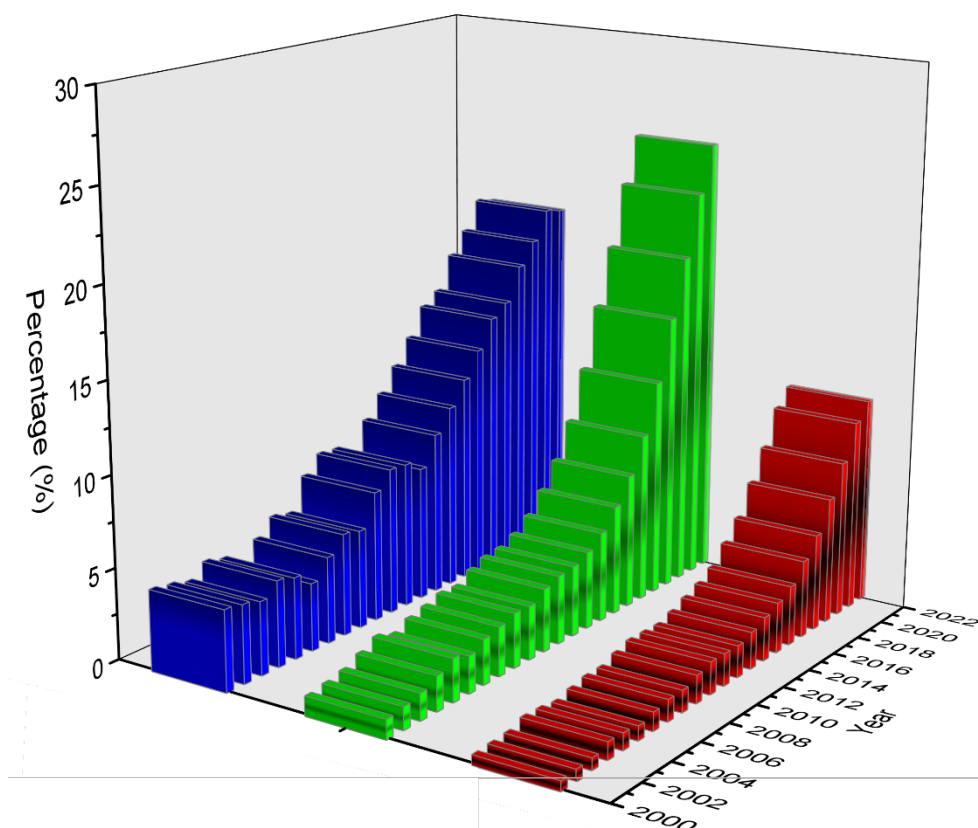


Fig. 1. (Blue) Publication percentage growth of 2D inorganic material-based electrochemical sensors in the field of 2D inorganic materials. Results were produced by dividing data retrieved using the keywords “2D” and “inorganic” and “electrochemical” and “sensors” with data generated from the keywords “2D” and “inorganic” and “materials”. (Green) Publication percentage growth of 2D material-based electrochemical sensors in the field of electrochemical sensing. Results were produced by dividing data generated for the keywords “2D” and “electrochemical” and “sensors” with data generated from the keywords “electrochemical” and “sensors”. (Red) Publication percentage growth of 2D inorganic material-based electrochemical sensors in the field of electrochemical sensing. Results were produced by dividing data retrieved using the keywords “2D” and “inorganic” and “electrochemical” and “sensors” with data generated from the keywords “electrochemical” and “sensors”. Data were obtained from Scopus® (Elsevier B.V) database over the time span 2000–2022.

It is within this thesis’ goal to highlight and emphasize upon the most characteristic works dealing with 2D inorganic materials production routes and properties as well as their implementation on contemporary electrochemical sensing devices. That being said, it is reasonable that some interesting articles may have been omitted due to space constraints. In this regard, **Table 1** has included review articles, focus on various related topics, along with the number of references therein and the publication year, to ensure that the reader can navigate efficiently through topics and research outputs not included or are out of the scope of this thesis.

Table 1. Review articles focus on the production, properties and analytical utility of 2D inorganic materials

Topic	Nr. of references	Year	Ref.
Graphene analogues of inorganic layered materials	419	2015	[16]
Exfoliation, characterization, and processing of layered materials	173	2016	[39]
Liquid exfoliation of layered materials	140	2013	[1]
Hydrothermal synthesis of inorganic nanostructures	372	2013	[40]
Electrochemical exfoliation of inorganic layered materials	130	2019	[41]
Monoelemental bottom-up deposition	144	2020	[42]
Chemistry of Group 14 graphene analogues	71	2019	[13]
Electronic structures of TMDs	215	2015	[43]
2D monoelemental pnictogens	50	2017	[15]
Two-dimensional materials for electrocatalysis	99	2018	[14]
Chemical sensing with 2D materials	531	2018	[22]
Monoelemental 2D nanomaterials in electrochemical sensing	98	2019	[44]
Metal oxide nanosheet gas sensors	171	2018	[38]
TMD-based flexible gas sensors	231	2020	[45]
Gas sensing applications with 2D materials	243	2017	[46]
Electrochemical sensors based on MoS ₂ nanomaterials	160	2019	[47]
MnO ₂ nanosheets for biosensing and biomedicine applications	109	2019	[48]
2D metal oxides and metal hydroxides for modification of polymeric membranes	121	2020	[49]
Synthesis, structure, properties, and applications of MXenes	334	2019	[50]
MXene: Sensing and biosensing	63	2018	[51]
MXene-based electrochemical sensors and biosensors	77	2019	[52]

1.2 Families of inorganic layered materials

1.2.1 Transition metal dichalcogenides (TMDs)

This grand MX₂ family of layered materials (where M is a transition metal and X is sulfur, selenium, or tellurium) has been in the spotlight for decades. Their crystal lattices consist of atomic layers of hexagonally-packed layers of metal atoms sandwiched between two layers of chalcogen atoms [53]. Bulk TMDs range from metallic (e.g. NbSe₂), semi metallic (e.g. TiS₂), semiconducting (e.g. 2H-MoS₂), and

insulating (e.g. TaS₂) [9, 43, 54, 55] while their 2D counterparts are able to display extremely different behavior per instance, due to the thickness dependency of their electronic properties. If the indirect-to-direct band gap transition of MoS₂ and WS₂ seems rather ordinary, TMDs such as TiS₂ display semimetallic-to-semiconducting transition while TaS₂ displays semiconducting-to-insulating transition (1T-TaS₂). On top of that, many TMD nanosheets exhibit 1T (metallic) and 2H (semiconducting) polymorphism depending on the synthetic procedure [56], a fact that expands their potential even more, since 1T form exhibits superior electrocatalytic activity, which can be useful in electrochemical sensing in solutions, while the 2H form can play an important role in gas-sensing applications. While TMD nanosheets are perhaps the only category that can be produced with every top-down method described below, there is an exception to this rule. Group 10 TMDs (for example, PtS₂, PtSe₂, PtTe₂) exhibit a strong covalent-like bonding instead of the common (weak) Van der Waals interactions that stems from a greater degree of hybridization between the metal 5d and chalcogen's *p* orbitals [57].

1.2.2 Transition metal oxides (TMOs)

Much like their dichalcogenide siblings, TMOs nanosheets share tunable band gap properties and a vast electrochemical interest due to their redox activity and strong ion-exchange properties [11]. Many TMO nanosheets (such as V₂O₅, MnO₂ etc.) can be produced via bottom-up and top-down approaches, though the majority of the reported literature focuses on hydrothermal and solvothermal methods [49].

1.2.3 MXenes

A 2D family that stems from ceramic MAX phases, which correspond to the general formula M_{n+1}AX_n (*n* is an integer from 1 to 3) where M stands for an early *d*-block transition metal (Sc, Ti, V, Cr, Zr, Nb, Mo, Hf, Ta, W), A represents an element from either Group 13 or 14 and X corresponds to carbon or nitrogen [12, 50]. MAX phases exhibit layered hexagonal structure with P6₃/mmc symmetry. The M-X bonds possess both an ionic and a covalent character while the M-A bonds exhibit metallic characteristics [51]. The most common route for the production of the MXenes includes an etching step of the MAX phase with a strong acid (commonly, HF) in room

temperature for a certain period of time [58]. This process produces thermodynamically stable $M_{n+1}X_nT_x$ phases, where T_x is derived by surface functionalization ($-O$, $-OH$, $-F$) induced by the HF and H_2O treatment. Other production routes include the use of different etchants, such as mixtures of strong acids with fluoride salts [52]. Pristine 2D MXenes (M_2X) exhibit a metallic character due to the overlap of the Fermi level on their d orbitals. However, different combination of functionalizing group causes the generation of new bands due to the hybridization between the d orbitals of the metal and the p orbitals of the functionalizing groups. This fact along with the facile electron donation from M both to X and to T, can transform the electronic properties of 2D MXenes leading to either a semiconducting or a semimetallic behavior [51]. For example, Ti_3C_2 is a metal while $Ti_3C_2F_2$ and $Ti_3C_2OH_2$ are semiconductors.

1.2.4 Monoelemental inorganic materials

Ever since the emergence of graphene, the -ene suffix has been adapted to indicate other single-layer 2D materials as well. Carbon, being a member of the Group 14 elements shares the same valence electronic configuration as Si, Ge, Sn. This fact led to the generation of their 2D allotropes known as silicene, germanene and stanene, respectively which are all arranged in a hexagonal honeycomb structure, like graphene. This similarity stops to the point where graphene possesses a planar structure while the other tetrels form buckled hexagonal structures due to different hybridization (graphene exhibits sp^2 while the rest exhibit sp^3) [44]. This has a significant impact on their individual electronic properties and is the main reason why they do not share the conductive nature of graphene, but adopt a semi-conducting or semi-metallic character. Another major group that has attracted attention are the elements of the Group 15, namely antimony, gray arsenic, bismuth (which form layered rhombohedral structures, with the exception of nitrogen) as well as orthorhombic yellow arsenic and black phosphorus. Hence, the 2D “pnictogen” allotropes, antimonene, arsenene, bismuthene and phosphorene [15]. Most of the monoelemental nanosheets mentioned above can be produced via top-down approaches, which favors their implementation in sensing devices, compared with bottom-up approaches, which limit their technological implementation.

1.2.5 Miscellaneous

Post transitional metal chalcogenides such as Group 15 selenides and tellurides are just as important compounds as TMDs. Compounds as Bi_2Se_3 , Bi_2Te_3 , Sb_2Te_3 etc. are narrow band gap semiconductors and topological insulators [59], which renders them excellent thermoelectric materials [60] and their 2D counterparts can be produced with both top-down and bottom-up approaches [61, 62]. Other post-transitional metal selenides and tellurides such as SnSe_2 , GaTe etc. exhibit extensive use in gas sensors [63, 64], exploiting their p-type semiconducting nature. Hexagonal boron nitride (h-BN) shares a similar structure with graphene but displays insulating properties with a band gap larger than 5 eV [65].

1.3 Production of 2D inorganic nanosheets

A general sketch of the most widely used methods and techniques have been utilized for the production of 2D nanosheets through “bottom-up” and “top-down” approaches is illustrated in **Fig.2**. Hydrothermal and solvothermal methods, which due to their simplicity constitute a popular choice for the production of many 2D inorganic materials, are not included in the above categorization, and they will be presented separately.

1.3.1 Hydrothermal and solvothermal methods

Hydrothermal and solvothermal (hence mentioned as hydro/solvo-thermal) methods involve heating the reactants in a closed vessel, an autoclave usually constructed from thick stainless steel to withstand high pressures and lined with non-reactive materials, such as Teflon. As the autoclave is heated, pressure increases, and the water or organic solvent used remains liquid above its normal boiling temperature. These conditions, in which the pressure is raised above atmospheric pressure and the temperature is raised above the boiling temperature of solvent, are known as hydrothermal or solvothermal conditions, and they are useful in metal oxide systems where the oxides are not soluble in a given solvent at atmospheric pressure but dissolve in the super-heated solvent of

the hydrothermal set up. Where even these conditions are insufficient to dissolve the starting materials, alkali or metal salts can be added whose anions form complexes with the solid and render it soluble [66]. For a comprehensive description of the main strategies have been developed for the hydro/solvo-thermal production of 2D inorganic nanomaterials, the reader is referred to Ref. [40]. Several examples of hydro/solvo-thermally produced inorganic nanosheets have been reported, with slight modifications per instance, retaining though some key characteristics. Synthetic proceduces for TMDs usually have four requirements to be successful, i) a transition metal source, ii) a dichalcogenide source, iii) a reducing agent and iv) a solvent. A single compound can play more than just one role exhibiting a few variations. For instance, WSe₂ nanosheets have been produced via an one-pot solvothermal method involving sodium tungstate (transition-metal source), elemental selenium (dichalcogenide source), sodium borohydride (reducing agent) in DMF (solvent) [67].

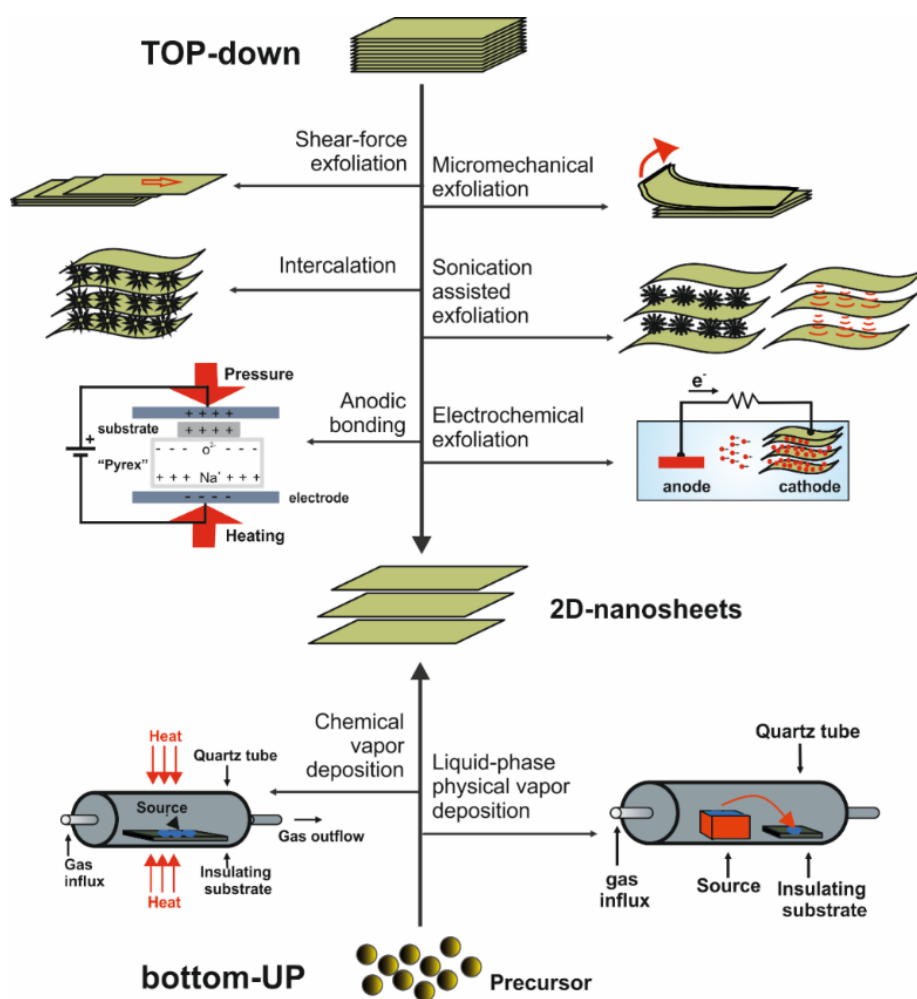


Fig. 2. Schematic representation of various “top-down” and “bottom-up” methods for the production of 2D inorganic nanosheets.

Other approaches utilize thioacetamide or thiourea acting simultaneously as sulfur sources and reducing agents reacting with transition-metal-based salts such as sodium orthovanadate [68], sodium molybdate [69, 70], tungsten(VI) chloride [30] etc. to produce the respective disulfide nanosheets (VS_2 , MoS_2 and WS_2) in water. Finally, ammonium tetrathiomolybdate has been employed as both a sulfur and a molybdenum source reacting with hydrazine hydrate in water to produce MoS_2 nanosheets [36]. Another example includes the solvothermal synthesis of boron carbon nitride (BCN) from a mixture containing boric acid, 2,4,6-tri(2-pyridyl)-1,3,5-triazine and ethylene glycol [33].

1.3.2 Bottom-up methods

Bottom-up methods are well known for their ability to produce high quality nanosheets through epitaxial growth on suitable substrates [71]. Bottom-up methods, such as molecular beam epitaxy and Van der Waals epitaxy however will not be discussed here, as the nanosheets produced by those methods, though of high quality, cannot be easily transferred to the electrode surface and thus their use in sensing applications is limited. For details on the uses of these methods to the preparation of inorganic nanosheets, the reader is referred to Ref. [42].

Gas-phase methods fix upon single-layer nanosheet growth of lateral sizes ranging from a few atomic units to several centimeters [71–73]. As they do not suffer from grain size limitations, they are only limited by the nature of the templating substrates, which greatly affect reaction kinetics by reducing the energetic penalty of parallel growth [74]. This is the main prerequisite for both physical vapor deposition (PVD) and chemical vapor deposition (CVD) techniques. Another important variable is the choice of an appropriate substrate. For instance, sapphire, SiO_2/Si and quartz substrates have been proved suitable for CVD growth of TMDs [75, 76]. While many variations of the CVD growth of nanosheets have been developed over the past years, the main advance concerns the transition from atmospheric pressure CVD (AP-CVD) [77] to low pressure CVD (LP-CVD) [78] and eventually to ultra-high vacuum CVD (UHV-CVD) [42]. This transition aims to the successful growth of nanosheets prone to oxidation, such as phosphorene [79] or silicene [80].

Liquid-phase methods are similar to gas-phase methods. The main difference is that they involve the decomposition of a precursor mixture by either thermal decomposition

into a solution or injection into a hot liquid (hot injection synthesis) [81]. Coordinating ligands are used in order to bind preferentially to the c-axis and hence raise the energetic penalty in the z-plane [6, 7]. However, removal of the coordinating ligands (e.g. oleylamine in TMD growth) can be problematic and often leads to restacking of the nanosheets [6].

1.3.3 Top-down methods

1.3.3.1 Micromechanical exfoliation

Micromechanical exfoliation relies on the introduction of either a peeling force or a shear-force to separate the crystal layers. It was first introduced in 1963 by Frindt and Yoffe [82], by peeling off very thin ($< 100 \text{ \AA}$) single crystals of MoS_2 from the face of a bulk MoS_2 crystal with the aid of an adhesive tape. The adhesion between the tape and the basal plane of the crystal is significantly stronger than the Van der Waals forces bind the layers together, and thus promotes the isolation of individual flakes. Interestingly, it was the same principle in 2004 that has led to the isolation of graphene with the today well-known “Scotch tape” method [5]. Even though this approach suffers from inherent scalability problems, it can produce atomically thin sheets of large dimensions and high crystal quality and has been applied for a variety of inorganic materials, such as TiO_2 nanotubes [83], Ti_3SiC_2 (a rare example of a 2D MAX phase isolation) [84], MoS_2 , WSe_2 , Bi_2Te_3 [85] and black phosphorus nanosheets [86].

On the same philosophy, the cleavage of TMDs crystals (NbSe_2 or MoS_2) with a silicone stamp has also been proposed as an improved methodology, compared with the “scotch-tape” method, because it does not leave traces of adhesive to the surface of the sheet [87]. Another approach relies on simple rubbing of lamellar crystals (for example, boron nitride, graphite, several dichalcogenides and complex oxides) onto a desired substrate in order to obtain enough shear-force to delaminate nanosheets from their bulk precursor [88]. This can be taken one step further by exploiting the friction generated between two fine-grain sandpapers and the powder of a bulk layered material to produce nanosheets with thickness greater than 100 layers. When enriched with a smooth rubbing step, this technique enables the production of single or few-layer nanosheets [88] directly on a flexible polymer substrate within 2 min under room temperature.

Anodic bonding, a bonding method used in microelectronics industry, has been used [89] by subjecting a borosilicate glass substrate (e.g. Pyrex[®]) and a precursor crystal to an electric field at elevated temperature and pressure to promote the decomposition of Na₂O (present in Pyrex[®] glass) to Na⁺ and O²⁻ ions. Migration of sodium cations produces a subsequent negative space charge and an electrostatic field between the crystal and the glass, which laminates the crystal and produces nanosheets strongly adhered to the glass surface. This electric field-promoted micromechanical technique had been originally proposed for the exfoliation of high quality, large size and high yield single-layer and few-layer graphene [90] while its applicability to MoS₂, NbSe₂, GaSe, GaS, InSe, CaCu₂Ox, CuGeO₃, TiS₂, and mica has also been demonstrated [89]. The key parameters of this technique, that is, the voltage and sample temperature, can be optimized to obtain large nanosheets ranging from 10 to several hundred micrometers [89].

While micromechanical methods present certain advantages such as economic and facile production of nanosheets, they are considered to be impractical as a scalable method and this feature has a direct effect to their limited use in the modification of electrode surfaces for electrochemical sensing applications.

1.3.3.2 Sonication-assisted exfoliation

It is by far the most known and used exfoliation method of layered materials as it is a highly practical approach for large-scale nanosheet production [1]. Its working principle involves transverse ultrasonic wave propagation through the liquid in alternating high-low pressure cycles that gives rise to two different forces [91, 92]; vibrational forces, which are able to overcome the Van der Waals interlayer forces by simultaneous introducing of tensile and compressive stress on the bulk material and cavitation forces, which are produced by the in-situ generation and implosion of cavitation bubbles within the liquid medium. An important parameter to take into consideration would be the liquid medium selection [39, 93].

Coleman et al. [8] have reported on the production of 2D nanosheets of several ILMs, such as MoS₂, WS₂, MoSe₂, MoTe₂, TaSe₂, NbSe₂, NiTe₂, BN, and Bi₂Te₃ in a number of solvents with varying surface tensions, while results have demonstrated that successful solvents are those with surface tension of about 30-40 mJ/m². Based on Hansen and Hilderbrand solubility parameters [94, 95], and in accordance with other

studies [96] on the liquid exfoliation of graphene, data show that the yield of exfoliation is increased when the energy of exfoliation (represented by the enthalpy of mixing per volume) becomes lower, and this condition is satisfied when the surface energies of the solid and the solvent match. Generally, various *N*-alkylpyrrolidones, such as *N*-cyclohexyl-pyrrolidone and *N*-dodecyl-pyrrolidone offered as a viable choice for all the examined materials by producing nanosheet dispersion of high concentrations, which are usually stable for months.

Another route to achieve equality between the surface energies of the liquid and the solid could be the use of surfactants, in which the head group interacts with the liquid and prevents nanosheet reaggregation by steric and/or electrostatic repulsion while the tail adsorbs to the nanosheet surface. Compared with solvents, the use of surfactants may offer an extra advantage in terms that their surface tension is concentration dependent. In this regards, they can provide a suitable dispersion medium for a variety of nanosheets, provided that their concentration remains below the critical micelle concentration [39] and that appropriate post treatment can ensure their fully removal.

Commonly used aqueous surfactants as exfoliation media include sodium dodecyl sulfate [97], sodium dodecyl benzyl sulfate [98], and sodium cholate [99, 100], which have been successfully used for the production of stable colloids of phosphorene [97], MoS₂ [98], and for bismuthene, arsenene, antimonene and WS₂ [99, 100], respectively.

1.3.3.3 Shear-force exfoliation

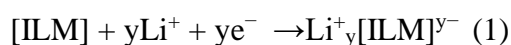
This process was introduced by Chen et al. in 2012 [101] for the exfoliation of graphite and boron nitride and involves the dispersion of the bulk material to an appropriate liquid medium inside a rotating tube. During the rotation, layered material accelerates to the walls of the tube by the arising centrifugal force. Subsequently, due to layers being parallel to the axis of rotation, a slippage of the material directly to the walls of the tube occurs, eventually leading to shear-induced displacement along the tube that results in the production of exfoliated nanosheets. A scale-up of this method to produce large quantities of graphene reported by Paton et al. [102] has shown that despite the initial hypothesis that shear-force exfoliation could occur only in a turbulent regime, this method could in fact produce nanosheets even in the presence of laminar flow. Remarkably, shear-force exfoliation was possible without the need of sophisticated rotation machineries, provided that a minimum shear rate of 10^4 s^{-1} was to be kept. In

simple terms, even household blenders could be used to exfoliate layered materials. Despite the limitation of these appliances to operate at high speeds, or continuously for time intervals longer than 10-15 min or to control overheating, they have successfully used for the exfoliation of various inorganic materials, such as MoS₂ and WS₂ [103], BN [101], GaSe₂ [63], bismuthene [104], antimonene [105] etc..

While the prerequisites of shear-force exfoliation method are identical to sonicated-assisted exfoliation regarding the choice of the optimum dispersion medium, the nanosheets produced by this method, usually remain intact since the process lacks long and high energy sessions that are intertwined with ultrasonication.

1.3.3.4 (Lithium) Intercalation

Intercalation of various substances between layered structures serves to the increase of the interlayer distance and thus the weakening of the Van der Waals forces between them. One vital parameter to this process is the correspondence of the intercalant's ionic radius and the interlayer distance. In most cases, a post-intercalation ultrasonication step in water is required to overcome the already weakened Van der Waals interlayer forces. Lithium intercalation is the most common practice to date due to its small atomic radius, the great expansion of its ionic radius during hydration [106], and the evolution of hydrogen gas during the reaction of metallic lithium with water. The many variations of lithium-based ion intercalation exfoliation procedures include the use of i) lithium metal [107], ii) lithium hydroxides [108], iii) LiBH₄ hydride [17, 109], iv) organo-lithium compounds [110–112] and v) the electrochemical lithium intercalation by using the bulk material as cathode [113]. The latter approach falls also in the next category deals with electrochemical exfoliation; however, for purposes of unity as regards the lithium-based intercalation methods, is presented here. In all these cases, the presence of a strong reducing compound (solvated electrons in liquid ammonia [107], ethylene glycol at high temperatures [108], butyl radicals [112], LiBH₄ hydride itself [17, 109], cathodic polarization regime [113] plays a vital role by reducing the bulk material (ILM), thus allowing Li⁺ to be inserted within its layers to maintain charge balance, according to the equation (1):



It is believed that the extend of this reducing power further converts intercalated Li^+ to metallic Li^0 , which then by reacting with water produces H_2 gas that delaminates the layered material [113]. Non-reduced intercalated Li^+ ions can assist the delamination process only by considering the great expansion of their ionic radius during hydration. Using lithium metal and liquid ammonia, colloids of Bi_2Te_3 and Bi_2Se_3 can be formed with relatively narrow particle size distributions centered around 10-20 nm [107]. To avoid the special reaction equipment and the extreme experimental conditions of a liquid ammonia atmosphere, Ren et al. [108] proposed a hydrothermal intercalation by employing lithium hydroxide in ethylene glycol and heat treatment at 200 °C, which allowed the formation of very thin Bi_2Te_3 nanosheets (3-4 nm) sized 200 nm in width and 1 mm in length. A relatively simple procedure that can be scaled up to 10-15 g batches involves the use of LiBH_4 hydride, lithiation of the layered material (WS_2 [17]) and chemical decomposition of BH_4^- to gaseous diborane (along with hydrogen gas) thus eliminating the need for extra clean-up steps. Using LiBH_4 [109], MoS_2 nanosheets with almost uniform thickness (ca. 4 nm), sized 2–10 μm in width and a satisfactory yield of more than 1.5 wt.% have been synthesized.

Lithium intercalation of ILMs via organometallic compounds, commonly n-butyl lithium in hexane, affords under mild conditions and has been used for the production of highly crystalline and uncontaminated stoichiometric products with various Group 4 (Ti, Zr, Hf), Group 5 (V, Nb) [112] and Group 6 (Mo, W) [111] layered dichalcogenides.

Electrochemical intercalation of lithium followed by exfoliation in water was reported for the synthesis of MoS_2 , WS_2 , TiS_2 , TaS_2 , and ZrS_2 nanosheets [114], while in order to address issues associated with low intercalation yield due to that partially intercalated pieces readily breaking off from the bulk material-based cathode, Zeng et. al [113] conducted a systematic study, synthesizing few-layer thick BN, NbSe_2 , WSe_2 , Sb_2Se_3 , and Bi_2Te_3 nanosheets through optimization of the cut-off voltage and discharge currents for each of the examined layered materials.

Different ion intercalation approaches have been reported sporadically such as acid-intercalated production of ~17 layer thick bismuthene [115], but since they share a similar pattern with the above methods, they will not be discussed further.

1.3.3.5 Electrochemical exfoliation

Electrochemical exfoliation of a bulk layered material is conducted through an intercalation process under potentiostatic or galvanostatic conditions in which the bulk layered material plays the role of anode or cathode while solvated ions and/or various electrolysis species act as the intercalators causing the expansion of the interlayer distance in the bulk material and eventually, the cleavage of the interlayer bonds/Van der Waals interactions and the formation of low dimensional 2D nanosheets. In this regard, respective approaches can be sorted in two main categories: i) anodic exfoliation, which is carried out in aqueous electrolytes [116] and ii) cathodic exfoliation, which is carried out in non-aqueous electrolytes containing alkali metal or quaternary ammonium salts [117, 118]. Despite being an electrochemical method, electrochemical exfoliation can be applied also to non-conductive materials, which in this case are made to an electrode as a composite with a conductive material. To overcome the issue associated with the detachment of partially exfoliated sheets from the anode, besides pure electrochemical remedies mentioned above [113], the inclusion of bulk materials in porous containers [118, 119], which also render binders for the fabrication of the working electrode unnecessary, has been proposed.

The anodic approach incorporates the intercalation of negatively charged electrolyte ions and the water electrolysis products into the positively charged anode bulk material. For instance, the anodic exfoliation of MoS₂ in aqueous Na₂SO₄ generates both ·OH and ·O radicals produced by H₂O oxidation and SO₄²⁻ anions, which are intercalated within MoS₂ layers [116]. Further oxidation reactions at the highly positive anode lead to evolution of O₂ and/or SO₂ gas, which in turn expands the interlayer distance. Gas eruption climaxes the process and detaches the MoS₂. While this approach is relatively facile and can readily produce few-layer nanosheets, it often compromises the quality of the products, especially regarding layered structures prone to oxidation (such as phosphorene) [41].

This obstacle can be surmounted by cathodic exfoliation where the highly negative voltage of cathode does not allow oxidation reactions to occur and aids cation intercalation in the interlayers of the bulk material. As mentioned in the previous paragraph, intercalation of lithium ions generated by a lithium foil anode [113] makes for a typical example of this type of electrochemical exfoliation process in which an

additional ultrasonication step might prove necessary to detach the weakened layered structures.

Other cathodic exfoliation approaches are based on the magnitude of the ionic radius of the intercalated cations, which are soluble in the electrolyte solution, and their size spans from small alkali metal ions such as Li^+ (0.76 Å), Na^+ (1.02 Å) and larger K^+ (1.38 Å), Cs^+ (1.69 Å) to bulky tetra-methylammonium (5.6 Å), tetra-ethylammonium (6.7 Å), tetra-butylammonium (8.3 Å) quaternary ammonium cations [118].

Interestingly, the expansion of the interlayer distance and the exfoliation of the bulk crystal can be boosted by the presence of the counterbalanced anion. This is demonstrated for the exfoliation of black phosphorous in the presence of tetra-n-butylammonium bisulfate, which was found to accelerate the exfoliation process due to the generation of solvated hydrogen protons ($\text{HSO}_4^- \rightarrow \text{H}^+ + \text{SO}_4^{2-}$) that also intercalated within layered materials and result in the production of hydrogen gas. Gas eruption assists not only the exfoliation of bulk material but also the intercalation of ions bigger than the pristine bulk material [for example tetra-butylammonium (8.3 Å) into black phosphorous with interlayer distance 5.6 Å], which further increases the volume expansion of the bulk crystal [118].

Given that key parameters such as the magnitude of the applied electric field, the electrolyte and size of the intercalant have been carefully optimized, electrochemical exfoliation has been successfully applied to the production of thin 2D nanosheets of various inorganic materials, such as black phosphorus [118, 119], antimony [120, 121], MoS_2 [114, 116, 117, 122], WS_2 , TiS_2 [114], BN, NbSe_2 , WSe_2 [113], Sb_2Se_3 , Bi_2Te_3 [113], $\delta\text{-MnO}_2$, g- C_3N_4 [117], Ti_3C_2 [123]. For a comprehensive description of the electrochemical exfoliation of inorganic layered materials the reader is referred to Ref. [41].

Table 2 outlines an overview of the aforementioned families of ILMs emphasizing on the methods have been used to produce the respective 2D inorganic nanosheets and the difference of the electronic properties of specific materials in bulk form and as 2D nanosheets.

Table 2. Overview of the referenced inorganic layered materials

Material family	Composition	Methods to produce inorganic 2D nanosheets	Electronic properties			Interlayer forces
				Bulk material	2D nanosheet	
Transition Metal Dichalcogenides (TMDs)	MX ₂ : M: Transition metal X: S, Se, Te	Micromechanical exfoliation [82, 87, 89], Ultrasonication [57, 124, 125], Shear-force exfoliation [103], Lithium intercalation [17, 126, 127], Electrochemical exfoliation [116, 117]	MoS ₂ , MoSe ₂ , WS ₂ , WSe ₂	Indirect band gap semiconductor	Direct band gap semiconductor (2H) or metallic (1T)	Weak Van der Waals
			TiS ₂	Semimetallic	Semiconducting	
			TaS ₂	Semiconducting	Insulating	
			VS ₂	Metallic	Metallic	
Transition Metal Oxides (TMOs)	MO _x : M: Transition metal	Hydro/solvo-thermal techniques are more commonly used [128, 129]	Semi conducting			Weak Van der Waals
MXenes	M _{n+1} X _n or M _{n+1} X _n T _x : M _{n+1} : early d-block transition metal X _n : C, N, CN T _x : -OH, -F, -Cl n: 1 – 3	Post- MAX phase etching (HF or LiF-HCl treatment), more commonly via ultrasonication [130–132]	Ti ₃ AlC ₂	Metallic	–	Strong Van der Waals
			Ti ₃ C ₂	–	Metallic	
			Ti ₃ C ₂ F ₂	–	Semiconducting	
			Ti ₃ C ₂ OH ₂	–	Semiconducting	
		HF-etching/ Intercalation [133]	V ₂ AlC	Metallic	–	
			V ₂ C	–	Metallic	
			V ₂ CT _x	–	Semiconducting	
Monoelemental	Pnictogens P, Sb, Bi, As	Micromechanical exfoliation [134], Ultrasonication [135–137], Shear-force exfoliation [105], Electro chemical exfoliation [119, 120]	Black phosphorus	Semiconducting	Semiconducting	Van der Waals
			Antimony	Semimetallic	Semiconducting	Pseudo-Van der Waals (As, Bi, Sb)
			Bismuth	Semimetallic	Semiconducting	
			Arsenic	Semimetallic	Semiconducting	
	Tetrels Si, Ge, Sn	Electrochemical exfoliation [41]	Silicon	Semiconducting	Semimetallic	Van der Waals
			Germanium	Semiconducting	Semimetallic	
			Tin	Metallic	Semi conducting	
Miscellaneous	Post-transition metal chalcogenides	Ultrasonication [29, 138], Shear-force exfoliation [63], Electrochemical exfoliation [41]	Bi ₂ Te ₃ , GaS, GaSe, GaTe, InSe, InTe, In ₂ Se ₃ , SnSe ₂	Semiconducting	Semi conducting	Weak Van der Waals
	Group 3 nitrides and carbon nitrides	Ultrasonication [94], Shear-force exfoliation [101]	h-BN	Insulating	Insulating	
			BCN	–	Semiconducting	

1.4 Analytical utility of 2D inorganic nanosheets

The analytical utility of 2D inorganic nanosheets will be presented for each material family separately, and the respective works will be further categorized, with respect to the phase (liquid or gas) of the target analyte, as i) electrochemical sensing applications and ii) gas-phase sensors. The major analytical figures of merit of the surveyed works are collectively presented in (Table 3) and (Table 4), respectively.

1.4.1 TMDs: Electrochemical sensing applications

MoS₂ nanosheets possess the lion's share of TMD-based electrochemical sensing devices for the determination of (bio)molecules with interest in various sectors in (bio)chemical analysis. For this reason, it is within this review's scope to select works that having been assessed in real samples, while for an extended survey of MoS₂ nanosheet-based sensors the reader is referred to Ref. [47].

Wang et al. [139] used hydrothermally produced MoS₂-NiCo₂O₄ nanocomposite towards non-enzymatic glucose determination with the MoS₂ playing a dual role, as i) a conducting surface thus promoting the formation of conducting pathways between NiCo₂O₄ nanoplates, which act as an electrocatalyst and ii) to prevent the restacking of NiCo₂O₄ nanoplates. The presence of MoS₂, which is inactive towards the oxidation of glucose, allows a significant lowering of the oxidation overpotential from 0.58 V (pure NiCo₂O₄ nanoplates) to 0.42 V (MoS₂-NiCo₂O₄ nanocomposite), while the sensor was applied to the determination of glucose in human blood samples, diluted with 0.1 M NaOH, and exhibited a limit of detection (LOD) of 0.15 μ M glucose.

Sha et al. [70] reported on a MoS₂-based flexible sensor for the determination of uric acid in highly diluted urine samples. MoS₂ was hydrothermally grown on an aluminum foil, which was used as the working electrode enabling the determination of the target over the concentration range from 10 to 400 μ M and a LOD of 1.17 μ M, while the sensor retained almost 72% of its original response after 150 bending cycles. Interestingly, the generation of mostly 1T-MoS₂ polymorph leads to metallic behavior and consequently to high conductivity which negates the necessity of other conducting phases.

Simultaneous determination of uric acid and dopamine was reported by Ma et al. [124] employing MoS₂ nanosheets decorated with PtNi NPs, produced by a co-reduction method. The LOD of the method for both targets was found to be 0.1 μ M, while the sensor exhibited good selectivity and wide detection ranges for the simultaneous detection of dopamine (0.5-150 μ M) and uric acid (0.5-600 μ M). The sensor was evaluated in diluted, spiked human urine samples using the standard addition method. Selvam et al. [36] developed a method for the simultaneous determination of uric acid and melatonin by utilizing a self-assembled hydrothermally produced AuNP–MoS₂ nanocomposite. The sensor showed a linear response over the concentration range from 0.033 to 10 μ M for both targets, exhibited a good operational stability by retaining more than 90% of its original activity after 50 CV cycles and was tested in highly diluted (1000-fold), spiked urine samples.

Hydrogen peroxide, an important biomarker for oxidative stress under the category of reactive oxygen species (ROS), was determined upon release from breast cancer 4T1 cells using a PtW/MoS₂ nanocomposite, which was synthesized through in-situ growth of PtW nanocrystals on the surface of MoS₂ nanosheets (**Fig. 3**) [125]. The sensor exhibited remarkably detection capabilities allowing the determination of H₂O₂ at concentrations as low as 5 nM with, however, a relative standard deviation of 22% (n=4).

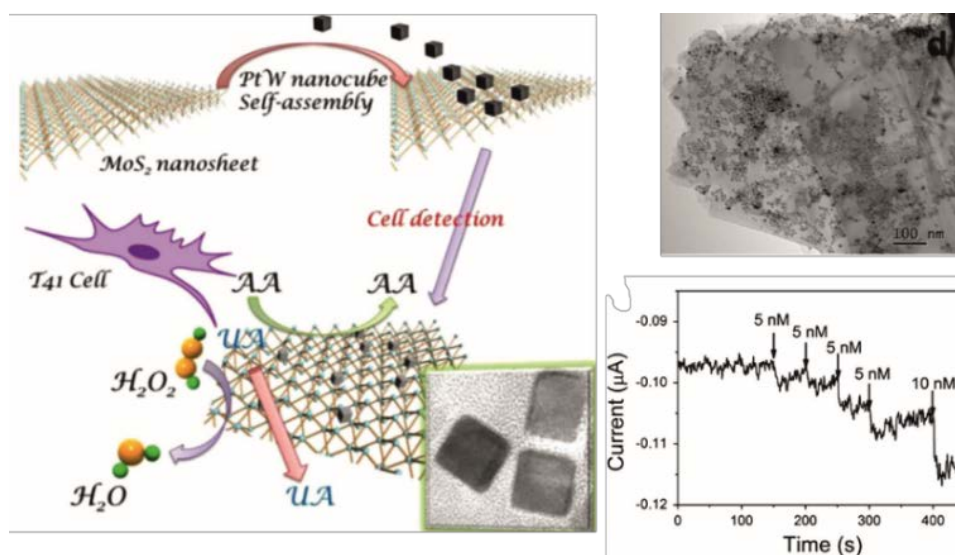


Fig. 3. (Left) Scheme for construction of PtW/MoS₂ nanocomposite acted as high specific sensing material for detecting H₂O₂ released from living cells (AA: ascorbic acid, UA: uric acid). (Right-top) TEM image of PtW/MoS₂ nanocomposite. (Right-bottom) The detection limit of PtW/MoS₂ nanocomposite material. Reprinted with permission from [125]. Copyright (2016) Elsevier.

WS₂ nanosheets produced by ball grind milling followed by reflux in sulfuric acid were used for the development of a WS₂–acetylene black composite, which was hydrothermally produced and used as a platform for the electrodeposition of AuNPs on a glassy carbon electrode (GCE) [140]. The WS₂–acetylene black composite offered a large specific surface area and consequently a high loading of AuNPs. The presence of the WS₂–acetylene black composite contributed to an efficient electron transfer as well as to an enhanced stability of the resulting DNA probe, which achieved a LOD of 0.12 fM and a linear relationship between the current and the logarithm of the concentration of the target DNA over the range 0.001–100 pM. The sensor was assessed in 10-fold diluted, spiked serum samples using the standard addition method.

An aptameric self-assembled DNA-WS₂ sensor was proposed for the determination of adenosine triphosphate (ATP) and Hg²⁺ ions [141]. This sensor works on the basis that WS₂ nanosheets exhibit greater affinity to single-stranded DNA (ssDNA) than double-stranded DNA (dsDNA) and thus can provide an effective sensing interface when combined with single-stranded, functional DNA or RNA structures, such as aptamers. We note that MoS₂ nanosheets have also been reported to possess different affinity to ssDNA and dsDNA [142]. In specific, 5–10 nm thick WS₂ nanosheets were used as an immobilization platform for (single-stranded) aptamers specific to ATP or Hg²⁺, which upon the binding reaction with their targets (ATP or Hg²⁺) formed duplex (double-stranded) and, due to their weak affinity to WS₂ nanosheets, are detached from the electrode surface (**Fig. 4**). The desorption of aptamers resulted in a variation of the charge-transfer resistance (R_{ct}) of the electrode-electrolyte interface, which is monitored with faradic electrochemical impedance spectroscopy (EIS) measurements. The detection range was 0.1 μ M–5 mM (LOD 1.5 nM), while for mercury ions, the analytical figures of merit were 0.1–500 nM and 0.5 pM. The applicability of the sensor was evaluated on 10-fold diluted, spiked human blood plasma samples.

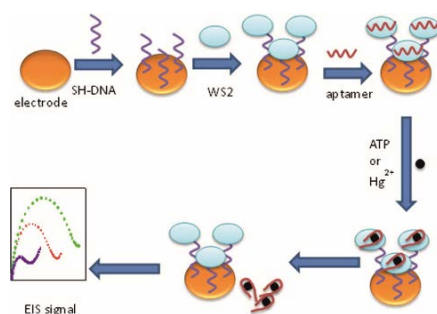


Fig. 4. Schematic illustration of the electrochemical sensing strategy for the detection of ATP or Hg²⁺. Reprinted with permission from [141]. Copyright (2017) Elsevier.

Hydrothermally produced WS₂ nanosheets were also drop-casted in a screen-printed electrode (SPE) and used as an electrocatalytic surface for the determination of the arsenical animal drug, roxarsone [30]. Based on differential pulse voltammetric measurements of the hydroxylamine-nitroso derivatives redox transition, the sensor exhibited a linear response over the concentration range from 0.05 to 500 μ M and a LOD of 0.03 μ M. The applicability of the sensor was successfully evaluated in meat samples. The results showed a good correlation with those obtained by a reference HPCL method.

WS₂ flakes decorated with catechin-capped gold nanoparticles (AuNP-CT) and carbon black (CB) were used for the simultaneous determination of hydroxycinnamic acids [143]. WS₂ nanoflakes were produced via ultrasonication, then were mixed with AuNP-CT and CB and finally, the composite material was used for the modification of SPEs. An illustration of the production and modification process is depicted in **Fig. 5**. This sensor achieved detection limits of 0.1 μ M (caffeic acid), and 0.4 μ M for sinapic acid and p-coumaric acids, highlighted with an excellent anti-fouling performance (RSD $I_{p,a}$ < 3%, n=15) and its applicability was studied extensively in real food samples with recovery values ranging from 87 to 109%.

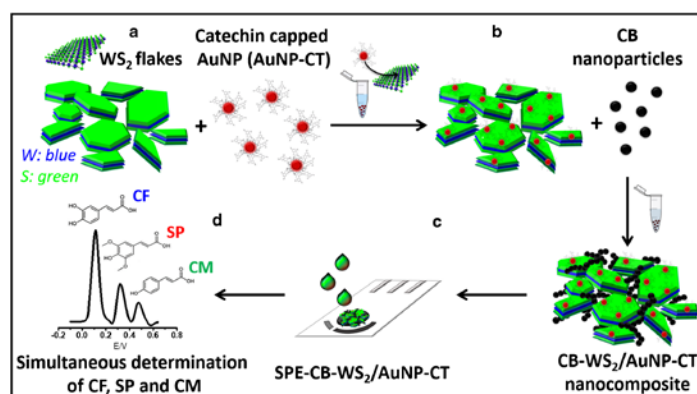


Fig. 5. Scheme of the SPE-CB-WS₂/AuNP-CT architecture for hydroxycinnamic acid structural analogs electrochemical sensing. (A) WS₂ decoration with AuNP-CT (B) Assembly of WS₂/AuNP-CT into CB. (C) SPE modification with the CB-WS₂/AuNP-CT nanocomposite. (D) DPV simultaneous determination of CF, SP, and CM. Reprinted with permission from [143]. Copyright (2020) Springer.

An electrochemical sensor using thiolated RNA probe immobilized on WSe₂ nanosheet/AuNP-modified electrode was reported for the determination of microRNA-21 (miRNA-21) [67]. The WSe₂ nanosheets were produced via a solvothermal method

and were found, due to their large specific surface area, to increase the loading of AuNPs as well as to accelerate the electron transfer rate of the horseradish peroxidase (HRP)-catalyzed H_2O_2 -hydroquinone detection system. The sensor exhibited a wide linear range from 0.0001 to 100 pM towards target miRNA with a LOD of 0.06 fM, and was tested in human serum samples from breast cancer patients.

Gan et al. [126] proposed a p-aminophenol/AuNP-decorated- H_xTiS_2 sensor for the determination of Cu^{2+} ions. The H_xTiS_2 nanosheets were produced via a lithium intercalation method. The working principle is based on the high thiophilicity of gold that enables bonding of AuNPs onto the TiS_2 platform that leads to the determination of the target ions at the picomolar concentration range. The LOD was estimated to be 0.09 nM while the detection range spans from 0.2 nM to 5 μM Cu^{2+} . The sensor showed a high selectivity over Cd^{2+} , Pb^{2+} , Ni^{2+} , and Hg^{2+} which is linked with steric effects derived from the inclusion of p-aminophenol to the sensing platform.

Toh et al. [144] reported a comparative study of Group 6 TMD (MoS_2 , MoSe_2 , WS_2 , and WSe_2) nanosheets towards the non-enzymatic chronoamperometric detection of H_2O_2 . All the examined TMD nanosheets were produced via a lithium intercalation method and exhibited 1T polymorph. 1T- WS_2 showed the most promising results and the respective sensor achieved a LOD of 2 nM. While this sensing device offers an interesting technological perspective by featuring a screen-printed lab-on-a-chip microfluidic technology, it does not feature a thorough analytical investigation on real samples. Its analytical applicability is demonstrated by a comparison between chronoamperometric responses upon injection of H_2O_2 in phosphate buffered saline (PBS) and 10% human serum in PBS.

Rohaizad et al. [57] reported a comparative study including three platinum dichalcogenides (PtX_2 , X=S, Se and Te) towards the development of a non-enzymatic chronoamperometric sensor for H_2O_2 . Bulk PtS_2 , PtSe_2 and PtTe_2 materials were prepared in a quartz glass ampoule by heating stoichiometric amounts of their respective elements, followed by ultrasonication in ultrapure water to produce nanosheets. Due to the covalent nature of Pt-X bond, interlayer chalcogen atoms also resulted in a covalent-like bonding, instead of the weaker Van der Waals interaction, and in a stronger interlayer interaction as we are going down the Group 6 elements. As a result, PtX_2 possess different electronic properties: PtS_2 is semiconducting, PtSe_2 is semimetallic and PtTe_2 is metallic [145]. In turn, different electronic properties showed to govern the electrocatalytic performance of the respective PtX_2 -modified GCEs.

Among the examined PtX_2 nanosheets, PtTe_2 gave the most promising results, achieving a LOD of $1.2\ \mu\text{M}$. Interestingly, even though Pt is recognized as one of the most efficient electrocatalyst for H_2O_2 , the respective dichalcogenides fall sort compared with other TMD, such as those of Group 6 (MoS_2 , MoSe_2 , WS_2 , and WSe_2) mentioned above [144].

1.4.2 TMDs: Gas-phase sensors

The semiconducting nature of the majority of TMD nanosheets along with their sensitivity to the atmospheric environment and high surface-to-volume ratio has shifted the attention to their implementation on gas-sensing devices.

Noble metal nanoparticles can successfully functionalize the surface of TMD nanosheets to enhance the gas-sensing detection capabilities of the respective analytical devices. Noble-metal NPs act as electron traps thus hindering the rapid recombination of electrons and holes, which also benefits the electronic properties of the sensing materials [146]. The selective detection of both oxygen-based (acetone, ethanol, and 2-propanol) and hydrocarbon-based (hexane, toluene, and benzene) volatile compounds by a AuNP-decorated MoS_2 nanoflake-modified interdigitated electrode was reported (**Fig. 6 top**) [147]. Oxygen-based VOCs donate electrons to the MoS_2 surface, thus producing an increase in electric current, which is further enhanced by the presence of the AuNPs that, though an electron donating effect, increase the electron concentration at the hybrid sensing surface, resulting in higher loading of adsorbed oxygen species (O_2^- and $\bar{\text{O}}$) that in turn, trap more electrons from MoS_2 (**Fig. 6 bottom (b,c,d)**). The response has a linear relationship with the concentration of acetone over the range 10-120 ppm while the response/recovery times were 100/385 s, respectively. The response of the sensor decreases at a rate of 0.15%/RH (RH 10-60%) and retains almost the 94% of its original response after 1000 bending cycles.

On the other hand, hydrocarbon-based VOCs adsorb onto the MoS_2 surface creating only dipole scattering through electron clouds of their methyl groups, thus producing a small change in signal (**Fig. 6 bottom (a)**).

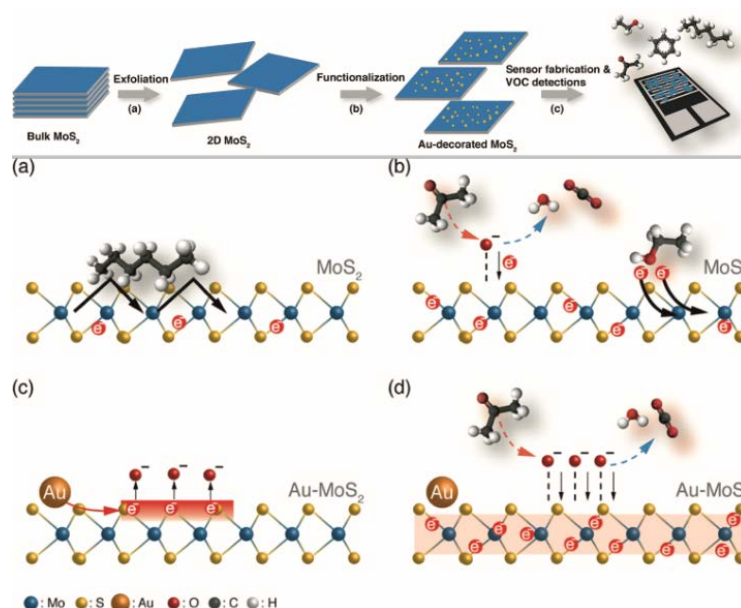


Fig. 6. (Top) Schematic process flows for the fabrication of MoS₂-based nanoflakes and gas sensors: (a) liquid-phase exfoliation of bulk MoS₂, (b) functionalization of 2D MoS₂ nanoflakes with Au NPs, and (c) fabrication of Au-decorated MoS₂ sensors for VOC detections. (Bottom) Schematic diagrams elucidating differences in sensing mechanisms of (a) hydrocarbon-based VOCs and (b) oxygen-based VOCs using MoS₂, as well as using Au-decorated MoS₂ to detect oxygen-based VOCs, (c, d). (a) Hydrocarbon-based VOC molecules adsorbed onto MoS₂ creating only dipole scattering through electron clouds of their methyl groups and thus contributing to a small change in electronic signals. (b) Upon exposure to oxygen-based VOCs, (right) the injection of electrons occurs by the electron-donating properties of ethanol; (left) the interaction between oxygen species (O₂⁻ and \bar{O}) adsorbed on MoS₂ and oxygen-based VOCs creating volatile species (CO₂ and H₂O), subsequently releasing electrons back to MoS₂; both mechanisms contribute to the increases of gas response for pristine MoS₂ sensor. (c) Decoration of Au NPs resulting in an increase of electron concentration on MoS₂, causing an increase of adsorbed oxygen species and thus (d) for the Au-decorated MoS₂ to have higher responsivity and selectivity toward oxygen-based VOCs because of the return of more electrons captured by adsorbed oxygen species on MoS₂ channel. Reprinted with permission from [147]. Copyright (2019) American Chemical Society.

MoSe₂ nanosheets have also been successfully incorporated into gas-sensing devices. Guo et al. [148] reported on an artificially intelligent flexible gas-sensor on an ultra large MoSe₂ nanosheet for the detection of ammonia gas and NO₂ (**Fig. 7a,b**). MoSe₂ nanosheets were isolated via a gold-assisted micromechanical exfoliation method and subsequently transferred to a flexible kapton tape substrate (**Fig. 7d**). Since MoSe₂ is an n-type semiconductor, the resulting sensor showed positive sensitivity through NH₃ detection (n-doping) and a negative sensitivity through the NO₂ detection (p-doping). NO₂ acts as an electron acceptor and reduces NO₂ into NO₂⁻, while NH₃ serves as an electron acceptor on n-type MoSe₂. Interestingly, the developed sensors can be integrated on human skin (**Fig. 7c**), showing a stable response with up to 30% tensile strain, attractive detection capabilities (NO₂: linear response over 2-10 ppm, LOD 10 ppb (**Fig. 7e-h**); NH₃: linear response over 5-12 ppm, LOD 20 ppb] and fast response

(250 s) and recovery (150 s) times (**Fig. 7i-l**). The sensor can wirelessly collect and store data to a cloud database, thus allowing to provide timely warnings and to be used as a point-of-care diagnostics device.

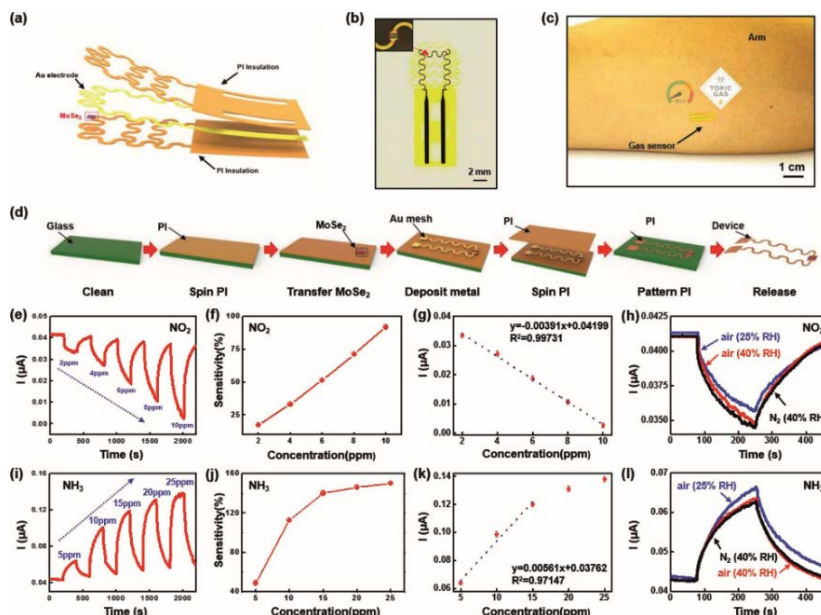


Fig. 7. Experiment on human skin and gas sensing properties of NO_2 and NH_3 : a) 3D schematic of the device structure with PI encapsulation and gold electrode as a contact pad. b) Optical image of the device, where the inset shows the OM image with a comb structure as an electrode. c) Patch on relaxed human skin to test and record gas data. d) Detailed fabrication process of e-GS. e) Response and f) sensitivity curve to different concentration of NO_2 , $V = 5$ V. g) Linear curve fitting of concentration–response curve, whose slope is used to extract the detection limitation. h) Response curve under different carrier gas conditions (air with 25% RH, air with 40% RH, and N_2 with 40% RH). i) Response and j) sensitivity curve relative to different concentration of NH_3 , $V = 5$ V. k) Linear curve fitting used to extract the detection limitation. l) Response curve under different carrier gas conditions. Reprinted with permission from [148]. Copyright (2019) Wiley VCH.

For a detailed description of recent developments on transition metal dichalcogenides-based flexible gas sensors the reader is referred to the comprehensive review in Ref. [45].

1.4.3 TMOs: Electrochemical sensing applications

MnO_2 nanosheets have attracted wide attention mostly due to their oxidase-mimicking properties, which render them important catalysts for the determination of various reducing compounds, such as glutathione, ascorbic acid, and H_2O_2 . Due to the low intrinsic electrical conductivity of MnO_2 ($10^{-5} - 10^{-6} \text{ S cm}^{-1}$), it is often used in

combination with various conductive nanomaterials, such as graphene, carbon nanotubes or metal nanoparticles [48]. However, MnO₂ nanosheets alone have been successfully used in the development of advanced electrochemical sensors. For instance, Shu et al. reported a MnO₂ nanosheet-modified GCE for the amperometric determination of H₂O₂ in SP2/0 cells [149]. This sensor showed a LOD of 0.005 μM and a concentration dependent sensitivity over the concentration ranges 0.025 – 2 μM and 10 – 454 μM.

MnO₂ nanosheets have also been incorporated into an ionic liquid-functionalized graphene/polydopamine composite for the simultaneous determination of guanine and adenine over the concentration range 10-300 μM [150]. The achieved LODs were 0.25 μM for guanine and 0.15 μM for adenine. This sensor is credited with good anti-fouling properties, attributed to the presence of a polydopamine protected coating over the electrode surface, by retaining the overwhelming of its original response to the targets after immersion for 30 min in 50 mg/mL BSA. The recovery of the method in 50-fold diluted, fetal bovine serum and mice whole blood spiked samples was 85.7-105.6%.

Ni(OH)₂ nanocaged MnO₂ nanosheets have been reported in a core-shell architecture for highly sensitive detection of dopamine [151]. MnO₂ nanosheets were wrapped around Ni(OH)₂ nanocages through a hydrothermal method by using KMnO₄ as starting compound. The sensor enabled the determination of dopamine at concentrations higher than 80 nM while the analytical applicability of the sensor was examined only to diluted dopamine hydrochloride injection and the recovery of the method was 92-101.7%.

Mahmoudian et al. [152] developed a Co₃O₄/Ni(OH)₂ sensor for the determination of glucose in green tea extracts. Solvothermally produced Co₃O₄ nanosheets were found to improve the sensitivity of the sensor compared with that achieved at pure Ni(OH)₂ modified electrode, while due to the negative charge of the modifying composite material under the alkaline working conditions (0.1 M NaOH), the designed sensor exhibited a satisfactory selective against ascorbates and urates based on a charge repelling mechanism.

Vabbina et al. [153], reported a comparable study between two ZnO nanostructures, namely 1D-ZnO rods and 2D-ZnO nanosheets, which were used for the construction of cortisol immunosensors in saliva (**Fig. 8a**). 20 nm thick 2D-ZnO nanosheets with an average lateral dimension of 5×5 nm demonstrated an increased chemical stability and higher loading of cortisol antibodies. Based on cyclic voltammetric measurements in the presence of hexacyanoferrate(III)/(II) as a redox probe (**Fig. 8b**), a cortisol

dependent decrease of the signal, due to the progressive decrease of the flux of the redox probe through the immunocomplex, was observed. The method allowed a LOD of 1 pM and a response proportional to the logarithm of the concentration of the target over the concentration range from 100 pM to 100 nM. Interestingly, the method showed an excellent correlation with the results obtained by a commercial ELISA kit in non-spiked saliva samples.

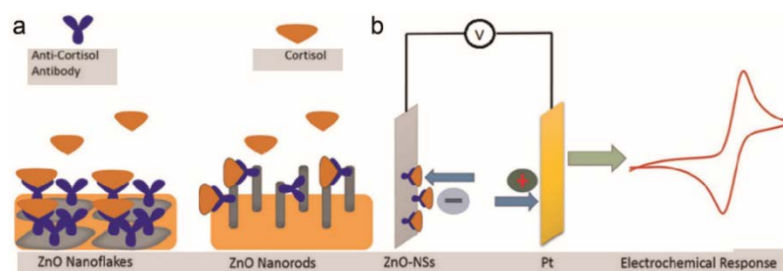


Fig. 8. (a) Illustration of ZnO-NRs and ZnO-NFs prepared using sonochemical method along with immobilization of monoclonal anti-cortisol antibody onto ZnO-Ns to fabricate electrochemical cortisol immunosensor. (b) Electrochemical response at the fabricated electrodes. Reprinted with permission from [153]. Copyright (2015) Elsevier.

1.4.4 TMOs: Gas-phase sensors

TiO₂ nanosheets produced via a facile surfactant self-assembly method were incorporated in an impedimetric humidity sensor [154]. The mesoporous structure of TiO₂ nanosheets provides shortened transport paths and direct diffusion channels for fast adsorption/desorption of water. The sensor performed efficiently over the %RH range 11-95% with a response time of 3 s and a recovery time of 50 s.

Another example is the growth of Co₃O₄@NiMoO₄ composite arrays for the detection of TEA [128]. A resistance increase is observed upon TEA adsorption due to the p-type semi conductivity of the composite and the n-doping of TEA. This sensor exhibited a LOD of 1 ppm and a linear response up to 100 ppm at an operating temperature of 250 °C. It is noteworthy that sensor's response was found to be ca. 4-fold higher than the pristine Co₃O₄ arrays and almost 9-fold higher than the pristine NiMoO₄.

1.4.5 MXenes: Electrochemical sensing applications

Lorencova et al. [155] proposed a highly stable Ti₃C₂T_x/PtNP composite-modified GCE for the amperometric determination of H₂O₂. Ti₃C₂T_x was produced by LiF-HCl etching

process and ultrasonication. Even though the response of the sensor was quite stable, the detection capabilities are rather poor as the linear response of the sensor spans over the concentration range from 490 μM to 53.6 mM. $\text{Ti}_3\text{C}_2\text{T}_x/\text{PtNP}/\text{GCE}$ also showed an electro catalytic response on the oxidation of common reducing compounds such as ascorbic acid, uric acid, acetaminophen and dopamine. Combined with a Nafion or a chitosan coating the resolution of the oxidation peaks of the afore-mentioned compounds is satisfactory, however data on the simultaneous determination of these compounds are not provided. A Nafion/ $\text{Ti}_3\text{C}_2\text{T}_x$ -modified GCE has also been proposed for the voltammetric determination of BrO_3^- ions [130]. The sensor achieved a LOD of 41 nM and a detection range of 50 nM – 5 μM and it was successfully applied to the determination of bromates in tap water samples spiked with KBr prior to ozonation treatment. The results are in good agreement with those obtained by ion chromatography.

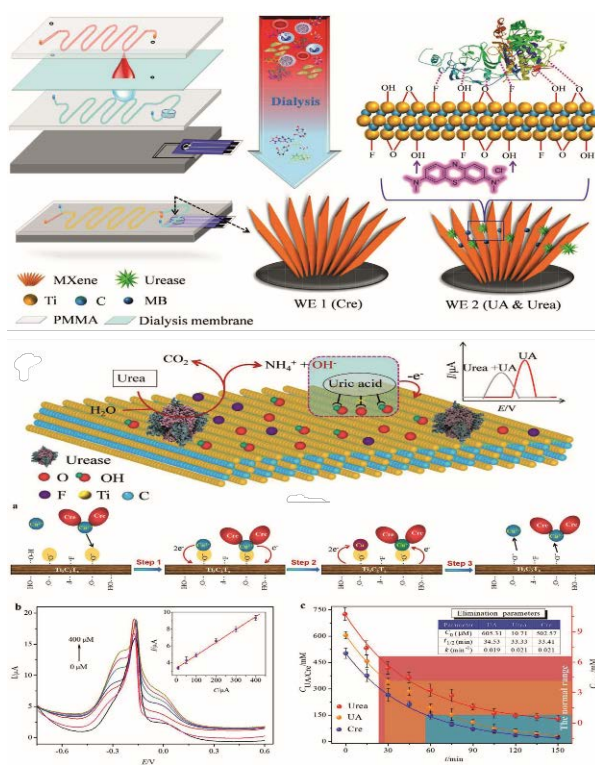


Fig. 9. (Top) schematic illustration of fabrication of MXene-enabled microfluidic chip. (Middle) schematic illustration of urea determination. (Bottom) a) schematic illustration of creatinine determination. b) SWV responses of the microfluidic chip toward different concentrations of Cre dissolved in 0.01 m AB isotonic solutions containing $20 \times 10^{-6} \mu\text{M}$ Cu^{2+} and the inset is the calibration curve of concentration of Cre and the stripping peak current of cuprous ions ($n = 3$). c) Concentration–time curves of UA, urea, and Cre in whole blood during hemodialysis. C_0 is the concentration of each target before dialysis; $t_{1/2}$ means the half-life of elimination; k represents the rate constant for elimination. Reprinted with permission from [156]. Copyright (2019) Wiley VCH.

An MXene-enabled electrochemical microfluidic (bio)sensor for the at-line analysis of whole blood serum and the determination of urea, uric acid and creatinine was proposed by Liu et. al [156] as a promising device for point-of-care use in hemodialysis treatment. $\text{Ti}_3\text{C}_2\text{T}_x$ nanosheets were produced via a 40 wt% HF etching process and subsequent ultrasonication and were incorporated in a multilayer (bio)sensing device incorporating i) an MXene modified screen-printed electrode (urease-methylene blue(MB)/MXene/SPE for the determination of uric acid (UA) and urea or MXene/SPE for the determination of creatinine), ii) a pair of PMMA plates bearing laser engraved flow channels, and iii) a dialysis membrane (molecular weight cut-off 1 kDa) sandwiched between PMMA plates that enables exclusion of fouling induced biopolymers towards the electrode surface (**Fig. 9**).

The sensing principles for the model targets (urea, uric acid and creatinine) are as follows: the determination of UA was established via a ratiometric method based on the peak current ratio of UA and MB [$I_{\text{UA}}/I_{\text{MB}}=f(\log C_{\text{UA}})$], which was used to produce a reference signal for intercalibration purposes. The detection range was 30-500 μM .

The determination of urea was based on the action of enzyme urease on urea and the enzymatically produced ammonia, which increases the pH of the solution (**Fig. 9**). With increasing pH, the peak potential (E) of both MB and UA shifted in more cathodic potential values allowing a linear relationship between C_{urea} and E_{UA} to be established over the range 0.1-3 mM. The determination of creatinine was conducted by feeding the measuring solution with cupric ions and the formation of a Cu^{2+} -creatinine complex, which through adsorptive stripping voltammetry measurement gave rise to anodic peak currents proportional to the amount of creatinine over the concentration range from 10 to 400 μM (**Fig. 9**). Remarkably, the MXene-based microfluidic (bio)sensing device was successfully applied to the examination of renal function among 105 healthy people showing an excellent agreement to a hospital reference method.

A composite AuNP/ $\text{Ti}_3\text{C}_2\text{T}_x$ film was utilized for the simultaneous determination of UA and folic acid [131]. $\text{Ti}_3\text{C}_2\text{T}_x$ nanosheets were produced via wet etching, DMSO intercalation and subsequent ultrasonication, while AuNPs were galvanically deposited onto the MXene nanosheets. The sensor exhibited wide detection ranges, 0.02-3580 μM for UA and 0.03– 20 μM for folic acid, while the LODs were found to be 6.2 nM and 11.5 nM, respectively. The sensor enabled the formation of two well-separated oxidation peaks at 0.35 V and 0.70 V vs. Ag/AgCl, respectively and used for the

determination of the targets in spiked serum samples. The recoveries were 97.1-98.8% and 96.8-98.0%, respectively.

Shankar et al. [132] reported on a $\text{Ti}_3\text{C}_2\text{T}_x$ -modified graphite carbon paste electrode for the electrochemical determination of adrenaline in spiked injection samples. The applicability of the sensor to complex biological samples is not demonstrated.

An elaborated MXene-based aptasensor was proposed for the determination of breast cancer marker Mucin1 in 100-fold diluted, spiked human serum samples [157]. Ti_3C_2 which were produced via HF etching were used as immobilization platform for cDNA-ferrocene electrochemical tags that through a competitive assay format on the fully functionalized cDNA-Fc/MXene/Apt/Au/GCE aptasensor are detached from the electrode surface resulting in a decreased redox response proportional to the concentration of Mucin1 over the range from 0.001 – 1.0×10^{-4} nM.

Another example is a 0D/2D heterojunction of $\text{Ti}_3\text{C}_2\text{T}_x$ nanosheets and iron phthalocyanine quantum dots (FePc QDs) for the impedimetric aptasensing of micro RNA-155 on gold electrodes [158]. $\text{Ti}_3\text{C}_2\text{T}_x$ nanosheets were produced via a HF etching and were ultrasonically mixed with FePc QDs to give a composite material through π -stacking interactions. The sensing principle is based on the hybridization between the immobilized cDNA and the micro RNA-155 (60 min), which in turn hinders the electron transfer of hexacyanoferrate(III)/(II) redox probe in faradic EIS measurements allowing a low LOD of 4.3 aM and a detection range from 0.01 fM to 10 pM miRNA-155.

An MXene-based stretchable, wearable biosensor for in vitro perspiration analysis was proposed by Lei et al. [159]. The biosensor incorporates a $\text{Ti}_3\text{C}_2\text{T}_x$ /Prussian blue (PB) composite that is combined with a superhydrophobic carbon fiber to i) create a solid–liquid–air tri-phase interface to protect the connector inside the sensor patch from sweat corrosion and ii) ensure a sufficient supply of O_2 and increase the stability of biosensors. The wearable biosensor patch consists of a sweat-uptake layer, a sensor layer (glucose, lactate, and pH sensors; the latter used to adjust the concentration of the target biomarkers through the calibration plot at different pH values), and a cover layer made of soft silicone rubber in which air holes were intentionally introduced to allow atmospheric oxygen to easily diffuse toward the sensing layer (**Fig. 10**). A rich-oxygen environment is indispensable for the action of glucose oxidase and lactic oxidase enzymes on their substrates and the formation of an abundant quantity of H_2O_2 , which in turn strengthens the signal and permits a more precise assay. $\text{Ti}_3\text{C}_2\text{T}_x$ was produced

by applying gentle delamination conditions, and mixed with carbon nanotubes and PB, which were used to enforce mechanical stability and to mediate the electro reduction of the enzymatically produced H_2O_2 , respectively.

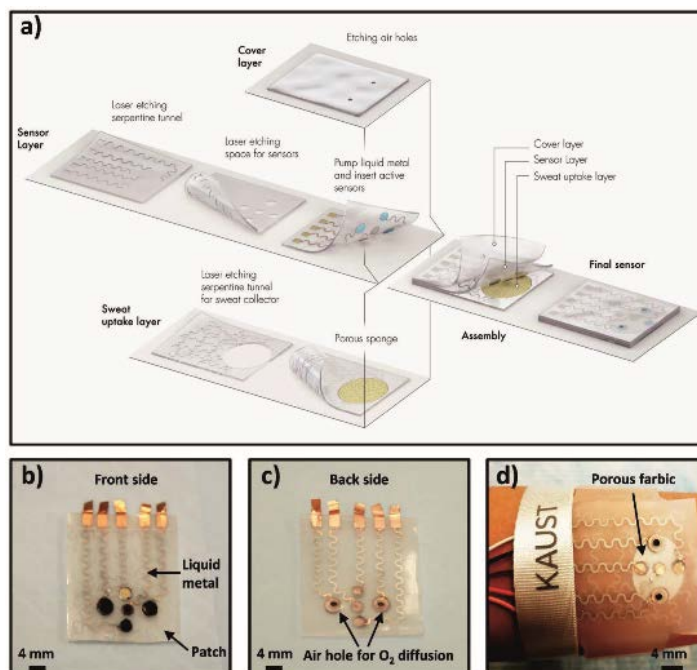


Fig. 10. Schematic drawings and corresponding images of the wearable biosensor patch. a) Schematic illustration of the sensor patch system, which is composed of a sweat-uptake layer, a sensor layer, and a cover layer. b) Front-side optical image of the sensor array (left and right), reference electrode (top), counter electrode (middle), and pH sensor (bottom). c) Back-side optical image of the sensor array. d) Optical images of the sensor wristband laminated on human skin. Reprinted with permission from [159]. Copyright (2019) Wiley VCH.

Koyappayil et al. [160] reported on the construction of a reagentless biosensor for the determination of β -hydroxybutyrate (β -HB) over the concentration range 0.36–17.9 mM (LOD 45 μM) by using $\text{Ti}_3\text{C}_2\text{T}_x$ nanosheets, which were produced by wet etching, as immobilization platform of β -hydroxybutyrate dehydrogenase (β -HBDG) and its coenzyme (NAD^+). Amperometric measurements were conducted with gold electrodes modified with hexaammineruthenium(III) chloride redox probe, which was used as charge-transfer mediator for the oxidation of the enzymatically produced NADH, regenerating thus NAD^+ on the sensing surface. The biosensor was applied to the determination of β -hydroxybutyrate in diluted, spiked real serum samples.

Song et al. reported on the development of electrochemically etched Nb_2CT_x nanosheets as chronoamperometric biosensors for the selective determination of

phosmet [161]. Electrochemical etching was carried out under potentiostatic conditions at 1 V in 0.5 M HCl for 4 h. The biosensor (E-etched Nb₂CT_x NS/GA/AChE) was assembled by mixing the final MXene with acetylcholinesterase (AChE) and glutaraldehyde (GA) to attain enhanced enzyme activity and electron transfer. A general schematic of the MXene production and the assembly of the biosensor is shown in **Fig. 11**. The assembled biosensor achieved an LOD of 1.44×10^{-10} M over a linear range of $2 \times 10^{-10} - 1 \times 10^{-9}$. The applicability of the biosensor was evaluated in apple samples with recovery values ranging from 98.05 to 107.77% (n=3).

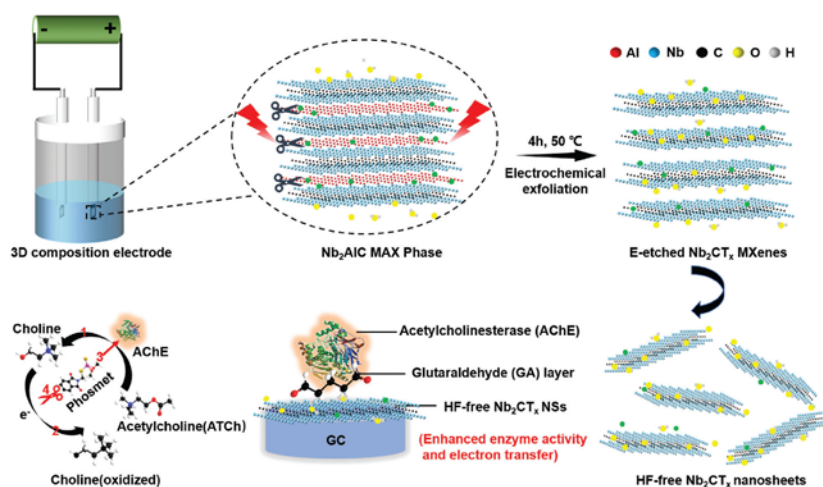


Fig. 11. Schematic for exfoliation and delamination process of Nb₂AlC MAX phase via electrochemical etching and the enzyme inhibition effect for phosmet detection by HF-free Nb₂CT_x/AChE based biosensor. Reprinted with permission from [161]. Copyright (2020) Wiley VCH.

Hydrothermally produced oxidized vanadium carbide (V₈C₇T_x) hybridized with nitrogen-doped graphene nanosheets (VC/NG NSs) were used for the voltammetric determination of clioquinol (CQL) [162]. A detailed illustration of the production process and its utilization in electrochemical applications is shown in **Fig. 12**. MXene was prepared through a hydrothermal etching process in H₂O₂. The electrocatalyst suspension was formed by mixing VC with NG isopropyl alcohol through an ultrasonication process. The material was drop-casted to a GCE and the modified electrode achieved an LOD of 9 nM over a linear range of 0.5 – 585 μ M. The method was evaluated in urine samples with appreciable recovery values (~98% (n=3)).

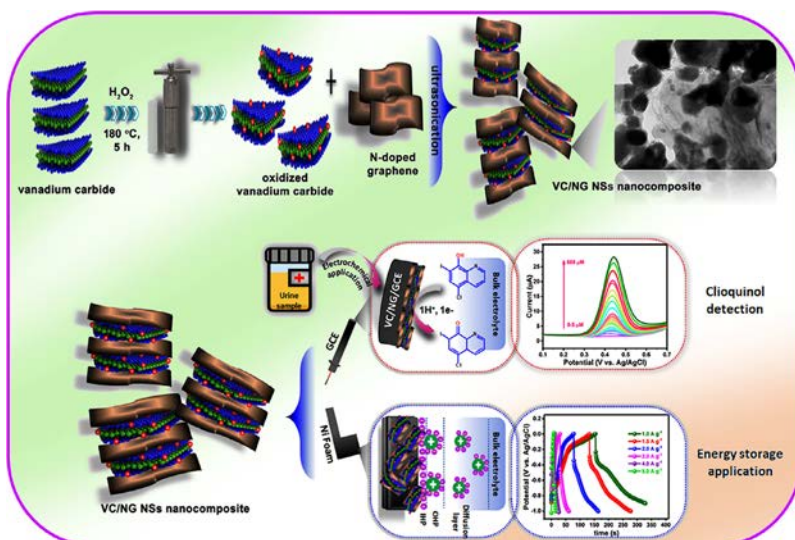


Fig 12. Schematic illustration for the preparation of VC/NG NSs nanocomposite and its electrochemical applications. Reprinted with permission from [162]. Copyright (2022) Elsevier.

1.4.6 MXene: Gas-phase sensors

Lee et al. [163] explored the development of a sensing platform for the detection of ethanol, methanol, acetone and ammonia gases utilizing $\text{Ti}_3\text{C}_2\text{T}_x$ nanosheets on a flexible polyimide substrate. $\text{Ti}_3\text{C}_2\text{T}_x$ nanosheets were produced via HCl-LiF etching and subsequent ultrasonication. Due to the n-doping of these VOCs (electron donors) and the p-type semi conductivity of the $\text{Ti}_3\text{C}_2\text{T}_x$ nanosheets, a resistance increase is observed upon gas-adsorption onto the sensing platform. Despite successful detection of all VOCs analytical parameters are only presented for acetone. The theoretical LOD for acetone was 9.27 ppm over a 25 - 200 ppm range at room temperature.

Kim et al. [164] further explored the sensing properties of the wet etched $\text{Ti}_3\text{C}_2\text{T}_x$ nanosheets onto a gold electrode. The sensor's applicability was tested in both n- and p-doping VOCs including acetone, ethanol, ammonia, propanal, nitrogen dioxide, sulfur dioxide and carbon dioxide, which were diluted in N_2 gas. Interestingly, the sensor displayed a positive resistance increase regardless of the doping nature of each gas. This is attributed to an untraditional gas sensing mechanism, which is prevalent due to the metallic conductivity of the Ti_3C_2 core. Nevertheless, the sensor showed superior sensing ability towards acetone, ethanol, and ammonia gases. Specifically, the LODs were found to be: i) 50 ppb for acetone over a 50-1000 ppb range, ii) 100 ppb for ethanol over a 100-1000 ppb range and iii) 100 ppb for ammonia over a 100-1000 ppb.

Composite MXene-based gas-sensors have also been proposed. For instance, Tai et al. [133] reported on a $\text{Ti}_3\text{C}_2\text{T}_x/\text{TiO}_2$ NPs gas sensor for the determination of ammonia at room temperature. $\text{Ti}_3\text{C}_2\text{T}_x$ nanosheets were prepared via a HF etching and tetramethylammonium hydroxide (TBAOH) intercalation. The sensing mechanism is based on the n-doping of NH_3 to the TiO_2 NPs, which increases its electron concentration but hampers the hole accumulation process of $\text{Ti}_3\text{C}_2\text{T}_x$, leading to an overall resistance increase that was proportional to the concentration of ammonia over the range from 2 to 10 ppm.

Despite $\text{Ti}_3\text{C}_2\text{T}_x$ nanosheets dominance on both MXene-based sensing applications in solution or in gas phase, a few exceptions to this rule have been recently reported. Lee et al. [165] developed a 2D vanadium carbide (V_2CT_x)-based gas sensor with ultra-high sensitivity towards nonpolar gases. V_2CT_x nanosheets were produced via a HF etching at room temperature and subsequent TBAOH intercalation. Sensor's performance was assessed towards 100 ppm of various reducing gases (n-doping) including hydrogen, ethanol, acetone, methane, ammonia, and hydrogen sulfide and showed positive resistance response, which is attributed to p-type semi conductivity of V_2CT_x . However, since the authors do not report experimental results for oxidizing gases (p-doping), the sensing mechanism cannot be conclusively explained as it is possible that V_2CT_x could adopt a similar behavior to $\text{Ti}_3\text{C}_2\text{T}_x$, which responds in a resistive manner for both gas types. The sensor achieved LODs of i) 11.2 ppm for acetone over a linear range of 25-200 ppm, ii) 9.4 ppm for methane over a linear range of 25-400 ppm, iii) 1.4 ppm for hydrogen over a linear range of 2-100 ppm, and 3.5 ppm for hydrogen sulfide over a linear range of 5-100 ppm.

1.4.7 Pnictogens: Electrochemical sensing applications

Implementation of monoelemental 2D materials in sensing applications has been a desideratum ever since the emergence of graphene. While “pnictogen” nanosheets have been explored in various electrochemical sensing applications with phosphorene being the most popular material among them [31, 105, 135–137, 166], this cannot be said for “tetrel” nanosheets, which are more often mentioned in theoretical works.

Niu et al. [135] explored the incorporation of a phosphorene- poly(3,4-ethylenedioxythiophene)-poly(styrenesulfonate) (PEDOT:PSS) heterojunction for the electrochemical detection of rutin, a common flavonoid glycoside. Due to fact that

phosphorene is not stable in ambient conditions and gradually degraded due to the interaction with oxygen and water, the phosphorene-PEDOT:PSS composite was prepared in a nitrogen-filled glovebox by mixing commercially phosphorene nanosheets and PEDOT:PSS in ethanol followed by ultrasonication and finally, the mixture was drop-casted on a GCE. The sensor showed linear dependence on the concentration of rutin within two ranges: 0.02-15 μM and 15-80 μM with a LOD of 7 nM. Analytical data are provided only in diluted medicinal rutin tablets.

The electroanalytical properties of the phosphorene-PEDOT:PSS composite, in this application in combination with surface confined hemin on a carbon ionic liquid electrode, were further explored through the voltammetric determination of i) trichloroacetic acid (TCA), ii) sodium nitrite and iii) H_2O_2 [136]. The sensor achieved LODs of i) 0.67 mM (detection range of 2-180 mM), ii) 0.33 mM (detection range of 1-10.5 mM) and iii) 1.33 mM (detection range of 4-35 mM), respectively and its applicability was evaluated for the determination of TCA in diluted medical facial peel solutions.

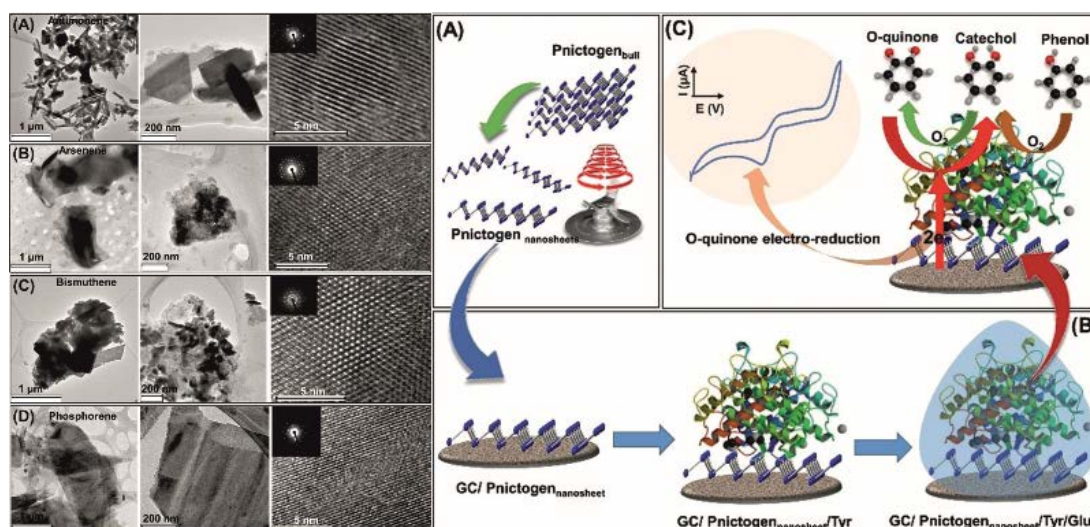


Fig. 13. (Left) Transmission electron microscopy at different magnifications (left and central panels), high-resolution TEM (right panels), and selective area diffraction (insets) of antimonene (A), arsenene (B), bismuthene (C), and phosphorene (D) shear exfoliated nanosheets. (Right) A) Shear exfoliated pnictogens using kitchen blender. B) Biosensor preparation using layer-by-layer drop-casted pnictogen nanosheets, tyrosinase (Tyr), and glutaraldehyde (Glu) onto a glassy carbon (GC) electrode. C) Chemical mechanism of phenol detection by biosensor based on exfoliated pnictogen and Tyr. Reprinted with permission from [105]. Copyright (2019) Wiley-VCH.

Ramalingam et al. [137] reported on a phosphorene-AuNP nanocomposite-based microfluidic aptasensor for the detection of okadaic acid, a by-product of “harmful algal blooms”. Phosphorene was produced via ultrasonication of black phosphorous in N-methylpyrrolidone for 8 h, while the formation of the phosphorene-Au NP nanocomposite was based on the in-situ reduction capacity of phosphorene nanosheets on HAuCl₄. The detection range was from 10 to 250 nM and the sensor was applied to the determination of the toxin in spiked extracts of fresh mussel samples. The recovery was 95-104%. A PEDOT NP/beta-cyclodextrin (β -CD)/phosphorene nanocomposite was employed for the simultaneous determination of clenbuterol (CLB) and ractopamine (RAC), which are being used as illegal farming growth promoters [31]. Phosphorene was purchased from a retailer. Sensing mechanism exploits the host-guest recognition ability of β -CD and the electrochemical sensing properties of PEDOT NPs. The response of the sensor was linear over the concentration range from 0.3 to 90 μ M CLB, and from 0.3 to 9.4 μ M for RAC. The LODs were 0.14 and 0.12 μ M, respectively. The sensor was employed for the simultaneous determination of CLB and RAC in (spiked) beef, feed, and bovine serum samples with good recoveries.

The implementation of both phosphorene and of the remaining pnictogen nanosheets (antimonene, bismuthene and arsenene) into enzymatic biosensors was examined by Mayorga-Martinez et al. [105]. Bulk pnictogens were shear-force exfoliated with commercial kitchen blenders in sodium cholate (SC) for 2 h (**Fig. 13, left**). Four different biosensors were constructed via layer-by-layer deposition of each pnictogen nanosheet and the enzyme (tyrosinase) and were assessed through phenol detection following the o-quinone electroreduction to catechol (**Fig. 13, right**). Antimonene-based biosensor exhibited the highest electrocatalytic activity and was employed for the chronoamperometric determination of phenol, achieving an LOD of 255 nM.

Antimonene was also explored by Mendiola et al. [167] for the development of a DNA biosensor. Antimonene nanosheets were functionalized with single stranded oligonucleotide (BRCA 1 synthetic sequence) for sensing of gene BRCA1 associated to breast cancer. Antimonene was produced through ultrasonication of bulk antimony in 2-propanol for 2 h and was subsequently drop-casted onto an Au-SPE. The sensor exploits the non-covalent but strong interactions between the oligonucleotide probe and antimonene nanosheets. Using thionine as redox probe, the sensor achieved a LOD of 28.3 pg μ L⁻¹ over a linear range of 0.1-20 ng mL⁻¹. The biosensor was used as a fast

and accurate screening method for mutation detection in BRAC1 gene from healthy or diseased patients, who has the mutation, directly in clinical samples.

1.4.8 Pnictogens: Gas-phase sensors

Phosphorene is a p-type semiconductor, which possesses a thickness-dependent band gap ranging from 0.3 – 2.0 eV, thus providing the opportunity of multiple analyte gas sensing. Cui et al. [134] reported on a phosphorene-based FET gas sensor with ultrahigh sensitivity towards NO₂, and layer dependent sensing performance. Bulk black phosphorus was micromechanically exfoliated via the “Scotch-tape” method and its nanosheets were incorporated into a FET. Since phosphorene is a p-type semiconductor and NO₂ is an electron acceptor (p-doping), an increase in conductance upon adsorption is observed. For a 4.8 nm thick phosphorene nanosheet a maximum sensitivity up to 190% at 20 ppb at room temperature was achieved, while the response was quite selective towards CO, H₂ and H₂S.

Mayorga-Martinez et al. [166] reported on the development of a methanol vapor sensing device, which is based on interdigitated gold electrodes modified with layered black phosphorus. Using EIS measurements at constant frequency (1 kHz), the method enabled reproducible measurements, stable response for at least 15 days, good selectivity over toluene, acetone, chloroform, dichloromethane, ethanol, isopropyl alcohol and water, while the LOD was 28 ppm. The same group also reported on a gas sensing device based on arsenene nanosheets, which were produced via ultrasonication in a variety of organic solvents, with *N*-methylpyrrolidone producing the most stable dispersion [168]. Arsenene nanosheets were drop-casted on an interdigitated electrode, which based on EIS measurements resulted in a frequency dependent selectivity toward methanol (10 Hz) or acetone (0.1 Hz).

1.4.9 Miscellaneous electrochemical sensing applications

Post transitional metal chalcogenides have been in the forefront of energy conversion science for their remarkable thickness dependent thermoelectric properties. Boron nitride is also employed in insulating applications. Their implementation on the development of electrochemical sensors is discussed below. 2D Bi₂Te₃ has been utilized for the ultrasensitive determination of Pb(II) and Cd(II) by Tseliou et al. [29]. Bi₂Te₃

was ultrasonicated in a variety of solvents. The dispersion of Bi_2Te_3 in 1+3+4 v/v 1-cyclohexyl-2-pyrrolidone (CHP)/acetone/ H_2O blend showed an excellent stability over a period of at least 5 months (**Fig. 14, inset**) and the few-layer Bi_2Te_3 nanosheets were mixed with graphene oxide prepared via a modified Staudenmaier method (**Fig. 14, left**). The mixed nanocomposite was drop-casted on a GCE and the resulting sensor achieved LODs of 0.1 ppb for Pb(II) and 0.2 ppb for Cd(II) over the same linear range of 0.5 – 20 ppb by employing anodic stripping voltammetry measurements and a preconcentration time of 240 s. **Fig. 14, right** shows the stripping voltammograms of GO/bulk Bi_2Te_3 films and GO/exfoliated Bi_2Te_3 hybrid film-modified GC electrodes, with the latter exhibiting ca. 5-fold higher stripping currents for Cd and ca. 12-fold higher for Pb. The sensor was successfully applied to the determination of the targets in tap water samples.

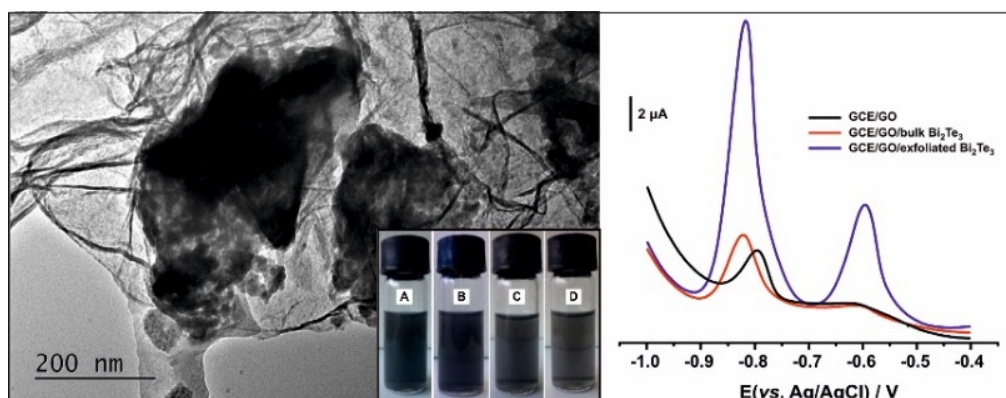


Fig. 14. (Left) TEM image of the graphene oxide/exfoliated Bi_2Te_3 hybrid material. (Right) SW voltammograms of (black line) GCE/GO, (red line) GCE/GO/bulk Bi_2Te_3 , and (blue line) GCE/GO/exfoliated Bi_2Te_3 in the presence of 10 mg L^{-1} Cd and 10 mg L^{-1} Pb in 0.1 M acetate buffer, pH 4.5. Deposition time 120 s at -1.6 V. (Inset) Photographs of a (A) fresh Bi_2Te_3 dispersion in 1+3+4 v/v CHP/acetone/ H_2O after (B) 1, (C) 3, and (D) 5 months. Reprinted with permission from [29]. Copyright (2017) Elsevier.

2D-hexagonal boron nitride (2D-hBN) has been explored for the electrochemical sensing of dopamine [169]. 2D-hBN was purchased from a retailer readily dispersed in ethanol and was drop-casted onto a carbon SPE. This sensor achieved a LOD of $0.65 \text{ } \mu\text{M}$ over a linear range of 3-75 $\text{ } \mu\text{M}$. 2D-hBN modified SPEs were shown to possess the ability to deconvolute the response of dopamine and two common electroactive

compounds (ascorbic and uric acids) in standard solutions; however, their performance was not examined in real-world samples.

AuNP-decorated BN nanosheets (AuNP/BNNSs) for the determination of cardiac biomarker myoglobin were also reported [34]. BNNSs were produced via an acidic oxidation/reduction treatment and then AuNPs deposited on their surface with a seed-mediated chemical reduction method. The nanocomposite was spin-coated onto a fluorine doped tin oxide (FTO) electrode upon which an aptamer was later immobilized. Based on voltammetric measurements of hexacyanoferrate(III)/(II) redox probe, the flux of which to the electrode surface is reduced proportionally to the concentration of myoglobin in the solution as a result of the formation of the aptamer-myoglobin complex on the electrode surface, the detection range was found to be 0.1-100 $\mu\text{g/mL}$.

Also, in this case, the aptasensors were not examined in real world samples.

AuNP/BNNSs were also explored, as an electrocatalyst, for the voltammetric determination of flavonoid luteolin [170]. BNNSs were prepared via a microwave irradiation exfoliation. Compared with bare GCE, AuNP/BNNS-modified electrode showed an enhanced performance on the oxidation of luteolin at a lower overpotential (ca. 180 mV). The detection range was 5-1200 pM and the sensor was successfully applied to the determination of luteolin in herbs and peanut hull samples. Data were in good agreement with those obtained by an HPLC method, while the recovery ranged from 98 to 103%.

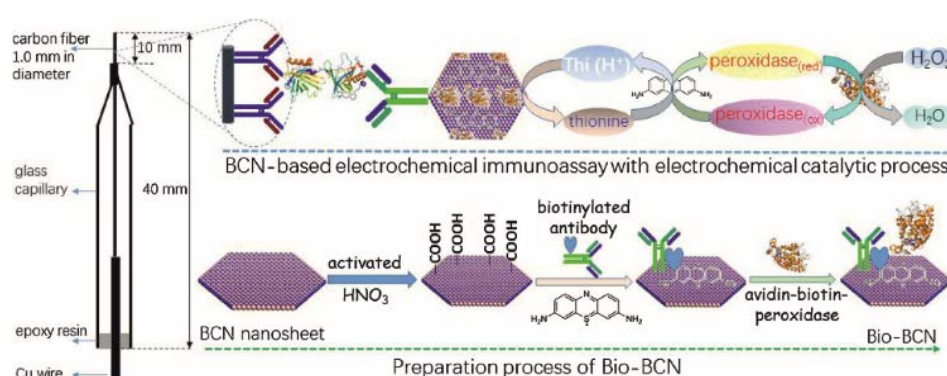


Fig. 15. Schematic illustration of boron carbon nitride (BCN) nanosheet-based electrochemical immunoassay toward lipocalin-2 (LCN2) on monoclonal mouse anti-human [5G5] lipocalin-2 antibody-modified carbon-fiber microelectrode by using peroxidase/thionine/biotinylated antibody-conjugated BCN nanosheets as the detection antibody. Reprinted with permission from [33]. Copyright (2018) Elsevier.

The ternary carbonitride counterpart of BN has also been employed in electrochemical sensing. For instance, Chen et al. [33] reported a boron carbon nitride (BCN) nanosheet-based immunosensor for the determination of lipocalin-2 (LCN2), a biomarker of kidney diseases, on an anti-LCN2-functionalized carbon-fiber microelectrode. BCN nanosheets were produced via a solvothermal method and conjugated with thionine, lipocalin-2 antibody and HRP. Functionalized BCN nanosheets displayed good dispersion thus enabling their use as electrochemical tags in a sandwich-type immunoassay (**Fig. 15**). Based on voltammetric measurements in the presence of H_2O_2 , the sensor achieved a LOD of 0.37 pg mL^{-1} over a linear range of $0.001\text{-}10 \text{ ng mL}^{-1}$. Interestingly, the method (both functionalized microelectrode and BCN NSs) showed an excellent long-term stability by retaining the 84% of its original response for one year. The accuracy of the method was evaluated in unspiked human serum samples containing LCN2 with respect to a commercial ELISA kit, and it was deemed satisfactory.

1.4.10 Miscellaneous gas phase sensors

Marvan et al. [63] reported on gallium and indium chalcogenide (GaS , GaSe , GaTe , In_2Se_3 , InSe and InTe) nanosheet-based gas sensors for the detection of various VOCs (methanol, ethanol, isopropyl alcohol and acetone). All bulk materials were shear-force exfoliated in an ethanol/deionized water mixture and the respective dispersions were drop-casted on gold interdigitated electrodes. All sensors possessed ohmic type metal–semiconductor junction right after the exfoliation, which, after a period of five months changed to Schottky type in the case of selenide samples indicating restacking and entrapping the solvent within their structure. Gas-sensing properties of the exfoliated material-based electrodes were assessed via EIS measurements. All nanosheets exhibited decent sensitivity towards methanol vapors except InTe , though the work does not provide additional analytical data.

Pawar et al. [138] reported on the gas ammonia and humidity sensing properties of a tin-doped indium oxide electrode modified with low dimensional SnSe_2 nanosheets, which were produced via ultrasonication in N-methyl-2-pyrrolidone for 10 h. The sensing mechanism for NH_3 relies on its electron donor ability and on the n-type semi conductivity of the SnSe_2 nanosheets, while humidity sensing is based on the proton

transfer between water molecules and the nanosheet surface. This work provides data on the thickness-dependent sensing properties for the humidity sensor. Sensors based on 170, 8 and 2.5 nm thick 2D SnSe₂ nanosheets showed similar response times, while the thickest nanosheets gave a >2-fold higher sensitivity compared with that obtained by the two thin nanosheets, which, however outperformed with respect to recovery time which calculated 12, 7, and 4 s, respectively. As regards for ammonia sensing, except for the thickest nanosheet-based sensors which displayed a sensitivity of ca. 100% and response/recovery times of 264/26 s, comparative data are not provided.

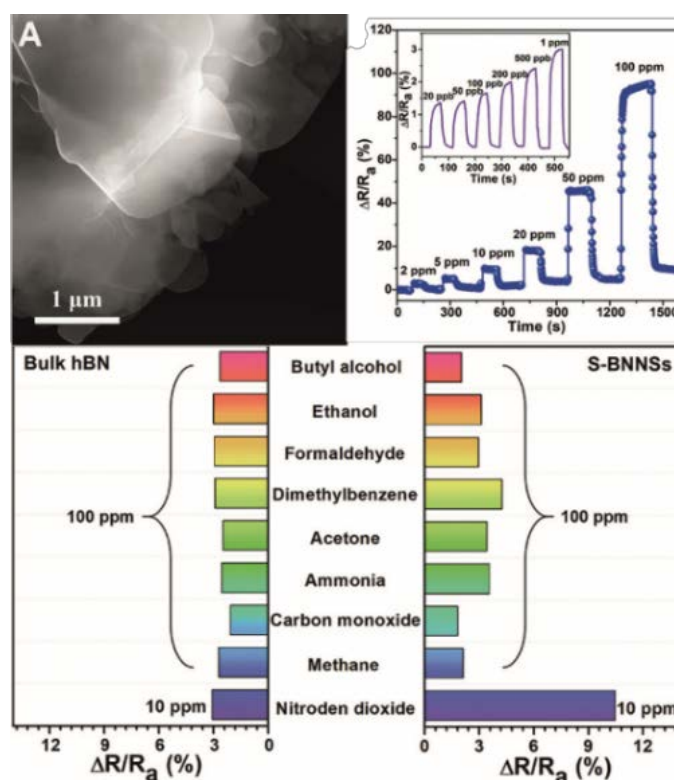


Fig. 16. (Top-left) SEM image of the as-exfoliated S-BNNSs. (Top-right) Dynamic response of the S-BNNS based sensor versus time upon exposure to NO₂ with the concentration increasing from 20 ppb to 100 ppm. The inset shows the dynamic response at concentrations below 1 ppm. (Bottom) Responses of the sensors based on S-BNNSs and bulk h-BN to various target gases, including methane, carbon monoxide, ammonia, acetone, dimethylbenzene, formaldehyde, ethanol, and butyl alcohol at concentrations of 100 ppm and 10 ppm NO₂. Reprinted with permission from [171]. Copyright (2019) Royal Society of Chemistry.

BN nanosheets (**Fig. 16, top-left**) have also been incorporated into a chemiresistor type NO₂ sensor [171]. Data evident that, compared with the bulk BN, chemically exfoliated sulfate-modified S-BNNSs perform an enhanced surface adsorption capability towards NO₂, which is accompanied by a strong charge transfer induced by adsorbed NO₂, and consequently to improved sensing properties. The responses of the sensors based on S-

BNNSs and bulk h-BN to various target gases, including methane, carbon monoxide, ammonia, acetone, dimethylbenzene, formaldehyde, ethanol, and butyl alcohol at a concentration of 100 ppm are quite similar while the high response of S-BNNSs-based sensors to 10 ppm NO₂ demonstrates an enhanced sensitivity over bulk h-BN-based sensor and good selectivity over the other tested gases (**Fig. 16, bottom**). The response of the sensor is linear over the concentration range from 20 ppb to 100 ppm NO₂ (LOD 18 ppb), while the response/recovery times are 7.5/14.4 s, respectively (**Fig. 16, top-right**).

Table 3. Overview of the referenced 2D inorganic nanosheet-based electrochemical (bio)sensors.

Materials	Synthetic method	Analyte	Detection Range / μM^*	LOD / μM^*	Ref.
MoS ₂ -NiCo ₂ O ₄	Hydrothermal	Glucose	i) 1 – 1600 ii) 1600 – 11100	0.152	[139]
MoS ₂	Hydrothermal	Uric acid	10 – 400	1.169	[70]
PtNi@MoS ₂	Ultrasonication	Uric acid Dopamine	UA: 0.5 – 1800 DA: 0.5 – 250	0.1	[124]
AuNP-MoS ₂	Hydrothermal	Uric acid Melatonin	0.033 – 10.0	0.0182 0.0157	[36]
PtW/MoS ₂	Ultrasonication	H ₂ O ₂	1 – 200	0.005	[125]
WS ₂ /acetylene black	Ultrasonication/ Hydrothermal	DNA	10 ⁻⁹ – 10 ⁻⁴	1.2 x 10 ⁻¹⁰	[140]
DNA-WS ₂	Hydrothermal	ATP Hg ²⁺	0.1 – 5000 0.0001 – 0.5	0.0015 0.5 x 10 ⁻⁶	[141]
WS ₂	Hydrothermal	Roxarsone	0.05 – 489.3	0.03	[30]
WS ₂ /AuNP-CT/CB	Ultrasonication	Caffeic acid	0.3 – 200	0.1	[143]
		Sinapic acid	0.6 – 300	0.2	
		p-Coumaric acids	0.9 – 175	0.3	
RNA-WSe ₂	Solvothermal	miRNA-21	10 ⁻¹⁰ – 10 ⁻⁴	0.6 x 10 ⁻¹⁰	[67]
p-aminophenol/ AuNP-H _x TiS ₂	Lithium intercalation	Cu ²⁺	0.0002 – 5	0.00009	[126]
1T-WS ₂	Lithium intercalation	H ₂ O ₂	i) 0.02 – 20 ii) 100 – 2000	0.002	[144]
PtTe ₂	Heating / Ultrasonication	H ₂ O ₂	i) 3 – 300 ii) 500 – 1100	1.2	[57]
MnO ₂	Electrochemical	H ₂ O ₂	i) 0.025 – 2 ii) 10 – 454	0.005	[149]
ilGr/PDA – MnO ₂	Wet-chemistry reaction	Guanine Adenine	10 – 300 10 – 300	0.25 0.15	[150]
Ni(OH) ₂ – MnO ₂	Wet-chemistry reaction/ Hydrothermal	Dopamine	0.02 – 16.3 18.3 – 118.58	0.00175	[151]
Ni(OH) ₂ – Co ₃ O ₄	Solvothermal	Glucose	5 – 40	1.08	[152]
Anti-cortisol/ZnO	Ultrasonication	Cortisol	10 ⁻⁶ – 10 ⁻¹	10 ⁻⁶	[153]
Ti ₃ C ₂ T _x	LiF – HCl etching	H ₂ O ₂	490 – 53300	0.448	[155]

Nafion/Ti ₃ C ₂ T _x	LiF – HCl etching	BrO ₃ [–]	0.05 – 5	0.041	[130]
Urease/MB/Ti ₃ C ₂ T _x	HF etching	Urea	0.1 – 3.0	0.02	[156]
Ti ₃ C ₂ T _x /SPE		Uric acid	30 – 500	5	
		Creatinine	10 – 400	1.2	
AuNP/Ti ₃ C ₂ T _x	HF etching/ intercalation	Uric acid	0.02 – 3580	0.0062	[131]
		Folic acid	0.03 – 1520	0.0115	
Ti ₃ C ₂ T _x	HF etching	Adrenaline	0.02 – 10	0.0095	[132]
cDNA–Fc/ Ti ₃ C ₂	HF etching	Mucin1	10 ^{–10} – 10 ^{–7}	0.33 x 10 ^{–6}	[157]
cDNA/FePc QDs/Ti ₃ C ₂ T _x	HF etching	miRNA–155	10 ^{–11} – 10 ^{–5}	4.3 x 10 ^{–12}	[158]
β-HBDG / Ti ₃ C ₂ T _x	HF etching	β-HB	360 – 17900	45	[160]
E-etched/Nb ₂ CT _x NS/GA/AChE	Electrochemical etching	Phosmet	2x10 ^{–4} – 10 ^{–3}	1.44 x 10 ^{–4}	[161]
VC/NG NSs	Hydrothermal	Clioquinol	0.5 – 585	0.009	[162]
Phosphorene/ PEDOT:PSS	Ultrasonication	Rutin	15.0 – 80.0	0.007	[135]
Phosphorene/ PEDOT:PSS	Ultrasonication	TCA	2000 – 180000	670	[136]
		NaNO ₂	1000 – 10500	330	
		H ₂ O ₂	4000 – 35000	1330	
Phosphorene/AuNC	Ultrasonication	Okadaic acid	0.01 – 0.25	8 x 10 ^{–6}	[137]
PEDOTNP/β–CD/ phosphorene	–	Clenbuterol	0.3 – 90	0.14	[31]
		Ractopamine	0.3 – 93.36	0.12	
Tyrosinase/Glu/ 2D pnictogens	Shear–force exfoliation	Phenol	–	0.255	[105]
Oligonucleotides/ antimonene	Ultrasonication	Gene BRCA1	0.1 – 20.0 ppm	28.3 ppb	[167]
Bi ₂ Te ₃ /graphene oxide	Ultrasonication	Pb ²⁺	0.5 – 20 ppb	0.1 ppb	[29]
		Cd ²⁺	0.5 – 20 ppb	0.2 ppb	
2D–hBN	–	Dopamine	3 – 75	0.65	[169]
AuNP/BNNSs	Acid treated redox process	Myoglobin	0.1 – 100 ppm	34.6 ppb	[34]
AuNP/BNNSs	Microwave exfoliation	Luteolin	5×10 ^{–6} – 1.2×10 ^{–3}	1.7 x 10 ^{–6}	[170]
Thionine/lipocalin–2 antibody/HRP/BCN	Solvothermal	Lipocalin–2	0.001 – 10 ppb	0.37 ppt	[33]

*Unless otherwise stated.

Table 4. Overview of the referenced 2D inorganic nanosheet-based gas sensors.

Materials	Synthetic method	Detected gases	Response/Recovery time (s)	Detection Range	LOD	Ref.
MoS ₂ /AuNPs	Ultrasonication	Acetone	100/385	10 – 120 ppm	10 ppm	[147]
MoSe ₂	Gold-assisted micromechanical exfoliation	NO ₂	20/1	2 – 10 ppm (NO ₂)	2 ppm	[148]
		NH ₃		5 – 25 ppm (NH ₃)	5 ppm	
TiO ₂	Surfactant self-assembly	Humidity	3/50	11 – 95% RH	–	[154]
Co ₃ O ₄ @NiMoO ₄	Hydrothermal	TEA	31/182	1 – 100 ppm	1 ppm	[128]
Ti ₃ C ₂ T _x	LiF-HCl etching	Acetone	–	25 – 200 ppm	9.2 ppm	[163]
Ti ₃ C ₂ T _x	LiF-HCl etching/ Ultrasonication	Acetone	–	50 – 1000 ppb	50 ppb	[164]
		Ethanol		100 – 1000 ppb	100 ppb	
Ti ₃ C ₂ T _x /TiO ₂	HF etching / TBAOH	NH ₃	33/277	100 – 1000 ppb	100 ppb	[133]
V ₂ CT _x	HF etching	H ₂	120/420	2 – 100 ppm	2 ppm	[165]
		CH ₄	480/330	25 – 400 ppm	9.4 ppm	
		Acetone	–	25 – 200 ppm	11 ppm	
		H ₂ S	–	5 – 100 ppm	3.5 ppm	
Phosphorene	Micromechanical exfoliation	NO ₂	–	20 – 100 ppb 200 – 1000 ppb	20 ppb	[134]
Phosphorene	Vapor transport growth	Methanol	–	380 – 1900 ppm	28 ppm	[166]
Arsenene	Ultrasonication	Methanol Acetone	–	–	–	[168]
SnSe ₂	Ultrasonication	Humidity	167/12	11 – 97% RH	–	[138]
h-BN	Acid exfoliation	NO ₂	7.5/14.4	0.2 – 100 ppm	18 ppb	[171]

Electroanalytical techniques

2.1 Cyclic voltammetry

Cyclic voltammetry is one of the most studied electrochemical techniques that provides vast qualitative data regarding electrochemical reactions and processes. Its wide use stems from its ability to offer valuable information on the thermodynamics of redox processes, on the kinetics of heterogeneous electron-transfer reactions and on coupled chemical reactions or adsorption processes. It is usually the first experiment conducted in a electroanalytical study since it can map the electrochemical process at hand, pinpointing the location of redox potentials of electroactive species and evaluating the effect of media upon the redox process [172].

Cyclic voltammetry involves a linear potential scan of a stationary working electrode, in an unstirred solution, using a triangular potential waveform. During the potential sweep the potentiostat measures the current produced from the application of the potential. The resulting plot of current (or current density) vs. potential is termed a *cyclic voltammogram*. It should be noted, that depending on the application, single or multiple scans can be employed [172].

Fig. 17. illustrates the voltammetric response of a reversible redox couple during a single potential cycle. A negative-going potential scan is chosen for the first half-cycle to reduce the oxidized form “O” present, starting from a potential value where no reduction takes place. When the applied potential approaches the formal potential (E^0) of the redox process, the cathodic current starts increasing, to the point where a peak is formed, resulting in the reduced form “R”. After transversing the potential region in which the reduction takes place by at least $90/n$ mV beyond the completion of the peak, the direction of the potential sweep is reversed. During the reverse scan, “R” molecules

are accumulated near the electrode surface and reoxidized back to “O”, thus producing an anodic peak [172].

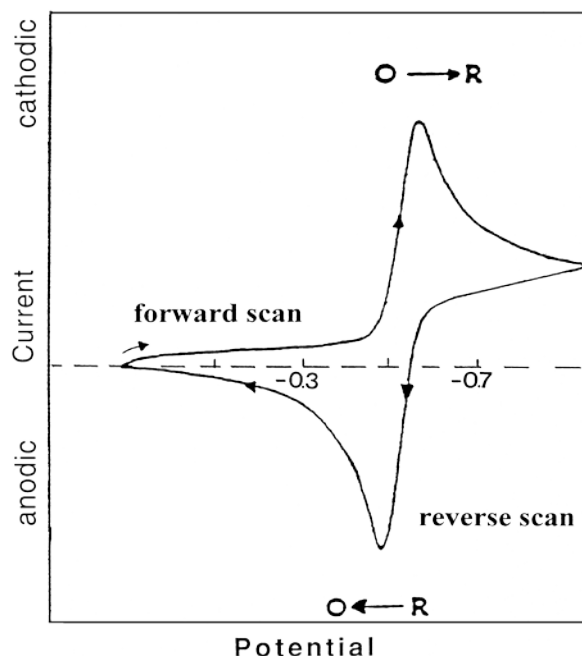


Fig. 17. Typical cyclic voltammogram for a reversible $O + ne^- \leftrightarrow R$ redox process.

2.1.1 Reversible systems

The peak current for a reversible couple (at 25 °C), is given by the Randles–Ševčík equation (2):

$$I_p = (2.69 \times 10^5) n^{3/2} A C D^{1/2} v^{1/2} \quad (2)$$

where n is the number of electrons, A is the electrode surface area (in cm^2), C is the concentration (in mol cm^{-3}), D is the diffusion coefficient (in $\text{cm}^2 \text{s}^{-1}$), and v is the scan rate (in V s^{-1}). Accordingly, the peak current is directly proportional to concentration and increases with the square root of scan rate [172].

Peak position on the potential axis (E_p) is related to the E^0 of the redox process. E^0 of a reversible couple is centered between $E_{p,a}$ and $E_{p,c}$, as per equation (3):

$$E^0 = \frac{E_{p,a} + E_{p,c}}{2} \quad (3)$$

Peak separation of a reversible couple is given by equation (4):

$$\Delta E_p = E_{p,a} - E_{p,c} = \frac{0.059}{n} V \quad (4)$$

Consequently, peak separation can be used to determine the number of electrons transferred and as a criterion for Nernstian behavior, since, for instance, an one electron Nernstian process exhibits a ΔE_p value of about 59 mV.

2.1.2 Irreversible and quasi-reversible systems

Irreversible processes are characterized by sluggish electron exchange, which leads both to wide peak separation and lowering of the peak current. Totally irreversible systems are related with peak potential shifting with the scan rate [173], as per equation (5):

$$E_p = E^0 - \frac{RT}{\alpha n_\alpha} \left[0.78 - \ln \frac{k^0}{D^{1/2}} + \ln \left(\frac{\alpha n_\alpha F v}{RT} \right)^{1/2} \right] \quad (5)$$

where α is the transfer coefficient, n_α is the number of electrons involved in the rate determining reaction, k^0 is the heterogeneous electron transfer rate constant (in cm s^{-1}), F is Faraday's constant (96485 C mol^{-1}), R is the gas constant ($8.314 \text{ J mol}^{-1} \text{ K}^{-1}$), and T is the temperature (in K). It is obvious that E_p occurs at potential higher than E^0 , with overpotential related to k^0 and α . Independently of k^0 , peak displacement can be compensated by an appropriate change of scan rate.

The peak current is given by equation (6) [173]:

$$I_p = (2.99 \times 10^5) n (a n_\alpha)^{1/2} A C D^{1/2} v^{1/2} \quad (6)$$

and is still proportional to bulk concentration, but is lower in height (depending on α). Assuming α to be 0.5, the ratio of reversible-to-irreversible current peaks is 1.27 (i.e. peak current of an irreversible process is about 80% of the peak of a reversible one).

For quasi-reversible systems (with $10^{-1} > k^0 > 10^{-5} \text{ cm s}^{-1}$), current is controlled by both charge transfer and mass transport. The shape of the cyclic voltammogram is a function of dimensionless kinetic parameter named ψ , established by Nicholson [174] which equals $k^0/(\pi D n \nu F/RT)^{1/2}$. This parameter ranges from 20 to 0.1, where 20 is the upper limit signifying the transition to a reversible process and 0.1 is the lower limit which signifies the transition to an irreversible process. **Fig. 18** demonstrates the simulated effect of k^0 to the ΔE_p in a simple one electron redox process produced by electrochemical simulation package (ESP) v.2.4 software.

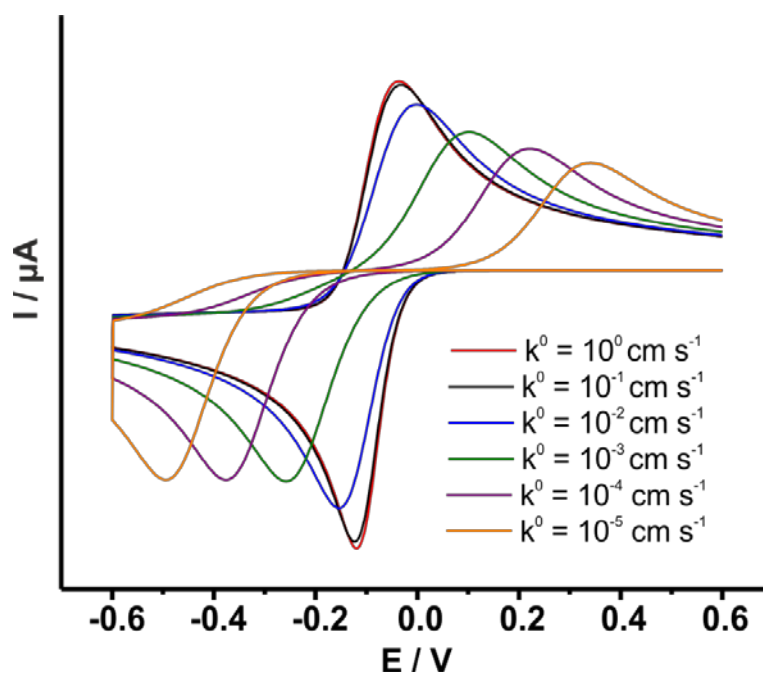


Fig. 18. Simulated cyclic voltammograms for a reversible $O + ne^- \leftrightarrow R$ redox process, with k^0 values ranging from 1 to $10^{-5} \text{ cm s}^{-1}$. Simulations were conducted using ESP v.2.4 software.

2.2 Polarography

Polarography is a subclass of voltammetry in which the working electrode is the *dropping mercury electrode* (DME). Because of the special properties of this electrode, particularly its renewable surface and wide cathodic potential, polarography has been widely used for the determination of many important reducible species. This classical technique was invented by J. Heyrovsky in Czechoslovakia in 1922, and had an enormous impact on the progress of electroanalysis (through many subsequent developments). Accordingly, Heyrovsky was awarded the 1959 Nobel Prize in Chemistry.

2.3 Pulse voltammetry

Pulse voltammetric techniques, introduced by Barker and Jenkins [175], aimed and succeeded at lowering the detection limits of voltammetric measurements. By substantially increasing the ratio between the faradaic and nonfaradaic currents, such techniques permit convenient quantitation down to the 10^{-8} M concentration level. Because of their greatly improved performance, modern pulse techniques have largely supplanted classical polarography in the analytical laboratory. The various pulse techniques are all based on a sampled current potential-step (chronoamperometric) experiment. A sequence of such short (typically 50 ms) potential steps is applied to the working electrode. After the potential is stepped, the charging current decays rapidly (exponentially) to a negligible value, while the faradaic current decays more slowly. Thus, by sampling the current late in the pulse life, an effective discrimination against the charging current is achieved.

The difference between the various pulse voltammetric techniques is the excitation waveform and the current sampling regime. Nowadays, the most widely used pulsed techniques are Normal-pulse voltammetry (NPV), Differential-pulse voltammetry (DPV) and Square-wave voltammetry (SWV).

2.3.1 Normal pulse voltammetry

Normal-pulse voltammetry consists of a series of pulses of increasing amplitude applied at a preselected time (4). Such a normal-pulse train is shown in **Fig. 19**. Between the pulses, the electrode is kept at a constant (base) potential at which no reaction of the analyte occurs. The amplitude of the pulse increases linearly with each drop. The current is measured about 40 ms after the pulse is applied, at which time the contribution of the charging current is nearly zero. In addition, because of the short pulse duration, the diffusion layer is thinner than that in DC polarography (i.e., there is larger flux of analyte) and hence the faradaic current is increased.

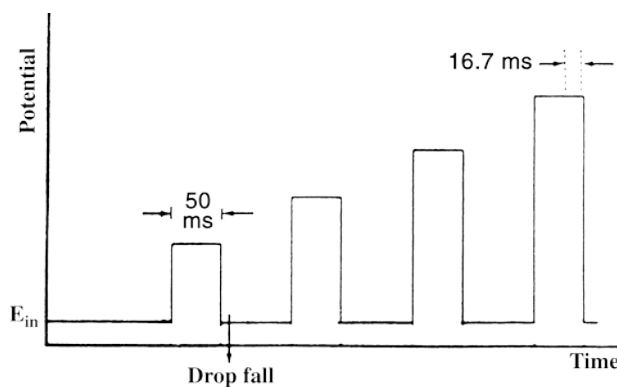


Fig. 19. Excitation signal for normal pulse voltammetry

2.3.2 Differential pulse voltammetry

Differential-pulse voltammetry (DPV) is an extremely useful technique for measuring trace levels of organic and inorganic species [176]. In differential-pulse voltammetry, fixed- magnitude pulses-superimposed on a linear potential ramp-are applied to the working electrode (**Fig. 20**). The current is sampled twice, just before the pulse application (at 1) and again late in the pulse life (after ~40 ms, at 2, when the charging current has decayed). The first current is instrumentally subtracted from the second, and this current difference [$\Delta i = i(t_2) - i(t_1)$] is plotted versus the applied potential. The resulting differential pulse voltammogram consists of current peaks, the height of which is proportional to the concentration of the corresponding analytes.

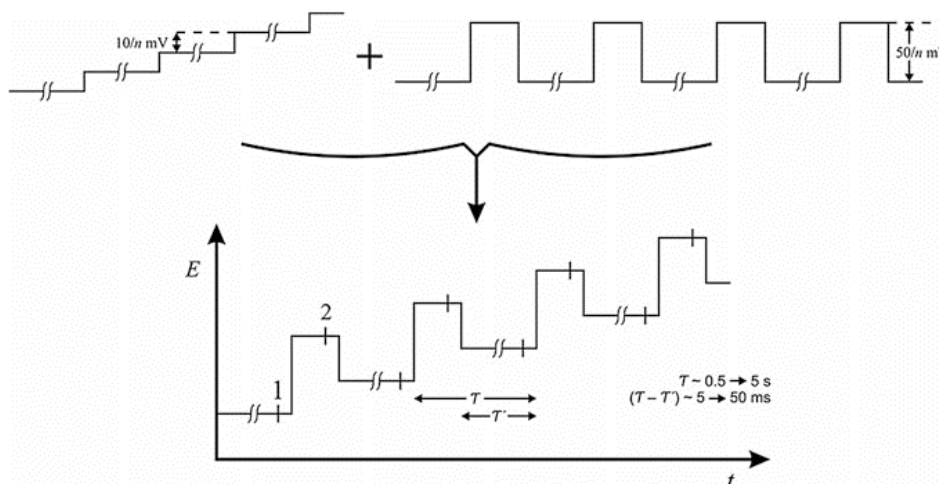


Fig.20. Differential pulse voltammetry waveform of pulses superimposed on a staircase

2.3.3 Square-pulse voltammetry

Square-wave voltammetry (SWV) is a large-amplitude differential technique in which a waveform composed of a symmetrical square wave, superimposed on a base staircase potential, is applied to the working electrode [176] (**Fig. 21**). The current is sampled twice during each square-wave cycle, once at the end of the forward pulse (at t_1) and once at the end of the reverse pulse (at t_2). Since the square-wave modulation amplitude is very large, the reverse pulses cause the reverse reaction of the product (of the forward pulse). The difference between the two measurements is plotted versus the base staircase potential. Excellent sensitivity accrues from the fact that the net current is larger than either the forward or reverse components (since it is the difference between them); the sensitivity is higher than that of differential pulse voltammetry (in which the reverse current is not used). Coupled with the effective discrimination against the charging background current, very low detection limits near 1×10^{-8} M can be attained. Comparison of square-wave and differential pulse voltammetry for reversible and irreversible cases indicated that the square-wave currents are 4 and 3.3 times higher, respectively, than the analogous differential-pulse response.

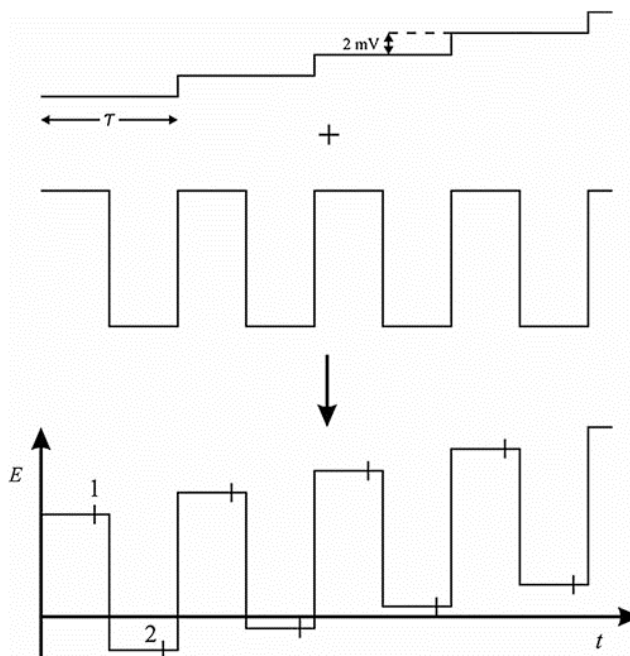


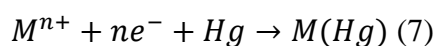
Fig. 21. Square wave voltammetry: waveform showing the summation of a staircase and a square wave.

2.4 Stripping analysis

Stripping analysis is an extremely sensitive electrochemical technique for measuring trace metals [177, 178]. Its remarkable sensitivity is attributed to the combination of an effective preconcentration step with advanced measurement procedures that generate an extremely favorable signal-to-background ratio. Since the metals are preconcentrated into the electrode by factors of 100 to 1000, detection limits are lowered by 2 to 3 orders of magnitude compared to solution-phase voltammetric measurements. Hence, four to six metals can be measured simultaneously in various matrices at concentration levels down to 10^{-10} M, utilizing relatively inexpensive instrumentation. The ability to obtain such low detection limits depends strongly on the degree to which contamination can be minimized. Expertise in ultratrace chemistry is required. Essentially, stripping analysis is a two-step technique. The first, or deposition, step involves the electrolytic deposition of a small portion of the metal ions in solution into the mercury electrode (or to non-toxic modern day electrodes such as Bismuth film electrode etc.) to preconcentrate the metals. This is followed by the stripping step (the measurement step), which involves the dissolution (stripping) of the deposit. Different versions of stripping analysis can be employed, depending upon the nature of the deposition and measurement steps.

2.4.1 Anodic stripping voltammetry

Anodic stripping voltammetry (ASV) is the most widely used form of stripping analysis. In this case, the metals are preconcentrated by electrodeposition into a small-volume mercury electrode (or to non-toxic modern day electrodes such as Bismuth film electrode etc.) [176]. The preconcentration is done by cathodic deposition at a controlled time and potential. The deposition potential is usually 0.3 – 0.5 V more negative than E^0 for the least easily reduced metal ion to be determined. The metal ions reach the mercury electrode by diffusion and convection, where they are reduced and concentrated as amalgams, as per equation (7):



The convective transport is achieved by electrode rotation or stirring of the solution (in conjunction with the electrode). Quiescent solutions can be used when using ultramicroelectrodes. The duration of the deposition step is selected according to the concentration level of the metal ions in question, from less than 0.5 min at the 10^{-7} M level to about 20 min at the 10^{-10} M level. Following the preselected time of the deposition, the forced convection is stopped, and the potential is scanned anodically, either linearly or in a more sensitive potential-time (pulse) waveform that discriminates against the charging background current (usually square-wave or differential-pulse ramps). Such pulse excitations also offer reduced oxygen interferences and analyte replating, respectively. anodic scan, the amalgamated (or alloyed) metals are reoxidized, stripped out of the electrode (in an order that is a function of each metal standard potential), and a current flows, as per equation (8):

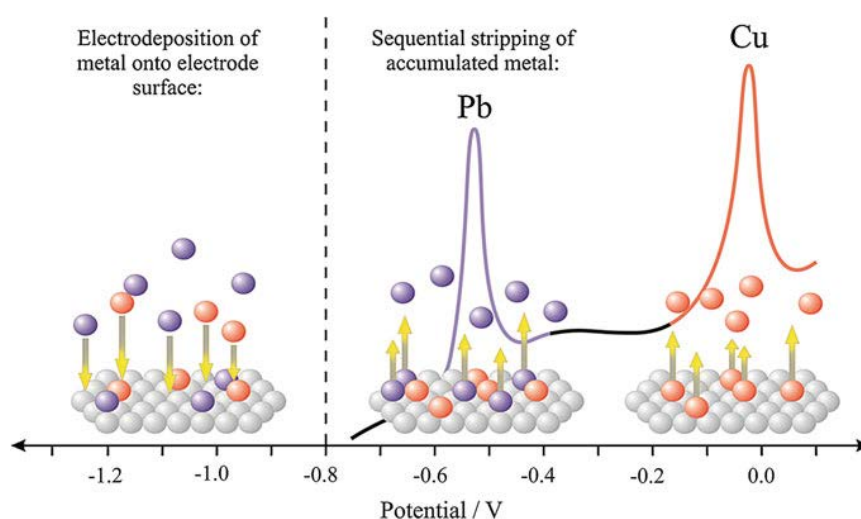
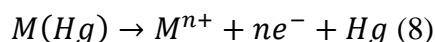


Fig. 22. A schematic representation of anodic stripping voltammetry showing the two key steps: electrodeposition and stripping

A schematic representation of ASV, along with the resulting stripping voltammogram, is shown in **Fig 22**. The voltammetric peak reflects the time- dependent concentration gradient of the metal in the mercury electrode during the potential scan. Peak potentials serve to identify the metals in the sample. The peak current depends upon various

parameters of the deposition and stripping steps, as well as on the characteristics of the metal ion and the electrode geometry.

The mercury film electrode has a higher surface-to-volume ratio than the hanging mercury drop electrode and consequently offers a more efficient preconcentration and higher sensitivity. In addition, the total exhaustion of thin mercury films results in sharper peaks and hence improved peak resolution in multicomponent analysis. The major types of interferences in ASV procedures are overlapping stripping peaks caused by a similarity in the oxidation potentials (e.g., of the Pb, Tl, Cd, Sn or Bi, Cu, Sb groups), the presence of surface-active organic compounds that adsorb on the mercury electrode and inhibit the metal deposition, and the formation of intermetallic compounds (e.g., Cu-Zn) which affects the peak size and position [178]. Knowledge of these interferences can allow prevention through adequate attention to key operations.

2.4.2 Replacement of mercury

As of January 1st 2022, European Union has prohibited the use of mercury as an electrode in manufacturing processes [179]. The fact that this highly toxic element should be completely replaced in electroanalytical applications, has been well-known for quite some time, which led to the emergence of many viable candidates over the years. Among them, solid electrodes such as glassy carbon electrodes (GCEs) [180], gold electrodes [181, 182] (GEs) and platinum electrodes (PtEs) have been at the forefront of this campaign, while liquid metal electrodes such as Galinstan [183, 184] (a Gallium-Indium alloy-based electrode) have also been evaluated. In trace metal determination applications such as anodic stripping voltammetry, the most widely studied electrodes consist of either bismuth film electrodes [185, 186] (BiFEs) or antimony film electrodes (SbFEs), since they have excellent alloying properties with heavy metals and also provide wide overpotentials over hydrogen evolution reaction (HER) similarly to mercury itself. The mass production of low-cost, disposable electrodes, spurred by the wide development of amperometric sensors, has led to the implementation of many thick and thin layer technologies in electroanalysis. Among them, screen-printing has solidified itself at the center of disposable electrode manufacturing due to its superb definition, simplicity and reproducibility.

2.5 Electrochemical impedance spectroscopy (EIS)

EIS offers kinetic and mechanistic data of various electrochemical systems and is widely used in corrosion studies, semi-conductor science, development of biochemical capacitors, impedimetric biosensors etc.

EIS comprises of the perturbation of a system in equilibrium or in static conditions, via the application of a sinuoidal signal and the simultaneous monitoring of the time or frequency response of the system toward the cause of the perturbation. An important advantage of EIS is the ability to simulate the electrochemical system under study through an equivalent electric circuit. The electrode/electrolyte interface under study can be simulated by an electrical electric circuit, which consists of a combination of electric components (such as resistances, capacitors, inductors etc.). In an electrochemical system the bulk properties of the electrolyte, the (slow) kinetics of an electrode reaction, homogeneous reactions that influence reactions at electrode surfaces and diffusion phenomena, impede the electron flux and can consequently be deemed analogs to ohmic, capacitive or inductive resistances, which in a similar manner impede the electron flux in an alternating current circuit.

2.5.1 Equivalent electric circuits

In a general sense, an electrochemical cell can be considered simply an impedance to a small sinusoidal excitation; hence we ought to be able to represent its performance by an *equivalent circuit* of resistors and capacitors that pass current with the same amplitude and phase angle that the real cell does under a given excitation. A frequently used circuit, called the Randles equivalent circuit, is shown in **Fig. 23**. The parallel elements are introduced because the total current through the working electrode/electrolyte interface is the sum of distinct contributions from the faradaic process, I_f , and double-layer charging, I_c . The double-layer capacitance is nearly a pure capacitance; hence it is represented in the equivalent circuit by the element Q . The faradaic process cannot be represented by simple linear circuit components like, R and C , whose values are independent of frequency, but must be considered as a general impedance, Z_f . Of course, all of the current must pass through the solution resistance; therefore R_s is inserted as a series element to represent this effect in the equivalent electric circuit.

The faradaic impedance has been considered in the literature in various ways. **Fig. 23** shows two equivalences that have been made. The simplest representation is to take the faradaic impedance as a series combination comprising the resistance, R , and the pseudocapacity, C_{ps} . An alternative is to separate a pure resistance, R_{ct} the charge-transfer resistance, from another general impedance, Z_w , the Warburg impedance, which represents a kind of resistance to mass transfer. In contrast to RQ and Qi , which are nearly ideal circuit elements, the components of the faradaic impedance are not ideal, because they change with frequency, ω . In fact, a chief objective of a faradaic impedance experiment is to discover the frequency dependencies of R and C_{ps} . Theory is then applied to transform these functions into chemical information.

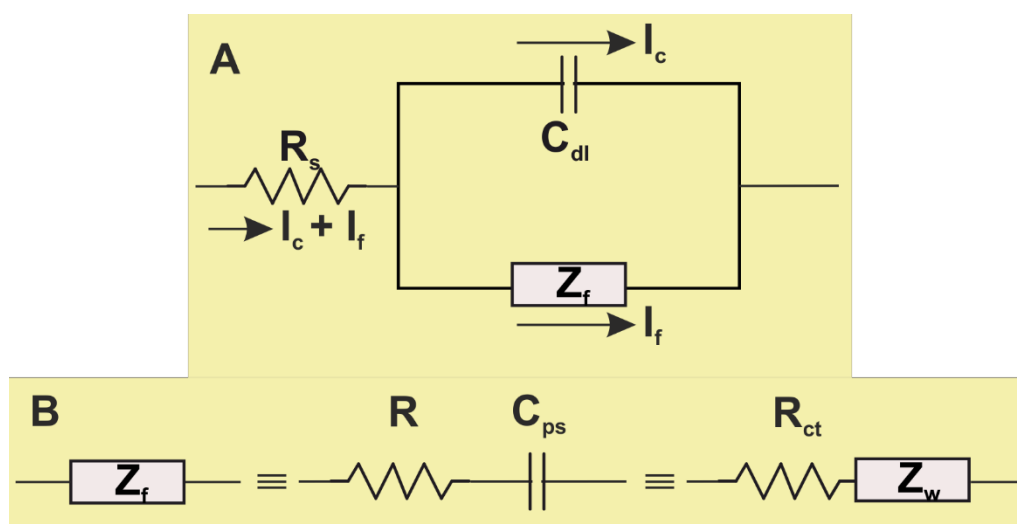


Fig. 23. A) Equivalent circuit of an electrochemical cell and B) subdivision of Z_f into R and C_{ps} , or into R_{ct} and Z_w .

2.5.2 Representation of impedance plots

The variation of impedance with frequency is often of interest and can be displayed in different ways. The two more popular are the Bode plot, where $\log(Z)$ and ϕ are plotted against $\log\omega$, and the Nyquist plot, a representation similar to the Cole-Cole plot in dielectric spectroscopy [187], where the imaginary part of impedance ($-Z''$) is plotted against the real part (Z') for different values of ω . The determining feature of the Nyquist plot is the R_{ct} and its relation to Z_w , which is controlled by the slope of the low-frequency part of the Nyquist plot (σ). As stated in **2.5.1**, R_s is not subjective to angular frequency, unlike R_{ct} and C_{dl} which present a semi-circled behavior, attributed

to their co-existence and a linear part coupled to it at a 45° angle, at low frequency region of the plot, attributed to the existence of Z_W . This is the most commonly used illustration of a Nyquist plot, which however strictly represents the behavior of a quasi-reversible redox system, where there is a distinct R_{ct} value related to heterogeneous electron transfer kinetics, as per equation (9) [188]:

$$R_{ct} = \frac{RT}{k^0 n^2 F^2 AC} \quad (9),$$

where k^0 is the heterogenous electron transfer rate (cm s^{-1}), n is the number of electrons transferred in the electrochemical reaction, F is Faraday's constant (96485 C mol^{-1}), R is the gas constant ($8.314 \text{ J mol}^{-1} \text{ K}^{-1}$), T is the temperature (K), A is the electroactive surface area (A) in cm^2 , and C is the concentration of the redox system at the electrode-electrolyte interface (in mol cm^{-3}). This is based on the assumption that this concentration is the same as the one in the solution (C^*) and that the concentration of the oxidated species is the same as the concentration of the reduced species ($C_{ox} = C_R = C$).

Additionally, σ can be correlated to the mass transfer kinetics as per equation (10):

$$\sigma = \frac{2RT}{n^2 F^2 (2D)^{1/2} C} \quad (10),$$

where D is the diffusion coefficient ($\text{cm}^2 \text{ s}^{-1}$), assuming that the diffusion coefficient of the oxidated and reduced species remains the same ($D_{ox} = D_R = D$), while the rest of the symbols have their aforementioned meaning. The impact of charge transfer and mass kinetics in a typical quasi-reversible system in the form of a Nyquist plot is depicted in **Fig. 24A**.

In reversible systems which typically show fast kinetics, R_{ct} becomes inconsequentially small in comparison with the solution resistance and the Warburg impedance over nearly the whole available range of σ . Then the system is so kinetically facile that mass transfer always plays a role, and the semicircular region is not well defined. For R_{ct} to be still correlated to the heterogeneous transfer kinetics, it should be

able to make a significant contribution to R , hence $R_{ct} \geq \sigma/\omega^{1/2}$ which leads to $k^0 \leq (D\omega/2)^{1/2}$.

On the other hand, If an electrochemical system is kinetically sluggish, as in an irreversible process, it will show a large R_{ct} value and may display a very limited frequency region where mass is a significant factor, as shown in **Fig. 24B**. In a case where R_{ct} is so large that the all the current follows a path through C_{dl} , the heterogeneous transfer kinetics can no longer be correlated to R_{ct} . The higher R_{ct} limit that can be used is $R_{ct} \leq 1/\omega C_{dl}$ that leads to $k^0 \geq RTC_{dl}\omega/F^2CA$.

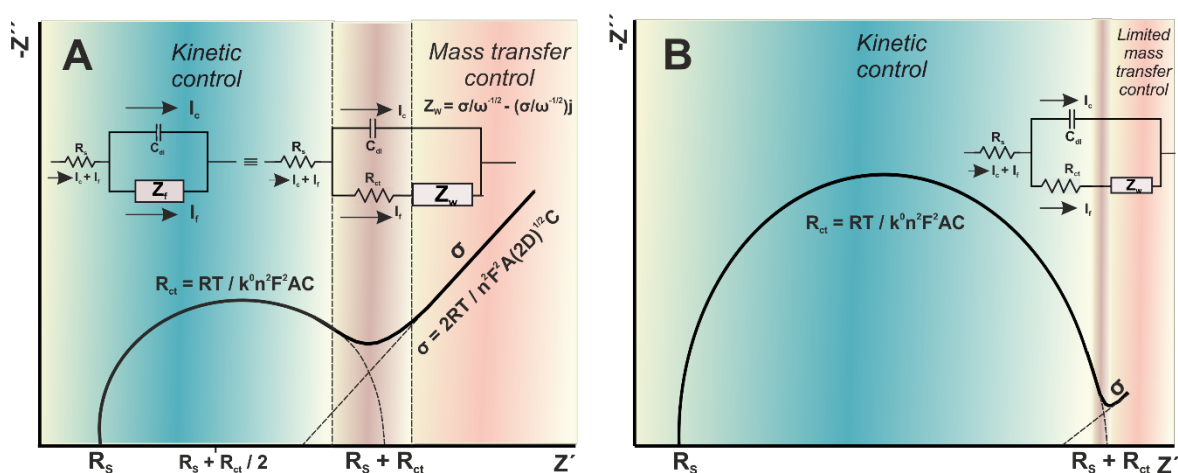


Fig. 24 (A) Nyquist plot of a quasi-reversible redox system, with regions of kinetic control and mass transfer at low and high frequencies respectively. (B) Nyquist plot of a slow-kinetics redox system, with limited mass transfer control due to increased charge-transfer resistance.

2.5.3 Influence of double-layer capacitance (C_{dl})

As shown in **Fig. 24A** the existence of the diffusion part of the plot at low frequencies is visualized with a 45° slope straight line, follow the semi circle. The extent of the distortion is influenced by the relative values of R_{ct} , σ , and C_{dl} . **Fig. 25** shows the simulated effect of the C_{dl} value, in a typical $R_1(Q[R_2W])$ equivalent circuit when all other parameters remain constant. R_1 equals to R_s , Q (also known as constant phase element (CPE)) is a mixed element which expresses the deviation of C_{dl} from the behavior of an ideal capacitor, due to the asperity of the electrode surface or the lack of homogeneity of a modifying layer deposited onto the electrode surface. Q is further divided to Y^0 which is the admittance (the reciprocal impedance) of the constant phase

element (CPE) in $s^n \text{ ohm}^{-1}$ and to n which is a measure of the deviation of the electrochemical system under study from ideal capacitive behavior. When n is considered to be 1, CPE assumes the behavior of an ideal capacitor. On the contrary when n is considered to be 0, CPE assumes the behavior of a pure resistance. R_2 is the R_{ct} and finally W is equal to Z_W . Simulation was conducted using the routine “fit & simulation v.1.7” in the FRA software, v.4.9 (Metrohm Autolab). To calculate the C_{dl} values from the simulated Y^0 and n values, equation (11) was used [189]:

$$C_{dl} = \frac{(Y_0 \times R_{ct_A})^{\frac{1}{n}}}{R_{ct_A}} \quad (11),$$

where Y^0 ranges from 10^{-6} to $10^{-2} s^n \text{ ohm}^{-1}$, R_{ct} is set to 1000 ohm and n is set to 1 to simplify the calculation process.

It is obvious that distortion increases along with C_{dl} , eventually causing a complete disruption of the semi-circle at extreme values (maroon line). In a real electrochemical system, the graphical approximation of the R_{ct} value for instance would yield a systematic error in moderately increased C_{dl} values up to 10^{-4} F and would be unrealizable in even larger values. In such cases the estimation of the R_{ct} and σ values becomes more difficult and should be conducted with caution, preferably using a fitting simulation software such as FRA.

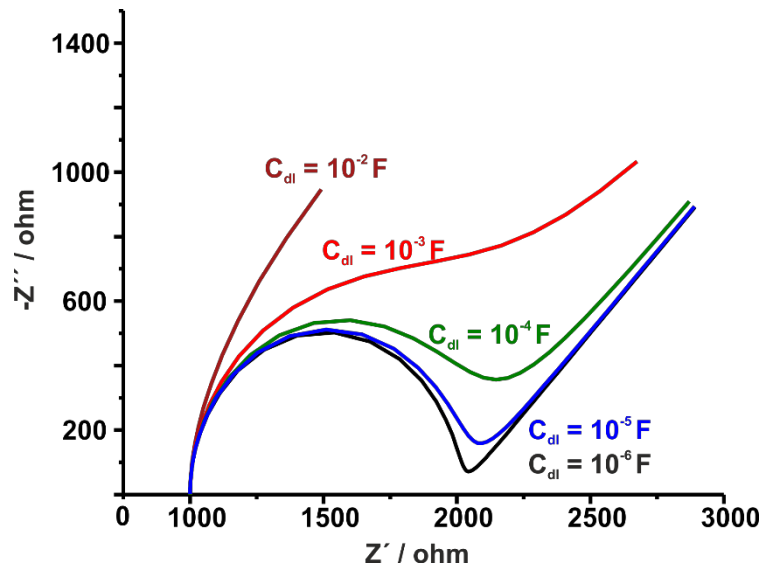


Fig. 25. Simulated nyquist plot of an ideal electrode surface with different C_{dl} values. $R_s = 1000 \text{ ohm}$, $n = 1$, (black line) $Y^0 = 10^{-6} s^n \text{ ohm}^{-1}$, (blue line) $Y^0 = 10^{-5} s^n \text{ ohm}^{-1}$, (green line) $Y^0 = 10^{-4} s^n \text{ ohm}^{-1}$, (red line) $Y^0 = 10^{-3} s^n \text{ ohm}^{-1}$ and (maroon line) $Y^0 = 10^{-2} s^n \text{ ohm}^{-1}$, $R_{ct} = 1000 \text{ ohm}$ and $Z_W = 10^{-2}$. Simulations were conducted using FRA v.4.9 software.

2.6 Fabrication of screen-printed electrodes (SPEs)

2.6.1 Thick-film sensors

Screen-printing is a proven technology used for the manufacture of devices in a wide range of industries, such as electronics and solar cells, through to the graphic arts [190]. The technique of screen-printing is capable of producing electrodes in the range of a few μm to 100 μm in thickness; the sensors can be hence defined as thick-film electrodes. Various geometries can be easily made by simple alteration of the screen design, and other features, such as reference, counter electrodes and dielectric layers can be added in further printing steps. Carbon is a low-cost material and when coupled with screen-printing manufacturing can produce sensors very economically in large numbers, allowing these to be viewed as disposable, ‘one shot’ devices. SPEs offer comparable electrochemical behaviour to more expensive electrode materials, such as glassy carbon, but can be used and discarded, hence removing the need for regeneration or pre-treatment between each measurement. This also allows for their use by relatively untrained personnel, as no knowledge of the more in-depth aspects of electrochemistry and preparation is needed [190].

2.6.2 Screen-printed technology

Screen printing technology relies on the transfer of an ink onto a substrate, by a mesh, excluding the areas made impermeable to the ink by a patterned stencil. A squeegee is moved across the screen to fill the open webbing openings with ink, and a reverse stroke then causes the screen to come in contact with the substrate momentarily. This leads to the ink to be poured to the substrate and be pulled out of the mesh apertures as the screen springs back after the blade has passed [191]. A basic illustration of the screen-printing process is depicted in **Fig. 26**, in which the movement of the squeegee (depicted in red) sweeps the paste (depicted in yellow) across the mesh area to print the required illustration as per the designed pattern.

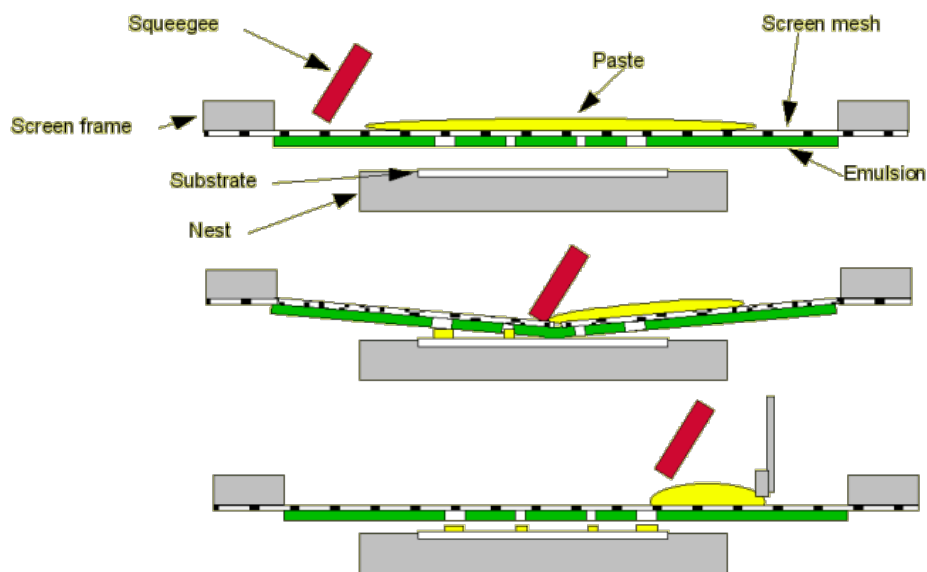


Fig. 26. The basic screen-printed process

The fundamental principles for all forms of graphic reproduction are the same. In simple terms, graphic reproduction takes a quantity of ink or other viscous compound and deposits it in a film of controlled pattern and thickness. In the case of screen printing this entails squeezing ink through a gauze or mesh on to a surface beneath.

The essential items for making a screen print are:

1. A screen, comprising a frame upon which is stretched a mesh.
2. A photo stencil of the required design attached to the mesh.
3. A squeegee, comprising a holder into which is fitted a flexible, resilient blade.
4. An ink or paste (These terms are used interchangeably).
5. A secure base on which to position the component to be printed.
6. An operator to combine these five items.

Three types of material are in general use today: Nylon, Polyester and Stainless Steel. One type will not satisfy the requirement for all types of work and sizes of screen. All three types of mesh are available in a bewildering quantity of weaves because they are multi-purpose; in addition to printing, they are also supplied for sieving, filtration and reinforcement.

The great majority of screen types falls into one of the four classifications mentioned in **Table 5**.

Classification	Typical mesh	Nylon or Polyester	Stainless Steel
Very heavy deposit, quality of outline not important	Under 100	54	80
Heavy deposit, good definition	100 - 200	186	200
All lettering & illustrations	200 - 325	305	325
Thin deposit, extra fine detail	320 - 380	330	325 UT

Table 5. Classification of different types of screens used in screen-printing

A photo negative and contact positive of the required size are made from the artwork as shown in **Fig. 27**. The image on the positive must be completely opaque to prevent light penetration. It is essential that the image appears in a particular way on the photopositive. Suppose that the feature which is to be produced on the substrate looks like a letter F. When looking at the side of the photopositive which is coated with the photographic emulsion, the image must look exactly like the feature, i.e. a black letter F.

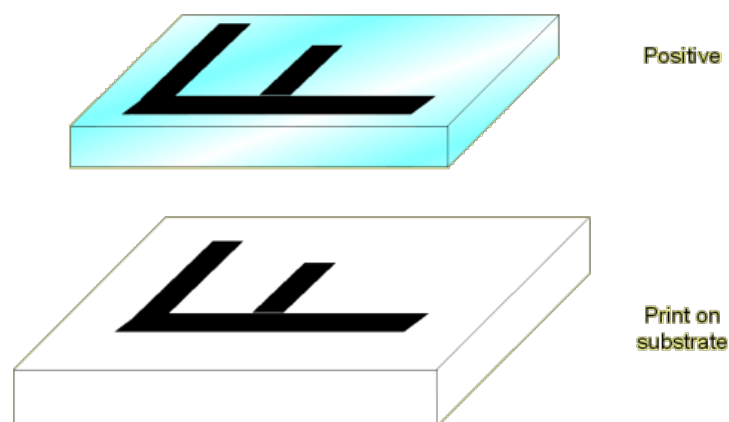


Fig. 27. Right reading positive

As depicted in **Fig. 28**, the photopositive is laid on the substrate side of the coated screen, the positive's emulsion in contact with the screen emulsion, and clamped firmly together. The screen is exposed to Ultra Violet light through the photopositive. This polymerises and hardens the emulsion but those areas which were protected from the UV by the opaque emulsion of the positive remain soft and soluble in water. After exposure, the screen is washed in water, which dissolves the unexposed portions, thus leaving defined open areas in the screen through which the printing paste can pass.

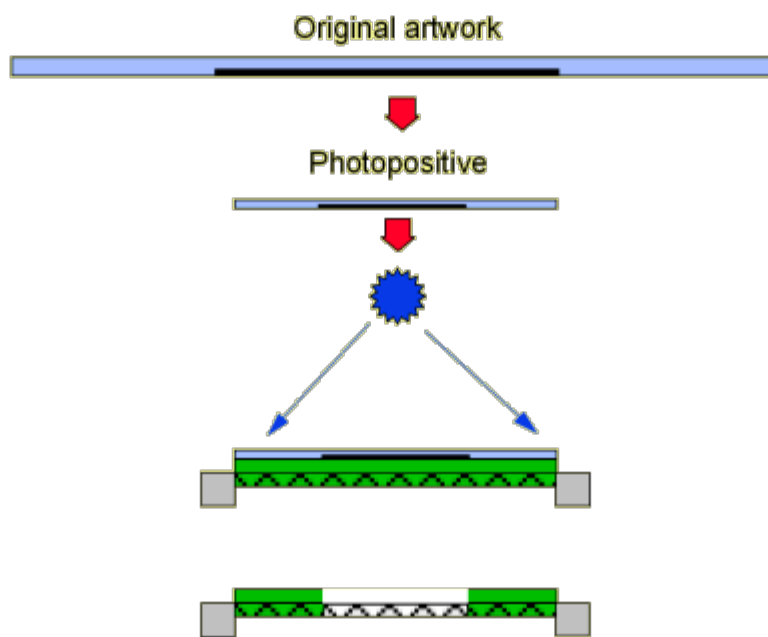


Fig 28. Process of screen exposure

Experimental

3.1 Materials

Bismuth (99.99% trace metal basis), sodium cholate hydrate (BioXtra 99%), potassium hexacyanoferrate(II), Nafion, ~5% in a mixture of lower aliphatic alcohols and water, antimony (powder, 99.99%), PEDOT:PSS dry redispersable pellets, 4-nitrotoluene (4-NT), 2 nitrotoluene (2-NT), 2,4-dinitrotoluene (2,4-DNT), 2,4,6-trinitrophenol (2,4,6-TNP), hexaamineruthenium(III) chloride, vanadium(V) oxide, 2-hydroxyphenylacetic acid (HPhAc), isopropyl alcohol (IPA), ascorbic acid (AA), uric acid (UA), dopamine and sodium acetate were purchased from Sigma-Aldrich. Graphite powder (99.9%) was purchased from Fluka. Silicotungstic acid hydrate ($\text{H}_4\text{SiO}_4 \cdot 12\text{WO}_3 \cdot \text{H}_2\text{O}$, SiW_{12}) was supplied by Aldrich. Acetic acid, dimethylformamide, sodium disodium phosphate monohydrate, ethylenediaminetetraacetic acid disodium salt dihydrate (EDTA-Na_2) and potassium chloride were purchased from Merck. Diclofenac sodium salt (DCF) and aceclofenac were purchased from Alfa Aesar. 5-hydroxydiclofenac (5OH-DCF) was obtained by LGC standards Ltd.. The graphite ink (Loctite EDAG PF-407A was gifted by Henkel Belgium.

Metal cation working solutions in double-distilled water (DDW) were prepared weekly from 1000 mg L^{-1} atomic absorption standard solutions (BDH) and kept at 4 °C. Stock solution of 4-NT was prepared in acetonitrile, while diluted working solutions were prepared in 0.1 M phosphate buffered saline (PBS), pH 7 and were stored at 4 °C. Stock solution of 10 mM DCF was prepared in DDW, while diluted working solutions were prepared in 0.1 M PBS, pH 7 and were stored at 4 °C. DDW was used throughout.

3.2 Apparatus

Voltammetric experiments and electrochemical impedance spectroscopy (EIS) measurements were performed with a PGSTAT12 electrochemical analyzer (Metrohm Autolab) in a single compartment three-electrode cell. Bare/modified GCEs (L-Chem, CZ) or plain/modified graphite SPEs (3 mm diameter) were used as working electrodes and a platinum wire served as the auxiliary electrode. The reference electrode was a Ag/AgCl 3 M KCl (IJ Cambria) electrode and all potentials hereafter are quoted to the potential of this electrode.

EIS spectra were recorded in:

- 9 mM SiW_{12} in 0.05 M phosphate buffer, pH 7 over the frequency range $0.1 - 10^5$ Hz using an excitation amplitude of 10 mV superimposed on a DC potential of -0.213 V, in **4.3.1.** as depicted in **Fig. 36B.**
- 5 mM SiW_{12} in 0.1 M PBS, pH 7 over the frequency range $0.1 - 10^5$ Hz using an excitation amplitude of 10 mV superimposed on a DC potential of -0.300 V, in **5.3.3.** as depicted in **Fig. 45B.**
- 5 + 5 mM potassium hexacyanoferrate(III)/(II) 0.1 M PBS pH 7 over the frequency range $0.1 - 10^5$ Hz using an excitation amplitude of 10 mV superimposed on a DC potential of 0.200 V, in **6.3.1.** as depicted in **Fig. 48.**

Non-faradic EIS experiments were conducted under the same experimental conditions in the absence of the redox probe. Cyclic voltammograms (CVs) were recorded in 0.1 M acetate buffer, pH 4.5 (as depicted in the inset graph of **Fig. 36B** in **4.3.1.**) or 0.1 M PBS, pH 7 (as depicted in **Fig. 42** in **5.3.1.**), at a scan rate of 0.05 V s^{-1} unless stated otherwise.

Square wave (SW) voltammograms were recorded in 0.1 M acetate buffer, pH 4.5 using the following waveform parameters: frequency: 50 Hz, step potential: 0.0015 V , amplitude: 0.050 V . Under these conditions the effective scan rate was 0.075 V s^{-1} .

Differential pulse (DP) voltammograms were recorded either in 0.1 M PBS, pH 7 using the following waveform parameters: step potential: 0.0015 V , amplitude: 0.05 V . Under these conditions the effective scan rate was 0.075 V s^{-1} , or in 0.1 M PBS, pH 7 using the following waveform parameters: step potential: 0.006 V , amplitude: 0.05 V , modulation time: 0.05 s . Under these conditions the effective scan rate was 0.03 V s^{-1} . SEM images were obtained on gold coated samples (Polaron SC7620 sputter coater, Thermo VG Scientific) using:

➤ a JEOL JSM6510LV scanning electron microscope equipped with an INCA PentaFETx3 (Oxford Instruments) energy dispersive X-ray (EDX) spectroscopy detector, in **3.5.1.**, as depicted in **Fig. 30A-D**.

➤ a Phenom Pharos desktop microscope with a FEG source equipped with EDX detector (Thermo Fischer), in **3.5.2.**, as depicted in **Fig. 32A-C**.

➤ a Zeiss Supra 35VP system at 1 kV, in **3.5.3.**, as depicted in **Fig. 35B**.

A Labram HR-Horiba scientific Raman system was used in order to record the spectra of bulk bismuth powder and of bismuthene deposits onto a glass slide covered with an aluminium adhesive tape. The 514.5 nm line of an argon ion laser operating at 1 mW at the focal plane was employed for the Raman excitation. Raman spectra in the range of 80 –1500 cm⁻¹ were collected with an acquisition time of 20 s. The spectra were baseline-subtracted with a linear baseline.

Attenuated total reflectance (ATR) infrared spectroscopy was conducted with a Spectrum Two instrument (Perkin Elmer). Spectra were collected as the average of 64 scans with a resolution of 4 cm⁻¹ from 400 to 4000 cm⁻¹, unless stated otherwise.

X-ray powder diffraction (Cu K α radiation, $k = 1.5418 \text{ \AA}$) was performed with a Brüker D8 advance or a Brüker D2 phaser in the range $20^\circ < 2\theta < 80^\circ$ with a resolution of 0.02° (2θ).

3.3 Synthesis of the materials

3.3.1 Shear force exfoliation of bismuthene/graphene

Exfoliation of bulk bismuth and graphite was conducted via a liquid shear force exfoliation method as a two-step process. Firstly, as a cleaning step, 8 g of bismuth (grinded to fine powder with the aid of a mortar and pestle) was dispersed in a sodium cholate solution (5 mg/mL) in 200 mL DDW and was partially exfoliated in a kitchen blender (AVEC, 400 W) for 20 min to negate any deactivation by ionic impurities. The resulting material was filtered through a 0.45 mm Millipore membrane under vacuum (KNF pump, 20 mbar), rinsed thoroughly with DDW to almost foamless washings and was left to dry overnight. The main exfoliation process was conducted on the dry, partially processed material with the aid of a DISPERMAT® AE dissolver for 1 h in 3000 rpm at 5 °C. The material was centrifuged at 750 rpm ($59.74 \times g$) for 30 min to

remove any unprocessed bismuth and subsequently filtered under vacuum (see above). The material was left to dry overnight resulting in a mass of 97 mg (1.2% yield). Graphene was produced in a similar manner with the only difference being the centrifugation rotation speed [3000 rpm ($955,89 \times g$) for 30 min] and resulted in a mass of 396 mg (4.9% yield). Hybrid 2D-Bi/Gra dispersion was prepared every two weeks by mixing 2 mg of bismuthene and 10 mg of graphene in 2.0 mL DMF overnight. Before use the dispersion was processed in an Elmasonic S40, 140 W sonication bath for 30 min.

3.3.2 Exfoliation of antimonene & antimonene/PEDOT:PSS

Bulk β -phase antimony was exfoliated using tip sonication assisted exfoliation in DDW or in a 1 mg mL⁻¹ PEDOT:PSS aqueous solution. All batches were sonicated via a tip ultrasonic homogenizer (MRC, 6.0 mm diameter probe, 250 W) in a glass vial of 20 mL capacity, placed in an ice bath, under the following conditions: power, 75%; process time, 9 s; rest time, 2 s; total duration, 2 h; probe immersion depth, 0.5 cm. *Production of Sbene*: Tip sonication of bulk β -phase antimony powder (1 g) was conducted in 10 mL DDW.

Preparation of Sbene oxide PEDOT:PSS: Tip sonication of bulk β -phase antimony powder (200 mg) was conducted in 10 mL 1 mg mL⁻¹ PEDOT: PSS aqueous solution filtered through a 0.45 μ m membrane (Millipore) to exclude agglomerated particles. At both batches, the sonication process is followed by a centrifugation step at 1000 rpm for 15 min, after which the supernatant was stored, while the sediment was discarded. Sbene dispersion was further filtered through a 0.45 μ m membrane (Millipore) under vacuum (KNF pump, 20 mbar), rinsed thoroughly with DDW and was left to dry overnight.

3.3.3 Exfoliation of bulk vanadium(V) oxide

Vanadium(V) oxide was exfoliated by a simple bath sonication (EMAG Emmi D30, 150 W) method. Typically, three batches of 50 (batch 1), 100 (batch 2) and 200 mg (batch 3) vanadium(V) oxide were sonicated in a blend of 75/25% v/v H₂O/IPA for 2 h at ambient conditions, followed by centrifugation at 3000 rpm for 15 min after which each working material, named as V₂O₅ NSs, was obtained as a supernatant.

3.4 Procedures

3.4.1 Modification of glassy carbon electrodes with bismuthene/graphene

GCE was polished with Al_2O_3 (0.01 mm grain size) over a fine polishing cloth (Struers 4000 grit), sonicated with ethanol, rinsed thoroughly with water and dried under nitrogen. The electrode surface was modified with the application of 10 μL of 2D-Bi/Gra dispersion, while the solvent was allowed to evaporate at 60 °C overnight. Then 5 μL 0.1% (v/v) Nafion in ethanol was dropped onto the modified electrode surface and allowed to air dry. For comparison purposes, GC electrodes were also modified with 1 mg mL^{-1} dispersions of pure bismuthene or grinded bulk bismuth in DMF and with 5 mg graphene mL^{-1} DMF.

3.4.2 Fabrication of screen-printing of electrodes and modification of their surface with antimonene and related composites or vanadium(V) oxide nanosheets

The screen template was designed with the CorelDRAW Graphics Suite X8 design software, followed by their development on illustration slides. To make the grids, the polyester screen printing mesh (SEFAR, 77/195-48) was initially stretched on the aluminum screen printing frame (SEFAR) using the pneumatic tabletop stretching machine (G-STRETCH 202 A1, Grunig), keeping the indicated tension at 28 N / cm with the fabric tension gauge TETKOMAT 7/50 (G-CHECK, Grunig). The mesh was adhered to the crate using a two-component screen adhesive (KIWOBOND® & KIWODUR® 1100 Power Grip), and after drying, the mesh was treated with the degreasing liquid (KIWO® Mesh X-CEL). The water-based photosensitive emulsion (POLYCOR® S-HR) was then spread by hand on the grid and left in the drying chamber at 40 °C (COMBINETUVE ETABLI 608/1, TIFLEX). The grid was then exposed to UV radiation under vacuum (COMBINETUVE ETABLI 608/1, TIFLEX) in the display room, having the appropriate design image transparency. After exposure, they were rinsed thoroughly with deionized water to remove photosensitive material that was not polymerized and to force the development of the mold design, being ready to use after drying. Suitable grids were fabricated to print the three layers described above to print the active surface of the working electrode.

Single layer graphite SPEs (3 mm working surface diameter) were fabricated over 175 μm thick polyester sheets (Mac Dermid, Autostat CUS7), using a semi-automatic screen-printer (E2, EKRA), and a polyurethane 75 durometer squeegee and conductive carbon ink (LOCTITE, EDAG PF 407A). After printing, electrodes were cured at 90 $^{\circ}\text{C}$ for 60 min at a conventional oven. The fabricated screen used throughout this thesis is shown in **Fig. 29A**, with a more focused depiction onto the printing area in **Fig. 29B**. The resulting screen-printed electrodes are shown in **Fig. 29C**.

The electro-active surface was modified by pipetting either 2 μL of Sbene or Sbene oxide/PEDOT:PSS or 6 μL of V_2O_5 NSs at the electrode surface, while the solvent was allowed to evaporate at ambient conditions overnight.

In every PEDOT:PSS related modification, an outer protective film (2 μL 0.2% v/v Nafion in DDW) was cast atop the electrode surface to prevent swelling and stripping of the modifying layer off during the cathodic scans (de-doping of PEDOT:PSS) [25] which led to a 90% loss of response after the first measurement.

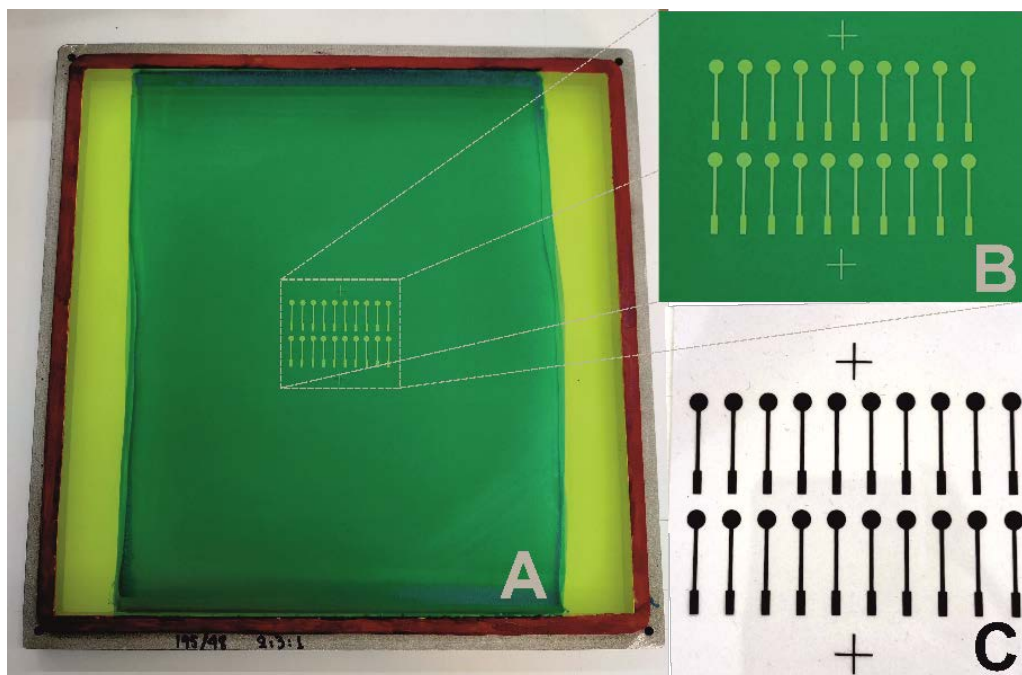


Fig. 29. (A) Fabricated screen used in this thesis, (B) Close-up image of the electrode printing area, and (C) printed working electrodes used in this thesis.

3.4.3 Analytical measurements

3.4.3.1 Determination of heavy metal ions with 2D-Bi/Gra-GCEs

2D-Bi/Gra-GCEs were immersed in the cell containing the standard solutions or the tap water samples (18.00 mL of the sample plus 2.00 mL of 1 M acetate buffer, pH 4.5 containing 20 mM potassium hexacyanoferrate(II) in order to diminish copper interference). Preconcentration of the targets was conducted at -1.2 V for 180 s under stirring. After an equilibration period of 10 s, an anodic voltammetric scan (stripping scan) was performed from -1.2 V to -0.35 V. The first 2 – 3 preconcentration/stripping analytical cycles were not considered to the quantification of the targets (conditioning of the electrodes), while between analytical cycles, two stripping scans (i.e. without the preconcentration step) were conducted to remove any remaining traces of metals from the electrode surface.

3.4.3.2 Antimonene passivation

Sbene/SPE modified with 5 mg mL^{-1} Sbene was passivated by applying 10 CV scans from 0.800 to -1.400 V in 0.1 M PBS pH 7 at a scan rate 0.05 V s^{-1} . Passivated Sbene/SPE was immersed in non-deoxygenated 0.1 M PBS, pH 7 and subjected to DP voltammetry scans over the potential range from 0.800 to -1.000 V until a stable baseline was reached (typically 1–2 scans) before the addition of the measured species.

3.4.3.3 Determination of 4-nitrotoluene

Sbene oxide/PEDOT:PSS/SPE was immersed in 10.00 mL 0.1 M PBS, pH 7 containing the calibrants or the unknown sample [9.00 mL sample spiked with a known concentration of the target + 1.00 mL 1 M PBS, pH 7]. The measuring solution was deoxygenated by purging nitrogen for 15 min. Measurements were conducted by performing DP voltammetry scans from -0.250 V to -1.000 V. The magnitudes of the peak currents at ca. -0.72 V were taken as a measure for the quantification of 4-NT. The concentration of the target in the spiked samples was determined by using the standard addition method.

3.4.3.4 Determination of diclofenac

Each measurement involves a preconcentration/conditioning step by applying three CVs from 0.800 to 0.000 V at a scan rate 0.025 V s^{-1} (total time 192 s) followed by a DP voltammogram from 0.000 to 0.800 V in 0.1 M PBS pH 7. The current of the anodic peak at ca. 0.36 V was taken as a measure for the quantification of DCF in the various standard solutions or the unknown samples. Solid EDTA- Na_2 was added to all tap water samples to a final concentration 1 mM to prevent complexation of DCF with various metal ions exist in water samples [192, 193]. Original and spiked with 50 nM DCF tap water samples were analyzed without any treatment by applying the standard addition method. Measurements were conducted in a polypropylene cell containing 8.00 mL sample and 2.00 mL 0.5 M PBS pH 7 following the protocol described above.

3.5 Morphological and structural characterization of the materials

3.5.1 Characterization of bismuthene/graphene

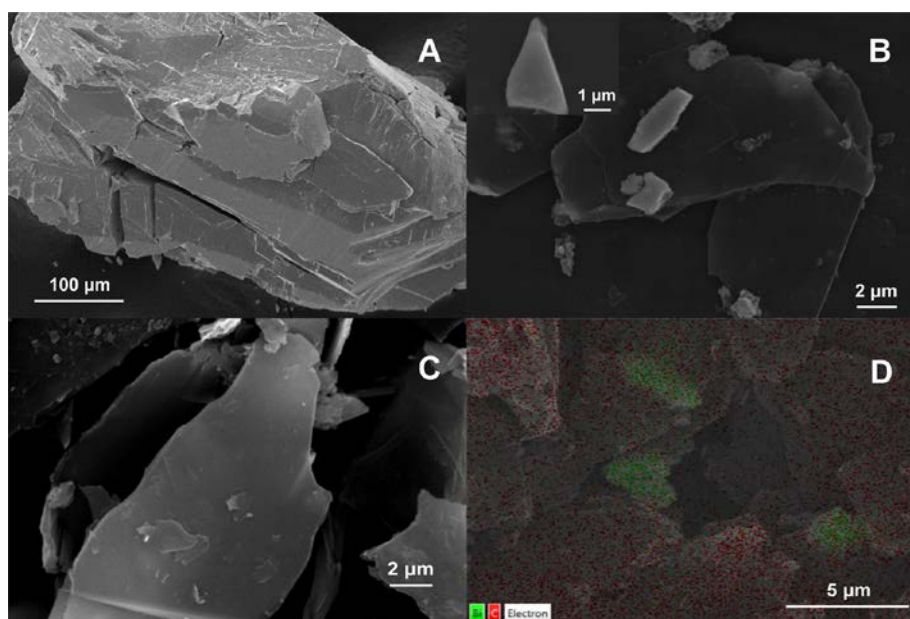


Fig. 30. SEM images of (A) bulk bismuth, (B) few-layer bismuthene, (C) few-layer graphene, and (D) EDX mapping analysis of the bismuthene/graphene nanocomposite

The SEM images of the exfoliated bismuthene and graphene materials along with the bulk bismuth which was used for comparison are shown in **Fig. 30A–C**, while the

successful formation of the hybrid suspension is proved by the EDS mapping analysis (**Fig. 30D**) showing the individual components at the nanocomposite material. Images at Fig. 17B and C refer to few-layer bismuthene and few-layer graphene, respectively, which were produced after 1 h in 3000 rpm at 5 °C (see above), and **Fig. 30D** to the dry spot of a few microliters of the 2D-Bi/Gra suspension.

Fig. 31A illustrates the ATR FT-IR spectra of both bulk bismuth and bismuthene. At least 5 peaks are apparent in bismuthene, while bismuth shows no measurable vibration peaks. We have chosen to focus our analysis on the peaks present at 845 cm^{-1} and 1385 cm^{-1} . These peaks are attributed to vibrations of the CO_3^{2-} ions which are embodied in the bismuthene structure due to the atmospheric CO_2 . As a matter of fact, this is indirect proof for the successful exfoliation of bismuth and hence the production of the nanosheets. The principle here is that due to a significantly higher surface to volume ratio, bismuth nanostructures, such as bismuth nanosheets [115], nanorods [194], are prone to a greater interaction with CO_2 [194] that can be utilized as an exfoliation parameter. In short, the comparison between the two spectra in **Fig. 31A** suggests the successful exfoliation of bismuthene based on the presence of bismuth-oxygencarbonate secondary phases on the surface of bismuthene and not to characteristic bismuth peaks [115, 194].

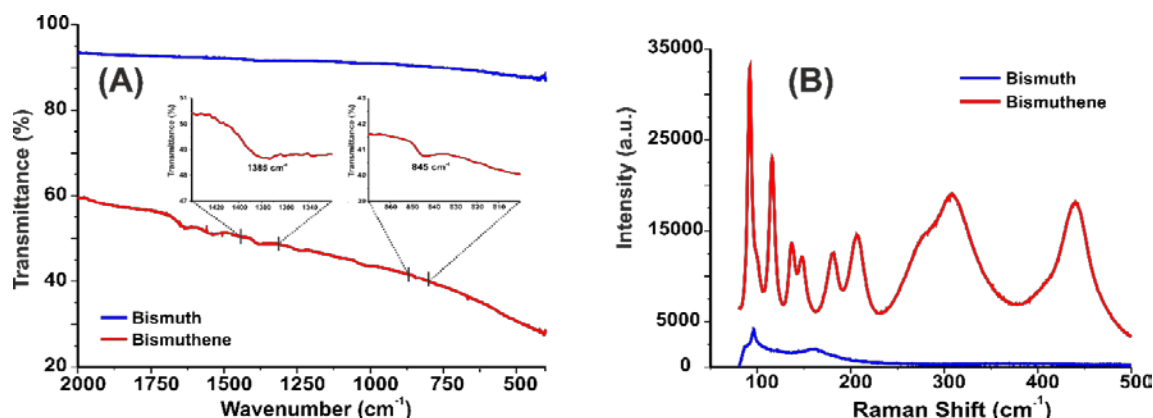


Fig. 31. (A) ATR-IR and (B) Raman spectra of (blue line) bulk bismuth and (red line) bismuthene.

Fig. 31B shows the Raman spectra of both bulk bismuth and bismuthene. Bismuth exhibits a characteristic peak at 96 cm^{-1} (A_{1g} mode of rhombohedral lattice) and a weak peak at 162 cm^{-1} attributed to second order harmonics [195, 196]. Bismuthene exhibits

a respective peak at 92 cm^{-1} (A_{1g} mode) and several peaks at 116 cm^{-1} , 137 cm^{-1} , 148 cm^{-1} , 182 cm^{-1} , 207 cm^{-1} , 308 cm^{-1} and 440 cm^{-1} related to the $\alpha\text{-Bi}_2\text{O}_3$ phase of the bismuthene surface [197, 198]. The in-plane vibration E_g phonon mode at 70 cm^{-1} was not visible due to the notch filter that was used in the experimental setup for cutting off the Rayleigh light. The use of this filter also led to the asymmetry of the observed spectra in the low wavelength region ($80\text{--}90\text{ cm}^{-1}$).

3.5.2 Characterization of antimonene & antimonene/PEDOT:PSS

SEM images in **Fig. 32** show that antimonene seems to adopt a sheet-like morphology with few-layer topology (**Fig. 32A**), as expected during a typical liquid phase exfoliation process of layered materials. However, the Sbene oxide/PEDOT:PSS composite adopt the morphology of a heterostructure where the Sbene oxide rich phases of the material indicated with green and blue color in the EDX mapping of the designated area in **Fig. 32B** follow a layered topology, while in the PEDOT:PSS rich phases indicated with light blue color in the EDX mapping in **Fig. 32C**, a reticulate topology is more prevalent. The two phases, however, seem to be closely stacked possibly due to π -stacking interactions between the buckled layer of antimonene oxide and the thiophene ring of PEDOT.

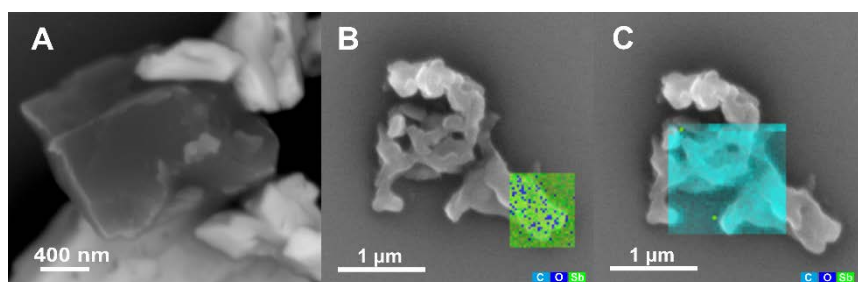


Fig. 32 SEM images of (A) antimonene nanosheets, (B,C) Sbene oxide/PEDOT:PSS with EDX data on the (B) Sbene oxide and (C) PEDOT:PSS rich phases.

Fig. 33 depicts the XRD patterns of (black line) bulk β -phase antimony, (blue line) tip sonication exfoliated Sbene, and (red line) Sbene oxide/ PEDOT:PSS nanocomposite. Compared with the XRD pattern of bulk β -phase antimony, the reduction of the (003), (012) and (006) peaks of Sbene suggests that tip sonication exfoliation afflicts the structure of the bulk material along the c-axis, thus producing few-layer Sbene with a

high degree of crystallinity as documented by the sharpness of the (012) diffraction [120, 199]. In addition, partial oxidation of Sbene (which is inevitable due to the ultrasonication conditions in air) [200] is documented by the emergence of scarcely seen (222) and (400) peaks, in accordance with the XRD pattern of standard cubic Sb_2O_3 (JCPDS 11–689). The XRD pattern of the PEDOT:PSS based nanocomposite shows that all characteristic Sb_2O_3 peaks are prevalent, while the antimony lattice peaks [(003), (012) and (006)] have completely diminished verifying that during the tip sonicated exfoliation of bulk β -phase antimony in the presence of PEDOT:PSS, the exfoliated Sbene nanosheets are transformed to Sbene oxide.

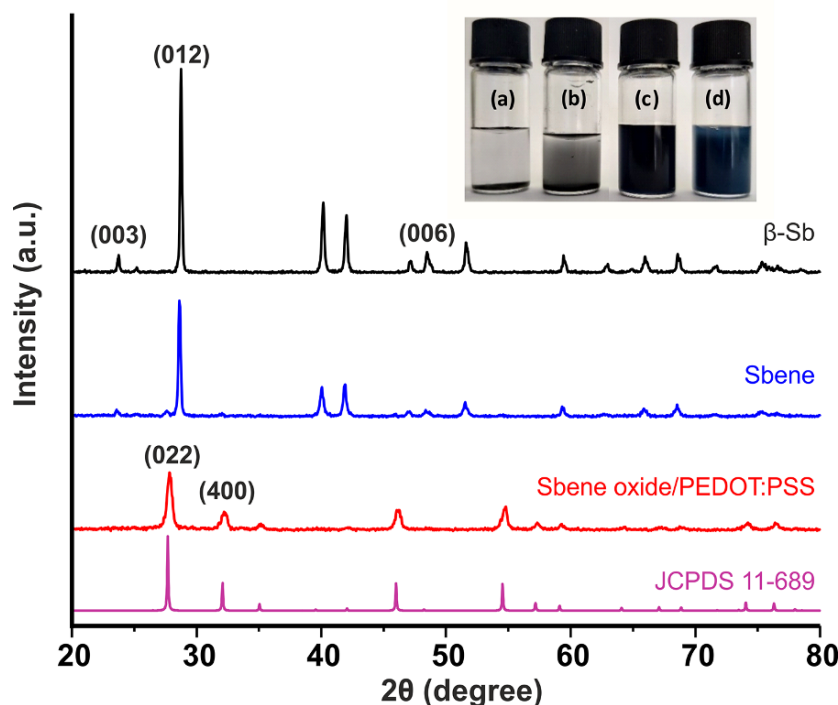


Fig. 33. XRD diffractograms of (black line) bulk β -phase antimony, (blue line) Sbene, (red line) Sbene oxide/PEDOT:PSS, and (magenta line) standard cubic Sb_2O_3 (JCPDS 11–689). Inset: Photos of (a) bulk β -phase antimony, (b) Sbene dispersion after the centrifugation step at 1000 rpm for 15 min, (c) PEDOT:PSS, and (d) Sbene oxide/PEDOT:PSS aqueous dispersions.

ATR-FTIR studies are illustrated between the 500 and 1500 cm^{-1} wavenumber range for reasons of clarity. The modification of the SPEs with Sbene oxide/PEDOT:PSS was evaluated by ATR-FTIR studies directly on the electrode surface (**Fig. 34**). For comparison, ATR-FTIR spectra were also acquired at plain SPE and SPEs modified with pristine PEDOT:PSS. Photos of the respective modified electrode surfaces are

illustrated as insets in **Fig. 34**. The ATR-FTIR spectrum of PEDOT:PSS/ SPE (blue line) exhibits the characteristic vibrations of $-\text{SO}_3\text{H}$ group emerging at 1130 and 570 cm^{-1} , the vibrations at 980 – 653 cm^{-1} attributed to C–S bond in the thiophene ring, as well as a peak at 1310 cm^{-1} attributed to the C–C stretching in the thiophene ring [201, 202]. The Sbene oxide/PEDOT:PSS/SPE (red line) exhibits the same peaks as pristine PEDOT:PSS, as well as an additional peak at 720 cm^{-1} attributed to Sb–O stretching vibration [203, 204], without however any other peaks that usually appear in Sb_2O_3 nanoparticles, such as the peak assigned to Sb=O bond at 964 cm^{-1} [203], hinting that Sbene oxide does not follow the pattern of Sb_2O_3 spectrum entirely. This observation can be attributed to the different length, polarity, and strength between the Sb=O bond in Sbene oxide and the conventional binary oxides of antimony [205].

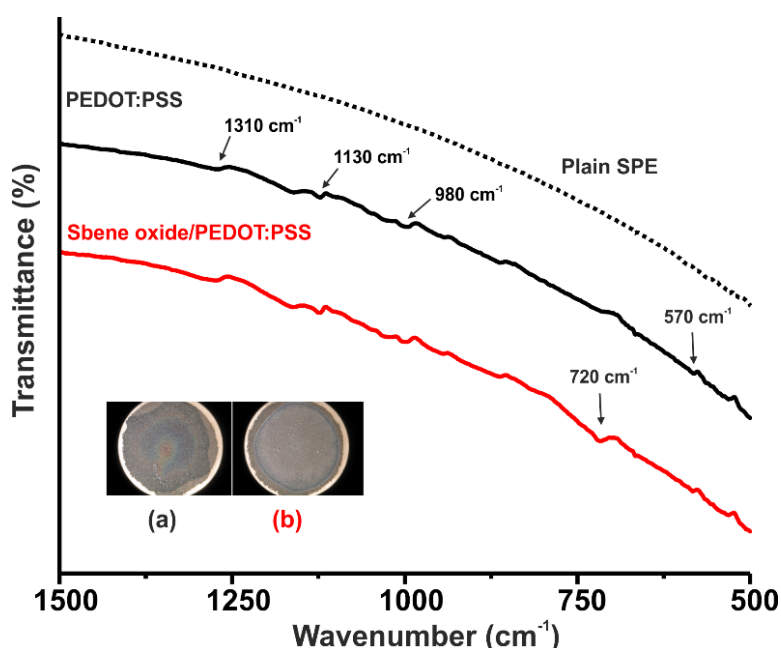


Fig. 34. ATR-FTIR spectra of (dashed line) plain SPE, (black line) PEDOT:PSS/ SPE, and (red line) Sbene oxide/PEDOT:PSS/SPE. Inset: Photos of SPEs surface modified with (a) PEDOT:PSS and (b) Sbene oxide/PEDOT:PSS.

3.5.3 Characterization of V_2O_5 nanosheets

Fig. 35A depicts the as-produced V_2O_5 NSs dispersion used as the electrode modifier. **Fig. 35B** illustrates the FE-SEM images of the V_2O_5 NSs which present 2D low dimensional morphology with most layers having dimensions of a few micrometers.

The large surface of V_2O_5 NSs can be attributed to the non-destructive ultrasonication process, since bath sonication does not develop high pressures usually leading to implosion of cavitation bubbles which are known to induce defects to the nanosheet layers or even severe fragmentation [206, 207]. **Fig. 35C** depicts the XRD patterns of both bulk V_2O_5 and exfoliated V_2O_5 NSs, which crystallize in orthorhombic crystal structure (space group: Pmmn, $a = 11.5160 \text{ \AA}$, $b = 3.5656 \text{ \AA}$ and $c = 4.3727 \text{ \AA}$, JCPDS No: 41–1426). In the XRD pattern of the V_2O_5 NSs, the relative intensities of the most planes are severely diminished, while by comparing the intensities of the most prominent (200), (001) and (110) facets in the exfoliated material we can assume that the (001) orientation is preferred [208]. In addition, the sharp pattern of the (001) peak and the remaining (200) and (110) peaks suggest that the sonication-induced exfoliation of the layered structure has not tampered with the crystallinity of the lattice.

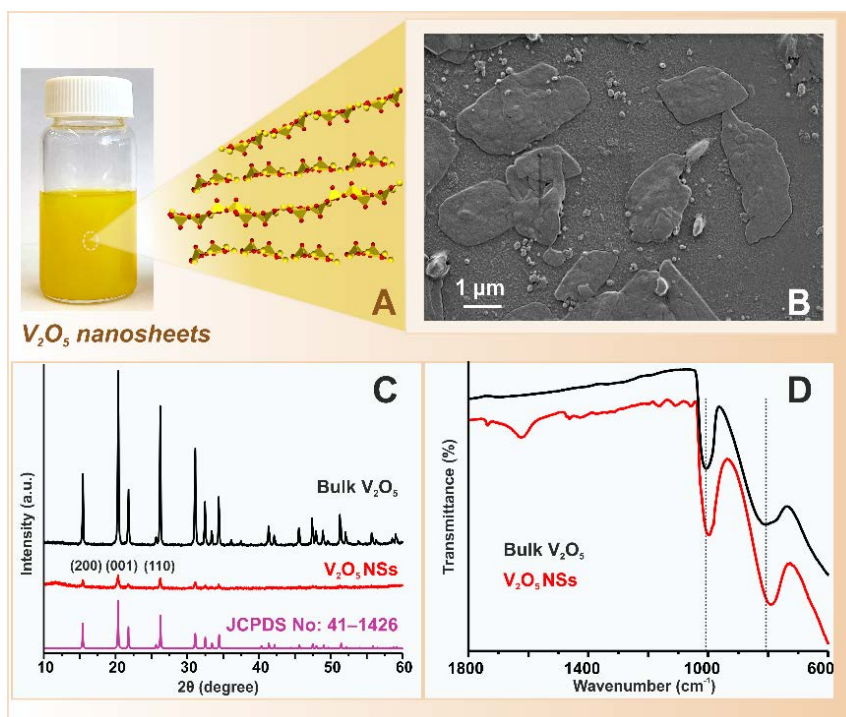


Fig.35. (A) The as-produced V_2O_5 NSs dispersion (batch 3), (B) FE-SEM image of the V_2O_5 nanosheets, (C) XRD patterns and (D) ATR-FT-IR spectra of (black line) bulk V_2O_5 and (red line) V_2O_5 NSs.

Fig. 35D shows the characteristic bands of both bulk V_2O_5 (black line) and V_2O_5 NSs (red line) originating from the asymmetric stretching of the V–O–V bond and the terminal stretching of oxygen in the V=O [209, 210]. Interestingly, the nanosheet-related spectrum depicts red shifts on both peaks (from 1005 cm^{-1} to 998 cm^{-1} and from

810 cm^{-1} to 794 cm^{-1}). This inclination could be explained by the phonon softening which occurs due to the decrease of the interlayer van der Waals interactions when bulk layered materials transit to ultra-thin nanosheets [211]. Also, an additional peak at 1625 cm^{-1} attributed to the H_2O scissoring band due to intercalated water molecules within V_2O_5 NSs during the ultrasonication process [212].

2D bismuthene/graphene modified electrodes for the ultra-sensitive stripping voltammetric determination of lead and cadmium

4.1 Abstract

Bismuth-based electrodes have been proved the most reliable replacement of highly toxic mercury for the anodic stripping (AS) and cathodic voltammetric determination of metal ions and organic compounds, respectively. Herein, we report for the first time on the implementation of two-dimensional (2D) bismuth, called “bismuthene”, for the AS voltammetric determination of Pb(II) and Cd(II) ions. Bulk bismuth was exfoliated by a facile and fast shear-force liquid phase exfoliation method. Exfoliated bismuthene layers were characterized by means of SEM, EDX, Raman, FT-IR, electrochemical impedance spectroscopy and cyclic voltammetry. Bismuthene colloids were mixed with dispersions of few-layer graphene, which was used as supporting material in order to achieve the desired adherence of bismuthene films onto the surface of glassy carbon electrode (GCE) as well as an effective electrical communication between them and with the electrode surface. The optimum loading of bismuthene in the bismuthene/graphene composite (2D-Bi/Gra) was investigated, while other parameters such as the deposition time and deposition potential were also examined. Under selected conditions and for a 3 min preconcentration time, the limit of detection (S/N 3) of each target ion was 0.3 mg L^{-1} . 2D-Bi/Gra/GCEs were successfully applied to the determination of Pb and Cd in tap water samples in the presence of potassium hexacyanoferrate(II) for the alleviation of copper interference. Results suggest that 2D

bismuthene/graphene modified electrodes offer great promise for the determination of sub-microgram per liter Pb and Cd and could contribute greatly in heavy metal ions and other organic compounds sensing applications.

4.2 Introduction

In the past few years extended focus was devoted at the exploitation of the extraordinary properties of two-dimensional (2D) layered materials starting with graphene [213], which has been on the spotlight for many years now. Research was also concentrated on other inorganic 2D materials such as transition metal oxides, transition metal dichalcogenides [214, 215], transition metal carbide- and carbon nitride-based MXenes [16] etc.. Other combinations of dichalcogenides with elements belonging to the VA group, such as Bi_2Te_3 , Bi_2Se_3 etc. [62, 216] have been used mostly for their excellent, thickness dependent thermoelectric properties, while attractive sensing capabilities of exfoliated Bi_2Te_3 -based electrodes [29] further emphasize upon the versatility of inorganic 2D materials. Extensive research efforts have also been focused on the exploration of the “exotic” properties of 2D layered monoelemental materials [15]. Silicene and germanene [217, 218] have already been widely implemented in a variety of applications, while other monoelemental layered structures such as stanene, are predicted to have great potential in applications related to air pollution [219]. The newest family of 2D layered materials with great potential in substituting bulk materials in a wide range of technological applications, are the elements that belong in the VA Group, which are also known as “pnictogens” [15, 220]. Phosphorene is the most studied 2D material of this group as it can exhibit excellent charge and thermal transport properties but is prone to oxidation in aqueous environments in the presence of oxygen leading to limited exploitation of its potential. Formation of these types of structures has been possible with sonication-assisted exfoliation, which however requires high power output and lengthy treatments that favor overheating during the sonication process, which can cause deformation of the 2D structure of the resulting materials. A promising alternative to this method is the shear force liquid phase exfoliation, which has been employed for the large scale production of graphene with either N-methyl pyrrolidone (NMP) or sodium cholate (SC) as dispersion media [102]. In this method, the formation of the desired 2D material

stems from the shearing of the thin film, which overcomes the large collective Van der Waals interactions between the layers with the aid of a dispersing medium [101]. During the shearing process the solvent acts as the dispersing medium, while surfactants can play a dual role acting not only as a dispersing medium but also as a stabilizer preventing the reaggregation of the exfoliated sheets [221]. Recently, shear force exfoliation for the production of 2D structures of the VA Group elements has been proposed with the aid of a commercial kitchen blender [105]. The resulting materials were applied on glassy carbon electrodes as modifiers of the electrode surface for biosensing purposes [105]. In this regard, our effort was focused on the production of 2D bismuth layers (bismuthene) and their implementation in anodic stripping voltammetry for the determination of trace metal ions. Bismuth has been proved the most promising replacement of highly toxic mercury for the anodic stripping (AS) and cathodic voltammetric determination of metal ions and organic compounds [185, 222]. Herein, we report a facile shear force liquid phase exfoliation method for the production of bismuthene in an aqueous surfactant medium (sodium cholate) as well as redispersion of bismuthene in dimethyl formamide (DMF), which allows facile cast of bismuthene films over glassy carbon electrode (GCE) by drop-casting. Since bismuthene is a direct band-gap semiconductor, a hybrid bismuthene/graphene (2D-Bi/Gra) dispersion in DMF was created to enhance adherence and electrical communication between the exfoliated bismuthene layers and the electrode surface. Graphene production was conducted similarly as bismuthene. 2Dbi/Gra dispersion showed a slow sedimentation rate while the resulting film over GCE's surface was stable for more than 40 analytical runs. Exfoliated materials were characterized by scanning electron microscopy (SEM), Raman, FT-IR shown previously in **3.5.1.**, electrochemical impedance spectroscopy (EIS) and cyclic voltammetry (CV) techniques. Finally, the applicability of 2D-Bi/Gra-modified GCE to the determination and recovery of Pb(II) and Cd(II) ions in tap water samples is demonstrated.

4.3 Results & discussion

4.3.1 Electrochemical studies

CVs for the bulk and the exfoliated material are illustrated in **Fig. 36A**. During the anodic scan both CVs depict one peak, which is attributed to the stripping of elemental

bismuth [Bi⁰/Bi(III)], while the following cathodic scan, in each CV, reveals a broad peak which is associated with the reduction of the Bi(III) ions generated during the anodic scan back to elemental bismuth, along with the reduction of oxygen. It seems quite obvious that the magnitude of both oxidation and reduction peaks is dependent upon the surface coverage of the electrode, whereas bismuthene appears to possess a more efficient electroactive surface due to greater specific surface compared with its bulk counterpart. Finally, the CV of the bismuthene/graphene hybrid-modified GC electrode shows a remarkable increase in magnitude of both redox peaks, which is attributed to: a) the successful interaction of the two materials leading to an effective electrical connection between the GC surface and the hybrid nanocomposite and b) a dramatic enhancement of the electrode's electrical conductivity, as it is also evidenced by the Nyquist plots illustrated in **Fig. 36B** which illustrates, in the form of Nyquist plots, the faradaic impedimetric behavior of bulk bismuth/GC, bismuthene/GC and bismuthene/graphene/GC electrodes in the presence of SiW₁₂, used as the redox probe. SiW₁₂ was selected instead of commonly used hexacyanoferrate(II)/(III) redox couple as at its formal potential ($E^0 = -0.219$ V) [223] Bi(0)/Bi(III) redox transition does not occur and thus the physicochemical properties of the coating layer are not altered. According to the Nyquist plots, bismuth modified GCE/ electrolyte interface exhibits the highest charge-transfer resistance (R_{ct}), of 600 kOhm, followed by that of the bismuthene/GC electrolyte interface (208 kOhm), while a considerably lower R_{ct} value (50 kOhm) was observed at the bismuthene-graphene/GCE electrolyte interface. It is noted, however, that these values do not directly reflect the conductivity of the coatings but also the electro catalytic properties of the resulting surfaces to the redox probe (SiW₁₂). In an attempt to distinguish between the coating's conductivity and electrocatalytic properties, impedimetric studies were also conducted in the absence of the redox probe (non-faradic impedimetric measurements). In this case however, $Z' = f(-Z'')$ plot-based visual comparison is not easy, and thus data are expressed with respect to the admittance Y (reciprocal of impedance, measured in Siemens) values of the modified electrode/electrolyte interfaces. The inset graph in **Fig. 36B** shows the admittance plots of the bismuth and bismuthene modified GCEs in 0.05 M phosphate buffer, and according to them, bismuthene modified electrode/electrolyte interface exhibits greater conductivity. This behavior can be explained considering an extended coverage of the electrode surface by exfoliated bismuthene films that behave as 2D

direct semiconductors possessing low band-gap energies (0.36 – 0.99 eV) and high carrier mobilities [224].

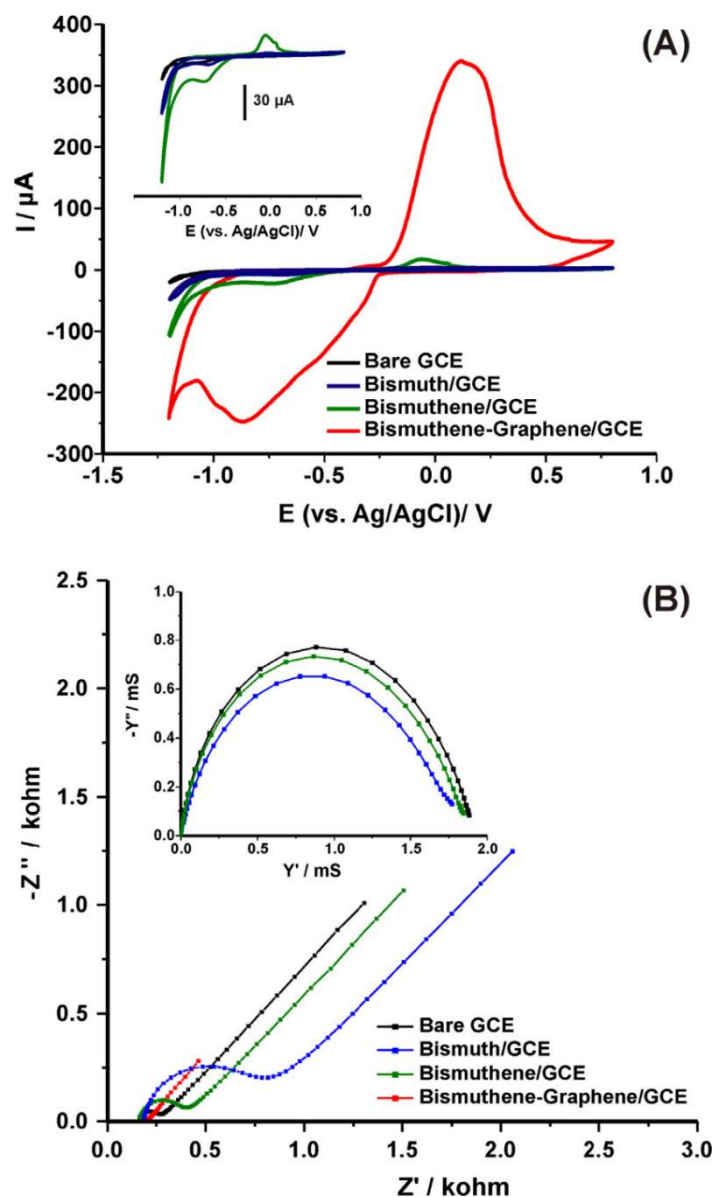


Fig. 36. (A) Cyclic voltammograms of (black line) plain, (blue line) bismuth, (green line) bismuthene and (red line) bismuthene-graphene modified GCEs in 0.1 M acetate buffer, pH 4.5. Scan rate 0.050 V s⁻¹. Inset graph shows at an enlarged scale the CVs of bismuth- and bismuthene-modified GCEs. (B) Nyquist plots of (black line) plain, (blue line) bulk bismuth, (green line) bismuthene and (red line) bismuthene/graphene-modified GCEs in 0.05 M phosphate buffer containing 9 mM SiW₁₂. Inset graph shows the admittance plots of the corresponding electrodes in 0.05 M phosphate buffer in the absence of a redox probe.

4.3.2 Optimization studies

Graphene was employed as supporting material in order to achieve the desired adherence of bismuthene films onto the surface of GCE as well as an effective electrical communication both between bismuthene films and also between them and the electrode surface. For this purpose, three mixed dispersions containing different ratios of bismuthene and graphene (1:10, 1:5, 1:2.5 w/w) were prepared in DMF and the performance of the respective electrodes towards the anodic stripping voltammetric detection of cadmium and lead was evaluated. SW voltammograms illustrated in **Fig. 37** demonstrate the effective deposition of bismuthene/graphene hybrid material on the electrode surface. The height of the bismuth stripping peak at ca. -0.11 V is attributed to the respective content of bismuthene in the hybrid modifying layer. It is obvious that the difference in each composition results in different electrode sensitivity towards Cd and Pb, as indicated by the magnitude of the stripping currents at ca. -0.77 V and -0.52 V, respectively. This comparison reveals that the 1:5 w/w dispersion endows the greatest sensitivity towards Cd and Pb, as it is more accurately depicted on the corresponding inset graph showing at an enlarged scale the pattern of SW voltammograms at the potential window from -1.2 to -0.4 V. The effect of the deposition potential and time on the performance and sensitivity of the selected electrode was also examined in the range from -1.0 to -1.6 V for a deposition time of 120 s (**Fig. 38A**) and in the time frame of 30 – 240 s at a deposition potential of -1.0 V (**Fig. 38B**). In each measurement the starting potential of the stripping scan was the same as the deposition potential. Even though the deposition potential of -1.0 V is superior in terms of stripping peaks magnitude at the examined concentration level ($10 \mu\text{g L}^{-1}$) of the targets, it lacks sensitivity for the detection of lower concentrations of Cd(II) ions (data not shown), while more cathodic deposition potentials (Fig. XA scans c, d) are affected by the reduction of hydrogen ions which results in reduced electrode response for both targets. To that end, a deposition potential of -1.2 V and a preconcentration time of 180 s were selected as a compromise between sensitivity and total time of measurement.

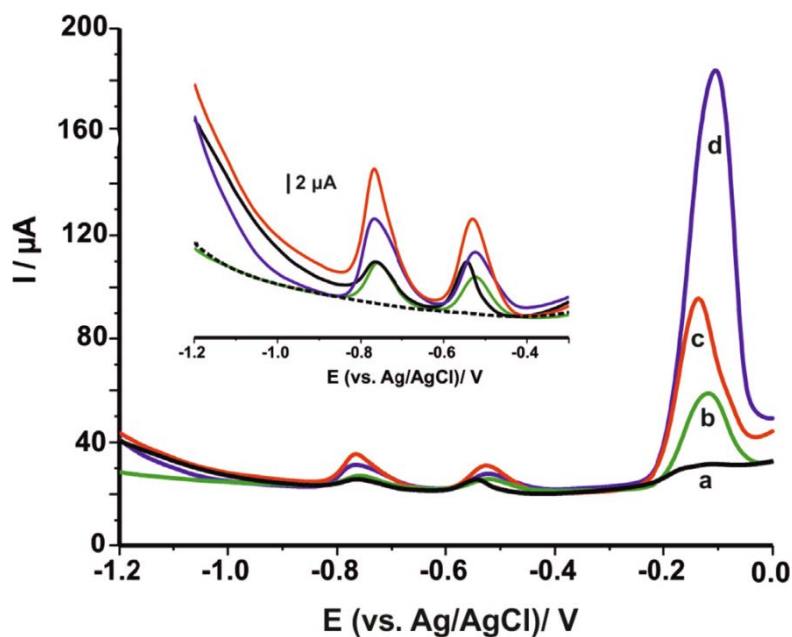


Fig. 37. SW stripping voltammograms of (a) graphene, (b) 1:10, (c) 1:5 and (d) 1:2.5 w/w bismuthene:graphene modified GCEs in 0.1 M acetate buffer, pH 4.5 containing $10 \mu\text{g L}^{-1}$ of each Cd(II) and Pb(II) ions. Deposition potential -1.2 V ; deposition time 120 s. Inset graph illustrates at an enlarged scale the impact of bismuthene content to the magnitude of the stripping currents.

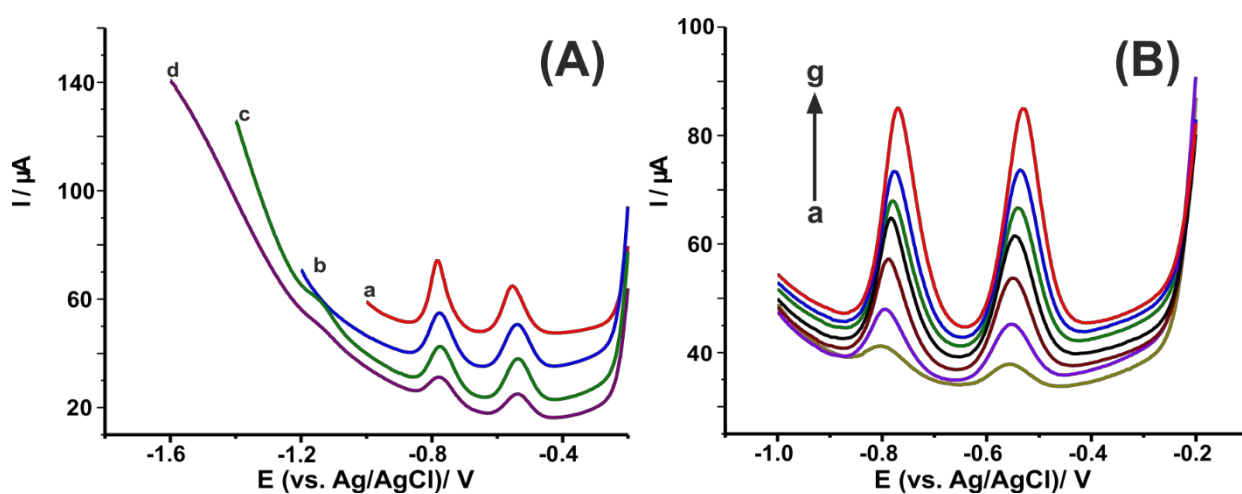


Fig. 38. SW stripping voltammograms of bismuthene:graphene 1:5 w/w modified GCEs in 0.1 M acetate buffer, pH 4.5, containing $20 \mu\text{g L}^{-1}$ Pb(II) and $20 \mu\text{g L}^{-1}$ Cd(II) at A) different deposition potentials (a) -1.0 , (b) -1.2 , (c) -1.4 , (d) -1.6 V and preconcentration time 120 s and B) different deposition times (a) 30, (b) 60, (c) 90, (d) 120, (e) 150, (f) 180, (g) 240 s and deposition potential -1.0 V .

4.3.3 Analytical performance

Under the selected values of the experimental conditions, a series of single SW stripping voltammograms with 2D-Bi/Gra/GCEs in the presence of mixtures containing

1.0 – 30.0 $\mu\text{g L}^{-1}$ of each metal ion were conducted (**Fig. 39**). By applying the least-squares method, a linear relationship was obtained between the magnitude of the current of the stripping peaks and the concentration of each metal ion in the range from 1.0 to 30.0 $\mu\text{g L}^{-1}$. Data fitted equations $I/\mu\text{A} = -0.51 + 3.12 [\text{Cd}/\mu\text{g L}^{-1}]$ ($R^2 = 0.9951$) and $I/\mu\text{A} = -0.83 + 1.91 [\text{Pb}/\mu\text{g L}^{-1}]$ ($R^2 = 0.9989$). Based on a signal-to-noise ratio of 3 (S/N 3), the limit of detection (LOD) for each target was found to be 0.3 $\mu\text{g L}^{-1}$. Based on these results, 2D-Bi/Gra/GCEs outperform the great majority of electrodes based on other bismuth precursors [225–234], while exhibit comparable detection capabilities with the electrodes based on exfoliated bismuth telluride and graphene composite [29], sparked generated bismuth nanoparticles [235] and multi-walled carbon nanotube/poly (pyrocatechol violet)/ bismuth film [236] (**Table 6**).

Table 6. An overview of various bismuth-modified electrodes for the determination of lead and cadmium.

Electrode	linear range, $\mu\text{g L}^{-1}$		LOD, $\mu\text{g L}^{-1}$		ref
	Pb	Cd	Pb	Cd	
GO/ <i>ex</i> -Bi ₂ Te ₃ -modified GCEs	0.5 - 20	1 - 20	0.1	0.2	[29]
BiF ₄ -CPE	20 - 100	20 - 100	1.2	9.8	[225]
Bi-xerogel/GCEs	2 - 17	0.5 - 9	1.3	0.37	[226]
Bi-SG screen printed electrode	2 - 32	3 - 14	1.2	1.4	[227]
BiPO ₄ graphite SPE	10 - 80	10 - 80	4	4.5	[228]
Planar Bi-SPE	25 - 400	25 - 400	8	9.3	[229]
Bi-Gra epoxy	20 - 70	10 - 90	19.1	35.8	[230]
Bismuth aluminate SPE	5 - 40	10 - 80	1.1	1.5	[231]
Bismuth citrate SPE	5 - 40	10 - 80	0.9	1.1	[231]
Bismuth zirconate SPE	5 - 40	10 - 80	1.4	3.2	[231]
Bi ₂ O ₃ SPE	5 - 40	10 - 80	1.0	2.0	[231]
Bi ₂ O ₃ -SPE	20 - 100	20 - 100	2.3	1.5	[232]
Bi ₂ O ₃ -SPE	20 - 300	20 - 300	8	16	[233]
BiOCl-MWCNT/GCE	5 - 50	5 - 50	0.57	1.2	[234]
Sparked Bi graphite SPE	0.5 - 12	0.5 - 12	0.2	0.2	[235]
Bi-poly(PCV)-MWCNT/GCE	1 - 200	1 - 300	0.4	0.2	[236]
2D bismuthene-graphene/GCE	1-30	1-30	0.3	0.3	<i>This work</i>

Abbreviations: BiF₄-CPE, carbon paste electrode modified with ammonium tetrafluorobismuthate; SPE, screen-printed electrode; Bi-SG, sol gel microspheres. Bi-Gra epoxy, graphite-epoxy composite electrode modified with Bi(NO₃)₃; GO/*ex*-Bi₂Te₃, graphene oxide/exfoliated bismuth telluride; BiOCl-MWCNT/CPE, bismuth oxychloride-multiwalled carbon nanotube modified glassy carbon electrode (GCE); Bi-poly(PCV)-MWCNT/GCE, GCE modified with multi-walled carbon nanotube/poly(pyrocatechol violet)/bismuth film.

The repeatability of 2D-Bi/Gra/GCEs in the presence of a mixture containing $10.0 \mu\text{g L}^{-1}$ for each target for fifteen successive measurements was 6.8% for Cd, and 3.4% for Pb, while the reproducibility among different electrodes was found to be $<1.4\%$ for Cd and $<3.3\%$ for Pb ($10.0 \mu\text{g L}^{-1}$ for each target, $n = 10$). Remarkably, 2D-Bi/ Gra/GCEs showed an excellent working stability allowing more than 40 measurements while keeping almost 95% of their original signal and thus a complete analysis (or a recovery study) including duplicate measurements of the sample and the standard additions, were conducted with a single electrode. Also when not in use, 2DBi/ Gra/GCEs were stored in a dust protective box and after three months they retained almost 95% of their original sensitivity.

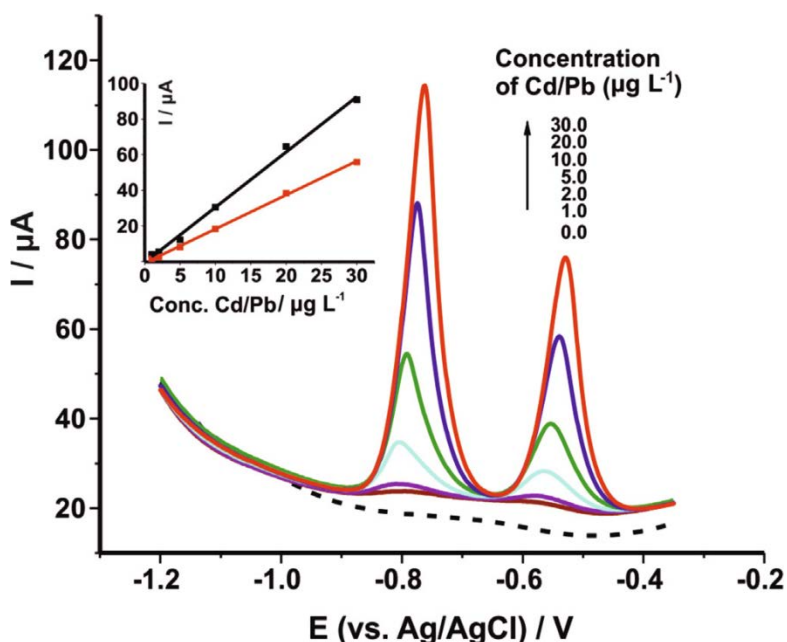


Fig. 39. SW stripping voltammograms of bismuthene:graphene 1:5 (w/w) modified GCEs in 0.1 M acetate buffer, pH 4.5, containing varying concentrations of 1,2,5,10,20 and $30 \mu\text{g L}^{-1}$ of each Pb(II) and Cd(II). Deposition potential, -1.2 V ; deposition time, 180 s. Inset graph depicts the corresponding calibration plots.

The modified electrodes were also applied to the simultaneous determination of lead and cadmium in two drinking water samples using the standard addition method. Based on the height of the stripping peaks obtained for each target before and after three additions of standard solutions of Pb(II) and Cd(II) (final concentration $3.0 \mu\text{g L}^{-1}$ each), the concentration of the targets were determined (**Table 7**). SW voltammograms for the determination and recovery of the targets in one of the analyzed samples are

illustrated in **Fig. 40**. The results were also compared with those obtained by a reference electrochemical method (V-086, Metrohm), and the relative errors were $<7\%$. Moreover, recovery studies were conducted after spiking the samples with $2.0 \mu\text{g L}^{-1}$ of each target ion. Recoveries were ranged from 98% to 99.1%.

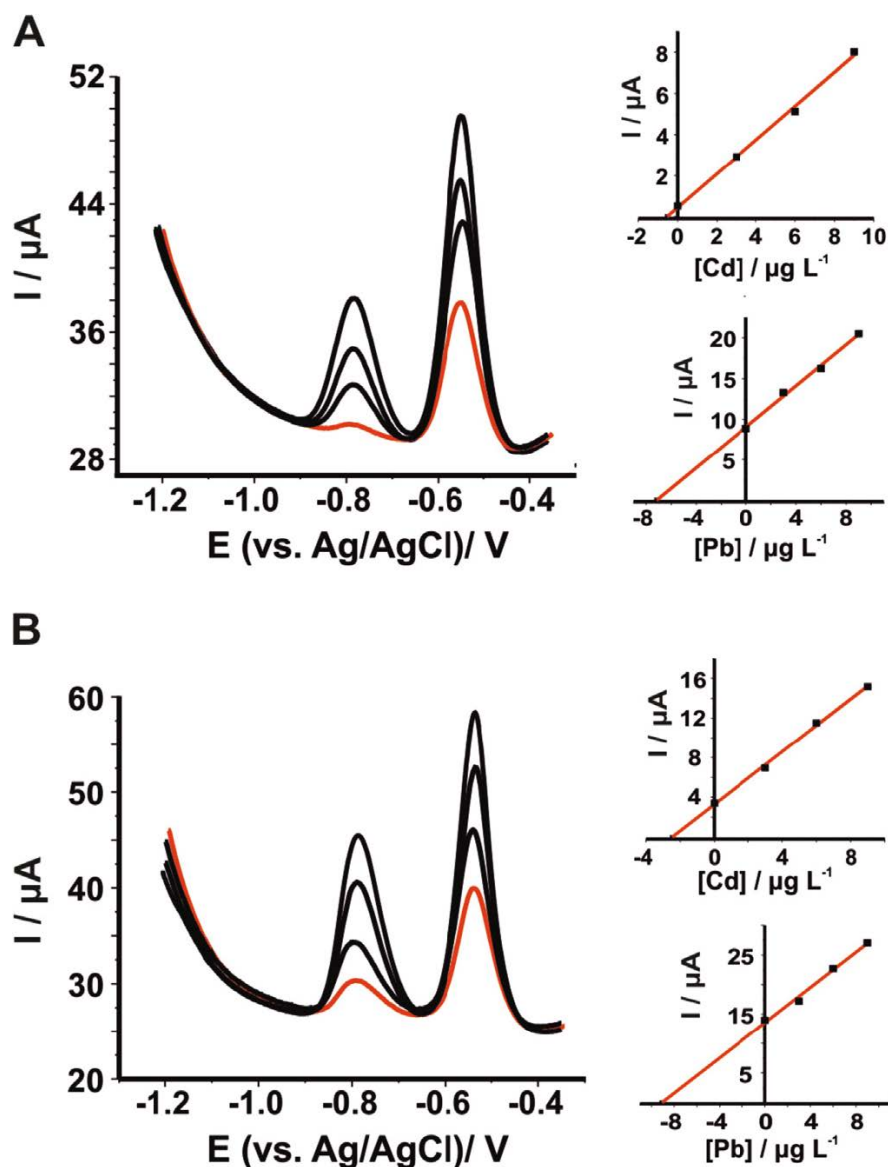


Fig. 40. SW voltammograms for the (A) determination and (B) recovery of Cd(II) and Pb(II) in a tap water sample (red line) before and after its fortification with $2.0 \mu\text{g L}^{-1}$ Cd(II) and $2.0 \mu\text{g L}^{-1}$ Pb(II), respectively by using the standard addition method (black lines, three additions of $3.0 \mu\text{g L}^{-1}$). The respective plots are illustrated at the right panel. Deposition potential, -1.2 V ; deposition time, 180s.

Table 7. Determination and recovery of Cd and Pb in drinking water samples. Values show the mean value \pm standard deviation of three measurements.

Sample (analyte)	amount added, $\mu\text{g L}^{-1}$	amount determined, $\mu\text{g L}^{-1}$	recovery, %	reference method, $\mu\text{g L}^{-1}$	relative error, %
tap water #1 (Cd)	0	0.59 \pm 0.03		0.61	-3.3
	2.0	2.56 \pm 0.15	98.8 \pm 1.3		
tap water #1 (Pb)	0	8.02 \pm 0.46		8.61	-6.8
	2.0	9.82 \pm 0.52	98.0 \pm 1.3		
tap water #2 (Cd)	0	n.d		n.d	-
	2.0	1.95 \pm 0.02	97.5 \pm 1.2		
tap water #2 (Pb)	0	2.52 \pm 0.14		2.42	4.1
	2.0	4.60 \pm 0.05	99.1 \pm 2.5		

5

Electrochemical performance of passivated antimonene nanosheets and of *in-situ* prepared antimonene oxide-PEDOT:PSS modified screen-printed graphite electrodes

5.1 Abstract

Herein, we present the production of antimonene nanosheets and the *in-situ* preparation of antimonene oxide/PEDOT:PSS nanocomposite via tip sonication of bulk β -phase antimony in water and aqueous PEDOT:PSS, respectively. Nanomaterials were characterized via SEM, EDX, XRD, FT-IR previously depicted in 3.5.2., electrochemical impedance spectroscopy and cyclic voltammetry, while the resulting modified graphite screen-printed electrodes (Sbene/SPE and Sbene oxide/PEDOT:PSS/SPE, respectively) were evaluated in the cathodic determination of 4-nitrotoluene (4-NT), which was used as a model compound, in the presence of dissolved oxygen and in deoxygenated environments. Data document the electrochemical passivation of Sbene/SPE, which, on the one hand, demonstrate a beneficial poor activity towards the oxygen reduction reaction, and on the other hand, enhanced detection capabilities, thus allowing the determination of 4-NT at the micromolar concentration level at non-deoxygenated solutions. As a result, passivated Sbene/SPE show great promise in sensing applications outside of the laboratory where the deoxygenation of the samples is a big obstacle. Moreover, data demonstrate enhanced detection capabilities for Nafion membrane protected Sbene oxide/PEDOT:PSS/SPE, in deoxygenated solutions, which exhibit a detection range from 50 to 5000 nM 4-NT, while achieving an LOD of 16.7 nM (S/N 3). Nafion

membrane is essential for the reusability of the electrodes. Sbene oxide/PEDOT:PSS/SPE was also used to the analysis of a spiked river water sample. Recovery was 97.9%.

5.2 Introduction

Despite the long history of antimony in electroanalytical applications, which is dated back to 1923 with the use of the antimony-antimony oxide bulk electrode as an indicator electrode in acid/base titrations [237, 238], its use in electroanalysis is very limited reaching a peak with the introduction of the antimony film electrode (SbFE) [239, 240], as a “green” alternative of toxic mercury, for the anodic stripping determination of trace heavy metal ions [239, 240]. However, SbFE or other antimony-based electrodes [241, 242] did not succeed to establish antimony as a competitive electrode material in electrocatalysis, since their use in the determination of other compounds, especially organic compounds with interest in clinical or environmental analysis was not analogous, while their poor detection capabilities in the few related works relegate them to an inferior competitive position compared with other electrodes [243–245]. Since the emergence of graphene, a new class of low dimensional materials, the inorganic layered materials (ILMs), has experienced increasing attention due to the fascinating properties of their two-dimensional (2D) nanosheets compared with that of the bulk counterparts [1, 9]. Antimony is a metalloid belonging in the Group XV elements, also known as “pnictogens”, along with bismuth, phosphorus, arsenic and nitrogen, most of which (with the exception of nitrogen) possess a rhombohedral crystal lattice which can be exfoliated into two-dimensional analogues adopting the suffix -ene, as per the graphite-graphene paradigm [15]. Few-layer antimonene (Sbene) produced via liquid phase [105, 199, 200, 246–250] and electrochemical [120, 251, 252] exfoliation has been utilized in a great deal of electrochemical applications [104, 120, 199, 247–249, 253]. Nonetheless, the exploration of Sbene in electroanalysis is very limited [105, 167], possibly due to its inherent semiconducting nature, which contradicts the direct electron transfer requirement of electrochemical sensors. Herein, we report for the first time on the preparation of Sbene and Sbene oxide nanosheet-based electrocatalytic surfaces and the assessment of their electroanalytic properties. Data demonstrate the preparation of a few-layer Sbene nanosheets with a minimum oxidation degree, which were used to

study the electrochemical passivation of their surface in neutral phosphate buffered solutions. For this purpose, Sbene nanosheets were produced through tip sonication of bulk β -phase antimony in double distilled water (DDW), while the resulting electrochemically passivated surfaces were assessed for the cathodic voltammetric determination of nitroaromatic compounds in non-deoxygenated solutions. This research also entails the *in-situ* sonochemical preparation of Sbene oxide nanosheets in poly(3,4-ethylenedioxythiophene): polystyrene sulfonate (PEDOT:PSS), which acts both as a stabilizer and as an ameliorating medium regarding charge transfer between Sbene layers and with the electrode surface, introducing a heterostructure with advanced electroanalytic properties. Data also demonstrate the implementation of Sbene oxide/PEDOT: PSS-modified graphite screen-printed electrodes (SPEs) to the determination of 4-nitrotoluene (4-NT), which was used as a model compound, in environmental samples.

5.3 Results & discussion

5.3.1 Electrochemical passivation of Sbene nanosheets

The electrochemical behavior of bulk β -phase antimony and Sbene modified SPEs was studied by cyclic voltammetry measurements in both non-deoxygenated and deoxygenated phosphate buffered neutral solutions. Bulk β -Sb/SPE in non-deoxygenated solution demonstrates a CV pattern (**Fig. 41A**, green line), which includes two cathodic peaks at ca. -0.85 V attributed to oxygen reduction, and at ca. -1.20 V attributed to the electroreduction of the passivating Sb_xO_y layer formed during the anodic scan at ca. -0.2 V similar with previous studies [254, 255]. Indeed, in the deoxygenated solution (**Fig. 41A**, black line), bulk β -Sb/SPE possesses only the peaks attributed to the electro formation/reduction of the Sb_xO_y layer, while the peak of oxygen reduction reaction is absent, as expected. On the contrary, the CVs of Sbene/SPE in deoxygenated solution (**Fig. 41A**, blue line; 16 scans) show no peaks during the cathodic scan of the potential and only a single peak during the anodic scan at ca. -0.18 V, the magnitude of which is constant for successive 16 scans. Considering the absence of dissolve oxygen in these experiments, we hypothesize that the peak at ca. -0.18 V is associated with the traces of Sbene oxide inevitably formed during the

exfoliation process, as documented by the presence of Sbene oxide (222) and (400) diffractions in the XRD pattern of Sbene (Fig. 1). In addition, data demonstrate that under the specific experimental conditions, that is, in the absence of dissolved oxygen and within the applied potential window, neither the growth of Sbene oxide nor its electro-reduction are favored.

On the other hand, in the presence of dissolved oxygen, Sbene/SPE (**Fig. 41B**, red line) exhibits a very sharp cathodic peak at ca. -1.0 V, coupled with a very intense peak at ca. -0.17 V that appears during the anodic scan of the potential. The CVs of bulk β -Sb/SPE (green line) and plain SPE (black line) (**Fig. 41B**) are presented for comparison. As it can be seen, the magnitude of the peaks at Sbene/SPE is considerable higher compared with that at the bulk β -Sb/SPE, while the sharp cathodic peak of Sbene/SPE at ca. -1.0 V is located between the oxygen reduction peak at both bulk β -Sb/SPE and plain SPE, and the electro-reduction of Sb_xO_y at bulk β -Sb/SPE.

We believe that the pair of these intensive peaks at Sbene/SPE is attributed to the oxygenation of Sbene nanosheets and the formation of Sbene oxide, in which oxygen atoms are coordinated to the Sb atoms of Sbene, through $\text{Sb}=\text{O}$ dative bonds, which in accordance with previous studies are formed at the surface of the exfoliated Sbene nanosheets [200, 205], and lead to a drastic alteration of its electronic properties [205]. Interestingly, Sbene oxides containing different concentrations of oxygen, transit from the indirect band gap of pristine Sbene to Sbene oxides exhibit tunable direct bandgaps with respect to the degree of the oxygenation process. It has been predicted, that the oxygenation process drastically lowers the band gap of Sbene and moreover, dramatically increases carrier mobility [205]. This fact explains the augmentation of the magnitude of both anodic and cathodic peaks at Sbene/SPE, since at the eventually formed Sbene oxide, the electrical communication between the nanosheets and with the electrode surface is more efficient. In line with the above discussion, CVs in **Fig. 41C** demonstrates that increased concentrations of Sbene on the electrode surface result in an increased magnitude of both peaks. Moreover, the kinetics of the oxygenation process is dependent on Sbene's concentration on the electrode surface. At Sbene/SPE modified with a 5 mg mL^{-1} Sbene suspension, the oxygenation process occurs very fast (after the second scan, CVs are almost identical), while at electrodes modified with a lower concentration of Sbene (1 mg mL^{-1}), the process proceeds gradually with each scan as shown in **Fig. 41D**, where during 20 scans, the magnitude of the oxygen reduction peak is gradually diminished giving rise to Sbene oxide related peaks.

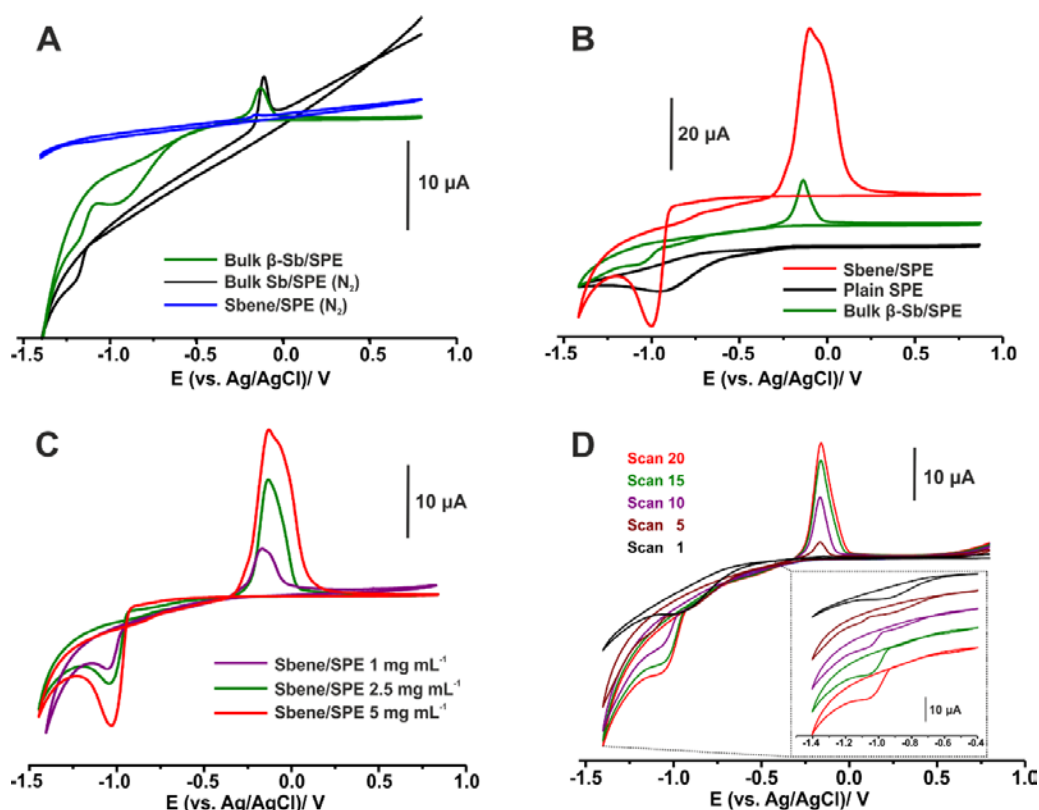


Fig. 41. (A) CVs of (green line) bulk β -Sb/SPE in non-deoxygenated 0.1 M PBS pH 7, (black line) bulk β -Sb/SPE and (blue line; a set of 16 scans) Sbene/SPE in deoxygenated 0.1 M PBS pH 7. (B) Comparative CVs (10th scan) of (black line) plain SPE, (green line) (5 mg mL⁻¹) bulk Sb/SPE and (red line) (5 mg mL⁻¹) Sbene/SPE in non-deoxygenated 0.1 M PBS pH 7. (C) Comparative CVs (10th scan) of Sbene/SPE modified with (purple line) 1, (green line) 2.5 and (red line) 5 mg mL⁻¹ Sbene aqueous suspension in non-deoxygenated 0.1 M PBS pH 7. (D) 1st, 5th, 10th, 15th, and 20th CV scan of (1 mg mL⁻¹) Sbene/SPEs in non-deoxygenated 0.1 M PBS pH 7. Inset graph shows the close view of the CVs at the potential range marked with the dashed lines, while for reasons of clarity, CVs are shifted along the y-axis. All CVs were recorded at a scan rate 0.05 V s⁻¹.

A detailed assessment of the oxygenation kinetics was conducted with EIS studies. **Fig. 42** shows the Nyquist plots of the 5 mg mL⁻¹ Sbene/SPE before and after the 1st, 10th and 20th CV scan. It is apparent that before the passivation process the electrode exhibits a very large charge transfer resistance ($R_{ct} = 992$ K Ω m) due to the semi-conducting nature of pristine Sbene (**Table 8**). Upon passivation R_{ct} drops to 82–89 K Ω m, even from the very first CV scan, which is correlated with the above mentioned alteration of Sbene's electronic properties during the passivation process. On the other hand, passivation-associated increase of the double layer capacitance (C_{dl}) shows slower kinetics as revealed by the data in **Table 8**.

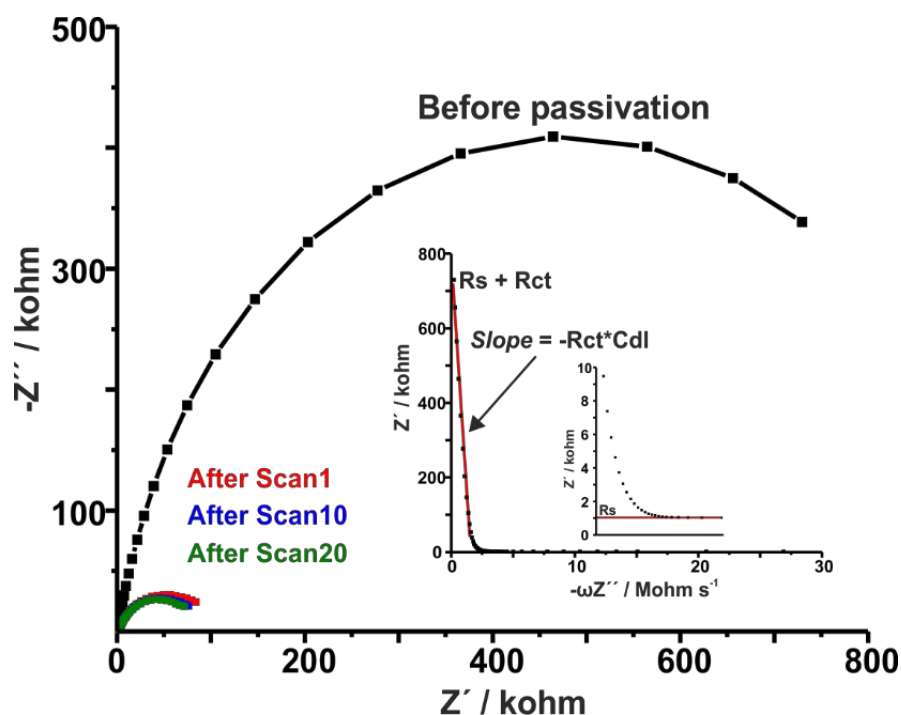


Fig. 42. Nyquist plots of (5 mg mL⁻¹) Sbene/SPE (black line) before and after the (red line) 1st, (blue line) 10th and (green line) 20th CV scan from 0.8 V to -1.4 V in 0.1 M PBS, pH 7 at 50 mV/s. Inset depicts the corresponding $Z' = f(-\omega Z'')$ plot of the Sbene/SPE before passivation as an example of the graphical approximation of the charge transfer resistance (R_{ct}) and subsequent calculation of the double layer capacitance (C_{dl}), as $\text{Slope} = -R_{ct} \times C_{dl}$, according to the method presented in Ref. [256]. Impedance measurements were taken over the frequency range 10⁵-0.1 Hz using an excitation amplitude of 10 mV superimposed on a DC potential of -0.400 V in 0.1 M PBS, pH 7.

Table 8. Charge transfer resistance (R_{ct}) and double layer capacitance (C_{dl}) values of (5 mg mL⁻¹) Sbene/SPEs before and after the 1st, 10th and 20th CV scan from 0.8 V to -1.4 V in 0.1 M PBS, pH 7 at 50 mV/s.

	R_{ctA} (KOhm)	Y_0 (s ⁿ Ohm ⁻¹) $\times 10^{-5}$	n	$\omega(Z'_{max})$ (s ⁻¹)	C_{dl1} (μF)	C_{dl2} (μF)	R_{ctB} (KOhm)	slope	C_{dl3} (μF)
Before passivation	992	0.0755	0.8763	1.464	0.720	0.725	750	0.5682	0.758
After 1 CV scan	81.8	0.1892	0.7862	10.54	1.148	1.139	76	0.0928	1.221
After 10 CV scans	89.0	0.4610	0.7216	3.412	3.276	3.269	76	0.2262	3.011
After 20 CV scans	85.8	0.5285	0.7175	3.412	3.737	3.871	71	0.2364	3.324

Y_0 , R_{ctA} and n values were calculated from the fitted impedance results with respect to a Randles' electric equivalent circuit and were used to calculate the double layer capacitance by using the equation (11) (C_{dl} as previously expressed in 2.5.3.) and equation (12) (C_{dl2}). $\omega_{(Z''_{max})}$ were found by using the routine «find min/max» in the FRA software, v.4.9 (Metrohm Autolab), as $\omega_{max}''=2\pi f_{(Z''_{max})}$.

$$Cdl = \frac{(Y_0 \times R_{ctA})^{\frac{1}{n}}}{R_{ctA}} \quad (11),$$

$$Cdl = Y_0 \times \omega_{(Z''_{max})}^{n-1} \quad (12), [257]$$

The double layer capacitance was also approximated (C_{dl3}) via a graphical method from the slope of the linear part of the plot $Z'' = f(-\omega Z')$, as per equation (13):

$$slope = -R_{ctB} \times Cdl, \quad (13), [256]$$

The determination of R_{ctB} , R_s is depicted in the inset graph in **Fig. 42**.

5.3.2 Implementation of Sbene/SPE in cathodic voltammetry

Data demonstrate that electrochemically passivated Sbene/SPE provides a wide cathodic potential window that can be utilized for the assay of various reducible compounds, the electrochemical detection of which is severely affected by the dissolved oxygen of the electrolyte. Since passivated Sbene/SPE does not exhibit the large cathodic peak attributed to the reduction of dissolved oxygen (**Fig. 41C**), it is expected to allow measurements to be conducted in non-deoxygenated solutions. Considering the practical difficulties associated with the deoxygenation of samples outside the laboratory, especially at drop-volume assays at biological samples, the potential utility of passivated Sbene/SPEs in the development of sensor for decentralized analysis applications was explored by conducting proof-of-concept comparative voltammetric measurements at standard solutions containing increasing concentrations of 1, 2 and 4 μ M 4-nitrotoluene (4-NT) in 0.1 M PBS pH 7 with plain and Sbene/SPEs.

As shown in **Fig. 43** signals derived from plain SPEs are severely hampered by the oxygen reduction peak at ca. -0.9 V, thus rendering quantification of 4-NT extremely

difficult. On the other hand, at passivated Sbene/SPEs the oxygen reduction peak is completely diminished due to the passivation process, thus allowing to receive reliable analytical signals in the presence of 4-NT at concentrations as low as 1 μM . Moreover, passivated Sbene/SPE show an electrocatalytic activity toward 4-NT, as documented by the shift of the reduction peak about 50 mV, compared with the corresponding reduction peak at the plain SPE.

The response of passivated Sbene/SPEs towards the oxygen reduction reaction is also dependent on electrochemical parameters under which the oxygenation process is occurred. DPVs illustrated in **Fig. 43, inset graph** show three successive scans, in pure electrolyte, starting from different anodic potentials, before (at 0.0 V) and at sufficient more anodic values (at 0.8 V) with respect to the oxygenation peak of Sbene. As can be seen, in the latter case, Sbene/SPE reaches a stable background signal within 1-2 scans while, in the former case, the stability of the background signal is very poor and after only 3 scans reverts to the background signal of the plain SPE (**Fig.43**). This behavior is probably associated with the extend of the passivation process at Sbene/SPEs under different anodic potentials, in correspondence with the growth of the Sb_xO_y layer in the bulk Sb electrodes at potentials more anodic of the electro-formation potential [254, 255].

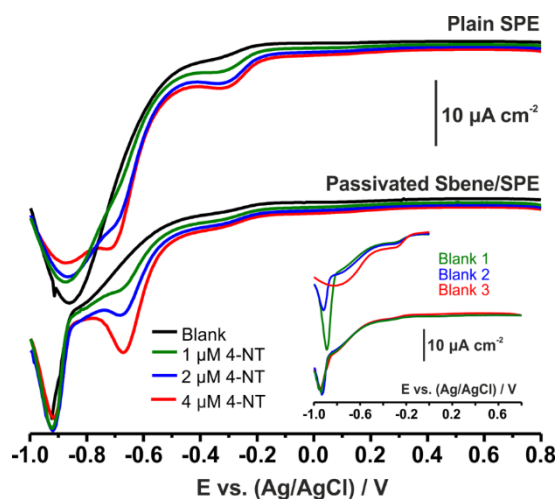


Fig. 43. Cathodic DP voltammetry measurements of (top) plain and (down) passivated Sbene/SPEs modified with 5 mg/mL Sbene in non-deoxygenated 0.1 M PBS pH 7 containing (green line) 1, (blue line) 2, and (red line) 4 μM 4-NT. The background signal for both electrodes is shown with a black line. Inset graph shows the stability of the background signal of Sbene/SPEs in 0.1 M PBS pH 7 upon three successive scans starting at 0.0 and 0.8 V.

Even though the detection capabilities of passivated Sbene/SPEs in non-deoxygenated compare favorably with those of previous works demonstrating detection ranges from 1 μM [258], 20 μM [259], 0.2 μM [260], 0.54 μM [261], 0.2 and 0.5 μM [262], our studies were extended to the investigation of Sbene-based composite nanomaterials aiming to improve the detection capabilities of the resulting sensors. Based on the findings shown in **Chapter 4** a Sbene/graphene nanocomposite was primarily investigated, which in the case of bismuthene had offered enhanced electroanalytical properties compared with that of the pristine exfoliated nanosheets. However, Sbene/graphene nanocomposite gave poor response, even lower than that of the plain SPEs, probably due to different surface tension values of the exfoliated materials a parameter which plays a key role in nanosheet dispersions [39]. Therefore, our attempts were directed to PEDOT:PSS, which in accordance with previous studies has been successfully combined with black phosphorene nanosheets [263], while the doping of Sbene quantum sheets in PEDOT:PSS has been proved to produce highly efficient OLEDs [264]. Our studies were conducted with two different PEDOT:PSS-based nanocomposites. The first was occurred by mixing under stirring, overnight, equal volumes of 2 mg mL^{-1} aqueous dispersions of Sbene and PEDOT:PSS followed by 30 min bath sonication, and the second one, as described in **3.3.2.**, by tip sonication of bulk β -phase antimony and PEDOT in DDW, which based on the XRD and ATR-FTIR data (**Fig. 33** and **Fig. 34** in **3.5.2.**) resulted in the in-situ formation of Sbene oxide/PEDOT:PSS nanocomposite.

Fig. 44 shows a direct comparison between the (black line) plain SPE, (blue line) Sbene/SPE, (green line) Sbene/PEDOT:PSS/SPE and (red line) Sbene oxide/PEDOT:PSS/SPE towards the electro reduction of 4-NT (solid line). Due to the large cathodic background signals of PEDOT:PSS based SPEs, all measurements were conducted in deoxygenated 0.1 M PBS pH 7. The cathodic peak corresponds to the electro reduction of the nitro group of 4-NT to hydroxylamine, according to the equation, $\text{R-NO}_2 + 4\text{e}^- + 4\text{H}^+ \rightarrow \text{R-NHOH} + \text{H}_2\text{O}$, with the Sbene/SPE showing a shifting of ca. +70 mV of the 4-NT reduction peak, compared with that observed at the plain SPE. On the other hand, Sbene/PEDOT:PSS/SPE showed no response besides a background shift, as concluded by the apparent signal changes for concentrations of 1 and 2 μM 4-NT. Finally, the Sbene oxide/PEDOT:PSS/SPE (also at concentrations of 1 and 2 μM 4-NT) showed both enhanced electrocatalytic activity identical to the Sbene/SPE (shifting of ca. 70 mV of the reduction peak compared with the DP

voltammogram of the plain SPE) and an appreciable enhanced sensitivity possibly thanks to better electrochemical communication between the Sbene oxide nanosheets and with the electrode surface mediated by PEDOT:PSS. Data indicate that Sbene oxide/PEDOT:PSS/SPE can offer as a promising electro catalytic sensing platform for the cathodic determination of nitroaromatic compounds, while detailed analytical studies for the determination of 4-NT are given in 5.3.4..

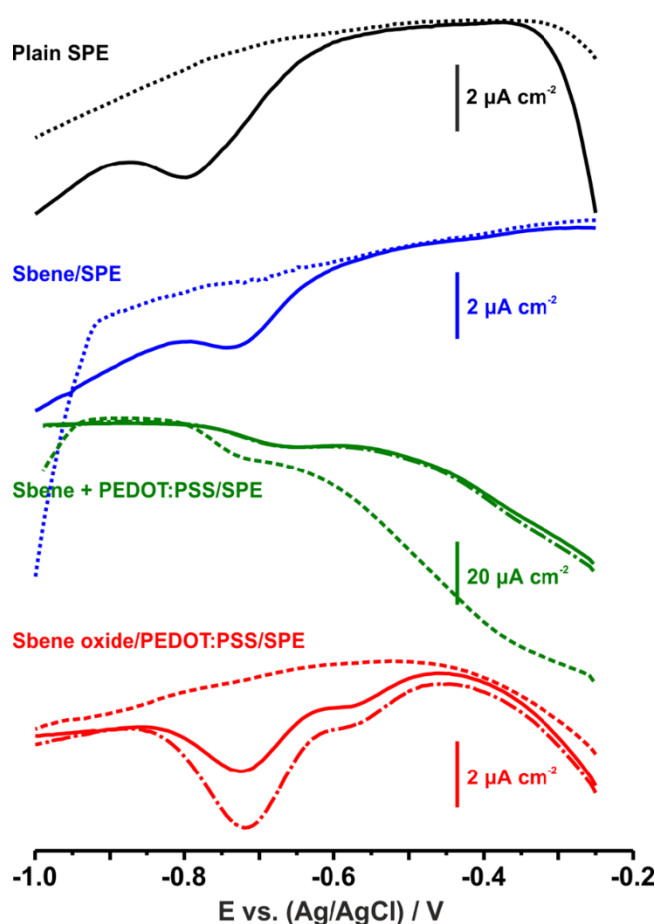


Fig. 44. DP voltammograms of (black line) plain SPE, (blue line) Sbene/SPE, (green line) Sbene/PEDOT:PSS/SPE and (red line) Sbene oxide/PEDOT:PSS/ SPE in deoxygenated 0.1 M PBS pH 7 (dashed line) before and after the addition of (solid lines) 1 and (dash-dotted line) 2 μM 4-NT.

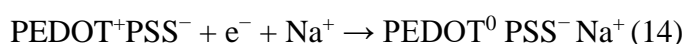
5.3.3 Electrochemical characterization of Sbene oxide/PEDOT:PSS

The cyclic voltammetry behavior of PEDOT:PSS/SPE (black line) and the Sbene oxide/PEDOT:PSS/SPE (red line) in deoxygenated 0.1 M PBS pH, are illustrated in

Fig. 45A. PEDOT:PSS/SPE exhibits a well anticipated pseudocapacitive behavior, derived from the electric double layer formed between the PEDOT⁺ and PSS⁻ grain boundaries, through a hole injection process (doping) which occurs during the anodic scan of the potential as well as an inverse hole extraction process (de-doping) during the cathodic scan. This de-doping process is associated with a decrease of conductivity leading to a dramatic lowering of the capacitive current at negative potentials [265, 266] and to the establishment of very low background signals which are beneficial for cathodic analytical measurements.

The same principle is also followed by the Sbene oxide/PEDOT:PSS/ SPE, proving that the exfoliated nanosheets are well incorporated into the PEDOT:PSS core, generating a substantial increase in pseudocapacitive current possibly due to Sbene oxide, which has been produced during the tip sonication process. It is thus reasonable to assume that the increase in pseudocapacitance produced in this case is a result of the Sbene oxide related redox peaks at ca. -1.1 and -0.16 V (**Figs. 41C and 45A**), similarly to the interpretation expressed by Feldberg [267] regarding redox switching conducting polymers.

The impedimetric behavior of the PEDOT:PSS/SPE and Sbene oxide/PEDOT:PSS/SPE in the presence of SiW₁₂ is illustrated, in the form of Nyquist plots, in **Fig. 45B**. PEDOT:PSS/SPE (**Fig. 45B**, black line) exhibits an almost ideal pseudocapacitor behavior in accordance with previous studies [202, 268], which can be sufficiently explained by considering PEDOT:PSS as a two-phase system, namely a hole conducting PEDOT rich phase and an ion conducting PSS rich phase [265]. The modeled electric circuit (**Fig. 45B**, inset graph) consists of two Randles' circuits in series, interjected by a constant phase element (CPE_{dl}), which represents the electric double layer formed between the PEDOT rich phase (first Randles' circuit) and the PSS rich phase (second Randles' circuit), and finally a Warburg impedance in series with the previous circuits which represents the diffusion of Na⁺ and K⁺ ions from the electrolyte that counterbalance the polymer according to the dedoping process, as per equation (14):



As for the Sbene oxide/PEDOT:PSS/SPE, its behavior can be considered very similar to pristine PEDOT:PSS, with the characteristic (almost parallel to y-axis)

pseudocapacitive pattern exhibiting a greater curvature attributed to an enhanced electron transfer process due to the electrocatalytic properties of Sbene oxide towards the redox probe. This behavior alters the modeling to a Warburg impedance element being integrated to the second time constant of the equivalent electric circuit and not in series with it.

Additionally, it is worth pointing out that since the majority of the components of the modelled electric circuits at the pristine and the Sbene oxide containing PEDOT:PSS remain similar, it can be implied, that there are distinct PEDOT:PSS and Sbene oxide phases within the composite, which coincides with the morphological characterization of Sbene oxide/PEDOT:PSS illustrated, along with that of Sbene, as previously shown **Fig. 32 (3.5.2.)**.

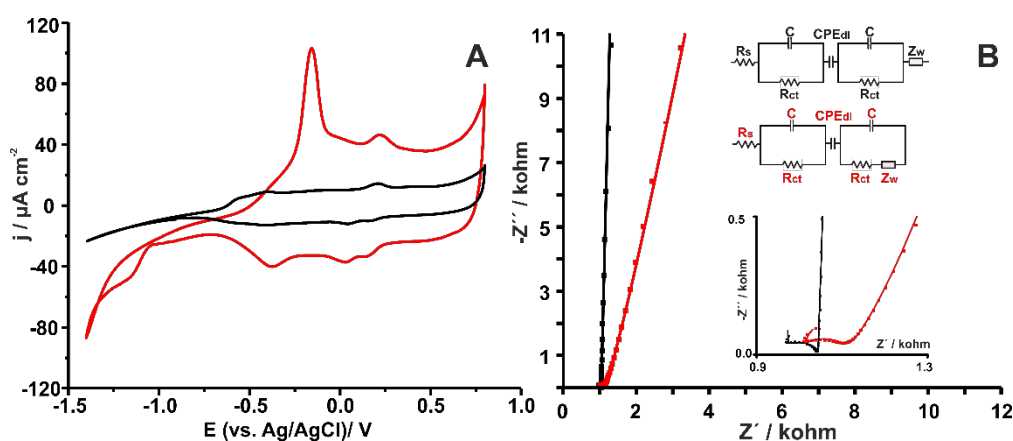


Fig. 45. (A) CVs of (black line) PEDOT:PSS/SPE and (red line) Sbene oxide/PEDOT:PSS/SPE in deoxygenated 0.1 M PBS pH 7 at a scan rate 0.05 V s^{-1} . (B) Nyquist plots of (black line) PEDOT:PSS/SPE and (red line) Sbene oxide/PEDOT:PSS/SPE with (inset graphs, upper panel) their respective equivalent electric circuits with components written with the respective color. Inset graph at the bottom panel shows the close view of the plot at high frequencies. Experimental conditions: 0.1 M PBS pH 7, containing 5 mM SiW_{12} ; Polarization voltage, -0.3 V .

5.3.4 Analytical performance and utility to real samples analysis

4-NT was chosen as a model nitroaromatic compound as it is a commonly used chemical in the manufacturing of various dyes and agricultural chemicals, explosives, and synthetic fibers, thus resulting in aquatic environments contamination. 4-NT has been classified as a toxic pollutant, while in order to protect aquatic life a limit value in

surface waters has been set at 70 ppb [269]. The response of Sbene oxide/PEDOT:PSS/SPE towards other nitroaromatic compounds, such as 2-NT, 2,4-DNT and 2,4,6-TNP was examined (**Fig. 46**). 2-NT and 2,4-DNT reduction peaks do not impede the determination of 4-NT, as they are emerging adversarial of the 4-NT peak at ca. -0.72 V. Interestingly, 2,4,6-TNP, a common reducible nitroaromatic compound, gave no sizeable response indicating that its presence does not interfere the determination of 4-NT.

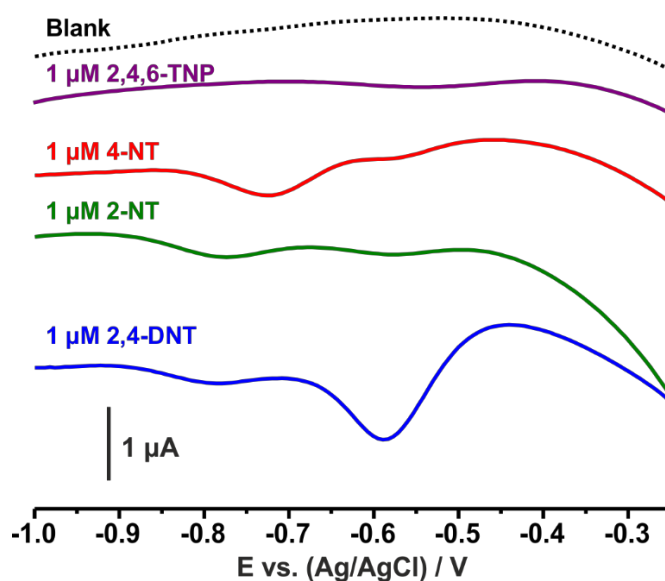


Fig. 46. Cathodic DP voltammetry measurements of the Sbene oxide/PEDOT:PSS/SPE in deoxygenated 0.1 M PBS pH 7 containing 1 μ M (purple line) 2,4,6-trinitrophenol (2,4,6-TNP), (green line) 2-nitrotoluene (2-NT) and (blue line) 2,4-dinitrotoluene (2,4-DNT).

Using the Sbene oxide/PEDOT:PSS/SPE and 4-NT standard solutions in 0.1 M PBS pH 7, a calibration plot, linear over the concentration range from 50 to 5000 nM 4-NT, with a determination coefficient $R^2 = 0.9979$, fitting the equation $I(\mu\text{A}) = 0.0056 + 0.0004 [4\text{-NT}(\text{nM})]$, was constructed (**Fig. 47A**), while the limit of detection (LOD) based on a signal-to-noise ratio of 3 (S/N 3) was found to be 16.7 nM.

The repeatability of the method was calculated 3.7% ($n=5$, 1000 nM 4-NT), while interelectrode reproducibility was assessed by comparing the response of five different Sbene oxide/PEDOT:PSS/SPEs to a 1000 nM 4-NT standard solution and was found to be 5.2%. Sbene oxide/PEDOT:PSS/SPEs also exhibited a very good working stability by retaining >95% of their original activity after 15 successive measurements.

The analytical figure of merits of our work compares favorably with those of previous methods on the electrochemical determination of 4-NT, which exhibit considerably lower detection capabilities and detection ranges from 1 μM [258], 20 μM [259], 0.2 μM [260], 0.54 μM [261], 0.2 and 0.5 μM [262].

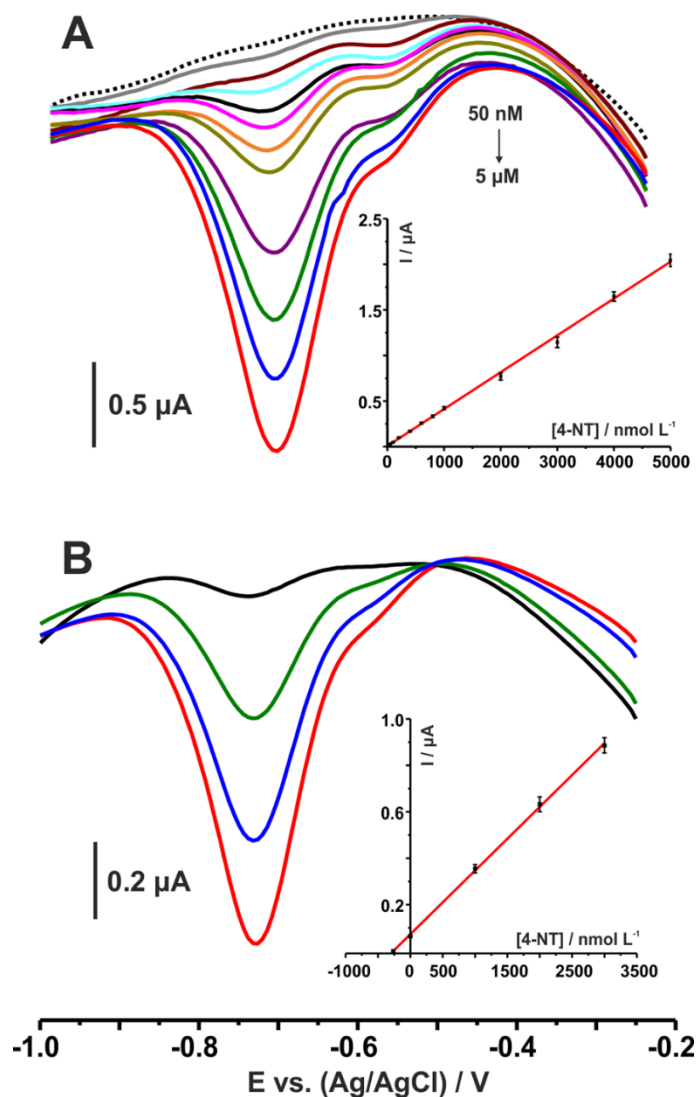


Fig. 47. (A) DP voltammograms of Sbene oxide/PEDOT:PSS/SPEs in deoxygenated 0.1 M PBS pH 7 containing varying concentrations of 50, 100, 200, 400, 600, 800, 1000, 2000, 3000, 4000 and 5000 nM 4-NT and (inset graph) the corresponding calibration plot. (B) DP voltammograms for the recovery of 4-NT in a river water sample (black line) fortified with 300 nM 4-NT by using the standard addition method (three additions of 1000 nM) in deoxygenated 0.1 M PBS pH 7. The corresponding plot is included as an inset. Error bars represent the standard deviation of three measurements.

Sbene oxide/PEDOT:PSS/SPEs were also employed for the determination of 4-NT in a river water sample from the region of Epirus by applying the standard addition method. Before the measurements the sample passed through a 0.45 μm Millipore filter in order to remove suspended particles. The original concentration of 4-NT was either nil or lower than the LOD of the method and thus the applicability of the method was evaluated by measuring the recovery at a sample spiked with 300 nM 4-NT. Spiking was conducted at the undiluted sample while the spiked concentration was chosen in line with the threshold value of 70 ppb 4-NT (510 nM) at surface water [269].

Based on the DP voltammograms and the respective standard addition plot shown in **Fig. 47B** and the inset graph, the recovery was 97.9%, thus demonstrating the ability of Sbene oxide/PEDOT:PSS/SPEs to be used for the fast screening of environmental samples.

Large surface vanadium pentoxide nanosheet modified screen-printed electrode for nanomolar diclofenac determination

6.1 Abstract

This work reports on the utilization of vanadium pentoxide nanosheet (V_2O_5 NS)-modified screen-printed electrodes (SPEs) for the nanomolar voltammetric determination of diclofenac (DCF). V_2O_5 NSs were produced with a facile bath sonication method in a blend of 75/25% v/v H_2O /isopropyl alcohol. The morphological, structural, and electrochemical characteristics of exfoliated V_2O_5 NSs were evaluated via SEM, XRD, FT-IR, as previously shown in **3.5.3.**, cyclic voltammetry (CV) and electrochemical impedance spectroscopy (EIS). V_2O_5 NSs showed a 2D low dimensional morphology with most layers having dimensions of a few micrometers. Diagnostic CV studies using 5-hydroxydiclofenac or 2-(2-hydroxyphenyl) acetic acid, which have been proposed in literature to be involved in the electro oxidation of DCF, suggested that the actual mechanism is more complicated and need to be further elucidated. CV and EIS data demonstrated that at $pH > 6$ V_2O_5 NSs deprived of their characteristic pseudocapacitive properties offering low background signals and enhanced electrocatalytic properties toward DCF. Among different preconcentration treatments examined, a short (192 s) cyclic potentiodynamic treatment was found to exhibit a stable, semi reversible pair of peaks of increased magnitude with successive cycles, and low background signal. The quantification of DCF was conducted using differential pulse voltammetry. A well-defined oxidation peak at ca. 380 mV at pH 7

vs. Ag/AgCl/3 M KCl was recorded and its height was found to be linearly correlated with the concentration of DCF over the range 20-200 nM, while a limit of detection ($3S_x/\text{slope}$) of 3.1 nM was achieved. The response of V₂O₅ NS/SPE was evaluated against common interfering compounds, while the accuracy of the method was evaluated in spiked tap water samples.

6.2 Introduction

Diclofenac (DCF), 2-[(2,6-dichlorophenyl)amino]benzeneacetic acid, is a non-steroidal anti-inflammatory drug (NSAID) commonly used to combat inflammation and pain associated with arthritis, osteoarthritis, rheumatoid arthritis, and ankylosing spondylitis [270]. However, common side effects include gastrointestinal ulceration and bleeding [271], while long-term use of DCF could lead to adverse cardiac effects [272]. DCF is frequently recognized as the world's most administered pain killer, and as a result its occurrence in various water bodies has been extensively studied in the recent decades [273–275]. DCF is also known to harmfully affect several environmental species, even at concentrations lower than 1 $\mu\text{g L}^{-1}$ [274]. DCF has been detected in surface waters, groundwater and drinking waters with global maximum measured environmental concentrations of 18.74 $\mu\text{g L}^{-1}$ [276], and even reaching alarmingly high concentration values in cases such as Pakistan where reported values peaked at 216 $\mu\text{g L}^{-1}$ in industrial zones [277]. European Union (EU) has included DCF to the water framework directive (2013/39/EC) as one of the prioritized molecules to be monitored in aquatic ecosystems [278]. These findings call for the establishment of low-cost, sensitive, reliable, and easy-to-perform methods enabling the fast screening of environmental and tap water samples.

Therefore, several methods for the determination of DCF based on capillary electrophoresis [279], high performance liquid chromatography [280, 281], solid phase extraction followed by ultra-high performance liquid chromatography-tandem mass spectrometry [282] have been proposed. Even though these methods offer very good detection capabilities, an intense research activity has also been devoted to the development of electroanalytical methods for the determination of DCF due to attractive analytical features associated with the use of electrochemical detectors in terms of portability, simplicity and the low-cost instrumentation that is required for

their implementation [283–295]. However, the analytical utility of these methods in water samples has been demonstrated only in samples spiked with high concentrations of DCF, such as 100 $\mu\text{M L}^{-1}$ [292], 0.5 μM [287], 1 μM [286], while at lower concentrations (0.2 μM) [293] the assay incurred with a prolonged preconcentration step of 18 min. Therefore, the development of electrochemical sensors with improved detection capabilities for DCF in water samples is highly desired.

In response, we propose here, a low-cost sensor based on graphite screen-printed electrode (SPE) modified with vanadium pentoxide nanosheets (V_2O_5 NSs) that enables the determination of DCF at the nanomolar concentration range in tap water samples. V_2O_5 based nanomaterials have been widely used in energy related applications [211, 296–298] due to their pseudocapacitance [297, 298] and intercalating properties toward alkali metal ions [208, 211, 296] but have been rather underused in electroanalytical applications. V_2O_5 NSs, a known two-dimensional member of the transition metal oxides, were produced via a facile bath sonication procedure in a blend of water and isopropyl alcohol and have been characterized with various physical and electrochemical techniques. The assay format is very simple involving a short (192 s) preconcentration step under cyclic potentiodynamic conditions which affords a substantial increase of the faradaic signal, while lowering the background signal. The analytical utility of V_2O_5 NSs/SPE is demonstrated by recovery studies in spiked tap water samples.

6.3 Results & discussion

6.3.1 Electrocatalytic studies

The electrocatalytic properties of the $\text{V}_2\text{O}_5\text{NS/SPE}$ versus a plain SPE were examined with CV experiments in 0.1 M PBS, pH 7 containing 5 mM hexacyanoferrate(III) as shown in **Fig. 48**. V_2O_5 NS/SPE showed enhanced interfacial electron-transfer kinetics compared with the plain SPE by manifesting a pair of symmetric, well-defined peaks with a notably lower potential peak separation value (ΔE_p) of 181 mV compared with the ΔE_p of 569 mV observed at the plain SPE. The heterogeneous electron transfer rate constant (k^0) for the V_2O_5 NS/SPE was calculated via cyclic voltammetry using the Nicholson method [174, 299], and was found to be $1.17 \times 10^{-3} \text{ cm s}^{-1}$. The respective k^0

of the plain SPE was calculated to be $2.33 \times 10^{-5} \text{ cm s}^{-1}$ using the Klingler-Kochi method [300].

EIS spectra in the form of Nyquist plots are shown in **Fig. 48 inset graph**. Reviewing on the Nyquist plot, it is fairly evident that the $\text{V}_2\text{O}_5\text{NS/SPE}$ in 0.1 M PBS, pH 7 containing 5 + 5 mM hexacyanoferrate(III)/(II), which was used as a redox probe, displays a dramatically lower charge transfer resistance (R_{ct}) of 1.35 kOhm compared with that at the plain SPE (9.48 kOhm). R_{ct} values were calculated by modeling the data to a Randles' equivalent electric circuit. k^0 value was also calculated based on the R_{ct} values of plain and V_2O_5 NS-modified SPES using equation (9) previously expressed in 2.5.2. [188, 301]:

$$k^0 = \frac{RT}{n^2 F^2 A C R_{ct}} \quad (9),$$

where n is the number of electrons transferred in the electrochemical reaction, F is Faraday's constant (96485 C mol^{-1}), R is the gas constant ($8.314 \text{ J mol}^{-1} \text{ K}^{-1}$), T is the temperature (K), R_{ct} is the charge transfer resistance in ohms and A is the electrode's active surface area in cm^2 , 0.085 cm^2 for plain SPE and 0.152 cm^2 for V_2O_5 NS/SPE, calculated via chronocoulometric measurements in the presence of 1 mM hexaammineruthenium(III) chloride in 0.1 M KCl [302].

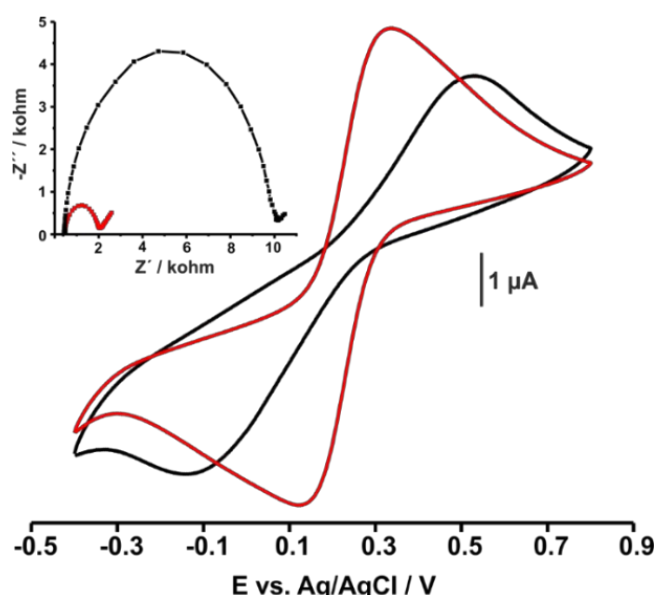


Fig. 48. CVs of (black line) plain SPE and (red line) $\text{V}_2\text{O}_5\text{NS/SPE}$ in 0.1 M PBS, pH 7, scan rate 0.05 V s^{-1} , in 0.1 M PBS, pH 7 containing 5 mM hexacyanoferrate(III). (Inset graph) Nyquist plots of (black line) plain SPE and (red line) $\text{V}_2\text{O}_5\text{NS/SPE}$ in 0.1 M PBS, pH 7 containing 5 + 5 mM hexacyanoferrate(III)/(II).

k^0 was calculated to be $6.61 \times 10^{-5} \text{ cm s}^{-1}$ for the plain SPE and $2.58 \times 10^{-4} \text{ cm s}^{-1}$ for the V_2O_5 NS/SPE. Conclusively, in both EIS and CV based calculation methods, V_2O_5 NS/SPE exhibits an outstanding increase of heterogeneous electron transfer compared with plain SPE, which is almost 4-fold (EIS-based method) [188, 301] and 50-fold (CV-based method) [174, 299, 300]. This leads us to believe that the modification of the SPE surface with V_2O_5 nanosheets instills advanced electrocatalytic properties to the electrode surface.

Interestingly, V_2O_5 NS/SPE showed a remarkable electrocatalytic properties towards DCF as well. **Fig. 49** features an electrocatalytic comparison between the V_2O_5 NS/SPE and the plain SPE in the presence of $5 \mu\text{M}$ DCF at pH 7 using a scan rate of 0.025 V s^{-1} . Surface modification with the V_2O_5 NSs ameliorates the electrocatalytic activity of the electrode surface towards the electro oxidation of DCF greatly both regarding the irreversible oxidation peak (Ia) at ca. 660 mV and the emerging reversible couple (IIa/IIc), centered at ca. 360 mV, which appeared during the second scan in accordance with previous studies [284, 288, 303]. Compared with the current/voltage characteristics at the CV of the plain SPE, V_2O_5 NSs electrocatalytic properties towards the electro oxidation of DCF can be supported by a) the distinct shift of all peaks towards less anodic potentials, b) the 2–3 times higher baseline corrected faradaic current magnitude of all peaks and c) the lower ΔE_p of the reversible couple (**Table 9**).

Table 9 . Comparison of the current/voltage characteristics between the plain SPE and the V_2O_5 NS/SPE in the presence of $5 \mu\text{M}$ DCF in 0.1 MPBS, pH 7. Data were retrieved from the CVs in Fig. 49.

	Peak Ia	Peak IIc	Peak IIa	ΔE_p (IIa/IIc)
Plain SPE				
Potential (mV)	700	302	397	95
Current (nA)	32.09	−51.24	81.69	-
V_2O_5 NS/SPE				
Potential (mV)	663	334	380	46
Current (nA)	78.24	−144.7	144.9	-

The electrocatalytic properties of V_2O_5 NSs towards the electro oxidation of DCF are also demonstrated by the EIS spectra illustrated in **Fig. 49, inset graph** in the form of Nyquist plots recorded in the absence and in the presence of various concentrations of DCF. An apparent semi-circle behavior form tendency with increasing concentrations

of DCF demonstrates an increased electron-transfer process between the electrode's surface and the analyte.

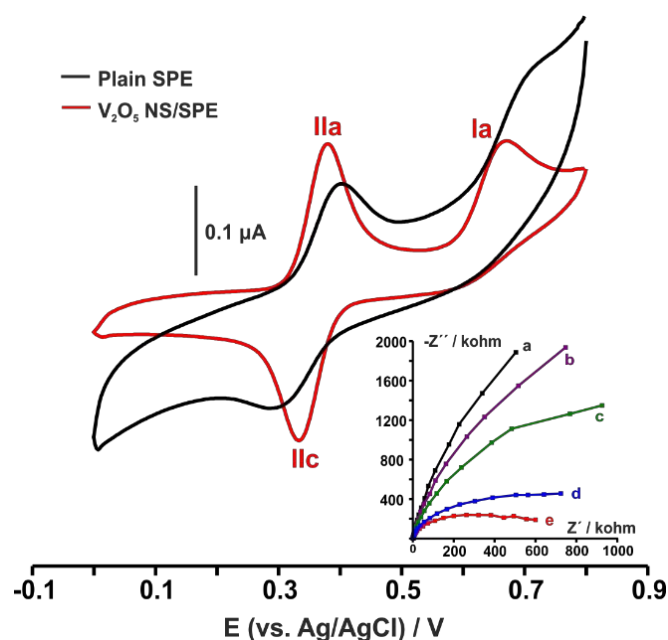


Fig. 49. CVs of (black line) plain SPE and (red line) V_2O_5 NS/SPE in 0.1 M PBS, pH 7 containing $5 \mu\text{M}$ DCF at a scan rate 0.025 V s^{-1} . (Inset graph) Nyquist plots of V_2O_5 NS/SPE in 0.1 M PBS, pH 7 containing (a) 0, (b) 5, (c) 10, (d) 20 and (e) $40 \mu\text{M L}^{-1}$ DCF. DC voltage, 0.800 V.

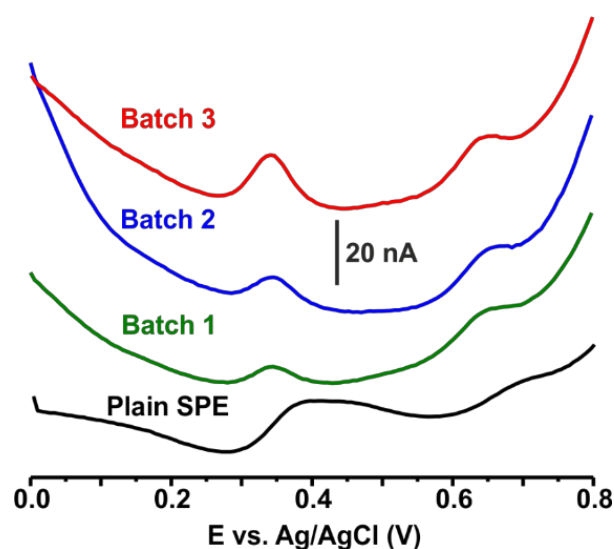


Fig. 50. DP voltammograms of V_2O_5 NS/SPE modified with (green line) batch 1, (blue line) batch 2 and (red line) batch 3 in of 100 nM DCF. The response of the (black line) plain SPE is also included for comparison purposes. Electrolyte: 0.1 M PBS, pH 7. Preconcentration/conditioning step: 3 CVs from 0.800 to 0.000 V at a scan rate 0.025 V s^{-1} .

The impact of the V₂O₅ NSs concentration on their electrocatalytic performance toward DCF was investigated by differential pulse voltammetry (DPV), as per **Fig. 50**, where the voltammetric responses of the 3 batches (namely batch 1, batch 2 and batch 3) in the presence of 100 nM DCF are shown. It is evident that batch 3 outperforms both the other two batches in terms of peak current and the plain SPE in terms of electrocatalytic activity since it produces two well-defined DCF-attributed peaks, in contrast with the plain SPE which produces a mixed response with no useful analytical signal. With this in mind, we have chosen batch 3-modified SPE which is quoted as V₂O₅ NSs/SPE for the rest of this chapter.

For the electro-oxidation of DCF two mechanisms have been proposed in literature. The first mechanism [284, 303] (**Fig. 50A**) involves the electrochemical transformation of diclofenac to 5-hydroxydiclofenac (5OH-DCF) through a 2e⁻/2H⁺ process (peak Ia), which is further oxidized to diclofenac-2,5-quinone imine through a reversible 2e⁻/2H⁺ process (peaks IIa/IIc). The second mechanism [288, 295] (**Fig. 50B**) involves the electrochemical decomposition of DCF (peak Ia) to 2,6 dichloroaniline and 2-hydroxyphenylacetic acid (HPhAc) through a 1e⁻/1H⁺ process, followed by the reversible redox reaction between HPhAc and 1-hydroxy-2-(hydroxyphenyl) ethanalate (peaks IIa/IIc) through a 1e⁻/1H⁺ process.

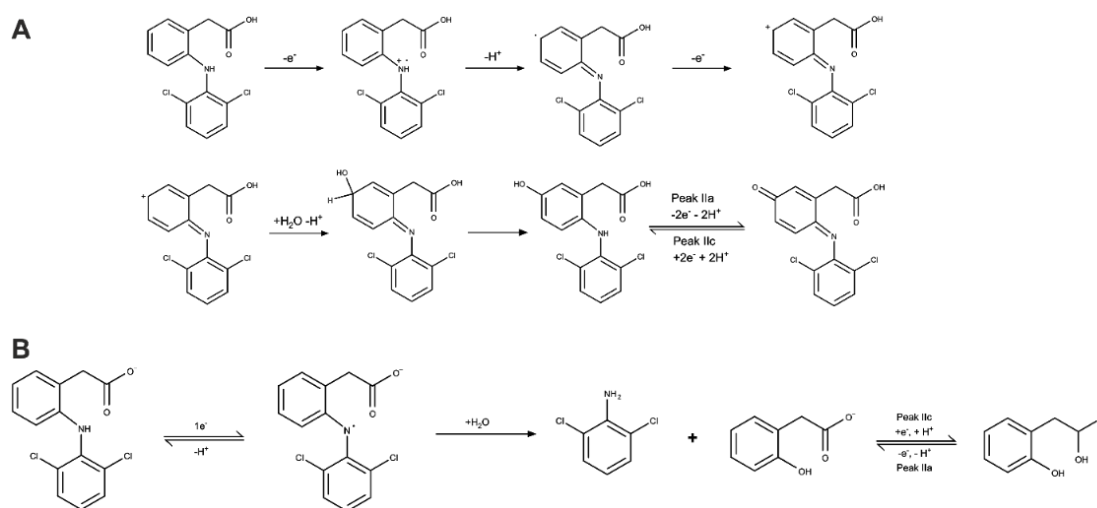


Fig. 50 Tentative mechanisms for the electro oxidation of DCF based on studies reported in (A) [284, 303] and (B) [288, 295]

We endeavored to distinguish the actual electro oxidation mechanism for DCF, by comparing the cyclic voltammetric response of V₂O₅ NS/SPE in 0.1 M PBS, pH 7

containing 5OH-DCF or HPhAc with the respective one of DCF under the same experimental conditions in terms of potential range, scan rate and the concentration of the examined compound. As evidenced in **Fig. 51** though (red line) DCF produces the semi-reversible redox couple centered at ca. 360 mV (peaks IIa/IIc), this is not the case for (green line) 5OH-DCF or (blue line) HPhAc, that is, the products that, respectively, according to the two different mechanisms suggested in literature, are electrochemically generated after the anodic scan (peak Ia) in the solution that originally contains only DCF. These data indicate that the actual mechanism of the electro oxidation of DCF is more complicated and may be subject to more factors than those that have been addressed in the literature so far.

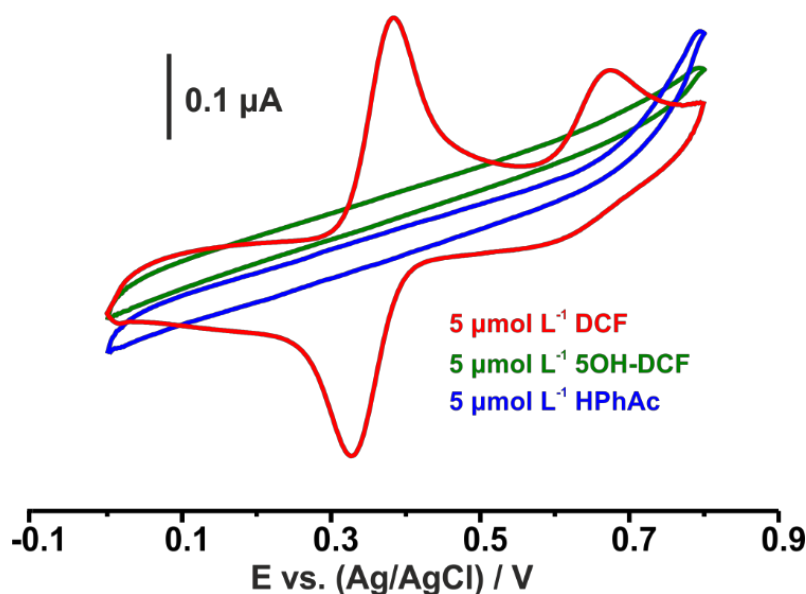


Fig. 51. CVs of V_2O_5 NS/SPE, in 0.1 M PBS, pH 7 in the presence of 5 μ M (red line) DCF, (green line) 5-hydroxydiclofenac (5OH-DCF) and (blue line) 2-hydroxyphenylacetic acid (HPhAc). Scan rate 0.05 $V s^{-1}$

Since the oxidation mechanism remains obscure and the number of electrons (n) participating in the redox reaction producing the pair of peaks IIa/IIc is not certain, we have calculated the heterogeneous electron transfer rate constant (k^0) for DCF by considering the $n=1$ and $n=2$. For both the V_2O_5 NS/SPE and plain SPE the k^0 was calculated by using the Nicholson method [174, 299] for 5 μ M at a scan rate 0.075 $V s^{-1}$. The choice of scan rate was made keeping in mind that this method requires the

$n\Delta E_p$ value to be between 61 and 212 mV, so a moderate scan rate value was opted. Considering $n=1$, the diffusion coefficient for diclofenac (D_{DCF}) was calculated to be $2.28 \times 10^{-5} \text{ cm}^2 \text{ s}^{-1}$ using the Randles–Ševčík equation [304], while the k^0 value for the plain SPE was found to be $1.75 \times 10^{-3} \text{ cm s}^{-1}$ and $1.07 \times 10^{-2} \text{ cm s}^{-1}$ for the V_2O_5 NS/SPE. Considering $n=2$, D_{DCF} was calculated to be $2.85 \times 10^{-6} \text{ cm}^2 \text{ s}^{-1}$, while k^0 value for the plain SPE was found to be $4.37 \times 10^{-4} \text{ cm s}^{-1}$ and $7.20 \times 10^{-4} \text{ cm s}^{-1}$ for V_2O_5 NS/SPE. A summary of the calculated heterogeneous electron transfer constants for both hexacyanoferrate(III)/(II) and DCF, is presented in **Table 10**. In any case, regardless of the number of electrons, V_2O_5 NS/SPE shows enhanced electron transfer kinetics compared with plain SPE (almost ten-fold when $n=1$ and almost two-fold when $n=2$) which further proves the electrocatalytic properties of V_2O_5 NSs toward DCF.

Table 10. A summary of the calculated heterogeneous electron transfer constants (k^0) for plain and V_2O_5 NS/SPE towards model redox probes or DCF.

	k^0 (cm s ⁻¹) hexacyanoferrate(II I) CV method	k^0 (cm s ⁻¹) hexacyanoferrate(III)/(II) EIS method	k^0 (cm s ⁻¹) DCF (IIa/IIc) CV method n = 1	k^0 (cm s ⁻¹) DCF (IIa/IIc) CV method n = 2
Plain SPE	$2.33 \times 10^{-5**}$	6.61×10^{-5}	$1.75 \times 10^{-3*}$	$4.37 \times 10^{-4**}$
V_2O_5 NS/SPE	$1.17 \times 10^{-3*}$	2.58×10^{-4}	$1.07 \times 10^{-2*}$	$7.20 \times 10^{-4*}$

*Calculated using the Nicholson method [174, 299]

**Calculated using the Klingler – Kochi method [300], due to very large $n\Delta E_p$ values at the respective CVs that exceed the limit of 212 mV of Nicholson method

6.3.2 Effect of scan rate and pH

Fig. 52 fixes upon the effect of scan rate on the cyclic voltammetric behavior of V_2O_5 NS/SPE for the electro oxidation of $5 \mu\text{M}$ DCF in 0.1 M PBS, pH at different scan rates from 0.025 to 0.5 V s^{-1} . As can be seen in the inset graph the magnitude of the current for both the anodic and the cathodic peaks of the semi-reversible redox process centered at ca. 0.360 V show a linear relationship with the square-root of scan rate, thus suggesting a diffusion-limited electrochemical process.

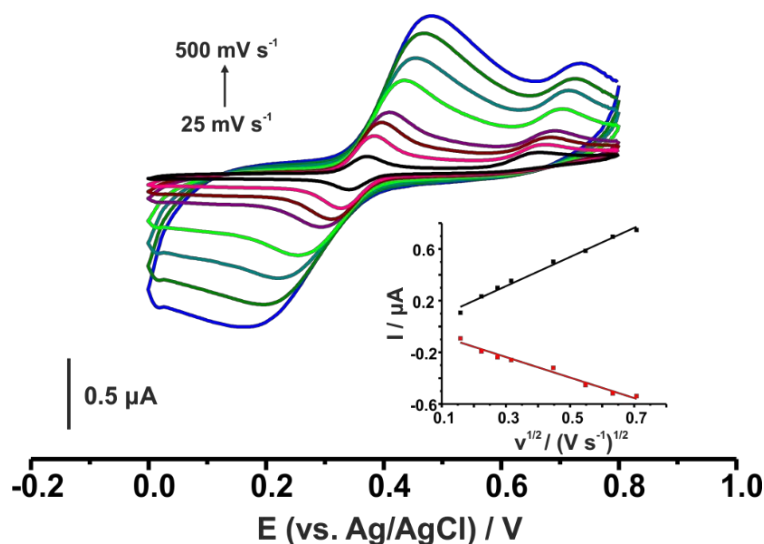


Fig. 52. CVs of V_2O_5 NS/SPE in 0.1 M PBS, pH 7, at various potential scan rates (0.025, 0.050, 0.075, 0.1, 0.2, 0.3, 0.4, and 0.5 $V s^{-1}$) in the presence of 5 μM DCF. Inset shows the corresponding I_p vs. $v^{1/2}$ plot.

The effect of the pH on the electrochemical behavior of V_2O_5 NS/SPE as well as the electro detection of DCF was investigated by cyclic voltammetry experiments in 0.1 M PBS over the pH range 6-10 (**Fig. 53A**). At $pH < 6$, V_2O_5 NSs exhibit increased pseudocapacitive properties resulting in capacitive currents of great magnitude, which hamper the sensing ability of V_2O_5 NS/SPE, as shown in **Fig. 53B** in which the first and third CV scan of V_2O_5 NS/SPE in the pure electrolyte at pH values 5, 6 and 7 are illustrated. The strong pseudocapacitive properties of V_2O_5 NS/SPEs, as per the equation $V_2O_5 + xH^+ + xe^- \leftrightarrow H_xV_2O_5$ [298], is evident by the stability of the CVs at pH 5. At pH 6, a seemingly broad pseudocapacitive behavior exists at the first scan but has been greatly diminished at the third scan. Therefore, the utilization of the V_2O_5 NS/SPE for analytical purposes is preferable at $pH > 6$ where its pseudocapacitance character is nil due to lack of protons, which are the intercalating species of the pseudocapacitor. According to **Fig. 53C (red line)**, the highest response towards the electro oxidation of DCF, with respect to the IIa peak, was obtained at pH 7, and therefore, it was selected as optimum. The dependence of $E^0 = (E_{p(IIa)} + E_{p(IIc)})/2$ with pH was also examined. As can be seen in **Fig. 53C (blue line)** the plot $E^0 = f(pH)$ shows a linear dependence fitting the equation $E^0 (V) = 0.734 - 0.054pH$ ($R^2 = 0.9988$). Slope value of $0.054 V pH^{-1}$ suggests that the redox reaction occurs under an equal number of electrons and protons mechanism.

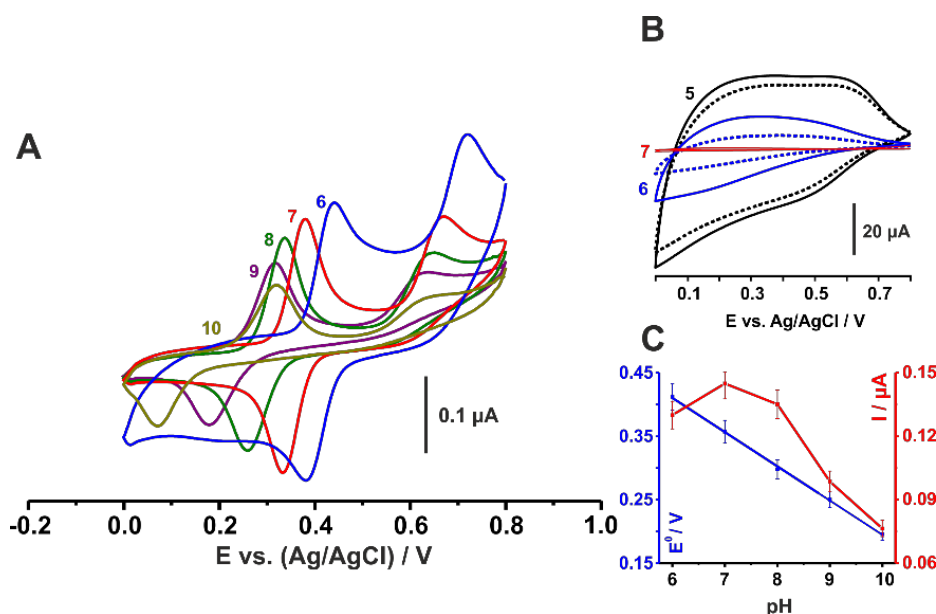


Fig. 53. (A) CVs of V_2O_5NS/SPE at scan rate 0.025 V s^{-1} , in 0.1 M PBS , at pH (blue line) 6, (red line) 7, (green line) 8, (purple line) 9 and (gold line) 10. Inset graph (B) shows the (solid line) first and (dot line) third scans of V_2O_5NS/SPE in the blank solution at (black line) pH 5, (blue line) pH 6 and (red line) pH 7. (C) Variation of (blue line) E^0 and (red line) anodic peak current of the IIa/IIc redox couple with pH. DCF concentration, $5 \mu\text{M}$.

6.3.3 Analytical performance

Due to the complexity of the oxidation mechanism of DCF, besides the commonly used potentiostatic preconcentration treatments, different preconcentration protocols were examined. Indeed, a direct comparison between a potentiostatic and a potentiodynamic preconcentration treatment was reported Aguilar-Lira et al. [288]. The potentiodynamic treatment was possible by employing two consecutive DPV scans between 0.1 and 0.8 V followed by a cleaning step at -0.5 V for 60 s in methanol, while the potentiostatic treatment involved the polarization of the electrode at 0.61 V for 50 s .

Fig. 54 elaborates on the diverse quantification procedures evaluated in the presence of 200 nM DCF . As mentioned above, it is imperative for the irreversible oxidation process to occur at ca. 660 mV , thus forcing the formation of the semi-reversible redox couple at ca. 360 mV . For this reason, a single DP voltammogram from 0 to 0.800 V (black line) depicts only the oxidation peak at 660 mV . The subsequent DP voltammogram however (gold line), enables the emergence of the oxidation peak IIa since the irreversible oxidation has already occurred. With this in mind, a deposition potential of 800 mV was applied for 30 (magenta line) and 60 s (purple line), which

enhanced the peak magnitude compared with that observed when two successive DP voltammograms were applied, but also input a sizeable background signal at ca. 480 mV which distorted the peak's symmetry by hindering the recovery of the baseline after the appearance of the oxidation peak. To address this issue, an additional treatment of 30 s (azure line) and 60 s (maroon line) at 0 mV was added to the corresponding treatments (e.g., 30 s at 800 mV with additional 30 s at 0 mV; 60 s at 800 mV with additional 60 s at 0 mV), achieving a slight increase in peak magnitude though deteriorating the background signal. Moreover, all the potentiostatic treatments caused a shift of the oxidation peak at more anodic potential indicating that impair the electrocatalytic properties of V_2O_5 NSs towards DCF.

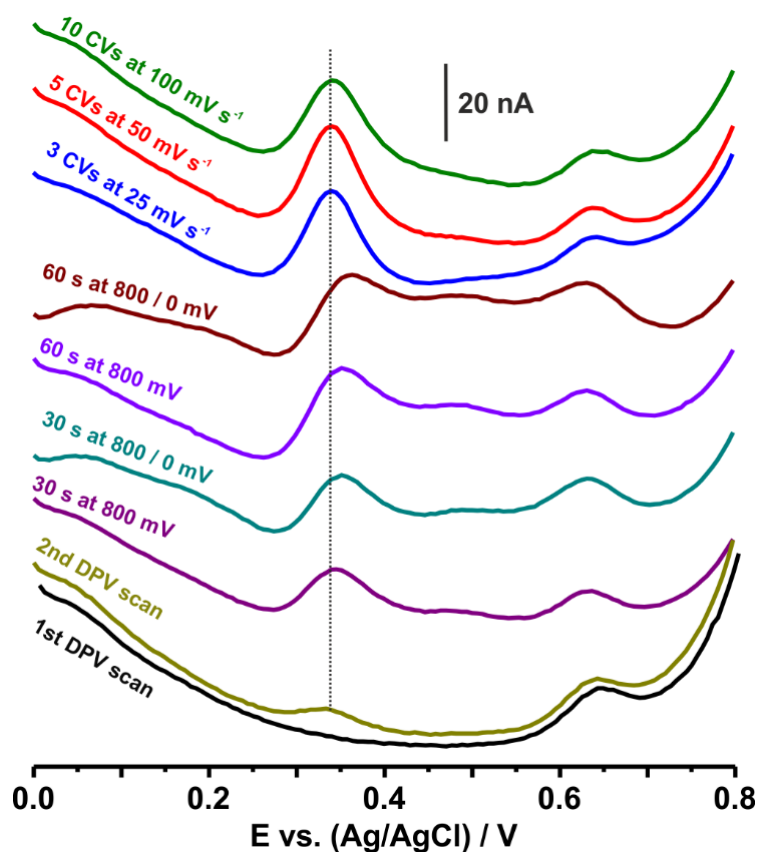


Fig. 54. DP voltammograms of V_2O_5 NS/SPEs after a single and two DP voltammograms as well as after various preconcentration treatments. Measurements were conducted in 0.1 M PBS, pH 7, containing 150 nM DCF.

Since such typical treatments were found ineffective, an alternative treatment, based on a cyclic potentiodynamic approach, was also investigated. CVs taken from 800 to 0 mV

(forward scan) and from 0 mV to 800 mV (backward scan) were found to increase the magnitude of the measuring peak (IIa) without introducing a large background signal, depending on both the number of the scans and the scan rate of the potential in each case. Particularly, three different scan rates were evaluated (0.025 V s^{-1} , 0.05 V s^{-1} , and 0.1 V s^{-1}) with enough number of scans as to procure stable signals for each measurement, without leading to lengthy treatments. All three approaches resulted in sufficient peak magnitudes without inducing any extra background signals and within relatively short treatment durations. Depending on the scan rate, a stable signal upon successive measurements was obtained. The treatment at 0.025 V s^{-1} produced a stable signal after 3 CV scans (total treatment time = 192 s), at 0.05 V s^{-1} after 5 CV scans (total treatment time = 160 s), and finally at 0.1 V s^{-1} after 10 scans (total treatment time = 160 s). Interestingly, the treatment under cyclic potentiodynamic conditions resulted also in the recovery of the oxidation potential of the IIa peak at ca. 0.36 V indicating that this treatment does not impair the electrocatalytic properties of V_2O_5 NS towards DCF. Taking as criteria, the magnitude of the peak and the recovery of the baseline after the oxidation peak, the treatment including 3 CV scans at 0.025 V s^{-1} was selected as optimum.

The relative responses between Ia and IIa peaks also justify our selection of IIa peak's magnitude as a measure for the quantification of DCF. To the best of our knowledge, the response of IIa peak for quantification purposes has been used only in two works [291, 305]. Based on the electrocatalytic properties of the respective electrocatalysts as well as the preconcentration mode in each case, the great majority of the relevant literature relies on the response of Ia peak [283, 284, 289, 290, 293, 294, 303, 306], which, however, is associated with surface confined species. Indeed, the strong adsorption of these species, in many cases, causes the deactivation of the electrode surface, thus necessitating the regeneration/cleaning of the electrode surface with mechanical [286, 303]/electrochemical [284] means, respectively, or even impose the use of the electrode as a disposable sensor [289].

The effect of the selected cyclic potentiodynamic treatment on the repeatability of the measurements, the reproducibility of the fabrication process and the working stability of the $\text{V}_2\text{O}_5\text{NS/SPE}$ was also investigated. The repeatability of the method for five successive measurements of a 150 nM DCF standard was found to be 3.7% (**Fig. 55**), while the reproducibility between different V_2O_5 NS/SPEs was 2.9% (200 nM DCF, $n=5$). V_2O_5 NS/SPEs retained their original activity for at least 15-20 analytical runs,

and thus a complete analysis (calibration plot or standard addition method) was conducted by a single electrode.

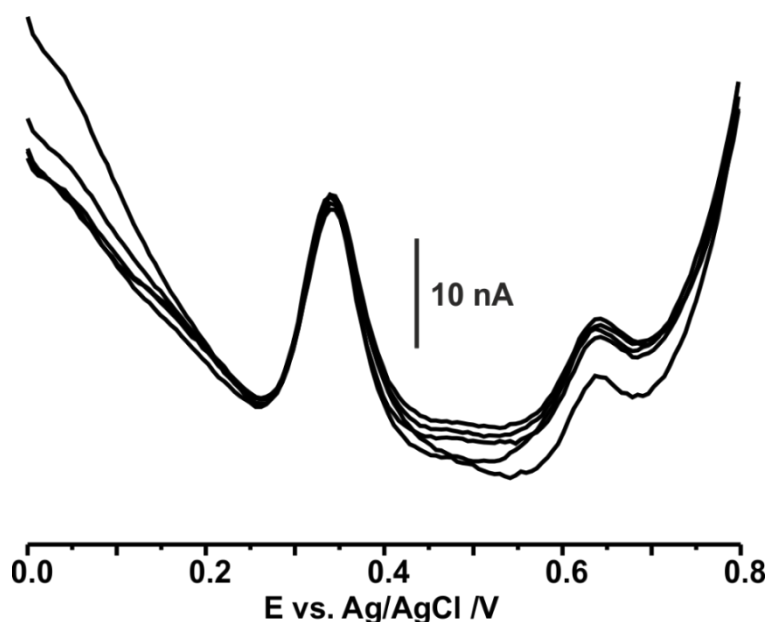


Fig. 55. Five successive measurements of DCF at a fixed concentration of 150 nM in 0.1 M PBS, pH 7.

6.3.4 Interference studies

The interference effect of common electro active compounds, such as uric acid, ascorbic acid, and dopamine was examined in mixed solutions containing DCF and the examined interferants at a 10-fold concentration excess. The effect of another electroactive non-steroidal anti-inflammatory drug, aceclofenac, which has a similar chemical structure to DCF was also examined in an equimolar mixture of the two drugs. As shown in **Fig. 56** ascorbic acid and aceclofenac cause the DCF's peak to broaden, however, do not affect its magnitude significantly (DCF's peak retains almost 90% of its original magnitude). In the presence of uric acid, the original response is retained at 76% because of the increase of the background signal next to DCF's peak. Dopamine also produces a large background signal at ca. 200 mV which however does not affect the magnitude of the DCF peak, though it slightly alters its shape. Data demonstrates that the response of V_2O_5NS/SPE is sufficiently selective towards DCF, however, the observed variations of the original response suggest the applicability of the method in real-world matrices to be conducted by using the standard addition method in order to

ensure that the sensitivity of the electrode in both the unknown samples and the DCF's standards is the same.

Finally, due to the complexing properties of DCF with various metal ions, such as Cu^{2+} , Zn^{2+} , Pb^{2+} , Hg^{2+} , Cd^{2+} [192, 193] etc. which collectively are present to various environmental samples in relatively high concentrations, all measurements were conducted in the presence of EDTA (see below).

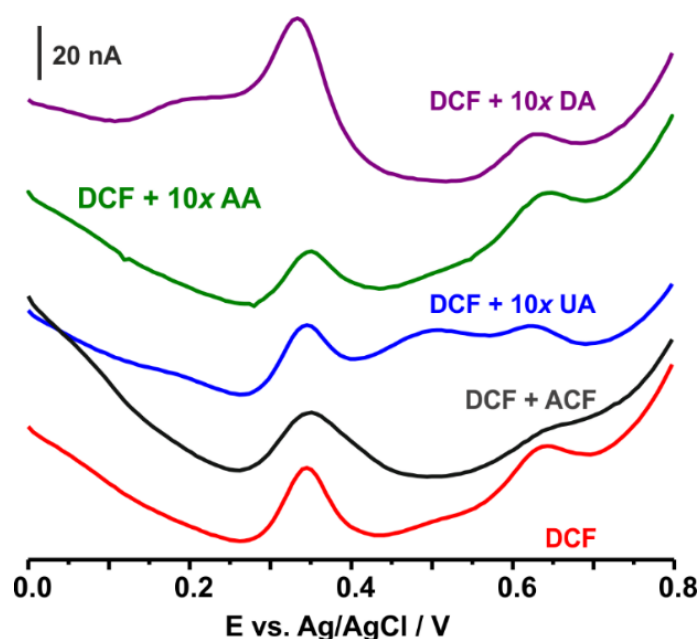


Fig. 56 DP voltammograms of $\text{V}_2\text{O}_5\text{NS/SPE}$ in 0.1 M PBS, pH 7, containing (red line) 0.2 μM DCF or mixtures of 0.2 μM DCF with (black line) 0.2 μM aceclofenac (ACF), (blue line) 2 μM uric acid (UA), (green line) 2 μM ascorbic acid (AA), and (purple line) 2 μM dopamine (DA).

6.3.5 Calibration features

Under the selected experimental conditions, a series of DP voltammograms of $\text{V}_2\text{O}_5\text{NS/SPE}$ in the presence of various concentrations of DCF were conducted. By applying the least squares method, a linear relationship between the peak IIa current and the concentration of DCF was obtained over the concentration range from 20 to 200 nM (**Fig. 57A**). Data fitted equation $I/\text{nA} = 0.132 + 0.175([\text{DCF}]/\text{nM})$ ($R^2 = 0.9993$). Based on the $3S_x/\text{slope}$ criterion, where S_x is the standard deviation of the blank solution, the limit of detection (LOD) was calculated to be 3.1 nM. Taking as criteria the detection range and the LOD of the method, $\text{V}_2\text{O}_5\text{NS/SPE}$ outperforms the majority of the electrodes used for the voltammetric determination of DCF [286, 289,

290, 292, 294, 305–307] or shows comparable analytical features with plain [303] or SWCNT-modified edge plane pyrolytic graphite electrodes [284], and MWCNT-carbon paste electrodes [293] (**Table 11**). Considering however, the high cost of edge plane pyrolytic graphite electrodes [284, 303], the need to regenerate the electrode surface after each measurement [303], and the long (18 min) preconcentration step used in Ref. [293], it is safe to say that $\text{V}_2\text{O}_5\text{NS/SPE}$ represent an advanced, low-cost electrochemical transducer for the determination of DCF.

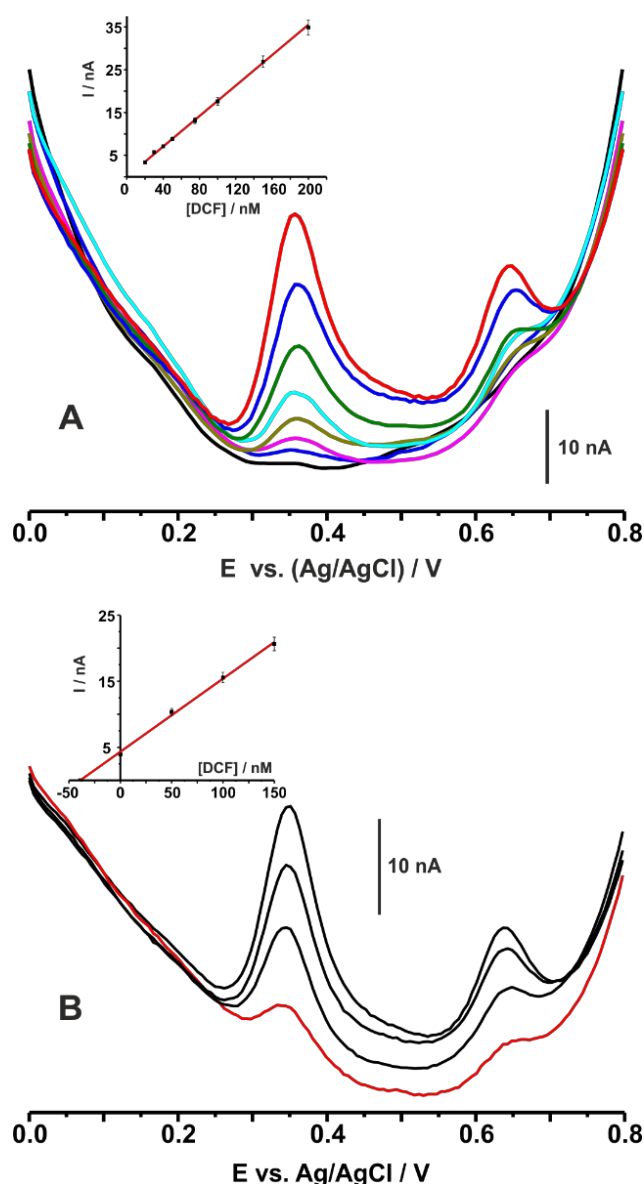


Fig. 57. (A) DP voltammograms of $\text{V}_2\text{O}_5\text{NS/SPE}$ in 0.1 M PBS, pH 7, containing various concentrations of 20, 30, 40, 50, 80, 100, 150 and 200 nM DCF. Preconcentration step: 3 CV scans at 0.025 V s^{-1} . Inset graph shows the respective calibration plot. (B) DP voltammograms of $\text{V}_2\text{O}_5\text{NS/SPE}$ for the determination of DCF in a tap water sample spiked with 50 nM DCF with the standard addition method (sample plus 3 additions of 50 nM DCF), in 0.1 M PBS, pH 7 containing 0.8 mM EDTA. Preconcentration step: 3 CV scans at 0.025 V s^{-1} . Inset graph shows the respective standard addition plot.

Table 11. An overview of various electrochemical methods for the determination of diclofenac.

Electrode	Detection range, μM	Detection limit, μM	Ref.
(G-MWCNT)-CPE	0.02 – 1	0.004	[293]
EPPGE	0.01 – 1	0.0062	[303]
SWCNT/EPPGE	0.001 – 0.5	0.00082	[284]
Au-PtNP/f-MWCNT/AuE	0.5 – 1000	0.3	[294]
PtNF/rGO/SPE	0.1 – 100	0.04	[283]
Paper-based electrode	0.1 – 5	0.07	[287]
CV-Fe- β -CD/ISE	0.1 - 10^4	0.11	[292]
ISE/SPE	50 - 10^4	32	[308]
CeO ₂ /SPE	0.1 – 25.6	0.4	[289]
PANi/rGO/MIP/CPE	17 – 272	3.7	[305]
ZnONF/SPE	0.01 – 40	0.11	[307]
MWCNT/Cu(OH) ₂ NP/IL-GCE	0.18 – 119	0.04	[286]
f-MWCNT/NC/GCE	0.05 – 250	0.02	[290]
MWCNT/CTS-Cu/GCE	0.3 – 200	0.021	[306]
Graphite (potentiodynamic)	8.19 – 111	2.45	[288]
Graphite (potentiostatic)	2.56 – 9.5	0.76	
GO-COOH/GCE	1.2 – 400	0.09	[285]
V ₂ O ₅ -NS/SPE	0.02 – 0.2	0.0031	<i>This work</i>

Abbreviations: (G-MWCNTs)-CPE, nanostructured multi-walled carbon nanotube/carbon-paste electrode; EPPGE, edge plane pyrolytic graphite electrode; SWCNT/EPPGE, EPPGE coated with single-wall carbon nanotubes; Au-PtNP/f-MWCNT/AuE, Au-Pt bimetallic nanoparticle decorated multi-walled carbon nanotube/gold electrode; PtNF/rGO/SPE, platinum nanoflowers/reduced graphene oxide/ SPE; CV-Fe- β -CD/ISE, crystal violet/ β -cyclodextrin/magnetite ion selective electrode, CeO₂-SPE, cerium dioxide/SPE; PANi/rGO/MIP/CPE, polyaniline and reduced graphene oxide molecularly imprinted polymer/CPE; ZnONF/SPE, zinc oxide nanoflower/SPE; MWCNT/Cu(OH)₂NP/IL-GCE, multi-walled carbon nanotube/copper hydroxide nanoparticle/ionic liquid GCE; f-MWCNT/NC/GCE, functionalized multi-walled carbon nanotubes nanocellulose composite/GCE; MWCNT/CTS-Cu/GCE, multi-walled carbon nanotubes chitosan copper complex/GCE; GO-COOH/GCE, carboxylated graphene oxide/GCE;

The analytical utility of V₂O₅ NS/SPEs were evaluated in three tap water samples spiked with 50 nM DCF. Before spiking, a pre-weighed amount of EDTA-Na₂ (final concentration 1 mM) was added to the samples to avoid complexation of DCF with various metal ions exist in water samples. Then, samples spiked with 50 mM DCF and mixed with the electrolyte (8.00 mL sample and 2.00 mL 0.5 M PBS). The determination of DCF was conducted with the standard addition method, as depicted on **Fig. 57B**.

The concentration of DCF was found to be 50.21 ± 1.51 nM, while the recovery of the method was $100.43 \pm 3.00\%$. Data indicates that V₂O₅NS/SPE can be used for the

determination of DCF in drinking water, even though full compliance with EC regulations, the maximum allowable concentration of DCF shared by the European Union is $0.1 \mu\text{g L}^{-1}$ (0.34 nM), requires the detection capabilities of the sensor to be further improved. It is, however, noted that the analytical utility of other methods in water samples has been demonstrated in samples spiked with considerably higher concentrations at the micromolar range [283, 286, 287, 292, 308].

Conclusions

- This thesis fixes upon the implementation of 2D inorganic nanosheets (two monoelemental pnictogens and one transitional metal oxide) produced via various top-down approaches on the determination of important analytes such as heavy metal ions, explosive and highly toxic compounds or overused pharmaceutical compounds. It should be stressed out that the majority of inorganic nanosheets are low to wide band gap semiconductors with some exceptions illustrating metallic properties [such as 1T polymorph of dichalcogenides, MXene-core (not taking into consideration electronic state deviations originating from various etching procedures), etc.]. This leads to the necessity of creating conjugated or composite forms of those materials with more conducting phases to ameliorate sensor sensitivity.
- Our first endeavor is the production shear-force exfoliated bismuthene which is a low band gap semiconductor [15] (bilayer bismuthene ranges from 0.18 to 0.23 eV) and its conjugation with similarly produced few-layer graphene for the anodic stripping voltammetric determination of heavy metal ions (Cd(II), Pb(II)). This highly conducting composite material achieved ultra-sensitive and simultaneous determination of both ions (with LODs of $0.33 \mu\text{g L}^{-1}$), thus exploiting the excellent alloying properties of bismuthene towards heavy metal ions and the high electronic conductivity of graphene.
- Our second effort was the production of few-layer antimonene, which is a wide band gap semiconductor with an indirect band gap of 2.28 eV [15] (predicted for monolayer β -Sb), with liquid-phase exfoliation (tip sonication) and the in-situ formation of a semi-conducting heterostructure with poly(3,4-ethylenedioxy thiophene):poly(styrene sulfonate) (PEDOT:PSS) for the nanomolar cathodic determination of 4-nitrotoluene (LOD was 16.7 nM).
- Finally, we have successfully utilized few-layer V_2O_5 nanosheets via a simple bath sonication procedure, which have a very wide band gap, predicted to be 4 eV for a monolayer [309]. Admittedly, while this great a band gap partially hampers electronic transfer, it can provide a great electroanalytical platform through the intercalation/deintercalation of ionic species which can enhance proton related redox reactions. This is proven by the nanomolar determination of diclofenac (a widely administered non-steroidal anti-inflammatory drug), via

the quantification of its electrochemically active oxidation product, thus reaching an LOD of 6.6 nM.

- The applicability of all the above mentioned nanosheets was evaluated in real tap water samples, in all cases achieving excellent recovery values.
- Data demonstrated for the first time the use of the studied nanomaterials for analytical purposes by using low-cost screen-printed electrodes.
- Compared with the bulk counterpart materials, the studied nanomaterials showed enhanced electroanalytical properties thus underpinning their advantages for use in modern analytical devices.
- V_2O_5 NSs aside, which can be produced in an easy-to-perform exfoliation process with a high yield, the other nanomaterials (bismuthene and antimonene) require a more elaborate process while the yield is low.

References

1. Valeria N, Manish C, G. KM, et al (2013) Liquid Exfoliation of Layered Materials. *Science* (80-) 340:1226419. <https://doi.org/10.1126/science.1226419>
2. Chhowalla M, Liu Z, Zhang H (2015) Two-dimensional transition metal dichalcogenide (TMD) nanosheets. *Chem Soc Rev* 44:2584–2586. <https://doi.org/10.1039/c5cs90037a>
3. Murphy DW, Hull GW (1975) Monodispersed tantalum disulfide and adsorption complexes with cations. *J Chem Phys* 62:973–978. <https://doi.org/10.1063/1.430513>
4. Sasaki T, Watanabe M, Hashizume H, et al (1996) Macromolecule-like aspects for a colloidal suspension of an exfoliated titanate. Pairwise association of nanosheets and dynamic reassembling process initiated from it. *J Am Chem Soc* 118:8329–8335. <https://doi.org/10.1021/ja960073b>
5. Novoselov KS, Geim AK, Morozov S V., et al (2004) Electric field in atomically thin carbon films. *Science* (80-) 306:666–669. <https://doi.org/10.1126/science.1102896>
6. Cheng L, Huang W, Gong Q, et al (2014) Ultrathin WS₂ nanoflakes as a high-performance electrocatalyst for the hydrogen evolution reaction. *Angew Chemie - Int Ed* 53:7860–7863. <https://doi.org/10.1002/anie.201402315>
7. Jeong S, Yoo D, Jang JT, et al (2012) Well-defined colloidal 2-D layered transition-metal chalcogenide nanocrystals via generalized synthetic protocols. *J Am Chem Soc* 134:18233–18236. <https://doi.org/10.1021/ja3089845>
8. Smith RJ, King PJ, Lotya M, et al (2011) Large-scale exfoliation of inorganic layered compounds in aqueous surfactant solutions. *Adv Mater* 23:3944–3948. <https://doi.org/10.1002/adma.201102584>
9. N. CJ, Mustafa L, Arlene O, et al (2011) Two-Dimensional Nanosheets Produced by Liquid Exfoliation of Layered Materials. *Science* (80-) 331:568–571. <https://doi.org/10.1126/science.1194975>
10. Komsa HP, Krasheninnikov A V. (2012) Effects of confinement and environment on the electronic structure and exciton binding energy of MoS₂ from first principles. *Phys Rev B - Condens Matter Mater Phys* 86:1–6. <https://doi.org/10.1103/PhysRevB.86.241201>

11. Dral AP, ten Elshof JE (2018) 2D metal oxide nanoflakes for sensing applications: Review and perspective. *Sensors Actuators, B Chem* 272:369–392. <https://doi.org/10.1016/j.snb.2018.05.157>
12. Gogotsi Y, Anasori B (2019) The Rise of MXenes. *ACS Nano* 13:8491–8494. <https://doi.org/10.1021/acsnano.9b06394>
13. Hartman T, Sofer Z (2019) Beyond Graphene: Chemistry of Group 14 Graphene Analogues: Silicene, Germanene, and Stanene. *ACS Nano* 13:8566–8576. <https://doi.org/10.1021/acsnano.9b04466>
14. Chia X, Pumera M (2018) Characteristics and performance of two-dimensional materials for electrocatalysis. *Nat Catal* 1:909–921. <https://doi.org/10.1038/s41929-018-0181-7>
15. Pumera M, Sofer Z (2017) 2D Monoelemental Arsenene, Antimonene, and Bismuthene: Beyond Black Phosphorus. *Adv Mater* 29:. <https://doi.org/10.1002/adma.201605299>
16. Bhimanapati GR, Lin Z, Meunier V, et al (2015) Recent Advances in Two-Dimensional Materials beyond Graphene. *ACS Nano* 9:11509–11539. <https://doi.org/10.1021/acsnano.5b05556>
17. Tsai HL, Heising J, Schindler JL, et al (1997) Exfoliated-Restacked Phase of WS₂. *Chem Mater* 9:879–882. <https://doi.org/10.1021/cm960579t>
18. Kostarelos K (2016) Translating graphene and 2D materials into medicine. *Nat Rev Mater* 1:1–2. <https://doi.org/10.1038/natrevmats.2016.84>
19. Zhang X, Hou L, Ciesielski A, Samorì P (2016) 2D Materials Beyond Graphene for High-Performance Energy Storage Applications. *Adv Energy Mater* 6:1600671. <https://doi.org/10.1002/aenm.201600671>
20. Xue Y, Zhang Q, Wang W, et al (2017) Opening Two-Dimensional Materials for Energy Conversion and Storage: A Concept. *Adv Energy Mater* 7:1–23. <https://doi.org/10.1002/aenm.201602684>
21. Deng D, Novoselov KS, Fu Q, et al (2016) Catalysis with two-dimensional materials and their heterostructures. *Nat Nanotechnol* 11:218–230. <https://doi.org/10.1038/nnano.2015.340>
22. Anichini C, Czepa W, Pakulski D, et al (2018) Chemical sensing with 2D materials. *Chem Soc Rev* 47:4860–4908. <https://doi.org/10.1039/c8cs00417j>
23. Cheng L, Wang X, Gong F, et al (2020) 2D Nanomaterials for Cancer Theranostic Applications. *Adv Mater* 32:1–23.

- <https://doi.org/10.1002/adma.201902333>
24. Li D, Gong Y, Chen Y, et al (2020) Recent Progress of Two-Dimensional Thermoelectric Materials. *Nano-Micro Lett* 12:36.
<https://doi.org/10.1007/s40820-020-0374-x>
 25. Chang YM, Lin HW, Li LJ, Chen HY (2020) Two-dimensional materials as anodes for sodium-ion batteries. *Mater Today Adv* 6:100054.
<https://doi.org/10.1016/j.mtadv.2020.100054>
 26. Tao H, Fan Q, Ma T, et al (2020) Two-dimensional materials for energy conversion and storage. *Prog Mater Sci* 111:100637.
<https://doi.org/10.1016/j.pmatsci.2020.100637>
 27. Faraji M, Yousefi M, Yousefzadeh S, et al (2019) Two-dimensional materials in semiconductor photoelectrocatalytic systems for water splitting. *Energy Environ Sci* 12:59–95. <https://doi.org/10.1039/c8ee00886h>
 28. Chen Y, Yang K, Jiang B, et al (2017) Emerging two-dimensional nanomaterials for electrochemical hydrogen evolution. *J Mater Chem A* 5:8187–8208. <https://doi.org/10.1039/c7ta00816c>
 29. Tseliou F, Avgeropoulos A, Falaras P, Prodromidis MI (2017) Low dimensional Bi₂Te₃-graphene oxide hybrid film-modified electrodes for ultra-sensitive stripping voltammetric detection of Pb(II) and Cd(II). *Electrochim Acta* 231:230–237. <https://doi.org/10.1016/j.electacta.2017.02.058>
 30. Govindasamy M, Wang SF, Jothiramalingam R, et al (2019) A screen-printed electrode modified with tungsten disulfide nanosheets for nanomolar detection of the arsenic drug roxarsone. *Microchim Acta* 186:420.
<https://doi.org/10.1007/s00604-019-3535-1>
 31. Ge Y, Qu M, Xu L, et al (2019) Phosphorene nanocomposite with high environmental stability and antifouling capability for simultaneous sensing of clenbuterol and ractopamine. *Microchim Acta* 186:836.
<https://doi.org/10.1007/s00604-019-3908-5>
 32. Yang T, Yu R, Chen H, et al (2016) Electrochemical preparation of thin-layered molybdenum disulfide-poly(m-aminobenzenesulfonic acid) nanocomposite for TNT detection. *J Electroanal Chem* 781:70–75.
<https://doi.org/10.1016/j.jelechem.2016.09.009>
 33. Chen Z, Lu M (2018) Thionine-coordinated BCN nanosheets for electrochemical enzyme immunoassay of lipocalin-2 on biofunctionalized

- carbon-fiber microelectrode. *Sensors Actuators, B Chem* 273:253–259.
<https://doi.org/10.1016/j.snb.2018.06.053>
34. Adeel M, Rahman MM, Lee JJ (2019) Label-free aptasensor for the detection of cardiac biomarker myoglobin based on gold nanoparticles decorated boron nitride nanosheets. *Biosens Bioelectron* 126:143–150.
<https://doi.org/10.1016/j.bios.2018.10.060>
 35. Zheng J, Diao J, Jin Y, et al (2018) An Inkjet Printed Ti₃C₂-GO Electrode for the Electrochemical Sensing of Hydrogen Peroxide . *J Electrochem Soc* 165:B227–B231. <https://doi.org/10.1149/2.0051807jes>
 36. Selvam SP, Hansa M, Yun K (2020) Simultaneous differential pulse voltammetric detection of uric acid and melatonin based on a self-assembled Au nanoparticle–MoS₂ nanoflake sensing platform. *Sensors Actuators, B Chem* 307:127683. <https://doi.org/10.1016/j.snb.2020.127683>
 37. Chia HL, Mayorga-Martinez CC, Antonatos N, et al (2020) MXene Titanium Carbide-based Biosensor: Strong Dependence of Exfoliation Method on Performance. *Anal Chem* 92:2452–2459.
<https://doi.org/10.1021/acs.analchem.9b03634>
 38. Joshi N, Hayasaka T, Liu Y, et al (2018) A review on chemiresistive room temperature gas sensors based on metal oxide nanostructures, graphene and 2D transition metal dichalcogenides. *Microchim Acta* 185:213.
<https://doi.org/10.1007/s00604-018-2750-5>
 39. Boland C, Coleman JN, Backes C, et al (2016) Guidelines for Exfoliation, Characterization and Processing of Layered Materials Produced by Liquid Exfoliation. *Chem Mater* 29:243–255.
<https://doi.org/10.1021/acs.chemmater.6b03335>
 40. Shi W, Song S, Zhang H (2013) Hydrothermal synthetic strategies of inorganic semiconducting nanostructures. *Chem Soc Rev* 42:5714–5743.
<https://doi.org/10.1039/c3cs60012b>
 41. Yang Y, Hou H, Zou G, et al (2019) Electrochemical exfoliation of graphene-like two-dimensional nanomaterials. *Nanoscale* 11:16–33.
<https://doi.org/10.1039/c8nr08227h>
 42. Antonatos N, Ghodrati H, Sofer Z (2020) Elements beyond graphene: Current state and perspectives of elemental monolayer deposition by bottom-up approach. *Appl Mater Today* 18:100502.

- <https://doi.org/10.1016/j.apmt.2019.100502>
43. Liu G Bin, Xiao D, Yao Y, et al (2015) Electronic structures and theoretical modelling of two-dimensional group-VIB transition metal dichalcogenides. *Chem Soc Rev* 44:2643–2663. <https://doi.org/10.1039/c4cs00301b>
 44. Mohamad Nasir MZ, Pumera M (2019) Emerging mono-elemental 2D nanomaterials for electrochemical sensing applications: From borophene to bismuthene. *TrAC - Trends Anal Chem* 121:115696. <https://doi.org/10.1016/j.trac.2019.115696>
 45. Kumar R, Goel N, Hojamberdiev M, Kumar M (2020) Transition metal dichalcogenides-based flexible gas sensors. *Sensors Actuators, A Phys* 303:111875. <https://doi.org/10.1016/j.sna.2020.111875>
 46. Yang S, Jiang C, Wei S huai (2017) Gas sensing in 2D materials. *Appl Phys Rev* 4:021304. <https://doi.org/10.1063/1.4983310>
 47. Vilian ATE, Dinesh B, Kang SM, et al (2019) Recent advances in molybdenum disulfide-based electrode materials for electroanalytical applications. *Microchim Acta* 186:203. <https://doi.org/10.1007/s00604-019-3287-y>
 48. Chen J, Meng H, Tian Y, et al (2019) Recent advances in functionalized MnO₂ nanosheets for biosensing and biomedicine applications. *Nanoscale Horizons* 4:434–444. <https://doi.org/10.1039/c8nh00274f>
 49. Safarpour M, Arefi-Oskoui S, Khataee A (2020) A review on two-dimensional metal oxide and metal hydroxide nanosheets for modification of polymeric membranes. *J Ind Eng Chem* 82:31–41. <https://doi.org/10.1016/j.jiec.2019.11.002>
 50. Ronchi RM, Arantes JT, Santos SF (2019) Synthesis, structure, properties and applications of MXenes: Current status and perspectives. *Ceram Int* 45:18167–18188. <https://doi.org/10.1016/j.ceramint.2019.06.114>
 51. Sinha A, Dhanjai, Zhao H, et al (2018) MXene: An emerging material for sensing and biosensing. *TrAC - Trends Anal Chem* 105:424–435. <https://doi.org/10.1016/j.trac.2018.05.021>
 52. Kalambate PK, Gadhari NS, Li X, et al (2019) Recent advances in MXene–based electrochemical sensors and biosensors. *TrAC - Trends Anal Chem* 120:115643. <https://doi.org/10.1016/j.trac.2019.115643>
 53. Wilson JA, Yoffe AD (1969) The transition metal dichalcogenides discussion and interpretation of the observed optical, electrical and structural properties.

- Adv Phys 18:193–335. <https://doi.org/10.1080/00018736900101307>
54. Dolui K, Pemmaraju C Das, Sanvito S (2012) Electric field effects on armchair MoS 2 nanoribbons. ACS Nano 6:4823–4834.
<https://doi.org/10.1021/nn301505x>
 55. Darancet P, Millis AJ, Marianetti CA (2014) Three-dimensional metallic and two-dimensional insulating behavior in octahedral tantalum dichalcogenides. Phys Rev B - Condens Matter Mater Phys 90:2–6.
<https://doi.org/10.1103/PhysRevB.90.045134>
 56. Ambrosi A, Sofer Z, Pumera M (2015) 2H → 1T phase transition and hydrogen evolution activity of MoS₂, MoSe₂, WS₂ and WSe₂ strongly depends on the MX₂ composition. Chem Commun 51:8450–8453.
<https://doi.org/10.1039/c5cc00803d>
 57. Rohaizad N, Mayorga-Martinez CC, Sofer Z, et al (2020) Layered platinum dichalcogenides (PtS₂, PtSe₂, PtTe₂) for non-enzymatic electrochemical sensor. Appl Mater Today 19:100606.
<https://doi.org/10.1016/j.apmt.2020.100606>
 58. Naguib M, Kurtoglu M, Presser V, et al (2011) Two-dimensional nanocrystals produced by exfoliation of Ti 3AlC 2. Adv Mater 23:4248–4253.
<https://doi.org/10.1002/adma.201102306>
 59. Kong D, Dang W, Cha JJ, et al (2010) Few-layer nanoplates of Bi₂Se₃ and Bi₂Te₃ with highly tunable chemical potential. Nano Lett 10:2245–2250.
<https://doi.org/10.1021/nl101260j>
 60. Wu Y, Lin Z, Tian Z, et al (2016) Fabrication of Microstructured thermoelectric Bi₂Te₃ thin films by seed layer assisted electrodeposition. Mater Sci Semicond Process 46:17–22.
<https://doi.org/10.1016/j.mssp.2016.01.014>
 61. Hong SS, Kundhikanjana W, Cha JJ, et al (2010) Ultrathin topological insulator Bi₂Se₃ nanoribbons exfoliated by atomic force microscopy. Nano Lett 10:3118–3122. <https://doi.org/10.1021/nl101884h>
 62. Teweldebrhan D, Goyal V, Balandin AA (2010) Exfoliation and characterization of bismuth telluride atomic quintuples and quasi-two-dimensional crystals. Nano Lett 10:1209–1218.
<https://doi.org/10.1021/nl903590b>
 63. Marvan P, Mazánek V, Sofer Z (2019) Shear-force exfoliation of indium and

- gallium chalcogenides for selective gas sensing applications. *Nanoscale* 11:4310–4317. <https://doi.org/10.1039/c8nr09294j>
64. Chen M, Li Z, Li W, et al (2018) Large-scale synthesis of single-crystalline self-standing SnSe₂ nanoplate arrays for wearable gas sensors. *Nanotechnology* 29:455501. <https://doi.org/10.1088/1361-6528/aade32>
 65. Büchner U (1977) Wave-Vector Dependence of the Electron Energy Losses of Boron Nitride and Graphite. *Phys Status Solidi* 81:227–234. <https://doi.org/10.1002/pssb.2220810124>
 66. Lesley Smart Moore Elaine (2005) *Solid State Chemistry*. CRC Press Taylor & Francis Group
 67. Chen YX, Zhang WJ, Huang KJ, et al (2017) An electrochemical microRNA sensing platform based on tungsten diselenide nanosheets and competitive RNA-RNA hybridization. *Analyst* 142:4843–4851. <https://doi.org/10.1039/c7an01244f>
 68. Feng J, Sun X, Wu C, et al (2011) Metallic few-layered VS₂ ultrathin nanosheets: High two-dimensional conductivity for in-plane supercapacitors. *J Am Chem Soc* 133:17832–17838. <https://doi.org/10.1021/ja207176c>
 69. Hou D, Zhou W, Liu X, et al (2015) Pt nanoparticles / MoS₂ nanosheets / carbon fibers as efficient catalyst for the hydrogen evolution reaction. *Electrochim Acta* 166:26–31
 70. Sha R, Vishnu N, Badhulika S (2019) MoS₂ based ultra-low-cost, flexible, non-enzymatic and non-invasive electrochemical sensor for highly selective detection of Uric acid in human urine samples. *Sensors Actuators, B Chem* 279:53–60. <https://doi.org/10.1016/j.snb.2018.09.106>
 71. Füchtbauer HG, Tuxen AK, Moses PG, et al (2013) Morphology and atomic-scale structure of single-layer WS₂ nanoclusters. *Phys Chem Chem Phys* 15:15971–15980. <https://doi.org/10.1039/c3cp51758f>
 72. Elías AL, Perea-López N, Castro-Beltrán A, et al (2013) Controlled synthesis and transfer of large-area WS₂ sheets: From single layer to few layers. *ACS Nano* 7:5235–5242. <https://doi.org/10.1021/nn400971k>
 73. Gutiérrez HR, Perea-López N, Elías AL, et al (2013) Extraordinary room-temperature photoluminescence in triangular WS₂ monolayers. *Nano Lett* 13:3447–3454. <https://doi.org/10.1021/nl3026357>
 74. Huang J.K, Pu J., Hsu C.L, Chiu M.H., Juang Z.Y., Chang Y.H., Chang W.H.,

- Iwasa Y., Takenobu T. LLJ (2014) Large-Area Synthesis of Highly Crystalline WSe₂ Monolayers and Device Applications. *ACS Nano* 8:923–930
75. Han A, Aljarb A, Liu S, et al (2019) Growth of 2H stacked WSe₂ bilayers on sapphire. *Nanoscale Horizons* 4:1434–1442.
<https://doi.org/10.1039/c9nh00260j>
 76. Özküçük GU, Odacı C, Şahin E, et al (2020) Glass-assisted CVD growth of large-area MoS₂, WS₂ and MoSe₂ monolayers on Si/SiO₂ substrate. *Mater Sci Semicond Process* 105:104679. <https://doi.org/10.1016/j.mssp.2019.104679>
 77. Huang CC, Al-Saab F, Wang Y, et al (2014) Scalable high-mobility MoS₂ thin films fabricated by an atmospheric pressure chemical vapor deposition process at ambient temperature. *Nanoscale* 6:12792–12797.
<https://doi.org/10.1039/c4nr04228j>
 78. Ji Q, Zhang Y, Gao T, et al (2013) Epitaxial monolayer MoS₂ on mica with novel photoluminescence. *Nano Lett* 13:3870–3877.
<https://doi.org/10.1021/nl401938t>
 79. Xu H, Han X, Li Z, et al (2018) Epitaxial Growth of Few-Layer Black Phosphorene Quantum Dots on Si Substrates. *Adv Mater Interfaces* 5:1–6.
<https://doi.org/10.1002/admi.201801048>
 80. Aufray B, Kara A, Vizzini S, et al (2010) Graphene-like silicon nanoribbons on Ag(110): A possible formation of silicene. *Appl Phys Lett* 96:1–4.
<https://doi.org/10.1063/1.3419932>
 81. Jang JT, Jeong S, Seo JW, et al (2011) Ultrathin zirconium disulfide nanodiscs. *J Am Chem Soc* 133:7636–7639. <https://doi.org/10.1021/ja200400n>
 82. Frindt RF, Yoffe AD (1963) Physical properties of layer structures : optical properties and photoconductivity of thin crystals of molybdenum disulphide. *Proc R Soc London Ser A Math Phys Sci* 273:69–83.
<https://doi.org/10.1098/rspa.1963.0075>
 83. Liao Y, Zhang D, Wang Q, et al (2015) Open-top TiO₂ nanotube arrays with enhanced photovoltaic and photochemical performances via a micromechanical cleavage approach. *J Mater Chem A* 3:14279–14283.
<https://doi.org/10.1039/c5ta02799c>
 84. Mahesh K V., Rashada R, Kiran M, et al (2015) Shear induced micromechanical synthesis of Ti₃SiC₂ MAXene nanosheets for functional applications. *RSC Adv* 5:51242–51247. <https://doi.org/10.1039/c5ra07756g>

85. Magda GZ, Petõ J, Dobrik G, et al (2015) Exfoliation of large-area transition metal chalcogenide single layers. *Sci Rep* 5:3–7.
<https://doi.org/10.1038/srep14714>
86. Suryawanshi SR, More MA, Late DJ (2016) Exfoliated 2D black phosphorus nanosheets: Field emission studies. *J Vac Sci Technol B, Nanotechnol Microelectron Mater Process Meas Phenom* 34:041803.
<https://doi.org/10.1116/1.4945433>
87. Castellanos-Gomez A, Agrat N, Rubio-Bollinger G (2010) Optical identification of atomically thin dichalcogenide crystals. *Appl Phys Lett* 96:94–97. <https://doi.org/10.1063/1.3442495>
88. Yu Y, Jiang S, Zhang G, et al (2012) Universal ultrafast sandpaper assisting rubbing method for room temperature fabrication of two-dimensional nanosheets directly on flexible polymer substrate. *Appl Phys Lett* 101:073113.
<https://doi.org/10.1063/1.4746755>
89. Gacem K, Boukhicha M, Chen Z, Shukla A (2012) High quality 2D crystals made by anodic bonding: A general technique for layered materials. *Nanotechnology* 23:1–6. <https://doi.org/10.1088/0957-4484/23/50/505709>
90. Moldt T, Eckmann A, Klar P, et al (2011) High-Yield Production and Transfer of Graphene Flakes Obtained by Anodic Bonding. *ACS Nano* 5:7700–7706.
<https://doi.org/10.1021/nn202293f>
91. Shen Z, Li J, Yi M, et al (2011) Preparation of graphene by jet cavitation. *Nanotechnology* 22:365306. <https://doi.org/10.1088/0957-4484/22/36/365306>
92. Lohse D (2005) Sonoluminescence: Cavitation hots up. *Nature* 434:33–34.
<https://doi.org/10.1038/434033a>
93. Štengl V, Henych J (2013) Strongly luminescent monolayered MoS₂ prepared by effective ultrasound exfoliation. *Nanoscale* 5:3387–3394.
<https://doi.org/10.1039/c3nr00192j>
94. May P, Khan U, Hughes JM, Coleman JN (2012) Role of solubility parameters in understanding the steric stabilization of exfoliated two-dimensional nanosheets by adsorbed polymers. *J Phys Chem C* 116:11393–11400.
<https://doi.org/10.1021/jp302365w>
95. Hughes JM, Aherne D, Coleman JN (2013) Generalizing solubility parameter theory to apply to one- and two-dimensional solutes and to incorporate dipolar interactions. *J Appl Polym Sci* 127:4483–4491.

- <https://doi.org/10.1002/app.38051>
96. Hernandez Y, Nicolosi V, Lotya M, et al (2008) High-yield production of graphene by liquid-phase exfoliation of graphite. *Nat Nanotechnol* 3:563–568. <https://doi.org/10.1038/nnano.2008.215>
 97. Kang J, Wells SA, Wood JD, et al (2016) Stable aqueous dispersions of optically and electronically active phosphorene. *Proc Natl Acad Sci U S A* 113:11688–11693. <https://doi.org/10.1073/pnas.1602215113>
 98. Guan Z, Wang C, Li W, et al (2018) A facile and clean process for exfoliating MoS₂ nanosheets assisted by a surface active agent in aqueous solution. *Nanotechnology* 29:. <https://doi.org/10.1088/1361-6528/aad676>
 99. Gusmão R, Sofer Z, Bouša D, Pumera M (2017) Pnictogen (As, Sb, Bi) Nanosheets for Electrochemical Applications Are Produced by Shear Exfoliation Using Kitchen Blenders. *Angew Chemie - Int Ed* 56:14417–14422. <https://doi.org/10.1002/anie.201706389>
 100. Griffin A, Nisi K, Pepper J, et al (2020) Effect of Surfactant Choice and Concentration on the Dimensions and Yield of Liquid-Phase-Exfoliated Nanosheets. *Chem Mater* 32:2852–2862. <https://doi.org/10.1021/acs.chemmater.9b04684>
 101. Chen X, Dobson JF, Raston CL (2012) Vortex fluidic exfoliation of graphite and boron nitride. *Chem Commun* 48:3703–3705. <https://doi.org/10.1039/c2cc17611d>
 102. Paton KR, Varrla E, Backes C, et al (2014) Scalable production of large quantities of defect-free few-layer graphene by shear exfoliation in liquids. *Nat Mater* 13:624–630. <https://doi.org/10.1038/nmat3944>
 103. Varrla E, Backes C, Paton KR, et al (2015) Large-scale production of size-controlled MoS₂ nanosheets by shear exfoliation. *Chem Mater* 27:1129–1139. <https://doi.org/10.1021/cm5044864>
 104. Mayorga-Martinez CC, Gusmão R, Sofer Z, Pumera M (2019) Pnictogen-Based Enzymatic Phenol Biosensors: Phosphorene, Arsenene, Antimonene, and Bismuthene. *Angew Chemie Int Ed* 58:134–138. <https://doi.org/https://doi.org/10.1002/anie.201808846>
 105. Mayorga-Martinez CC, Gusmão R, Sofer Z, Pumera M (2019) Pnictogen-Based Enzymatic Phenol Biosensors: Phosphorene, Arsenene, Antimonene, and Bismuthene. *Angew Chemie - Int Ed* 58:134–138.

- <https://doi.org/10.1002/anie.201808846>
106. Mähler J, Persson I (2012) A study of the hydration of the alkali metal ions in aqueous solution. *Inorg Chem* 51:425–438. <https://doi.org/10.1021/ic2018693>
 107. Ding Z, Viculis L, Nakawatase J, Kaner RB (2001) Intercalation and solution processing of bismuth telluride and bismuth selenide. *Adv Mater* 13:797–800. [https://doi.org/10.1002/1521-4095\(200106\)13:11<797::AID-ADMA797>3.0.CO;2-U](https://doi.org/10.1002/1521-4095(200106)13:11<797::AID-ADMA797>3.0.CO;2-U)
 108. Ren L, Qi X, Liu Y, et al (2012) Large-scale production of ultrathin topological insulator bismuth telluride nanosheets by a hydrothermal intercalation and exfoliation route. *J Mater Chem* 22:4921–4926. <https://doi.org/10.1039/c2jm15973b>
 109. Zhu J, Wang H, Liu J, et al (2017) Exfoliation of MoS₂ and h-BN nanosheets by hydrolysis of LiBH₄. *Nanotechnology* 28:115604. <https://doi.org/10.1088/1361-6528/aa5964>
 110. Joensen P, Frindt RF, Morrison SR (1986) Single-layer MoS₂. *Mater Res Bull* 21:457–461. [https://doi.org/10.1016/0025-5408\(86\)90011-5](https://doi.org/10.1016/0025-5408(86)90011-5)
 111. Loo AH, Bonanni A, Sofer Z, Pumera M (2015) Exfoliated transition metal dichalcogenides (MoS₂, MoSe₂, WS₂, WSe₂): An electrochemical impedance spectroscopic investigation. *Electrochem commun* 50:39–42. <https://doi.org/10.1016/j.elecom.2014.10.018>
 112. Dines MB (1975) Lithium intercalation via n-Butyllithium of the layered transition metal dichalcogenides. *Mater Res Bull* 10:287–291. [https://doi.org/10.1016/0025-5408\(75\)90115-4](https://doi.org/10.1016/0025-5408(75)90115-4)
 113. Zeng Z, Sun T, Zhu J, et al (2012) An effective method for the fabrication of few-layer-thick inorganic nanosheets. *Angew Chemie - Int Ed* 51:9052–9056. <https://doi.org/10.1002/anie.201204208>
 114. Zeng Z, Yin Z, Huang X, et al (2011) Single-layer semiconducting nanosheets: High-yield preparation and device fabrication. *Angew Chemie - Int Ed* 50:11093–11097. <https://doi.org/10.1002/anie.201106004>
 115. Yang QQ, Liu RT, Huang C, et al (2018) 2D bismuthene fabricated: Via acid-intercalated exfoliation showing strong nonlinear near-infrared responses for mode-locking lasers. *Nanoscale* 10:21106–21115. <https://doi.org/10.1039/c8nr06797j>
 116. Liu N, Kim P, Kim JH, et al (2014) Large-area atomically thin MoS₂

- nanosheets prepared using electrochemical exfoliation. *ACS Nano* 8:6902–6910. <https://doi.org/10.1021/nn5016242>
117. Li F, Xue M, Zhang X, et al (2018) Advanced Composite 2D Energy Materials by Simultaneous Anodic and Cathodic Exfoliation. *Adv Energy Mater* 8:1–8. <https://doi.org/10.1002/aenm.201702794>
 118. Yang S, Zhang K, Ricciardulli AG, et al (2018) A Delamination Strategy for Thinly Layered Defect-Free High-Mobility Black Phosphorus Flakes. *Angew Chemie - Int Ed* 57:4677–4681. <https://doi.org/10.1002/anie.201801265>
 119. Xiao H, Zhao M, Zhang J, et al (2018) Electrochemical cathode exfoliation of bulky black phosphorus into few-layer phosphorene nanosheets. *Electrochem commun* 89:10–13. <https://doi.org/10.1016/j.elecom.2018.02.010>
 120. Li F, Xue M, Li J, et al (2017) Unlocking the Electrocatalytic Activity of Antimony for CO₂ Reduction by Two-Dimensional Engineering of the Bulk Material. *Angew Chemie - Int Ed* 56:14718–14722. <https://doi.org/10.1002/anie.201710038>
 121. Lu L, Tang X, Cao R, et al (2017) Broadband Nonlinear Optical Response in Few-Layer Antimonene and Antimonene Quantum Dots: A Promising Optical Kerr Media with Enhanced Stability. *Adv Opt Mater* 5:1–9. <https://doi.org/10.1002/adom.201700301>
 122. Lin Z, Liu Y, Halim U, et al (2018) Solution-processable 2D semiconductors for high-performance large-area electronics. *Nature* 562:254–258. <https://doi.org/10.1038/s41586-018-0574-4>
 123. Yang S, Zhang P, Wang F, et al (2018) Fluoride-Free Synthesis of Two-Dimensional Titanium Carbide (MXene) Using A Binary Aqueous System. *Angew Chemie* 130:15717–15721. <https://doi.org/10.1002/ange.201809662>
 124. Ma L, Zhang Q, Wu C, et al (2019) PtNi bimetallic nanoparticles loaded MoS₂ nanosheets: Preparation and electrochemical sensing application for the detection of dopamine and uric acid. *Anal Chim Acta* 1055:17–25. <https://doi.org/10.1016/j.aca.2018.12.025>
 125. Zhu L, Zhang Y, Xu P, et al (2016) PtW/MoS₂ hybrid nanocomposite for electrochemical sensing of H₂O₂ released from living cells. *Biosens Bioelectron* 80:601–606. <https://doi.org/10.1016/j.bios.2016.02.019>
 126. Gan X, Zhao H, Quan X, Zhang Y (2016) An Electrochemical Sensor based on p-aminothiophenol/Au Nanoparticle-Decorated HxTiS₂ Nanosheets for

- Specific Detection of Picomolar Cu (II). *Electrochim Acta* 190:480–489.
<https://doi.org/10.1016/j.electacta.2015.12.145>
127. Cui S, Wen Z, Huang X, et al (2015) Stabilizing MoS₂ nanosheets through SnO₂ nanocrystal decoration for high-performance gas sensing in air. *Small* 11:2305–2313. <https://doi.org/10.1002/sml.201402923>
 128. Xu K, Tang Q, Zhao W, et al (2020) In situ growth of Co₃O₄@NiMoO₄ composite arrays on alumina substrate with improved triethylamine sensing performance. *Sensors Actuators, B Chem* 302:127154.
<https://doi.org/10.1016/j.snb.2019.127154>
 129. Xu H, Ju J, Li W, et al (2016) Superior triethylamine-sensing properties based on TiO₂/SnO₂ n-n heterojunction nanosheets directly grown on ceramic tubes. *Sensors Actuators, B Chem* 228:634–642.
<https://doi.org/10.1016/j.snb.2016.01.059>
 130. Rasheed PA, Pandey RP, Rasool K, Mahmoud KA (2018) Ultra-sensitive electrocatalytic detection of bromate in drinking water based on Nafion/Ti₃C₂Tx (MXene) modified glassy carbon electrode. *Sensors Actuators, B Chem* 265:652–659. <https://doi.org/10.1016/j.snb.2018.03.103>
 131. Elumalai S, Mani V, Jeromiyas N, et al (2020) A composite film prepared from titanium carbide Ti₃C₂Tx (MXene) and gold nanoparticles for voltammetric determination of uric acid and folic acid. *Microchim Acta* 187:33.
<https://doi.org/10.1007/s00604-019-4018-0>
 132. Shankar SS, Shereema RM, Rakhi RB (2018) Electrochemical Determination of Adrenaline Using MXene/Graphite Composite Paste Electrodes. *ACS Appl Mater Interfaces* 10:43343–43351. <https://doi.org/10.1021/acsami.8b11741>
 133. Tai H, Duan Z, He Z, et al (2019) Enhanced ammonia response of Ti₃C₂Tx nanosheets supported by TiO₂ nanoparticles at room temperature. *Sensors Actuators, B Chem* 298:126874. <https://doi.org/10.1016/j.snb.2019.126874>
 134. Cui S, Pu H, Wells SA, et al (2015) Ultrahigh sensitivity and layer-dependent sensing performance of phosphorene-based gas sensors. *Nat Commun* 6:.
<https://doi.org/10.1038/ncomms9632>
 135. Niu X, Weng W, Yin C, et al (2018) Black phosphorene modified glassy carbon electrode for the sensitive voltammetric detection of rutin. *J Electroanal Chem* 811:78–83. <https://doi.org/10.1016/j.jelechem.2018.01.038>
 136. Li X, Luo G, Xie H, et al (2019) Voltammetric sensing performances of a

- carbon ionic liquid electrode modified with black phosphorene and hemin. *Microchim Acta* 186:304. <https://doi.org/10.1007/s00604-019-3421-x>
137. Ramalingam S, Chand R, Singh CB, Singh A (2019) Phosphorene-gold nanocomposite based microfluidic aptasensor for the detection of okadaic acid. *Biosens Bioelectron* 135:14–21. <https://doi.org/10.1016/j.bios.2019.03.056>
 138. Pawar M, Kadam S, Late DJ (2017) High-Performance Sensing Behavior Using Electronic Ink of 2D SnSe₂ Nanosheets. *ChemistrySelect* 2:4068–4075. <https://doi.org/10.1002/slct.201700261>
 139. Wang S, Zhang S, Liu M, et al (2018) MoS₂ as connector inspired high electrocatalytic performance of NiCo₂O₄ nanoplates towards glucose. *Sensors Actuators, B Chem* 254:1101–1109. <https://doi.org/10.1016/j.snb.2017.08.011>
 140. Shuai HL, Huang KJ, Chen YX (2016) A layered tungsten disulfide/acetylene black composite based DNA biosensing platform coupled with hybridization chain reaction for signal amplification. *J Mater Chem B* 4:1186–1196. <https://doi.org/10.1039/c5tb02214b>
 141. Li, Aixue, Zhang Jian, Qiu Jichuan, Zhao Zhenhuan, Wang Cheng, Zhao Chunjiang LH (2017) A novel aptameric biosensor based on the self-assembled DNA–WS₂ nanosheet architecture. *Talanta* 163:78–84
 142. Zhu C, Zeng Z, Li H, et al (2013) Single-layer MoS₂-based nanoprobe for homogeneous detection of biomolecules. *J Am Chem Soc* 135:5998–6001. <https://doi.org/10.1021/ja4019572>
 143. Della Pelle F, Rojas D, Silveri F, et al (2020) Class-selective voltammetric determination of hydroxycinnamic acids structural analogs using a WS₂/catechin-capped AuNPs/carbon black-based nanocomposite sensor. *Microchim Acta* 187:296. <https://doi.org/10.1007/s00604-020-04281-z>
 144. Toh RJ, Mayorga-Martinez CC, Han J, et al (2017) Group 6 Layered Transition-Metal Dichalcogenides in Lab-on-a-Chip Devices: 1T-Phase WS₂ for Microfluidics Non-Enzymatic Detection of Hydrogen Peroxide. *Anal Chem* 89:4978–4985. <https://doi.org/10.1021/acs.analchem.7b00302>
 145. Guo GY, Liang WY (1986) The electronic structures of platinum dichalcogenides: PtS₂, PtSe₂ and PtTe₂. *J Phys C Solid State Phys* 19:995–1008. <https://doi.org/10.1088/0022-3719/19/7/011>
 146. Han TL, Wan YT, Li JJ, et al (2017) In situ gold nanoparticle-decorated three-dimensional tin dioxide nanostructures for sensitive and selective gas-sensing

- detection of volatile organic compounds. *J Mater Chem C* 5:6193–6201.
<https://doi.org/10.1039/c7tc01496a>
147. Chen WY, Yen CC, Xue S, et al (2019) Surface Functionalization of Layered Molybdenum Disulfide for the Selective Detection of Volatile Organic Compounds at Room Temperature. *ACS Appl Mater Interfaces* 11:34135–34143. <https://doi.org/10.1021/acsami.9b13827>
 148. Guo S, Yang D, Zhang S, et al (2019) Development of a Cloud-Based Epidermal MoSe₂ Device for Hazardous Gas Sensing. *Adv Funct Mater* 29:1–10. <https://doi.org/10.1002/adfm.201900138>
 149. Shu Y, Xu J, Chen J, et al (2017) Ultrasensitive electrochemical detection of H₂O₂ in living cells based on ultrathin MnO₂ nanosheets. *Sensors Actuators, B Chem* 252:72–78. <https://doi.org/10.1016/j.snb.2017.05.124>
 150. Zhang S, Zhuang X, Chen D, et al (2019) Simultaneous voltammetric determination of guanine and adenine using MnO₂ nanosheets and ionic liquid-functionalized graphene combined with a permeation-selective polydopamine membrane. *Microchim Acta* 186:450. <https://doi.org/10.1007/s00604-019-3577-4>
 151. Yang T, Tian L, Zhou E, et al (2019) Design of Ni(OH)₂ nanocages@MnO₂ nanosheets core-shell architecture to jointly facilitate electrocatalytic dynamic for highly sensitive detection of dopamine. *Biosens Bioelectron* 143:111634. <https://doi.org/10.1016/j.bios.2019.111634>
 152. Mahmoudian MR, Basirun WJ, Woi PM, et al (2016) Synthesis and characterization of Co₃O₄ ultra-nanosheets and Co₃O₄ ultra-nanosheet-Ni(OH)₂ as non-enzymatic electrochemical sensors for glucose detection. *Mater Sci Eng C* 59:500–508. <https://doi.org/10.1016/j.msec.2015.10.055>
 153. Vabbina PK, Kaushik A, Pokhrel N, et al (2015) Electrochemical cortisol immunosensors based on sonochemically synthesized zinc oxide 1D nanorods and 2D nanoflakes. *Biosens Bioelectron* 63:124–130. <https://doi.org/10.1016/j.bios.2014.07.026>
 154. Gong M, Li Y, Guo Y, et al (2018) 2D TiO₂ nanosheets for ultrasensitive humidity sensing application benefited by abundant surface oxygen vacancy defects. *Sensors Actuators, B Chem* 262:350–358. <https://doi.org/10.1016/j.snb.2018.01.187>
 155. Lorencova L, Bertok T, Filip J, et al (2018) Highly stable Ti₃C₂T_x (MXene)/Pt

- nanoparticles-modified glassy carbon electrode for H₂O₂ and small molecules sensing applications. *Sensors Actuators, B Chem* 263:360–368.
<https://doi.org/10.1016/j.snb.2018.02.124>
156. Liu J, Jiang X, Zhang R, et al (2019) MXene-Enabled Electrochemical Microfluidic Biosensor: Applications toward Multicomponent Continuous Monitoring in Whole Blood. *Adv Funct Mater* 29:1–9.
<https://doi.org/10.1002/adfm.201807326>
 157. Wang H, Sun J, Lu L, et al (2020) Competitive electrochemical aptasensor based on a cDNA-ferrocene/MXene probe for detection of breast cancer marker Mucin1. *Anal Chim Acta* 1094:18–25.
<https://doi.org/10.1016/j.aca.2019.10.003>
 158. Duan F, Guo C, Hu M, et al (2020) Construction of the 0D/2D heterojunction of Ti₃C₂T_x MXene nanosheets and iron phthalocyanine quantum dots for the impedimetric aptasensing of microRNA-155. *Sensors Actuators, B Chem* 310:127844. <https://doi.org/10.1016/j.snb.2020.127844>
 159. Lei Y, Zhao W, Zhang Y, et al (2019) A MXene-Based Wearable Biosensor System for High-Performance In Vitro Perspiration Analysis. *Small* 15:1901190. <https://doi.org/10.1002/sml.201901190>
 160. Koyappayil A, Chavan SG, Mohammadniaei M, et al (2020) β -Hydroxybutyrate dehydrogenase decorated MXene nanosheets for the amperometric determination of β -hydroxybutyrate. *Microchim Acta* 187:277.
<https://doi.org/10.1007/s00604-020-04258-y>
 161. Song M, Pang S-Y, Guo F, et al (2020) Fluoride-Free 2D Niobium Carbide MXenes as Stable and Biocompatible Nanoplatfoms for Electrochemical Biosensors with Ultrahigh Sensitivity. *Adv Sci* 7:2001546.
<https://doi.org/https://doi.org/10.1002/advs.202001546>
 162. Devi RK, Ganesan M, Chen T-W, et al (2022) Vanadium carbide and nitrogen-doped graphene nanosheets based layered architecture for electrochemical evaluation of clioquinol detection and energy storage application. *Electrochim Acta* 408:139930.
<https://doi.org/https://doi.org/10.1016/j.electacta.2022.139930>
 163. Lee E, Vahidmohammadi A, Prorok BC, et al (2017) Room Temperature Gas Sensing of Two-Dimensional Titanium Carbide (MXene). *ACS Appl Mater Interfaces* 9:37184–37190. <https://doi.org/10.1021/acsami.7b11055>

164. Kim SJ, Koh HJ, Ren CE, et al (2018) Metallic Ti₃C₂T_x MXene Gas Sensors with Ultrahigh Signal-to-Noise Ratio. *ACS Nano* 12:986–993.
<https://doi.org/10.1021/acsnano.7b07460>
165. Lee E, Vahidmohammadi A, Yoon YS, et al (2019) Two-Dimensional Vanadium Carbide MXene for Gas Sensors with Ultrahigh Sensitivity Toward Nonpolar Gases. *ACS Sensors* 4:1603–1611.
<https://doi.org/10.1021/acssensors.9b00303>
166. Mayorga-Martinez CC, Sofer Z, Pumera M (2015) Layered Black Phosphorus as a Selective Vapor Sensor. *Angew Chemie - Int Ed* 54:14317–14320.
<https://doi.org/10.1002/anie.201505015>
167. García-Mendiola T, Gutiérrez-Sánchez C, Gibaja C, et al (2020) Functionalization of a Few-Layer Antimonene with Oligonucleotides for DNA Sensing. *ACS Appl Nano Mater* 3:3625–3633.
<https://doi.org/10.1021/acsanm.0c00335>
168. Beladi-Mousavi SM, Pourrahimi AM, Sofer Z, Pumera M (2019) Atomically Thin 2D-Arsenene by Liquid-Phased Exfoliation: Toward Selective Vapor Sensing. *Adv Funct Mater* 29:1–7. <https://doi.org/10.1002/adfm.201807004>
169. Khan AF, Brownson DAC, Randviir EP, et al (2016) 2D Hexagonal Boron Nitride (2D-hBN) Explored for the Electrochemical Sensing of Dopamine. *Anal Chem* 88:9729–9737. <https://doi.org/10.1021/acs.analchem.6b02638>
170. Fu L, Liu Z, Huang Y, et al (2018) Square wave voltammetric quantitative determination of flavonoid luteolin in peanut hulls and Perilla based on Au NPs loaded boron nitride nanosheets. *J Electroanal Chem* 817:128–133.
<https://doi.org/10.1016/j.jelechem.2018.04.009>
171. He Y, Li D, Gao W, et al (2019) High-performance NO₂ sensors based on spontaneously functionalized hexagonal boron nitride nanosheets: Via chemical exfoliation. *Nanoscale* 11:21909–21916.
<https://doi.org/10.1039/c9nr07153a>
172. Wang J (2006) Study of Electrode Reactions and Interfacial Properties. *Anal. Electrochem.* 29–66
173. Delahay P (1953) Theory of Irreversible Waves in Oscillographic Polarography. *J Am Chem Soc* 75:1190–1196.
<https://doi.org/10.1021/ja01101a054>
174. Nicholson RS (1965) Theory and Application of Cyclic Voltammetry for

- Measurement of Electrode Reaction Kinetics. *Anal Chem* 37:1351–1355.
<https://doi.org/10.1021/ac60230a016>
175. Barker GC, Jenkins IL (1952) Square-wave polarography. *Analyst* 77:685–696.
<https://doi.org/10.1039/AN9527700685>
 176. Wang J (2006) Controlled-Potential Techniques. *Anal. Electrochem.* 67–114
 177. Wang J (1985) Stripping Analysis: Principles, Instrumentation and applications. VCH Publishers Inc., New York
 178. Copeland TR, Osteryoung RA, Skogerboe RK (1974) Elimination of copper-zinc intermetallic interferences in anodic stripping voltammetry. *Anal Chem* 46:2093–2097. <https://doi.org/10.1021/ac60350a036>
 179. Modasia D, Modasia R (2021) Regulation (EU) 2017/852 of the European Parliament and of the Council of 17 May 2017 on mercury, and repealing Regulation (EC) No 1102/2008. *Off J Eur Union* 28:42–43
 180. Van der Linden WE, Dieker JW (1980) Glassy carbon as electrode material in electro- analytical chemistry. *Anal Chim Acta* 119:1–24.
[https://doi.org/https://doi.org/10.1016/S0003-2670\(00\)00025-8](https://doi.org/https://doi.org/10.1016/S0003-2670(00)00025-8)
 181. Li D, Li J, Jia X, et al (2012) Electrochemical determination of arsenic(III) on mercaptoethylamine modified Au electrode in neutral media. *Anal Chim Acta* 733:23–27. <https://doi.org/https://doi.org/10.1016/j.aca.2012.04.030>
 182. Raj CR, Ohsaka T (2001) Electroanalysis of ascorbate and dopamine at a gold electrode modified with a positively charged self-assembled monolayer. *J Electroanal Chem* 496:44–49. [https://doi.org/https://doi.org/10.1016/S0022-0728\(00\)00335-1](https://doi.org/https://doi.org/10.1016/S0022-0728(00)00335-1)
 183. Surmann P, Channaa H (2015) Anodic Stripping Voltammetry with Galinstan as Working Electrode. *Electroanalysis* 27:1726–1732.
<https://doi.org/https://doi.org/10.1002/elan.201400752>
 184. Channaa, H. and Surmann P (2009) Voltammetric analysis of N-containing drugs using the hanging galinstan drop electrode (HGDE). *Die Pharm - An Int J Pharm Sci* 64:
 185. Wang J, Lu J, Hocevar SB, et al (2000) Bismuth-coated carbon electrodes for anodic stripping voltammetry. *Anal Chem* 72:3218–3222.
<https://doi.org/10.1021/ac000108x>
 186. Wang J, Lu J (2000) Bismuth film electrodes for adsorptive stripping voltammetry of trace nickel. *Electrochem commun* 2:390–393.

- [https://doi.org/10.1016/S1388-2481\(00\)00045-X](https://doi.org/10.1016/S1388-2481(00)00045-X)
187. Cole KS, Cole RH (1941) Dispersion and Absorption in Dielectrics I. Alternating Current Characteristics. *J Chem Phys* 9:341–351.
<https://doi.org/10.1063/1.1750906>
 188. Sluyters JH (1960) On the impedance of galvanic cells: I. Theory. *Recl des Trav Chim des Pays-Bas* 79:1092–1100.
<https://doi.org/https://doi.org/10.1002/recl.19600791013>
 189. Connor P, Schuch J, Kaiser B, Jaegermann W (2020) The Determination of Electrochemical Active Surface Area and Specific Capacity Revisited for the System MnOx as an Oxygen Evolution Catalyst. *Zeitschrift fur Phys Chemie* 234:979–994. <https://doi.org/10.1515/zpch-2019-1514>
 190. Honeychurch KC (2012) 13 - Printed thick-film biosensors. In: Prudenziati M, Hormadaly JBT-PF (eds) *Woodhead Publishing Series in Electronic and Optical Materials*. Woodhead Publishing, pp 366–409
 191. Mishra RK, Nunes GS, Souto L, Marty JL (2018) Screen Printed Technology—An Application Towards Biosensor Development. In: Wandelt KBT-E of IC (ed). Elsevier, Oxford, pp 487–498
 192. Fini A, Fazio G, Gonzalez-Rodriguez M, et al (1999) Formation of ion-pairs in aqueous solutions of diclofenac salts. *Int J Pharm* 187:163–173.
[https://doi.org/https://doi.org/10.1016/S0378-5173\(99\)00180-5](https://doi.org/https://doi.org/10.1016/S0378-5173(99)00180-5)
 193. Kovala-Demertzi D, Mentzafos D, Terzis A (1993) Metal complexes of the anti-inflammatory drug sodium [2-[(2,6-dichlorophenyl)amino]phenyl]acetate (diclofenac sodium). Molecular and crystal structure of cadmium diclofenac. *Polyhedron* 12:1361–1370. [https://doi.org/https://doi.org/10.1016/S0277-5387\(00\)84327-2](https://doi.org/https://doi.org/10.1016/S0277-5387(00)84327-2)
 194. Lingam K, Reppert J, Dickel D, et al (2012) Reexamination of infrared spectra of Bi nanorods: L-T transition or extrinsic phases. *Nano* 7
 195. Lannin JS, Calleja JM, Cardona M (1975) Second-order Raman scattering in the group-Vb semimetals: Bi, Sb, and As. *Phys Rev B* 12:585–593.
<https://doi.org/10.1103/PhysRevB.12.585>
 196. Díaz-Guerra C, Almodóvar P, Camacho-López M, et al (2017) Formation of β -Bi₂O₃ and δ -Bi₂O₃ during laser irradiation of Bi films studied in-situ by spatially resolved Raman spectroscopy. *J Alloys Compd* 723:520–526.
<https://doi.org/10.1016/j.jallcom.2017.06.263>

197. Pereira ALJ, Gomis O, Bulou A, et al (1997) Related content Raman spectra and lattice dynamics of single- Raman spectra and lattice dynamics of single-crystal
198. In J, Yoon I, Seo K, et al (2011) Polymorph-tuned synthesis of α -And β -Bi₂O₃ nanowires and determination of their growth direction from polarized raman single nanowire microscopy. *Chem - A Eur J* 17:1304–1309.
<https://doi.org/10.1002/chem.201001684>
199. Mohamed Ismail M, Vigneshwaran J, Arunbalaji S, et al (2020) Antimonene nanosheets with enhanced electrochemical performance for energy storage applications. *Dalt Trans* 49:13717–13725.
<https://doi.org/10.1039/D0DT01753A>
200. Assebban M, Gibaja C, Fickert M, et al (2020) Unveiling the oxidation behavior of liquid-phase exfoliated antimony nanosheets. *2D Mater* 7:25039.
<https://doi.org/10.1088/2053-1583/ab755e>
201. Xu T, Yang D, Zhang S, et al (2021) Antifreezing and stretchable all-gel-state supercapacitor with enhanced capacitances established by graphene/PEDOT-polyvinyl alcohol hydrogel fibers with dual networks. *Carbon N Y* 171:201–210. <https://doi.org/10.1016/j.carbon.2020.08.071>
202. Zhao Q, Jamal R, Zhang L, et al (2014) The structure and properties of PEDOT synthesized by template-free solution method. *Nanoscale Res Lett* 9:557.
<https://doi.org/10.1186/1556-276X-9-557>
203. Kaviyarasu K, Sajan D, Devarajan PA (2013) A rapid and versatile method for solvothermal synthesis of Sb₂O₃ nanocrystals under mild conditions. *Appl Nanosci* 3:529–533. <https://doi.org/10.1007/s13204-012-0156-y>
204. Zhang L, Pan C-L, Liu Y (2012) Gram-scale synthesis and optical properties of Sb₂O₃ octahedron microcrystals. *Mater Lett* 75:29–32.
<https://doi.org/https://doi.org/10.1016/j.matlet.2012.01.119>
205. Zhang S, Zhou W, Ma Y, et al (2017) Antimonene Oxides: Emerging Tunable Direct Bandgap Semiconductor and Novel Topological Insulator. *Nano Lett* 17:3434–3440. <https://doi.org/10.1021/acs.nanolett.7b00297>
206. Baig Z, Mamat O, Mustapha M, et al (2018) Investigation of tip sonication effects on structural quality of graphene nanoplatelets (GNPs) for superior solvent dispersion. *Ultrason Sonochem* 45:133–149.
<https://doi.org/https://doi.org/10.1016/j.ultsonch.2018.03.007>

207. Lotya M, King PJ, Khan U, et al (2010) High-Concentration, Surfactant-Stabilized Graphene Dispersions. *ACS Nano* 4:3155–3162.
<https://doi.org/10.1021/nn1005304>
208. Rui X, Lu Z, Yu H, et al (2013) Ultrathin V₂O₅ nanosheet cathodes: realizing ultrafast reversible lithium storage. *Nanoscale* 5:556–560.
<https://doi.org/10.1039/C2NR33422D>
209. Surya Bhaskaram D, Cheruku R, Govindaraj G (2016) Reduced graphene oxide wrapped V₂O₅ nanoparticles: green synthesis and electrical properties. *J Mater Sci Mater Electron* 27:10855–10863. <https://doi.org/10.1007/s10854-016-5194-x>
210. Shafeeq KM, Athira VP, Kishor CHR, Aneesh PM (2020) Structural and optical properties of V₂O₅ nanostructures grown by thermal decomposition technique. *Appl Phys A* 126:586. <https://doi.org/10.1007/s00339-020-03770-5>
211. Wang C, Yi Y, Li H, et al (2020) Rapid gas-assisted exfoliation promises V₂O₅ nanosheets for high performance lithium-sulfur batteries. *Nano Energy* 67:104253. <https://doi.org/https://doi.org/10.1016/j.nanoen.2019.104253>
212. Trachioti MG, Prodromidis MI (2020) Humidity impedimetric sensor based on vanadium pentoxide xerogel modified screen-printed graphite electrochemical cell. *Talanta* 216:121003.
<https://doi.org/https://doi.org/10.1016/j.talanta.2020.121003>
213. Novoselov KS, Geim AK, Morozov S V., et al (2004) Electric field in atomically thin carbon films. *Science* (80-) 306:666–669.
<https://doi.org/10.1126/science.1102896>
214. Radisavljevic B, Radenovic A, Brivio J, et al (2011) Single-layer MoS₂ transistors. *Nat Nanotechnol* 6:147–150.
<https://doi.org/10.1038/nnano.2010.279>
215. Eftekhari A (2017) Tungsten dichalcogenides (WS₂, WSe₂, and WTe₂): Materials chemistry and applications. *J. Mater. Chem. A* 5:18299–18325
216. Hsieh D, Xia Y, Qian D, et al (2009) A tunable topological insulator in the spin helical Dirac transport regime. *Nature* 460:1101–1105.
<https://doi.org/10.1038/nature08234>
217. Tao L, Cinquanta E, Chiappe D, et al (2015) Silicene field-effect transistors operating at room temperature. *Nat Nanotechnol* 10:227–231.
<https://doi.org/10.1038/nnano.2014.325>

218. Ni Z, Liu Q, Tang K, et al (2012) Tunable bandgap in silicene and germanene. *Nano Lett* 12:113–118. <https://doi.org/10.1021/nl203065e>
219. Takahashi L, Takahashi K (2015) Low temperature pollutant trapping and dissociation over two-dimensional tin. *Phys Chem Chem Phys* 17:21394–21396. <https://doi.org/10.1039/c5cp03382a>
220. Sturala J, Sofer Z, Pumera M (2019) Chemistry of Layered Pnictogens: Phosphorus, Arsenic, Antimony, and Bismuth. *Angew. Chemie - Int. Ed.* 58:7551–7557
221. Backes C, Higgins TM, Kelly A, et al Guidelines for Exfoliation , Characterisation and Processing of Layered Materials Produced by Liquid Exfoliation. 1–37
222. Jovanovski V, Hočevár SB, Ogorevc B (2017) Bismuth electrodes in contemporary electroanalysis. *Curr Opin Electrochem* 3:114–122. <https://doi.org/10.1016/j.coelec.2017.07.008>
223. Mantzila AG, Strongylis C, Tsikaris V, Prodromidis MI (2007) Assessment of the interaction between a synthetic epitope of troponin C and its specific antibody using a label-free faradaic impedimetric immunosensor and α -Keggin silicotungstic heteropolyacid as a redox probe. *Biosens Bioelectron.* <https://doi.org/10.1016/j.bios.2007.04.017>
224. Zhang S, Xie M, Li F, et al (2016) Semiconducting Group 15 Monolayers: A Broad Range of Band Gaps and High Carrier Mobilities. *Angew Chemie - Int Ed* 55:1666–1669. <https://doi.org/10.1002/anie.201507568>
225. Sopha H, Baldrianová L, Tesařová E, et al (2010) A new type of bismuth electrode for electrochemical stripping analysis based on the ammonium tetrafluorobismuthate bulk-modified carbon paste. *Electroanalysis* 22:1489–1493. <https://doi.org/10.1002/elan.201070010>
226. Dimovasilis PA, Prodromidis MI (2013) Bismuth-dispersed xerogel-based composite films for trace Pb(II) and Cd(II) voltammetric determination. *Anal Chim Acta* 769:49–55. <https://doi.org/10.1016/j.aca.2013.01.040>
227. Dimovasilis PA, Prodromidis MI (2016) Preparation of Screen-Printed Compatible Bismuth-Modified Sol-Gel Microspheres: Application to the Stripping Voltammetric Determination of Lead and Cadmium. *Anal Lett* 49:979–989. <https://doi.org/10.1080/00032719.2015.1027896>
228. Malakhova NA, Stojko NY, Brainina KZ (2007) Novel approach to bismuth

- modifying procedure for voltammetric thick film carbon containing electrodes. *Electrochem commun* 9:221–227. <https://doi.org/10.1016/j.elecom.2006.09.003>
229. Zou Z, Jang A, MacKnight E, et al (2008) Environmentally friendly disposable sensors with microfabricated on-chip planar bismuth electrode for in situ heavy metal ions measurement. *Sensors Actuators, B Chem* 134:18–24. <https://doi.org/10.1016/j.snb.2008.04.005>
 230. Castañeda MT, Pérez B, Pumera M, et al (2005) Sensitive stripping voltammetry of heavy metals by using a composite sensor based on a built-in bismuth precursor. *Analyst* 130:971–976. <https://doi.org/10.1039/b502486m>
 231. Lezi N, Economou A, Dimovasilis PA, et al (2012) Disposable screen-printed sensors modified with bismuth precursor compounds for the rapid voltammetric screening of trace Pb(II) and Cd(II). *Anal Chim Acta* 728:1–8. <https://doi.org/10.1016/j.aca.2012.03.036>
 232. Hwang GH, Han WK, Park JS, Kang SG (2008) An electrochemical sensor based on the reduction of screen-printed bismuth oxide for the determination of trace lead and cadmium. *Sensors Actuators, B Chem* 135:309–316. <https://doi.org/10.1016/j.snb.2008.08.039>
 233. Kadara RO, Tothill IE (2008) Development of disposable bulk-modified screen-printed electrode based on bismuth oxide for stripping chronopotentiometric analysis of lead (II) and cadmium (II) in soil and water samples. *Anal Chim Acta* 623:76–81. <https://doi.org/10.1016/j.aca.2008.06.010>
 234. Cerovac S, Guzsvány V, Kónya Z, et al (2015) Trace level voltammetric determination of lead and cadmium in sediment pore water by a bismuth-oxychloride particle-multiwalled carbon nanotube composite modified glassy carbon electrode. *Talanta* 134:640–649. <https://doi.org/10.1016/j.talanta.2014.12.002>
 235. Riman D, Jirovsky D, Hrbac J, Prodromidis MI (2015) Green and facile electrode modification by spark discharge: Bismuth oxide-screen printed electrodes for the screening of ultra-trace Cd(II) and Pb(II). *Electrochem commun* 50:20–23. <https://doi.org/10.1016/j.elecom.2014.11.003>
 236. Chamjangali MA, Kouhestani H, Masdarolomoor F, Daneshinejad H (2015) A voltammetric sensor based on the glassy carbon electrode modified with multi-walled carbon nanotube/poly(pyrocatechol violet)/bismuth film for determination of cadmium and lead as environmental pollutants. *Sensors*

- Actuators, B Chem 216:384–393. <https://doi.org/10.1016/j.snb.2015.04.058>
237. Uhl A, Kestranek W (1923) Die elektrometrische Titration von Säuren und Basen mit der Antimon-Indikatorelektrode. Monatshefte für Chemie und verwandte Teile anderer Wissenschaften 44:29–34.
<https://doi.org/10.1007/BF01526524>
 238. Stock JT, Purdy WC, Garcia LM (1958) The Antimony-Antimony Oxide Electrode. Chem Rev 58:611–626. <https://doi.org/10.1021/cr50022a001>
 239. Hocevar SB, Švancara I, Ogorevc B, Vytřas K (2007) Antimony Film Electrode for Electrochemical Stripping Analysis. Anal Chem 79:8639–8643.
<https://doi.org/10.1021/ac070478m>
 240. Serrano N, Díaz-Cruz JM, Ariño C, Esteban M (2016) Antimony- based electrodes for analytical determinations. TrAC Trends Anal Chem 77:203–213.
<https://doi.org/https://doi.org/10.1016/j.trac.2016.01.011>
 241. Maczuga M, Economou A, Bobrowski A, Prodromidis MI (2013) Novel screen-printed antimony and tin voltammetric sensors for anodic stripping detection of Pb(II) and Cd(II). Electrochim Acta 114:758–765.
<https://doi.org/https://doi.org/10.1016/j.electacta.2013.10.075>
 242. Kokkinos C, Economou A (2014) Disposable microfabricated 3-electrode electrochemical devices with integrated antimony working electrode for stripping voltammetric determination of selected trace metals. Sensors Actuators B Chem 192:572–577.
<https://doi.org/https://doi.org/10.1016/j.snb.2013.11.040>
 243. Nigović B, Hocevar SB (2011) Antimony film electrode for direct cathodic measurement of sulfasalazine. Electrochim Acta 58:523–527.
<https://doi.org/https://doi.org/10.1016/j.electacta.2011.09.087>
 244. Nigović B, Hocevar SB (2013) Square-wave voltammetric determination of pantoprazole using ex situ plated antimony-film electrode. Electrochim Acta 109:818–822. <https://doi.org/https://doi.org/10.1016/j.electacta.2013.07.173>
 245. Rodríguez JA, Juárez MG, Galán-Vidal CA, et al (2015) Determination of Allura Red and Tartrazine in Food Samples by Sequential Injection Analysis Combined with Voltammetric Detection at Antimony Film Electrode. Electroanalysis 27:2329–2334.
<https://doi.org/https://doi.org/10.1002/elan.201500295>
 246. Gibaja C, Assebban M, Torres I, et al (2019) Liquid phase exfoliation of

- antimonene: systematic optimization, characterization and electrocatalytic properties. *J Mater Chem A* 7:22475–22486.
<https://doi.org/10.1039/C9TA06072C>
247. Ren X, Li Z, Qiao H, et al (2019) Few-Layer Antimonene Nanosheet: A Metal-Free Bifunctional Electrocatalyst for Effective Water Splitting. *ACS Appl Energy Mater* 2:4774–4781. <https://doi.org/10.1021/acsaem.9b00423>
 248. Martínez-Periñán E, Down MP, Gibaja C, et al (2018) Antimonene: A Novel 2D Nanomaterial for Supercapacitor Applications. *Adv Energy Mater* 8:1–8. <https://doi.org/10.1002/aenm.201702606>
 249. Gao Y, Tian W, Huo C, et al (2019) Tailoring natural layered β -phase antimony into few layer antimonene for Li storage with high rate capabilities. *J Mater Chem A* 7:3238–3243. <https://doi.org/10.1039/C8TA11218E>
 250. Gusmão R, Sofer Z, Bouša D, Pumera M (2017) Pnictogen (As, Sb, Bi) Nanosheets for Electrochemical Applications Are Produced by Shear Exfoliation Using Kitchen Blenders. *Angew Chemie Int Ed* 56:14417–14422. <https://doi.org/https://doi.org/10.1002/anie.201706389>
 251. Marzo AML, Gusmão R, Sofer Z, Pumera M (2020) Towards Antimonene and 2D Antimony Telluride through Electrochemical Exfoliation. *Chem - A Eur J* 1–8. <https://doi.org/10.1002/chem.201905245>
 252. Li L, Zhang D, Cao M, et al (2020) Electrochemical synthesis of 2D antimony, bismuth and their compounds. *J Mater Chem C* 8:9464–9475. <https://doi.org/10.1039/D0TC01960G>
 253. Gibaja C, Assebban M, Torres I, et al (2019) Liquid phase exfoliation of antimonene: systematic optimization, characterization and electrocatalytic properties. *J Mater Chem A* 7:22475–22486. <https://doi.org/10.1039/C9TA06072C>
 254. Linarez Pérez OE, Pérez MA, Teijelo ML (2009) Characterization of the anodic growth and dissolution of antimony oxide films. *J Electroanal Chem* 632:64–71. <https://doi.org/https://doi.org/10.1016/j.jelechem.2009.03.018>
 255. Neupane S, Mishra D, Nakarmi KB, et al (2021) Preparation of antimony oxide in different media and its effect on the pH measurement. *Anal Bioanal Electrochem* 13:127–138
 256. Dean JA (1995) *Basics of Electrochemical Impedance Spectroscopy*. Princet Applied Res

257. Hsu CH, Mansfeld F (2001) Concerning the conversion of the constant phase element parameter Y_0 into a capacitance. *Corrosion* 57:747–748.
<https://doi.org/10.5006/1.3280607>
258. Mohammad A, Ahmad K, Qureshi A, et al (2018) Zinc oxide-graphitic carbon nitride nanohybrid as an efficient electrochemical sensor and photocatalyst. *Sensors Actuators B Chem* 277:467–476.
<https://doi.org/https://doi.org/10.1016/j.snb.2018.07.086>
259. Yuan S, Bo X, Guo L (2018) In-situ growth of iron-based metal-organic framework crystal on ordered mesoporous carbon for efficient electrocatalysis of p-nitrotoluene and hydrazine. *Anal Chim Acta* 1024:73–83.
<https://doi.org/https://doi.org/10.1016/j.aca.2018.03.064>
260. Ahmad K, Mohammad A, Mobin SM (2017) Hydrothermally grown α -MnO₂ nanorods as highly efficient low cost counter-electrode material for dye-sensitized solar cells and electrochemical sensing applications. *Electrochim Acta* 252:549–557.
<https://doi.org/https://doi.org/10.1016/j.electacta.2017.09.010>
261. Fakhari AR, Ahmar H (2011) A new method based on headspace adsorptive accumulation using a carboxylated multi-walled carbon nanotubes modified electrode: application for trace determination of nitrobenzene and nitrotoluene in water and wastewater. *Anal Methods* 3:2593–2598.
<https://doi.org/10.1039/C1AY05302G>
262. Yang R, Wei Y, Yu Y, et al (2012) Make it different: The plasma treated multi-walled carbon nanotubes improve electrochemical performances toward nitroaromatic compounds. *Electrochim Acta* 76:354–362.
<https://doi.org/https://doi.org/10.1016/j.electacta.2012.05.029>
263. Lee J-Y, Lin Y-J (2016) Effect of incorporation of black phosphorus into PEDOT:PSS on conductivity and electron–phonon coupling. *Synth Met* 212:180–185. <https://doi.org/https://doi.org/10.1016/j.synthmet.2015.12.018>
264. Wang Z, Gao L, Wei X, et al (2020) Energy level engineering of PEDOT:PSS by antimonene quantum sheet doping for highly efficient OLEDs. *J Mater Chem C* 8:1796–1802. <https://doi.org/10.1039/C9TC06049A>
265. Volkov A V, Wijeratne K, Mitraka E, et al (2017) Understanding the Capacitance of PEDOT:PSS. *Adv Funct Mater* 27:1700329.
<https://doi.org/https://doi.org/10.1002/adfm.201700329>

266. Hillman AR, Daisley SJ, Bruckenstein S (2008) Ion and solvent transfers and trapping phenomena during n-doping of PEDOT films. *Electrochim Acta* 53:3763–3771. <https://doi.org/10.1016/j.electacta.2007.10.062>
267. Feldberg SW (1984) Reinterpretation of polypyrrole electrochemistry. Consideration of capacitive currents in redox switching of conducting polymers. *J Am Chem Soc* 106:4671–4674. <https://doi.org/10.1021/ja00329a004>
268. Vacca A, Mascia M, Rizzardini S, et al (2015) Preparation and characterisation of transparent and flexible PEDOT:PSS/PANI electrodes by ink-jet printing and electropolymerisation. *RSC Adv* 5:79600–79606. <https://doi.org/10.1039/C5RA15295J>
269. OECD LU-O for EC and D (2003) 4-Nitrotoluene: SIDS initial assessment report for SIAM 17: Arona, Italy, 11-14 November 2003. UNEP Publications
270. Moreno MM, Garidel P, Suwalsky M, et al (2009) The membrane-activity of Ibuprofen, Diclofenac, and Naproxen: A physico-chemical study with lecithin phospholipids. *Biochim Biophys Acta - Biomembr* 1788:1296–1303. <https://doi.org/10.1016/j.bbamem.2009.01.016>
271. J. Carson, WM. Notis EO (1990) Colonic Ulceration and Bleeding during Diclofenac Therapy. *N Engl J Med* 323:135. <https://doi.org/10.1056/NEJM199007123230216>
272. Sondergaard KB, Weeke P, Wissenberg M, et al (2017) Non-steroidal anti-inflammatory drug use is associated with increased risk of out-of-hospital cardiac arrest: a nationwide case–time–control study. *Eur Hear J - Cardiovasc Pharmacother* 3:100–107. <https://doi.org/10.1093/ehjcvp/pvw041>
273. Zhang Y, Geißen S-U, Gal C (2008) Carbamazepine and diclofenac: Removal in wastewater treatment plants and occurrence in water bodies. *Chemosphere* 73:1151–1161. <https://doi.org/10.1016/j.chemosphere.2008.07.086>
274. Vieno N, Sillanpää M (2014) Fate of diclofenac in municipal wastewater treatment plant — A review. *Environ Int* 69:28–39. <https://doi.org/10.1016/j.envint.2014.03.021>
275. Pérez-Estrada LA, Malato S, Gernjak W, et al (2005) Photo-Fenton Degradation of Diclofenac: Identification of Main Intermediates and Degradation Pathway. *Environ Sci Technol* 39:8300–8306.

- <https://doi.org/10.1021/es050794n>
276. aus der Beek T, Weber F-A, Bergmann A, et al (2016) Pharmaceuticals in the environment—Global occurrences and perspectives. *Environ Toxicol Chem* 35:823–835. <https://doi.org/https://doi.org/10.1002/etc.3339>
 277. Hanif H, Waseem A, Kali S, et al (2020) Environmental risk assessment of diclofenac residues in surface waters and wastewater: a hidden global threat to aquatic ecosystem. *Environ Monit Assess* 192:204. <https://doi.org/10.1007/s10661-020-8151-3>
 278. (2013) Directive 2013/39/EU of the European Parliament and of the Council. *Fundam Texts Eur Priv Law* 2013:1–17. <https://doi.org/10.5040/9781782258674.0032>
 279. Cunha RR, Gimenes DT, Munoz RAA, et al (2013) Simultaneous determination of diclofenac and its common counter-ions in less than 1 minute using capillary electrophoresis with contactless conductivity detection. *Electrophoresis* 34:1423–1428. <https://doi.org/https://doi.org/10.1002/elps.201300008>
 280. González L, Yuln G, Volonté MG (1999) Determination of cyanocobalamin, betamethasone, and diclofenac sodium in pharmaceutical formulations, by high performance liquid chromatography. *J Pharm Biomed Anal* 20:487–492. [https://doi.org/https://doi.org/10.1016/S0731-7085\(99\)00046-1](https://doi.org/https://doi.org/10.1016/S0731-7085(99)00046-1)
 281. Arcelloni C, Lanzi R, Pedercini S, et al (2001) High-performance liquid chromatographic determination of diclofenac in human plasma after solid-phase extraction. *J Chromatogr B Biomed Sci Appl* 763:195–200. [https://doi.org/https://doi.org/10.1016/S0378-4347\(01\)00383-8](https://doi.org/https://doi.org/10.1016/S0378-4347(01)00383-8)
 282. Paíga P, Santos LHMLM, Delerue-Matos C (2017) Development of a multi-residue method for the determination of human and veterinary pharmaceuticals and some of their metabolites in aqueous environmental matrices by SPE-UHPLC–MS/MS. *J Pharm Biomed Anal* 135:75–86. <https://doi.org/https://doi.org/10.1016/j.jpba.2016.12.013>
 283. Kimuam K, Rodthongkum N, Ngamrojanavanich N, et al (2020) Single step preparation of platinum nanoflowers/reduced graphene oxide electrode as a novel platform for diclofenac sensor. *Microchem J* 155:104744. <https://doi.org/https://doi.org/10.1016/j.microc.2020.104744>
 284. Goyal RN, Chatterjee S, Rana ARS (2010) The effect of modifying an edge-

- plane pyrolytic graphite electrode with single-wall carbon nanotubes on its use for sensing diclofenac. *Carbon N Y* 48:4136–4144.
<https://doi.org/https://doi.org/10.1016/j.carbon.2010.07.024>
285. Karuppiah C, Cheemalapati S, Chen S-M, Palanisamy S (2015) Carboxyl-functionalized graphene oxide-modified electrode for the electrochemical determination of nonsteroidal anti-inflammatory drug diclofenac. *Ionics (Kiel)* 21:231–238. <https://doi.org/10.1007/s11581-014-1161-9>
 286. Arvand M, Gholizadeh TM, Zanjanchi MA (2012) MWCNTs/Cu(OH)₂ nanoparticles/IL nanocomposite modified glassy carbon electrode as a voltammetric sensor for determination of the non-steroidal anti-inflammatory drug diclofenac. *Mater Sci Eng C* 32:1682–1689.
<https://doi.org/https://doi.org/10.1016/j.msec.2012.04.066>
 287. Costa-Rama E, Nouws HPA, Delerue-Matos C, et al (2019) Preconcentration and sensitive determination of the anti-inflammatory drug diclofenac on a paper-based electroanalytical platform. *Anal Chim Acta* 1074:89–97.
<https://doi.org/https://doi.org/10.1016/j.aca.2019.05.016>
 288. Aguilar-Lira GY, Álvarez-Romero GA, Zamora-Suárez A, et al (2017) New insights on diclofenac electrochemistry using graphite as working electrode. *J Electroanal Chem* 794:182–188.
<https://doi.org/https://doi.org/10.1016/j.jelechem.2017.03.050>
 289. de Carvalho RC, Betts AJ, Cassidy JF (2020) Diclofenac determination using CeO₂ nanoparticle modified screen-printed electrodes – A study of background correction. *Microchem J* 158:105258.
<https://doi.org/https://doi.org/10.1016/j.microc.2020.105258>
 290. Shalauddin M, Akhter S, Basirun WJ, et al (2019) Hybrid nanocellulose/f-MWCNTs nanocomposite for the electrochemical sensing of diclofenac sodium in pharmaceutical drugs and biological fluids. *Electrochim Acta* 304:323–333.
<https://doi.org/https://doi.org/10.1016/j.electacta.2019.03.003>
 291. Mekassa B, Baker PGL, Chandravanshi BS, Tessema M (2018) Synthesis, characterization, and preparation of nickel nanoparticles decorated electrochemically reduced graphene oxide modified electrode for electrochemical sensing of diclofenac. *J Solid State Electrochem* 22:3607–3619. <https://doi.org/10.1007/s10008-018-4071-3>
 292. Elbalkiny HT, Yehia AM, Riad SM, Elsayharty YS (2019) Potentiometric

- diclofenac detection in wastewater using functionalized nanoparticles. *Microchem J* 145:90–95.
<https://doi.org/https://doi.org/10.1016/j.microc.2018.10.017>
293. Amra S, Bourouina M, Bourouina Bacha S, Hauchard D (2021) Preconcentration and Successful Selective Detection of Traces of Diclofenac in Water using a Nanostructured Modified Carbon Paste Electrode. *Electroanalysis* 33:936–946.
<https://doi.org/https://doi.org/10.1002/elan.202060415>
 294. Eteya MM, Rounaghi GH, Deiminiat B (2019) Fabrication of a new electrochemical sensor based on AuPt bimetallic nanoparticles decorated multi-walled carbon nanotubes for determination of diclofenac. *Microchem J* 144:254–260. <https://doi.org/https://doi.org/10.1016/j.microc.2018.09.009>
 295. Cid-Cerón MM, Guzmán-Hernández DS, Ramírez-Silva MT, et al (2016) NEW INSIGHTS ON THE KINETICS AND MECHANISM OF THE ELECTROCHEMICAL OXIDATION OF DICLOFENAC IN NEUTRAL AQUEOUS MEDIUM. *Electrochim Acta* 199:92–98.
<https://doi.org/https://doi.org/10.1016/j.electacta.2016.03.094>
 296. Zhang C (John), Park S-H, O'Brien SE, et al (2017) Liquid exfoliation of interlayer spacing-tunable 2D vanadium oxide nanosheets: High capacity and rate handling Li-ion battery cathodes. *Nano Energy* 39:151–161.
<https://doi.org/https://doi.org/10.1016/j.nanoen.2017.06.044>
 297. Chen Y, Muthukumar K, Leban L, Li J (2020) Microwave-assisted high-yield exfoliation of vanadium pentoxide nanoribbons for supercapacitor applications. *Electrochim Acta* 330:135200.
<https://doi.org/https://doi.org/10.1016/j.electacta.2019.135200>
 298. Li L, Peng S, Wu H Bin, et al (2015) A Flexible Quasi-Solid-State Asymmetric Electrochemical Capacitor Based on Hierarchical Porous V₂O₅ Nanosheets on Carbon Nanofibers. *Adv Energy Mater* 5:1500753.
<https://doi.org/https://doi.org/10.1002/aenm.201500753>
 299. Lavagnini I, Antiochia R, Magno F (2004) An extended method for the practical evaluation of the standard rate constant from cyclic voltammetric data. *Electroanalysis* 16:505–506. <https://doi.org/10.1002/elan.200302851>
 300. Klingler RJ, Kochi JK (1981) Electron-transfer kinetics from cyclic voltammetry. Quantitative description of electrochemical reversibility. *J Phys*

- Chem 85:1731–1741. <https://doi.org/10.1021/j150612a028>
301. Randviir EP (2018) A cross examination of electron transfer rate constants for carbon screen-printed electrodes using Electrochemical Impedance Spectroscopy and cyclic voltammetry. *Electrochim Acta* 286:179–186. <https://doi.org/10.1016/j.electacta.2018.08.021>
 302. Ferrari AGM, Foster CW, Kelly PJ, et al (2018) Determination of the electrochemical area of screen-printed electrochemical sensing platforms. *Biosensors* 8:1–10. <https://doi.org/10.3390/bios8020053>
 303. Goyal RN, Chatterjee S, Agrawal B (2010) Electrochemical investigations of diclofenac at edge plane pyrolytic graphite electrode and its determination in human urine. *Sensors Actuators B Chem* 145:743–748. <https://doi.org/https://doi.org/10.1016/j.snb.2010.01.038>
 304. Bard AJ, Faulkner Larry R. (2001) *Electrochemical methods : Fundamentals and Applications*, Wiley, New York
 305. Mostafavi M, Yaftian MR, Piri F, Shayani-Jam H (2018) A new diclofenac molecularly imprinted electrochemical sensor based upon a polyaniline/reduced graphene oxide nano-composite. *Biosens Bioelectron* 122:160–167. <https://doi.org/https://doi.org/10.1016/j.bios.2018.09.047>
 306. Shalauddin M, Akhter S, Bagheri S, et al (2017) Immobilized copper ions on MWCNTS-Chitosan thin film: Enhanced amperometric sensor for electrochemical determination of diclofenac sodium in aqueous solution. *Int J Hydrogen Energy* 42:19951–19960. <https://doi.org/https://doi.org/10.1016/j.ijhydene.2017.06.163>
 307. Zhang C, Cao Z, Zhang G, et al (2020) An electrochemical sensor based on plasma-treated zinc oxide nanoflowers for the simultaneous detection of dopamine and diclofenac sodium. *Microchem J* 158:105237. <https://doi.org/https://doi.org/10.1016/j.microc.2020.105237>
 308. Hussien EM, Derar AR (2019) Selective Determination of Diclofenac and Clomiphene with a Single Planar Solid-State Potentiometric Ion Selective Electrode. *J Electrochem Soc* 166:B780–B786. <https://doi.org/10.1149/2.0701910jes>
 309. Das T, Tosoni S, Pacchioni G (2019) Structural and electronic properties of bulk and ultrathin layers of V₂O₅ and MoO₃. *Comput Mater Sci* 163:230–240. <https://doi.org/https://doi.org/10.1016/j.commatsci.2019.03.027>

Synopsis

Bismuth-based electrodes have been proved the most reliable replacement of highly toxic mercury for the anodic stripping (AS) and cathodic voltammetric determination of metal ions and organic compounds, respectively. In the first section of the experimental part (**Chapter 4**), we report for the first time on the implementation of two-dimensional (2D) bismuth, called “bismuthene”, for the AS voltammetric determination of Pb(II) and Cd(II) ions. Bulk bismuth was exfoliated by a facile and fast shear-force liquid phase exfoliation method. Exfoliated bismuthene layers were characterized by means of SEM, EDX, Raman, FT-IR, electrochemical impedance spectroscopy and cyclic voltammetry. Bismuthene colloids were mixed with dispersions of few-layer graphene, which was used as supporting material in order to achieve the desired adherence of bismuthene films onto the surface of glassy carbon electrode (GCE) as well as an effective electrical communication between them and with the electrode surface. The optimum loading of bismuthene in the bismuthene/graphene composite (2D-Bi/Gra) was investigated, while other parameters such as the deposition time and deposition potential were also examined. Under selected conditions and for a 3 min preconcentration time, the limit of detection (S/N 3) of each target ion was 0.3 mg L^{-1} . 2D-Bi/Gra/GCEs were successfully applied to the determination of Pb and Cd in tap water samples in the presence of potassium hexacyanoferrate(II) for the alleviation of copper interference. Results suggest that 2D bismuthene/graphene modified electrodes offer great promise for the determination of sub-microgram per liter Pb and Cd and could contribute greatly in heavy metal ions and other organic compounds sensing applications.

In the second section of the experimental part (**Chapter 5**), we present the production of antimonene nanosheets and the *in-situ* preparation of antimonene oxide/PEDOT:PSS nanocomposite via tip sonication of bulk β -phase antimony in water and aqueous PEDOT:PSS, respectively. Nanomaterials were characterized via SEM, EDX, XRD, FT-IR, electrochemical impedance spectroscopy and cyclic voltammetry, while the resulting modified graphite screen-printed electrodes (Sbene/SPE and Sbene oxide/PEDOT:PSS/SPE, respectively) were evaluated in the cathodic determination of 4-nitrotoluene (4-NT), which was used as a model compound, in the presence of dissolved oxygen and in deoxygenated environments. Data document the electrochemical passivation of Sbene/SPEs, which, on the one hand, demonstrate a beneficial poor activity towards the oxygen reduction reaction, and on the other hand, enhanced detection capabilities, thus allowing the determination of 4-NT at the micromolar concentration level at non-deoxygenated solutions. As a result, passivated Sbene/SPEs show great promise in sensing applications outside of the laboratory where the deoxygenation of the samples is a big obstacle. Data demonstrate enhanced detection capabilities for Nafion membrane protected Sbene oxide/PEDOT:PSS/SPEs, in deoxygenated solutions, which exhibit a detection range from 50 to 5000 nM 4-NT, while achieving an LOD of 16.7 nM (S/N 3). Nafion membrane is essential for the reusability of the electrodes. Sbene oxide/PEDOT:PSS/SPE was also used to the analysis of a spiked river water sample. Recovery was 97.9%.

The third and final section of the experimental part (**Chapter 6**) reports on the utilization of vanadium pentoxide nanosheet (V_2O_5 NS)-modified screen-printed electrodes (SPEs) for the nanomolar voltammetric determination of diclofenac (DCF). V_2O_5 NSs were produced with a facile bath sonication method in a blend of 75/25% v/v H_2O /isopropyl alcohol. The morphological, structural, and electrochemical

characteristics of exfoliated V_2O_5 NSs were evaluated via scanning electron microscopy, X-ray diffraction, infrared spectroscopy, cyclic voltammetry (CV) and electrochemical impedance spectroscopy (EIS). V_2O_5 NSs showed a 2D morphology with most layers having dimensions of a few micrometers. Diagnostic CV studies using 5-hydroxydiclofenac or 2-(2-hydroxyphenyl) acetic acid, which have been proposed in literature to be involved in the electro oxidation of DCF, suggested that the actual mechanism is more complicated and need to be further elucidated. CV and EIS data demonstrated that at $\text{pH} > 6$ V_2O_5 NSs deprived of their characteristic pseudocapacitive properties offering low background signals and enhanced electrocatalytic properties toward DCF. Among different preconcentration treatments examined, a short (192 s) cyclic potentiodynamic treatment was found to exhibit a stable, semi reversible pair of peaks of increased magnitude with successive cycles, and low background signal. The quantification of DCF was conducted using differential pulse voltammetry. A well-defined oxidation peak at ca. 380 mV at pH 7 vs. Ag/AgCl/3 M KCl was recorded and its height was found to be linearly correlated with the concentration of DCF over the range 20-200 nM, while a limit of detection ($3S_x/\text{slope}$) of 3.1 nM was achieved. The response of V_2O_5 NS/SPE was evaluated against common interfering compounds, while the accuracy of the method was evaluated in spiked tap water samples.

Σύνοψη

Τα ηλεκτρόδια με βάση το βισμούθιο έχουν αποδειχθεί τα πιο αξιόπιστα υποκατάστατα του εξαιρετικά τοξικού υδραργύρου για τον ανοδικό αναδιαλυτικό και τον καθοδικό βολταμμετρικό προσδιορισμό μεταλλικών ιόντων και οργανικών ενώσεων, αντίστοιχα. Στο πρώτο κομμάτι του πειραματικού μέρους (**Κεφάλαιο 4**) αναφέρεται για πρώτη φορά η σύνθεση και εφαρμογή του δισδιάστατου (2D) βισμούθιου, που ονομάζεται "βισμούθενιο", για τον βολταμμετρικό προσδιορισμό των ιόντων Pb(II) και Cd(II). Η απομόνωση φύλλων βισμούθενίου πραγματοποιήθηκε με μια εύκολη και γρήγορη μέθοδο αποφυλλοποίησης υγρής φάσης μέσω διάτμητικών τάσεων. Τα φύλλα βισμούθενίου χαρακτηρίστηκαν με διάφορες τεχνικές όπως SEM, EDX, Raman, FT-IR, φασματοσκοπία ηλεκτροχημικής εμπεδής και κυκλική βολταμμετρία. Τα κολλοειδή σωματίδια βισμούθενίου αναμίχθηκαν με εναιωρήματα ολιγοστρωματικού γραφενίου, το οποίο χρησιμοποιήθηκε ως υποστηρικτικό υλικό προκειμένου να επιτευχθεί η επιθυμητή προσκόλληση των φύλλων βισμούθενίου στην επιφάνεια του ηλεκτροδίου υαλώδους άνθρακα (GCE) καθώς και μια αποτελεσματική ηλεκτρική επικοινωνία τόσο μεταξύ τους όσο και με την επιφάνεια του ηλεκτροδίου. Διερευνήθηκε η βέλτιστη αναλογία βισμούθενίου στο σύνθετο υλικό βισμούθενιο/γραφενίου (2D-Bi/Gra), ενώ εξετάστηκαν και άλλες παράμετροι όπως ο χρόνος και το δυναμικό εναπόθεσης. Υπό τις επιλεγμένες συνθήκες και για χρόνο προσυγκέντρωσης 3 λεπτών, το όριο ανίχνευσης (S/N 3) για το κάθε κατιόν βρέθηκε $0,3 \mu\text{g L}^{-1}$. Τα ηλεκτρόδια 2D-Bi/Gra/GCE χρησιμοποιήθηκαν με επιτυχία στον προσδιορισμό ιόντων Pb(II) και Cd(II) σε δείγματα νερού βρύσης παρουσία σιδηροκυανιούχου καλίου που αποσκοπεί στην άρση της παρεμπόδισης ιόντων χαλκού. Σύμφωνα με τα πειραματικά δεδομένα, τα ηλεκτρόδια 2D-Bi/Gra/GCE μπορούν να χρησιμοποιηθούν για τον προσδιορισμό ιόντων Pb(II) και Cd(II) σε συγκεντρώσεις μικρότερες του ενός μικρογραμμαρίου ανά λίτρο (ppb) και δυνητικά θα μπορούσαν να χρησιμοποιηθούν και για τον προσδιορισμό διάφορων οργανικών ενώσεων οι οποίες παρουσιάζουν οξειδοαναγωγικές ιδιότητες σε συμβατικά ηλεκτρόδια βισμούθιου.

Στο δεύτερο κομμάτι του πειραματικού μέρους (**Κεφάλαιο 5**), αναφέρεται η παραγωγή νανοφύλλων αντιμονενίου και η επί τόπου παρασκευή του οξειδίου του αντιμονενίου/PEDOT:PSS νανοςύνθετου υλικού με υπέρηχους σε μείγμα από αντιμόνιο β-κρυσταλλικής φάσης και υδατικό διάλυμα PEDOT:PSS. Τα νανοϋλικά χαρακτηρίστηκαν με διάφορες τεχνικές όπως SEM, EDX, XRD, FT-IR, φασματοσκοπία ηλεκτροχημικής εμπεδής και κυκλική βολταμμετρία. Τα προκύπτοντα τροποποιημένα ηλεκτρόδια γραφίτη που παρασκευάστηκαν με εκτύπωσης μέσω πλέγματος (Sbene/SPE και Sbene oxide/PEDOT:PSS/SPE, αντίστοιχα) χρησιμοποιήθηκαν για τον καθοδικό προσδιορισμό του 4-νιτροτολουολίου (4-NT), το οποίο χρησιμοποιήθηκε ως πρότυπη ένωση, παρουσία διαλυμένου οξυγόνου και σε αποοξυγονωμένα διαλύματα. Τα δεδομένα τεκμηριώνουν την ηλεκτροχημική παθητικοποίηση του Sbene/SPE, η οποία, αφενός, μειώνει την ηλεκτροκαταλυτική απόδοση των ηλεκτροδίων στην αναγωγή του διαλυτού οξυγόνου, αφετέρου, επιτρέπει τη χρήση τους για τον προσδιορισμό του 4-NT σε μη αποοξυγονωμένα διαλύματα σε επίπεδο μικρομοριακών συγκεντρώσεων. Ως αποτέλεσμα, το παθητικοποιημένο Sbene/SPE μπορεί να χρησιμοποιηθεί σε αναλυτικές εφαρμογές εκτός εργαστηρίου όπου η αποοξυγόνωση των δειγμάτων αποτελεί περιοριστικό παράγοντα. Σύμφωνα με τα πειραματικά δεδομένα τα ηλεκτρόδια Sbene/PEDOT:PSS/SPE, σε αποοξυγονωμένα διαλύματα και μετά την

κάλυψη της επιφάνειας τους με Nafion, παρουσιάζουν πολύ καλή αναλυτική συμπεριφορά για τον προσδιορισμό του 4-NT. Η γραμμική περιοχή της μεθόδου εκτείνεται στο εύρος συγκεντρώσεων από 50 έως 5000 nM 4-NT, ενώ το LOD βρέθηκε 16,7 nM (S/N). Επίσης τα ηλεκτρόδια Sbene/PEDOT:PSS/SPE χρησιμοποιήθηκαν με επιτυχία για τον προσδιορισμό του 4-NT σε ένα εμβολιασμένο δείγμα νερού ποταμού. Η ανάκτηση ήταν 97,9%. Στο τρίτο και τελευταίο κομμάτι του πειραματικού μέρους (**Κεφάλαιο 6**), παρουσιάζεται η χρήση ηλεκτροδίων γραφίτη τροποποιημένων με νανοφύλλα πεντοξειδίου του βαναδίου (V_2O_5 NS) για τον βολταμμετρικό προσδιορισμό της δικλοφενάκης (DCF). Τα V_2O_5 NSs παρήχθησαν με μια εύκολη μέθοδο σε λουτρό υπερήχων σε μείγμα 75/25% v/v H_2O /ισοπροπυλική αλκοόλη. Τα μορφολογικά, δομικά και ηλεκτροχημικά χαρακτηριστικά των αποφυλλοποιημένων V_2O_5 NSs αξιολογήθηκαν με διάφορες τεχνικές όπως SEM, XRD, FT-IR, φασματοσκοπία ηλεκτροχημικής εμπέδησης και κυκλική βολταμμετρία. Τα V_2O_5 NSs έδειξαν δισδιάστατη μορφολογία με τις περισσότερες στρώσεις να έχουν διαστάσεις λίγων μικρομέτρων. Πραγματοποιήθηκαν διαγνωστικές μελέτες κυκλικής βολταμμετρίας παρουσία 5-υδροξυδικλοφενάκης ή 2-(2-υδροξυφαινυλ) οξικού οξέος, τα οποία σύμφωνα με τη βιβλιογραφία παράγονται ως ενδιάμεσα και συμμετέχουν στην ηλεκτροοξείδωση της DCF. Τα αποτελέσματα υποδεικνύουν ότι ο πραγματικός μηχανισμός είναι πιο περίπλοκος και πρέπει να διευκρινιστεί περαιτέρω. Τα δεδομένα κυκλικής βολταμμετρίας και φασματοσκοπίας ηλεκτροχημικής εμπέδησης έδειξαν ότι σε pH>6 τα V_2O_5 NSs στερούνται των χαρακτηριστικών ψευδοχωρητικών ιδιοτήτων τους, προσφέροντας χαμηλά σήματα υποβάθρου και βελτιωμένες ηλεκτροκαταλυτικές ιδιότητες προς την DCF. Μεταξύ των διαφορετικών μεθόδων προσυγκέντρωσης που εξετάστηκαν, τα καλύτερα αποτελέσματα παρατηρήκαν με την εφαρμογή μια σύντομης (192 δευτερόλεπτα) κυκλικής βολταμμομετρικής μεθόδου η οποία οδηγεί στη λήψη αυξημένων σημάτων, ανά διαδοχικούς κύκλους, και χαμηλό σήμα υποβάθρου. Η ποσοτικοποίηση της DCF πραγματοποιήθηκε με διαφορική παλμική βολταμμετρία ως προς το ύψος της κορυφής οξείδωσης η οποία καταγράφεται περίπου στα 380 mV σε pH 7 ως προς το ηλεκτρόδιο αναφοράς Ag/AgCl/3 M KCl. Το μετρούμενο ρεύμα συσχετίζεται γραμμικά με τη συγκέντρωση της DCF στην περιοχή 20-200 nM. Το όριο ανίχνευσης βρέθηκε (3Sx/κλίση) βρέθηκε 3,1 nM. Στην συνέχεια εξετάστηκε η παρεμποδιστική δράση διαφόρων ουσιών και τέλος, τα προτεινόμενα ηλεκτρόδια χρησιμοποιήθηκαν για τον προσδιορισμό της DCF σε εμβολιασμένα δείγματα νερού δικτύου.

Publications

- A.C. Lazanas, K. Tsirka, A.S. Paipetis, M.I. Prodromidis*, 2D bismuthene/graphene modified electrodes for the ultra-sensitive stripping voltammetric determination of lead and cadmium, *Electrochim. Acta.* 336 (2020) 135726.
- A.C. Lazanas, M.I. Prodromidis*, Two-dimensional inorganic nanosheets: production and utility in the development of novel electrochemical (bio)sensors and gas-sensing applications, *Microchim. Acta.* 188 (2021) 6.
- A.C. Lazanas, M.I. Prodromidis*, Electrochemical performance of passivated antimonene nanosheets and of in-situ prepared antimonene oxide-PEDOT:PSS modified screen-printed graphite electrodes, *Electrochim. Acta.* 410 (2022) 140033.
- A.C. Lazanas, M.I. Prodromidis*, Large surface vanadium pentoxide nanosheet modified screen-printed electrode for nanomolar diclofenac determination, *Electrochim. Acta.* (2022) 140919.

Conference presentations

- **A. Lazanas, A. Paipetis, M. Prodromidis**, *Advanced sensors for heavy metals based on monoelemental 2d bismuthene and graphene nanocomposites produced by shear-force liquid exfoliation*, Euroanalysis XX Conference, 1st – 5th September 2019, Istanbul, Turkey. Poster presentation.
- **A. Lazanas, A. Paipetis, M. Prodromidis**, *Advanced sensors for heavy metals based on monoelemental 2d bismuthene and graphene nanocomposites produced by shear-force liquid exfoliation*, 11th International Conference on Instrumental Methods of Analysis (IMA 2019), 22nd– 25th September 2019, Ioannina, Greece. Poster presentation.
- **A. Lazanas, M. Prodromidis**, *Utilization of semiconducting bismuthene, antimonene and V₂O₅ 2D nanosheets in electrochemical sensing*, Trends in nanotechnology conference 2021, 4th – 8th October 2021, Tirana, Albania. Oral presentation (A. Lazanas).
- **A. Lazanas, M. Prodromidis**, *Two-dimensional Pnictogens (Monoelemental Nanosheets of Bi or Sb) as Transducing Materials in Electrochemical Sensing*, Sensors 2021, 20th - 22nd October, Milan, Italy. Poster presentation.
- **A. Ch. Lazanas, M. I. Prodromidis**, *Large surface vanadium pentoxide nanosheet modified screen-printed electrode for nanomolar diclofenac determination*, 11th European conference on pesticides and related organic micropollutants in the environment, 23rd – 27th June 2022, Ioannina, Greece. Oral presentation (A. Lazanas).